# THE TECTONIC EVOLUTION OF THE PIONEER METAMORPHIC CORE COMPLEX, SOUTH-CENTRAL IDAHO

by

David Scott Silverberg

B.S., Magna Cum Laude, Geology, Western Washington University
1983

M.S., Geology, Western Washington University
1985

Submitted to the Department of
Earth, Atmospheric, and Planetary Sciences
In Partial Fulfillment of the Requirements for the Degree of

Doctor of Philosophy

at the

Massachusetts Institute of Technology

June, 1990



Signature of Author: _____
Department of Earth, Atmospheric & Planetary Sciences, M.I.T.

Certified by: _____
Dr. Kip V. Hodges
Thesis Supervisor

Accepted by: _____
Dr. Thomas H. Jordan
Chairman, Department of Earth, Atmospheric & Planetary Sciences

# THE TECTONIC EVOLUTION OF THE PIONEER METAMORPHIC CORE COMPLEX, SOUTH-CENTRAL IDAHO

by

David Scott Silverberg

Submitted to the Department of Earth, Atmospheric, and Planetary Sciences
on June 12, 1990 in partial fulfillment of the requirements for the degree of
Doctor of Philosophy

## ABSTRACT

South-central Idaho had a tectonic evolution characterized by a Jurassic to Cretaceous continental magmatic arc (the Bitteroot Batholith) accompanied by compression in the Sevier fold and thrust belt to the east. This was followed by crustal extension in the hinterland of the Sevier Belt during the Eocene Challis magmatic episode. Eocene extension ranges from the Shuswap Complex in British Columbia to the north margin of the Snake River Plain. Oligocene to Miocene extension has been documented in the northern Basin and Range just south of the Snake River Plain. The WNW-ESE axis of extension for this event was similar to that for Eocene extension in the Bitteroot Mylonite Zone, 300 km north of the Snake River Plain. This study addresses aspects of the tectonic evolution of the Pioneer Metamorphic Core Complex, the first exposure of middle-crust metamorphic tectonites north of the Snake River Plain. This area is unique in that it separates two regions of extension with similar kinematics but different ages of extension, and the extension post-dates compression by a minimum of 30 million years, suggesting no dynamic linkage between compression and extension.

The infrastructure of the Pioneer Metamorphic Core Complex comprises a parautochthonous basement, one compression-related nappe, and three extension-related allochthons. The structural framework is a result of at least three distinct episodes of extensional deformation of Paleogene age superimposed on Mesozoic Sevier compressional structures. In total, five deformational events are observed in the infrastructure of the Pioneer Metamorphic Core Complex.

$D_1$ structures are observed only in the lowest structural level, the parautochthonous basement. Characterization of this event is difficult due to penetrative $D_2$ deformation. Isoclinal $F_2$ folds in the parautochthon and three metasedimentary allochthons are overturned to the east. High-grade metamorphism of the parautochthon and a minimum of greenschist facies metamorphism of the allochthons accompanied this deformation. $F_2$ folds locally double the stratigraphic thickness of the allochthons. A single $D_2$ thrust fault, which delineates the Pioneer Cabin nappe, crosscuts early $F_2$ folds in its footwall. A drag fold in the hanging wall indicates east-directed transport. The autochthon cooled below 800 K by 79 Ma, an age similar to that of many other magmatic, metamorphic and deformational events in the region.

$D_3$ extension resulted in the development of three extensional allochthons: the Southeast Corner Allochthon, the Paymaster Allochthon and the Big Basin Allochthon. Extensional faults propagated down-section until the Hyndman Shear Zone decoupled the metasedimentary allochthons from the parautochthon. At roughly 48 Ma the Pioneer Intrusive Suite (coeval with the Challis volcanic-plutonic episode in this region) was

emplaced along the still active or re-activated Hyndman Shear Zone. It is plausible that some of the early extensional faulting grouped here with $D_3$ is actually Cretaceous in age. In any case, the advective thermal pulse caused by the intrusion of the Pioneer Intrusive Suite in Eocene time resulted in a low pressure - high temperature metamorphism. Moderate development of a shear foliation in the Pioneer Intrusive Suite and adjacent country rock suggests waning movement in the Hyndman Shear Zone. Low-angle normal-sense shear with hanging wall transport to the south-southwest is constrained by mylonitic lineations and asymmetric fabrics. Thermobarometric calculations suggest maximum pressures of roughly 360 MPa at temperatures in excess of 950 K. Final equilibration of pelitic schists in the Late Eocene at roughly 240 MPa and 840 K, suggests a decompressional pressure-temperature path that has a nominal slope of 1.3 MPa/K, implying roughly 4.4 km of unroofing. When coupled with thermochronometric data, this suggests a time-integrated unroofing rate of 1.5 km/my from 48 to 45 Ma, compatible with either very rapid erosion or active tectonic unroofing.

$D_4$ extension was characterized by motion along the Wildhorse Detachment Fault System. This fault system has both ductile and brittle components. Ductile deformation is restricted to a less than 150 m wide shear zone that crosscuts all previous structures in the Wildhorse Gneiss Complex, the East Fork Group and the Pioneer Intrusive Suite. Lineations are constant in trend, N68°W, along variously oriented segments of the shear zone suggesting that the original shear zone geometry was curviplanar. Quartz fabrics, asymmetric porphyroclasts, and S-C fabrics suggest that the hanging wall moved down to the WNW. Final equilibration of metamorphic pelites constrains the maximum paleodepth of the footwall to be 7.5-8.4 km at the onset of Oligocene extension. Mylonites from the shear zone cooled roughly 50 K/my from 36 to 33 Ma, effectively dating ductile deformation on at least one segment of the fault. As the infrastructure passed through the ductile-brittle transition, brittle structures overprinted earlier ductile structures and a series of brittle detachment faults developed, some of which incised the infrastructure. The eastern margin of the core is bound by a late-$D_4$ antithetic fault, the White Mountain Fault, here considered part of the Wildhorse Detachment Fault System. Tectonic models for regional Oligocene extension in south-central Idaho must accomodate the inferred 23 km maximum horizontal slip of the Wildhorse Detachment Fault System.

$D_5$ faults are moderately dipping normal faults with stratigraphic throw less than 200 m. They are observed in the footwall, hanging wall, and cross-cutting the Wildhorse Detachment Fault System. The associated deformation was strictly brittle and may be associated with Miocene to recent ENE-WSW extension.

Thesis Supervisor:

Dr. Kip V. Hodges, Associate Professor of Geology

## ACKNOWLEDGEMENTS

M.I.T. is a strange, sometimes trying, yet wonderful institution in which to pursue advanced research. An individual brings with him all the baggage and biases of his foundational studies and finds any assumptions quickly challenged by a highly eager community of proven and aspiring scholars. Inevitably, this close-knit working and recreating group develops into something akin to a dysfunctional family, replete with much joy and turmoil, as intense individuals and relationships evolve. The extended family stretches to Harvard University, with whom most of us have significant collegial professional ties.

Acknowledgements as such, are often testimonials of eternal gratitude to those with whom we passed this shared experience of four to seven years. Five years in the life of this young scientist inevitably included friendships and collegial relations that were born, developed, sometimes flowered and sometimes died. For a field tectonicist, professional perception invariably develops through the exposure to different approaches, different orogenic belts, and different flavors of practicing geoscientists. From 1985 to 1990, the Cambridge geoscience community provided what was the most exciting group of field tectonics-oriented scientists collected in one city in a long while, perhaps akin to the Bay area (Berkeley & Stanford) in the 1960's.

There have been many remarkable moments of discovery and learning, both scientific and cultural. Gregory Bateson's old adage of "the map is not the territory" was driven home in countless exposures to new territory and novel ways of mapping that territory. In the more obvious sense, watching B.C. Burchfiel spontaneously pick up a piece of chalk and draw several complete cross-sections through the European Alps. And then in a more abstract sense, such as in the rites of J.B. Thompson's courses when he would consider an n-component system, take an analytic tack, plot that system in free energy-entropy-volume space and then translate that into a geometrical solution. In both of these cases, perspective proved essential. The relevance of the solutions, in these cases models of crustal architecture or chemical systems, were only so valuable as they helped explain natural phenomena. These types of pedagogical experiences proved to me that the aesthetic fulfillment of good science rivals any other for the initiated secular humanist.

The graduate seminars of 1985-1988 were superb opportunities for scientific discourse and cooperative learning exercises. These seminars were facilitated by Terri Bowers, Clark Burchfiel, Phil England, Tim Grove, Stan Hart, Kip Hodges, Tom Jordan,

Patrick LeFort, Marsha McNutt, Wiki Royden, Jane Selverstone, J.B. Thompson, and Brian Wernicke. Graduate student participants in these seminars included: Roy Adams, Elaine Aliberti, Ximena Barrientos, David Dinter, Cindy Ebinger, Tanya Furman, Philippe Gurriet, Don Hickmot, Mary Hubbard, Tom Juster, Jim Knapp, Bryan Kriens, Allison MacFarlane, Larry McKenna, Laurence Page, Carolyn Ruppel, Barbara Sheffels, Vincent Salters, Liz Schermer, Tom Sisson, Zeke Snow, Joann Stock, Kurt Sternlof, Cathy Summa, Peter Tilke, Dan Tormey, Mark Van Baalen, Gilles Wust. This wild and crazy group of people did a rather remarkable dance that dove deep in the well of scientific and human potential. I am grateful to them all.

The opportunities to work in the Pioneer Mountains of Idaho, the Garwhal Himalaya of India, and the Pennine Alps of Switzerland and Italy were greatly facilitated by my Ph.D. advisor Kip Hodges. Kip's office door was always open and his particular flair for the interdisciplinary approach to problems in tectonics is rather unique. His knack for identifying the best natural experiments and getting research projects funded through the National Science Foundation provided me financial support for the first four years of this study. The comraderie and empathy he showed for my work in the lesser-developed world (India) and the over-developed world (Switzerland) led to many a hysterical moment. Having arrived in India an orthodox atheist, I returned to America a fanatical atheist. Kip seemed to understand. The "colorforms" society of Ketchum, Idaho was rather plain in comparison, but provided the testing ground for many of the scientific approaches I attempted to master during my tenure at M.I.T..

The technical and secretarial support at M.I.T. from Nancy Dallaire, Anita Killian, Liz Scorsello, Meredith Smith and Judith Stein helped me through the administrative ropes.

The last year of this study was supported by my employment at The Center for Field Research-Earthwatch, a non-profit organization dedicated to bridging scholarly research with public education. The office I have shared with archaeologists, anthropologists, biologists, public health specialists, writers and photographers has proven the most remarkable place to decompress imaginable. As one's eyes turn from the mountains to the people and back again, the perspectives offered by my peers at Earthwatch, particularly in cultural anthropology, have been priceless. The staff at The Center for Field Research have been insightful and a joy to work with: Jim Chiarelli, Sharon Collinge, Dick Estes, Margaret MacLean, Heidi Palola, Dee Robbins, Brian Rosborough, Peggy Savage and Catherine Schlager. The beauty engendered by social and natural science investigations

facilitated by this organization has in a certain sense revitalized my love for humanity and I am forever in their debt.

Many friends and family provided invaluable support and fun through the last five years. Paul Benzaquin, Joan Brody, Brian Burgoon, Susan & Stephen & Sonia Cropper, Peggy Dinter, Tim & Patricia East, Charles Earl, Marc Fawcett, Victoria Freeman, Rohann Gregory, Elana Greenfield, Marc James, Roger Karapin, Dara Kessler, Eric Kessler, Jane Loubier, John & Pam & Pat MacFarlane, Angela McKormick, Mary Jo Naive, Sharon O'Brien, Greg Reller, Jim Sevigny, Mildred Silverberg, Stuart & Mesa Somer, Liz Spizman must all be thanked for helping put things in perspective on many occasions. My parents, Joan Podel, and Jack & Eileen Silverberg provided the genes and nurturing environment essential for an inquisitive life. Their love is so deep and so unqualified, their humor so uplifting, that I feel profoundly fortunate to be their son.

My sincerest appreciation and love goes to Allison Macfarlane. She has been remarkably supportive and understanding while I worked on this dissertation. Her intelligence, beauty, spirit and humor are more than I ever expected to find when I moved to Cambridge five years ago. The two years we have made a home together on Beacon Hill have been the most wonderful of my life.

## TABLE OF CONTENTS

PLATES

# INTRODUCTION

Cordilleran metamorphic core complexes are arched, isolated uplifts of metamorphic and plutonic rocks (the "infrastructure") juxtaposed by a normal-sense detachment fault system against a hanging wall of distended units that are usually unmetamorphosed ("the suprastructure"). They occur from British Columbia at least as far south as the Mojave Desert. Most contemporary studies have attempted to constrain the geometry, kinematics and timing of these core complexes in order to understand their tectonic significance.

The fact that many of these complexes occur in the hinterland of the Jurassic-Cretaceous Sevier-Laramide compressional belts suggested to many workers a dynamic linkage between compression and extension (e.g., Coney and Harmes, 1984). In early papers, workers suggested that the buoyant rise of these complexes activated the foreland fold and thrust systems (e.g., Price and Mountjoy, 1970). More recently, the reverse tack has been taken and the argument has been made that early compression and thickening of the crust resulted in extensional deviatoric stresses related to gravitational collapse (Wernicke et al., 1987). Unfortunately, the temporal relations between compression and extension vary greatly in the Cordillera and there is no simple short-term causal connection. It is equally plausible that the driving mechanism for early Tertiary extension in the North American Cordillera was similar to that which causes present-day extension in the Basin and Range Province.

The south-central Idaho region is of interest because it forms an apparent boundary between several distinctive tectonic provinces. It lies in the hinterland of the Mesozoic Sevier-Laramide compressional orogenic belt, the southern margin of a documented Eocene magmatic and extensional zone, the northern margin of an Oligocene to Miocene extensional zone, and the northern boundary of the Miocene to Recent Basin and Range

Province. Before this study, Oligocene extension had not been identified north of the Snake River Plain and the southern extent of Eocene extension was poorly understood.

This study addresses the tectonic evolution of the south-central Idaho region as elucidated in the infrastructure of the Pioneer Metamorphic Core Complex. An interdisciplinary effort which involved field mapping, microstructural analysis, quantitative metamorphic petrology, and $^{40}Ar$-$^{39}Ar$ thermochronology has constrained many aspects of the region's geologic history.

Fieldwork was conducted during the summers of 1985-1988. A geologic map was produced at a scale of 1:24,000 and is included as Plate 1. The JEOL 733 microprobe at MIT was used for the petrologic investigations. The $^{40}Ar$-$^{39}Ar$ analyses were done in Dr. John Sutter's laboratory at the USGS Reston facility. The results of this effort are presented in three separate chapters: 1) Multiphase extension in the south-central Idaho region: Structural evolution of the Pioneer Metamorphic Core Complex; 2) Petrologic constraints on the tectonic evolution of the Pioneer Metamorphic Core Complex: Depth-temperature-time paths in the upper amphibolite facies; and 3) Thermal evolution of the Pioneer Metamorphic Core Complex, south-central Idaho: Diachronous Paleogene extension of the middle crust. Each paper has been written in the style appropriate for the intended journal of publication (the *Geological Society of America Bulletin*, the *Journal of Petrology*, and *Tectonics*, respectively).

## References

Coney, P.J. and Harmes, T.A., 1984, Cordilleran metamorphic core complexes: Cenozoic extensional relics of Mesozoic compression, Geology, 12, p. 550-554.

Price, R.A. and Mountjoy, E.W., 1970, Geologic structure of the Canadian Rocky Mountains between Bow and Athabasca Rivers-A progress report: Geological Association of Canada Special Paper No. 6, p. 7-25.

Wernicke, B.P., Christiansen, R.L., England, P.C. and Sonder, L.J., 1987, Tectonomagmatic evolution of Cenozoic extension in the North American Cordillera., in *Continental Extensional Tectonics*, edited by Coward, M.P., Dewey, J.F. and Hancock, P.L., p. 203-221, Geological Society of London, Oxford.

# CHAPTER 1: MULTIPHASE EXTENSION IN THE SOUTH-CENTRAL IDAHO REGION: STRUCTURAL EVOLUTION OF THE PIONEER METAMORPHIC CORE COMPLEX

David S. Silverberg

***Abstract***

The infrastructure of the Pioneer Metamorphic Core Complex is a result of at least three distinct episodes of extensional deformation of Paleogene age superimposed on Mesozoic Sevier compressional structures. In total, five deformational events are observed in the infrastructure of the Pioneer Metamorphic Core Complex. $D_1$ structures are observed only in the lowest structural level, the parautochthonous basement composed of the Pre-cambrian (X?) Wildhorse Gneiss Complex. Characterization of this event is difficult due to penetrative $D_2$ deformation.

Isoclinal $F_2$ folds in the Wildhorse Gneiss Complex, the Pre-cambrian (Y?) Hyndman Group and the Ordovician East Fork Group are overturned to the east. High-grade metamorphism of the basement and a minimum of greenschist facies metamorphism of the Hyndman and East Fork Groups accompanied this deformation. $F_2$ folds locally double the stratigraphic thickness of the Hyndman and East Fork Groups. A single $D_2$ thrust fault, which delineates the Pioneer Cabin nappe, crosscuts early $F_2$ folds in its footwall. A drag fold in the hanging wall indicates east-directed transport. The basement cooled below 800K by 79 Ma, an age similar to that of many other magmatic, metamorphic and deformational events in the region.

$D_3$ extension resulted in the development of three extensional allochthons: the Southeast Corner Allochthon, the Paymaster Allochthon and the Big Basin Allochthon.

Extensional faults propagated down-section until the Hyndman Shear Zone decoupled the Hyndman and East Fork Groups from the parautochthon. At roughly 48 Ma the Pioneer Intrusive Suite (coeval with the Challis volcanic-plutonic episode in this region) was emplaced along the still active or re-activated Hyndman Shear Zone. It is plausible that some of the early extensional faulting grouped here with $D_3$ is actually Cretaceous in age. In any case, the advective thermal pulse caused by the intrusion of the Pioneer Intrusive Suite in Eocene time resulted in a low pressure - high temperature metamorphism. Moderate development of a shear foliation in the Pioneer Intrusive Suite and adjacent country rock suggests waning movement in the Hyndman Shear Zone. Low-angle normal-sense shear with hanging wall transport to the south-southwest is constrained by mylonitic lineations and asymmetric fabrics. Thermobarometric calculations suggest maximum pressures of roughly 360 MPa at temperatures in excess of 950 K. Final equilibration of pelitic schists in the Late Eocene at roughly 240 MPa and 840 K, suggests a decompressional pressure-temperature path that has a nominal slope of 1.3 MPa/K, implying roughly 4.4 km of unroofing. When coupled with recent thermochronometric data, this suggests a time-integrated unroofing rate of 1.5 km/my from 48 to 45 Ma, compatible with either "passive" or "active" tectonic unroofing.

$D_4$ extension was characterized by motion along the Wildhorse Detachment Fault System. This fault system has both ductile and brittle components. Ductile deformation is restricted to a less than 150 m wide shear zone that crosscuts all previous structures in the Wildhorse Gneiss Complex, the East Fork Group and the Pioneer Intrusive Suite. Lineations are constant in trend, N68°W, along variously oriented segments of the shear zone suggesting that the original shear zone geometry was curviplanar. Quartz fabrics, asymmetric porphyroclasts, and S-C fabrics suggest that the hanging wall moved down to the WNW. Final equilibration of metamorphic pelites constrains the maximum paleodepth

of the footwall to be 7.5-8.4 km at the onset of Oligocene extension. Mylonites from the shear zone cooled roughly 50 K/my from 36 to 33 Ma, effectively dating ductile deformation on at least one segment of the fault. As the infrastructure passed through the ductile-brittle transition, brittle structures overprinted earlier ductile structures and a series of brittle detachment faults developed, some of which incised the infrastructure. The eastern margin of the core is bound by a late-$D_4$ antithetic fault, the White Mountain Fault, here considered part of the Wildhorse Detachment Fault System. Tectonic models for regional Oligocene extension in south-central Idaho must accomodate the inferred 23 km maximum horizontal slip of the Wildhorse Detachment Fault System.

D5 faults are moderately dipping normal faults with stratigraphic throw less than 200 m. They are observed in the footwall, hanging wall, and cross-cutting the Wildhorse Detachment Fault System. The associated deformation is strictly brittle and may be associated with Miocene to recent ENE-WSW extension.

## *Introduction*

The "Eocene transition" of the inboard Pacific Northwest refers to a time interval of profound change from predominantly compressional and transpressive tectonics to extensional and transtensional tectonics in the hinterland of the Jurassic to Cretaceous Sevier-Laramide orogenic belt (Parrish and others, 1990). The age of preeminent compression ranged from Middle Cretaceous to Paleocene (Armstrong, 1975; Brown and others, 1986). The expanse of Eocene extension ranges from northern British Columbia to the eastern Snake River Plain of southern Idaho. Thus, The interval between the cessation of compressional orogeny and the onset of Eocene magmatism and extensional tectonics was highly variable along the length of the hinterland.

A second "transition" occurred with the cessation of Challis-age magmatism and extension in the Idaho and Canadian hinterland, and the development of the Cascade Arc system between 38 and 45 million years ago. This latter transition happens to coincide with the change in plate interaction at 40-42 Ma that is well documented by both hot spot (Engebretson and others, 1984) and global plate circuit (Stock and Molnar, 1988) reconstructions. Extension in the northern Great Basin had started by the Early to Middle Oligocene (Saltzer and Hodges, 1986; Silverberg and others, in preparation).

The thermal and mechanical effects of these two tectonic shifts are not well understood. The metamorphic tectonites of the inboard extensional domains may provide key data to constrain the relationships among plate margin interaction, compression, extension and volcanism. In mid-crustal exposures higher paleotemperatures facilitated kinetically rate-limited processes; ductile strain expresses paleodeviatoric stresses, and the topologies of depth-temperature-time curves constrain rate processes in the evolution of the uppermost lithosphere.

The Pioneer Metamorphic Core Complex of south-central Idaho provides six kilometers of structural relief in a superbly exposed window. The relatively limited extent of the extensional fabrics in the infrastructure allows observation of two pre-Tertiary compression-related fabrics. Mid-crustal metamorphic tectonites have been intruded by the Eocene Pioneer Intrusive Suite (Dover, 1981; Silverberg and others, in preparation). Lithologies within the complex, including the Pioneer Intrusive Suite, were further affected by three Tertiary extensional events. The intrusive and metasedimentary rocks provide constraints on the timing and style of unroofing mechanisms at mid- to upper-crustal depths in a region for which there have been few published data. In this paper, the great variety of structures observed are here described, interpreted, and placed in a regional framework.

## *Geologic Setting*

The Pioneer Mountains of south-central Idaho (latitude 43°45'N, longitude 114°E; Fig. 1) are located north of the Miocene Snake River Plain, east of the Cretaceous-Eocene Atlanta Lobe of the Idaho Batholith, south of the Salmon River Arch and west of the seismically active Lost River Range.

The Pioneer Mountains lie in the eroded Devonian-Missisipian Antler orogenic belt and the hinterland of the Jurassic-Cretaceous Sevier-Laramide orogenic belt. Estimates of the minimum amount of shortening in the Idaho-Wyoming sector of the Sevier foreland, derived from well-constrained palinspastic reconstructions, range from 140 to 150 km (Royse and others, 1975). The amount of Mesozoic shortening in the hinterland is presently not well constrained. Any attempt to estimate the amount of Mesozoic shortening in this zone must consider the superposition of large scale Cenozoic extension.

Tertiary extension has been documented along the eastern margin of the Bitterroot lobe (Garmezy and Sutter, 1983) and this suggests a possible southward extension of well documented Eocene extension in southern British Columbia (Parrish and others, 1985, Parrish and others, 1988). Still further south, the Trans-Challis Fault System (Bennett, 1986) is a system of normal and transfer faults that developed in central Idaho during the Challis volcanic and plutonic episode, roughly 46-52 million years ago (Armstrong, 1975). The Lewis and Clark Fault System is thought to delineate the northern margin of this fault system. There are no extensional structures of Challis age recognized south of the Snake River Plain.

Miocene to Holocene extensional faults occur directly to the east of the Pioneer Mountains in the Lost River, Lemhi and Beaverhead Ranges. A $M_S$=7.3 earthquake occurred at the base of the Lost River Range in 1983. The typical horst and graben

structural style dominates the topography in this region. Few faults with significant offset in the Pioneer Mountains are thought to be of late Tertiary age

### *Pioneer Metamorphic Core Complex*

Dover (1969, 1981, 1983) generated the first regional geologic map of the Pioneer Mountains (Fig. 2). Building on the work of Umpleby and others (1930), Cook (1956) and Holm (1962), Dover constrained the basic stratigraphic and structural geometric relations of the area. The lithostratigraphy of Dover (1983) was adopted for this study (Fig. 3). The basic structure of the Pioneer Mountains is best described in terms of a metamorphic and plutonic infrastructure, structurally overlain by a predominantly sedimentary and volcanic suprastructure (Fig. 4; Dover, 1966). The infrastructure may be subdivided further into: 1) a parautochthon, consisting of the Precambrian (X?) Wildhorse Gneiss Complex; 2) an allochthon which includes Precambrian-Ordovician high-grade metasediments of the Hyndman and East Fork Groups that occur in both compressional and extensional nappes; and 3) an intrusive complex (the Eocene Pioneer Intrusive Suite). The parautochthon crops out in two domal structures in Kane Creek and Wildhorse Creek (Fig. 2). The two areas are separated by a septum of the Eocene Pioneer Intrusive Suite that is predominantly granodioritic. It is impossible to determine if both areas are connected at depth or if one or both are actually floating in the Pioneer Intrusive Suite.

The Pioneer Intrusive Suite was emplaced roughly 48-50 million years ago (Zartman, unpublished; Silverberg and others, in preparation) at a depth of 11-13 km and was the heat source for a low pressure-high temperature metamorphism in rocks of the Hyndman and East Fork Groups (Silverberg, in preparation). The temperature exceeded 950 K at the thermal culmination (orthoclase-sillimanite zone).

The infrastructure is separated from the suprastructure by the Wildhorse Detachment Fault System (Wust, 1986, 1987). This fault system consists of a ductile shear zone, a sequence of brittle detachment faults and a late antithetic normal fault known as the White Mountain Fault.

The presence of brittle extensional structures at the suprastructure/infrastructure contact was first recognized by Holm (1962) and further documented by Dover (1966, 1969, 1981, 1982), O'Neill (1985), O'Neill and Pavlis (1985, 1988), and Wust (1985, 1986, 1987). O'Neill (1985) and Wust (1985) described ductile structures associated with extension, suggesting that these were limited in extent to a "carapace" of mylonitic quartzites at the structurally highest levels of the core in the Kane Creek area (Fig. 2). O'Neill and Pavlis (1988) cite Wust (1987) for brief descriptions of S-C fabrics although no data indicative of the sense of shear was published.

The suprastructure is a stack of both compressional and extensional nappes. They are composed of low-grade Ordovician to Permian sedimentary rocks. The 48 Ma Summit Creek Stock cuts across folds and thrust faults in the suprastructure (Dover, 1966; Zartman, unpublished; Silverberg and others, in preparation). The suprastructure is unconformably overlain by the Eocene Challis Volcanic sequence dated between 45-52 Ma in this region (Armstrong, 1975).

## Infrastructure Stratigraphy

*Precambrian(X?) Wildhorse Gneiss Complex*

Marbles and quartzofeldspathic, psammitic, and amphibolitic gneisses of the Wildhorse Gneiss Complex form the parautochthonous basement of the infrastructure (Figs. 2, 3 and 4) The presence of a metacarbonate horizon in the Wildhorse dome strongly suggests a sedimentary origin for some of the complex. The presence of meta-

pelitic interbeds suggests that the paragneiss protolith was an intercalated sequence of arkosic sandstone and mudstone. The sedimentary pile was then injected by a series of amphibolitic dikes and sills. Subsequently, these rocks were deformed and then injected by quartz monzonite magma that now contains xenoliths of the foliated country rock. The quartz monzonite subsequently attained a gneissic foliation that parallels the regional tectonite fabric.

Paragneisses and orthogneisses of the Wildhorse Gneiss complex give Rb-Sr whole-rock model ages that clearly identify the complex as Precambrian (Zartman, unpublished).

*Precambrian(Y?) Hyndman and Ordovician East Fork Groups*

Metapelites, quartzites, metaconglomerates, and calc-silicate gneisses of the Precambrian (Y?) Hyndman Group are unconformably overlain by the marbles and quartzites of the Ordovician East Fork Group. Following Dover (1981), four distinctive lithologic units were mapped separately for each group. The only fossil control is in the Kinnikinnik Quartzite Formation of the East Fork Group, which yields crinoids identified as Ordovician in age (Dover, 1981).

## Suprastructure Stratigraphy

The suprastructure nappe complex has been divided into four allochthonous units by Skipp (1987; Fig. 2). These low grade units are comprised of the Ordovician-Silurian Phi Kappa and Trail Creek Formations, the Devonian Milligan Formation , the Missisipian Copper Basin Formation and the Pennsylvanian to Permian Wood River Formation. Skipp (1987) interprets these allochthonous units to be part of three regional thrust plates: (1) the Phi Kappa plate (Dover, 1981), (2) the Copper Basin plate (Skipp and Hait, 1977), and (3) the Milligan-Wood River-Grand Prize thrust complex (Hall, 1986)

*Phi Kappa and Trail Creek Formations*

These lower Paleozoic units are dominantly siliceous argillite and siltstone. Minor amounts of carbonate and sandstone are present. They are interpreted to have been deposited in the outer continental shelf and continental slope environment. The lithologies are similar to those found in the Antler overthrust assemblage (Churkin, 1962).

*Devonian Milligan Formation*

The Milligan Formation consists of siliceous argillite. It has been correlated with the Woodruff Formation of the Antler overthrust assemblage (Poole, 1974).

*Mississippian Copper Basin Formation*

The Copper Basin Formation consists of argillite, siltstone, sandstone, quartzite-pebble conglomerate and carbonate. It has been correlated with various facies of the Antler Flysch Sequence (Nilsen, 1977).

*Pennsylvanian-Permian Wood River Formation*

The Wood River Formation consists of limestone and calcareous siltstone and sandstone. The faulted base is a chert-pebble conglomerate that has been previously interpreted as an unconformity with the underlying Milligan formation, hence the designation of a Wood River-Milligan-Grand Prize Thrust Complex (Hall, 1986). This formation has been correlated with the Antler Overlap sequence (Poole, 1974).

*Tertiary Redbed Conglomerate*

There are no documented Mesozoic sedimentary units in the Pioneer Mountains. A red conglomerate locally underlies the Challis Volcanics. Wust (1986) conducted a detailed study of this conglomerate and concluded that the clasts are derived from Paleozoic sedimentary units in the suprastructure.

## Igneous Rocks

Intrusive rocks in the Pioneer Mountains include three representatives of the Eocene Challis volcanic-plutonic event: the Pioneer Intrusive Suite, the Summit Creek Stock and the Challis Volcanics.

*Eocene Pioneer Intrusive Suite*

The Pioneer Intrusive Suite occurs in two distinct yet connected structural settings in the infrastructure (Fig. 2): (1) along the Hyndman Shear Zone where it separates the Wildhorse Gneiss unit from the Hyndman and East Fork Groups, and (2) in the eastern portion of the window where it forms a large stock-like body. It ranges in lithology from pyroxenite to quartz diorite to clinopyroxene-hornblende-biotite granodiorite to hornblende-biotite quartz monzonite (Dover, 1966, 1981; Silverberg and others, in preparation). The distribution of rock types is irregular, however the more felsic assemblages occur chiefly in the eastern part of the infrastructure.

Contact relations between the different compositional phases of the Pioneer Intrusive Suite are highly variable which is not unusual for a magmatic series. In the headwater cirque of Kane Creek, a contact between dark-colored hornblende-biotite granodiorite and light-colored biotite leucogranodiorite is sharply transitional over a 10 cm interval. The transition zone does not have a significant grain size differential, but rather is delineated by a change in the mode of mafic phases. Pegmatite and aplite veins crosscut the transitional

contact. Both granodiorite phases and the transition zone contain randomly oriented xenoliths (>20 cm, longest exposed dimension) of Wildhorse Gneiss Complex Mafic Gneiss that display a schistosity oblique to both the strike of the transition zone and the nearby country rock contact. This observation suggests that the contact is an effect of original magmatic differentiation, rather than cross-cutting intrusive relations.

In the eastern outcrop belt of the Pioneer Intrusive Suite quartz monzonite is the dominant phase with subordinate granodiorite. Large blocks of granodiorite are observed to have dikes and veins that feed from the enclosing quartz monzonite, suggesting that the quartz monzonite is younger than the granodiorite.

Undisturbed mafic dikes in the Wildhorse Gneiss Complex are correlative with the Pioneer Intrusive Suite. In addition, a series of aplitic and pegmatitic sills and dikes are observed to locally crosscut these late mafic dikes. These aplites and pegmatites may be late differentiates of the Pioneer Intrusive Suite. Observations by O'Neill and Pavlis (1988) in Kane Creek suggest that emplacement of the quartz monzonite phase at least locally outlasted granodioritic magmatism. In this same area, hornblende-biotite granodiorite fills fractures in the pyroxenite. Cross-cutting relations at internal contacts of the Pioneer Intrusive Suite indicate that the intruding rock is always more felsic than the intruded rock, suggesting the intrusive series is tapping a magma chamber undergoing differentiation. Many of the internal contacts are gradational.

The crystallization age of the eastern quartz monzonite phase is 48 Ma based on U-Pb isotopic analyses of zircon (Zartman, unpublished). The granodiorite phase of the Pioneer Intrusive Suite yields hornblende $^{40}Ar/^{39}Ar$ correlation ages and plateau dates of 54 Ma to 45 Ma (Silverberg and others, in preparation).

*Eocene Summit Creek Stock*

The Summit Creek Stock is located four kilometers northwest of the Pioneer Window. It intrudes into the Phi Kappa and Copper Basin Thrust plates and is a fine to medium grained quartz monzonite with an emplacment age of roughly 48 Ma (Armstrong, 1975; Zartman, unpublished; Silverberg and others, in preparation).

*Eocene Challis Volcanics*

The Challis volcanics are andesitic to rhyolitic flow rocks. They outcrop extensively in the suprastructure and can be found in fault contact with the infrastructure at several localities. The age of Challis volcanics in the Pioneer Mountains range from 46 Ma to 48 Ma (Armstrong, 1975).

## *Structural History*

Field data for this study were collected during the summers of 1985-1988. Fieldwork was largely restricted to the infrastructure and the Wildhorse Detachment Fault System. Observations of mesoscopic structures have been augmented with microstructural analysis of rocks in thin section which allows these lower-order fabrics to be related to large-scale structures. The temporal relationships of structures were determined using crosscutting relationships and available geochronologic data (Armstrong, 1975, 1976; Zartman, unpublished; Silverberg and others, in preparation). Inter-unit correlation of structures was made by comparison of the orientation, style and position in local temporal sequences. Five major groups of structures were distinguished that are likely to represent distinct episodes of deformation ($D_1$-$D_5$). Fig. 5 illustrates the deformation sequence for each rock unit. Fig. 6 illustrates the relationship between metamorphism and deformation for each event. Fig. 7 shows cooling curves for rock units as presented in Silverberg and others (in preparation). The deformation episodes are discussed from oldest to youngest.

## $D_1$

Structures associated with the earliest phase of deformation, $D_1$, are restricted to the Wildhorse Gneiss Complex. Only cryptic evidence of this deformation persists due to the penetrative nature of $D_2$ deformation. Evidence for this early event includes: (1) obscure $F_1$ folds that are later refolded by $D_2$ structures with associated development of dome and basin structures; (2) the preservation of an early schistosity in amphibolite and psammitic schist xenoliths (2 cm-3 m in length) in the orthogneiss, which contain an oblique $S_2$ schistosity. Holm (1962) presented alpha and beta plots of schistosity in the Wildhorse Dome that suggested an early regional folding event about an axis that plunges 15° to N70°W in the Wildhorse Creek Dome. Dover (1966) suggested the possibility of two stages of penetrative deformation. O'Neill and Pavlis (1987) reported obscure $F_1$ folds in the Kane Creek area. It is very difficult to discern the overall geometry of $D_1$ due to later deformation.

## $D_2$

### *Wildhorse Gneiss Complex*

*Descriptive Structural Geology*

In the Wildhorse Gneiss Complex (Fig. 8), the predominant fabric is a bedding-parallel schistosity, $S_2$, that is also largely parallel to the axial plane of $F_2$ folds. $F_2$ folds are tight to isoclinal with axial planes usually overturned to the northeast. In the calc-silicate marble unit, mesoscopic folds have amplitudes $> 2$ m with wavelengths of roughly 3 m. Figs. 9 and 10 are synoptic plots of poles to $S_2$ for both the Wildhorse Creek and the Kane Creek domes.

Short (<2 m) discrete shear zones offset distinctive mafic lithologic horizons, yet these themselves are truncated by a penetrative planar fabric in more felsic lithologies. This contrast in deformation mechanisms is probably the result of rheological contrast between the mafic and felsic lithologies.

*Physical Conditions and Timing*

The temperature attendant to $D_2$ is constrained by the presence of a garnet-sillimanite schist horizon in the Mafic Gneiss member of the Wildhorse Gneiss Complex. This lithologic horizon is discontinuous and locally separates into two or three roughly parallel layers that are interlayered with amphibolitic schist, psammitic schist, orthogneiss or granodiorite. The $S_2$ schistosity in the garnet-sillimanite schist is parallel to the $S_2$ schistosity in adjacent lithologies. The syn-kinematic metamorphic assemblage indicates upper amphibolite facies conditions in the orthoclase-sillimanite zone. Aplitic and pegmatitic sills and dikes, which locally cross cut the $S_2$ schistosity, feed from relatively undisturbed felsic layers of the gneissic tectonite. The high temperatures associated with $D_2$ locally outlasted deformation and resulted in partial melts of the paragneisses.

The minimum age of $D_2$ is constrained as pre-79 Ma by a hornblende $^{40}Ar/^{39}Ar$ plateau date from a sample of the Mafic Schist member, although several disturbed argon release spectra for amphiboles suggest ages as old as 138 Ma (Silverberg and others, in preparation).

*Interpretive Structural Geology*

Locally, a lineation is defined by feldspar porphyroclasts or syn-kinematic hornblende and sillimanite porphyroblasts. These latter mineral lineations are both parallel and orthogonal to fold axes. Asymmetry of feldspar porphyroclasts suggests transport to the

northeast, although asymmetric porphroclasts were not observed with enough frequency to give a statistically meaningful interpretation.

Normal-sense riedel-type shears in mafic lithologies indicate a top-to-the-NE sense of shear.

## *Hyndman and East Fork Groups*

### *Descriptive Structural Geology*

The Hyndman and East Fork Groups display only a single penetrative deformational fabric that is described as $D_2$ here because it is similar in geometry and style to that of $D_2$ in the Wildhorse Gneiss Complex. The dominant mesoscopic fabric is a schistosity that is parallel to compositional layering. An intersection lineation forms when the schistosity is slightly inclined to compositional layering.

$F_2$ fold forms are diverse. In the Pelitic Schist unit, the following fold types were observed: (1) shallow open folds with amplitude of 8 cm and wavelength of 40 cm; (2) tight chevron folds with amplitude of 1.2 m and wavelength of 40 cm; (3) overturned sub-isoclinal folds with amplitude 3.5 m and wavelength of 3.0 m; (4) large folds with amplitude greater than 50 meters overturned to the northeast. Fold limbs frequently display minor sympathetic folds with Z-forms on the upright western limbs. The development of such diverse fold types in a constant rheology is enigmatic and suggests heterogeneous strain.

In the Saturday Mountain Formation and the Banded Calc-Silicate unit, mesoscale tight to isoclinal folds are overturned to the northeast, with their lower limbs frequently attenuated and occasionally forming minor reverse faults. These folds range in amplitude from 40-60 cm with a wavelength of 50-60 cm; hinges vary from sharp to rounded.

The Hyndman and East Fork Groups crop out in three structural sheets bound by $D_3$ normal faults (Fig. 11): the Big Basin Allochthon, the Paymaster Allochthon and the SE Corner Allochthon. In addition there is one $D_2$ thrust nappe: the Pioneer Cabin Allochthon.

Big Basin Allochthon

For the Big Basin Allochthon, a synoptic plot of poles to $S_2$ schistosity shows a strong concentration in the NE quadrant (Fig. 12). A poorly defined girdle suggests later folding about an axis that plunges 2° to S55°E. $F_2$ axes in the Big Basin Sheet display a concentration in the NW and SE quadrants (Fig. 13). They fall roughly on a girdle that suggests the fold axes could have been rotated into the $D_2$ transport direction associated with compression along a NE-SW axis (28°; N47°E).

Paymaster Allochthon

For the Paymaster Allochthon, a synoptic plot of poles to schistosity weakly defines a girdle that suggests folding about an axis that plunges 18° to S4°E (Fig. 14). The inter-axial angle between the Big Basin and Paymaster Allochthon $F_2$ fold sets is 43°. The discordance in fold axes may be primary and reflect heterogeneous strain, or may be secondary and indicate $D_3$ clockwise rotation of the Paymaster Allochthon relative to the Big Basin Allochthon.

Southeast Corner Allochthon

The Southwest Corner Allochthon consists of the Kinnikinnik Quartzite and Ella Marble of the East Fork Group. The $S_2$ schistosity strikes NE with a moderate dip to the SE. It was not studied in detail.

Pioneer Cabin Thrust Nappe

North of Pioneer Cabin, along the Pioneer Cabin Ridge, a thrust sheet comprised of the Ella Marble and Kinnikinik Quartzite Formations is thrust over the Saturday Mountain Formation (Fig. 15). The fault cuts down-section placing the Ella Marble directly on top of the Saturday Mountain Formation. Approaching the fault plane, the Ella Marble forms an apparent drag fold. The late-$D_2$ fault plane crosscuts $F_2$ folds in the underlying Saturday Mountain Formation. Thus, thrust sense faulting followed the $D_2$ regional folding. The fault zone rocks are entirely recrystallized due to late-$D_3$ metamorphism. This is the only fault interpreted as a thrust fault in the infrastructure and is so interpreted because it places older over younger rock units and has a top-to-the-east sense of shear inferred from the drag fold.

*Physical Conditions and Timing*

All high temperature phases (garnet, sillimanite, andalusite, and cordierite) are post-kinematic with respect to the development of $S_2$ in the Hyndman and East Fork Groups. The present distribution of reaction isograds is an effect of the late-$D_3$ intrusion of the Eocene Pioneer Intrusive Suite (Silverberg, in preparation). At the farthest reaches of the thermal aurole associated with the Pioneer Intrusive Suite, in the Paymaster Allochthon, the mineral assemblages are indicative of upper greenschist facies. It is impossible to constrain $D_2$ conditions in the Big Basin Allochthon and the Hyndman and East Fork Groups as a whole due to subsequent $D_3$ deformation and late-$D_3$ metamorphism. If the $D_2$ folding event in the Hyndman and East Fork Groups is contemporaneous with that documented in the Wildhorse Gneiss Complex, its age predates low pressure-high temperature metamorphism by a minimum of 30 million years.

*Interpretive Structural Geology*

The $D_2$ folding events in the Wildhorse Gneiss Complex and the Hyndman and East Fork Groups were broadly co-axial. The systematic northwest trend of fold axes and northeastward overturning of folds observed in all metamorphic units of the infrastructure suggests a northeast vergence for $D_2$ deformation. It is plausible that the $F_2$ axes of the Big Basin Sheet have been rotated into the direction of transport in a large-scale sheath-fold manner. The Pioneer Cabin Thrust Nappe contains a drag fold in its hanging wall that suggests top-to-the-east sense of shear.

## $D_3$

### *Wildhorse Gneiss Complex*

For the Wildhorse Creek area, $S_2$ schistosity defines a girdle that strikes N59°E with a dip of 82° to the northwest (Fig. 9). This best cylindrical fit for the data suggests folding about an axis 8°, S31°E. For the Kane Creek area, $S_2$ schistosity defines a girdle that strikes N20°E with a dip of 77° to the east. This best cylindrical fit for the data suggests folding about an axis that plunges 13° to N70°W. The inter-axial angle for the $F_3$ fold axes in the Wildhorse and Kane Creek areas is 44°. These broad $F_3$ folds are most easily related to the $D_3$ extensional event along a NE - SW axis of extension. It is plausible that the domes experienced broad folding during uplift in response to tectonic unloading.

If the Wildhorse Creek and Kane Creek domes are coherently connected at depth the interaxial angle between $F_3$ fold axes in the domes may indicate dislocation and counter-clockwise rotation of the Kane Creek dome.

### *The Hyndman Fault System*

A number of faults that imbricate the Hyndman and East Fork Groups may be components of a linked extensional fault system that soles into the Hyndman Shear Zone, which in turn separates the Hyndman and East Fork Groups from the Wildhorse Gneiss Complex (Fig. 16). These previously unnamed faults were interpreted by Dover (1983) to have thrust displacement with hanging wall transport to the northeast. The fact that these faults always place younger rock units on older rock units suggests that they have normal-sense displacement. The faults cut $D_2$ fabrics in the adjacent units.

Fabrics in the fault zones are ductile, with brittle deformation locally overprinting ductile deformation, suggesting that some minor amount of reactivation has occurred. Many of the fault zone rocks are recrystallized suggesting movement prior to the late-$D_3$ metamorphism. The faults with observable displacement in this fault system are discussed below. Because the absolute and relative age of motion of the allochthons is not well constrained, they are discussed from the structurally highest allochthon downwards.

Southeast Corner Fault

The Southeast Corner Fault is a low- to moderate-angle fault that bounds the Southeast Corner allochthon in the southeastern corner of the infrastrucure. The fault plane is curviplanar and roughly wraps around the footwall following both the White Mountain Fault (striking NNE) and the southeastern limit of the Wildhorse Detachment Fault System (striking ENE). The dip of the fault, as determined by three-point solutions, ranges from 34°SE along its NE trace to 21° SE along its SW trace. It is a younger-over-older fault that places the Kinnikinnik Quartzite over the Clayton Mine Quartzite. Rocks within the Southeast Corner Fault zone were highly recrystallized during late $D_3$ metamorphism. The SW trace of the Southeast Corner Fault projects into the Wildhorse Detachment Fault System at an acute angle. The actual contact is covered by non-stratified deposits of glacial

drift. The NE trace of the Southeast Corner Fault projects into the Hyndman Shear Zone. This contact is covered by both nonstratified deposits of glacial drift and Holocene colluvium.

Interpretive Structural Geology

The curviplanar orientation of the fault may be primary or it may be a result of transposition associated with $D_4$ deformation. The post-kinematic recrystallization of the fault zone rocks prevents determination of transport direction and the only timing constraint is that they must be older than roughly 48 Ma, the minimum age of late-$D_3$ metamorphism.

Paymaster Fault

The Paymaster Fault is a low-angle fault that bounds the Paymaster Allochthon in the southern portion of the window. The strike and dip of the fault as determined by three-point solution is roughly N75°W 13°SW. The Paymaster Fault is a younger-over-older fault that places the Clayton Mine Quartzite over units in the Hyndman Group. The maximum amount of stratigraphic throw, 680 m, occurs in the East Fork of the Wood River where the Clayton Mine Quartzite rests directly on top of the Pelitic Schist Unit. The fault truncates large-scale $F_2$ folds in its footwall. Rocks within the Paymaster Fault zone were highly recrystallized during late-$D_3$ metamorphism, in a manner similar to rocks in the Southeastern Corner Fault zone

Interpretive Structural Geology

The discordance between the $D_2$ internal fabrics of the hanging wall (Paymaster allochthon) and those of the footwall (Big Basin allochthon) suggests that clockwise rotation of the Paymaster allochthon accompanied southwest-directed, normal-sense

displacement. In addition, along the western trace of the Paymaster Fault in Big Basin, distinctive marker horizons composed of the Clayton Mine Quartzite and Ella Marble in both the footwall and hanging wall indicate displacement of the hanging wall by clock-wise rotation and normal-sense shear. Eastward, the fault trace is highly oblique to the D3 shear fabrics within the Hyndman Shear Zone. Thus it would seem that most of the extension occurred prior to late-D3 emplacement of the Pioneer Intrusive Suite. The apparent sequence of activity of the Paymaster and Hyndman Fault zones suggests that propagation of extensional faults stepped down or incised into deeper structural levels. A corollary of this hypothesis is that the basal fault plane/surface intersection or "breakaway zone" (Gibbs, 1984) may have migrated northeastward with time.

Hyndman Shear Zone

The Wildhorse Gneiss Complex is separated from the Hyndman and East Fork Groups by the Hyndman Shear Zone. The Hyndman Shear Zone is the structurally lowest normal-sense shear zone exposed in the infrastructure. The Pioneer Intrusive Suite was emplaced along the shear zone. D3 deformation resulted in a locally mylonitic fabric in both the Pioneer Intrusive Suite and the Hyndman and East Fork Groups. The Wildhorse Gneiss Unit does not display an S3 foliation.

The Pelitic Schist member of the Hyndman Group is mylonitic at its contact with the granodiorite. The S3 shear fabric of the granodiorite is parallel to the S3 foliation of the Pelitic Schist. At distances greater than 25 m from the contact with the Pioneer Intrusive Suite, sillimanite porphyroblasts are randomly oriented. This suggests that shear was localized at the contact.

The contact between the Pioneer Intrusive Suite and the Wildhorse Gneiss Complex is quite sharp. Within 2-3 m of the contact, the intrusives become mylonitic with a moderately developed augen gneiss structure.

The shear foliation of the Pioneer Intrusive Suite is defined by preferred orientation of broken hornblende phenocrysts and a second generation of biotite (biotite II) that clearly post-dates broken primary biotite (biotite I). In rocks with a well-developed $S_3$ shear fabric, plagioclase and microcline display a moderate degree of cataclasis. Recrystallized quartz and mica fill the fractures in feldspar and hornblende. The long dimensions of oscillatory zones and albite law interfaces in the plagioclase phenocrysts are often sub-parallel to the shear foliation. Quartz sub-grains range in size from 0.1 to 0.2 mm and form lenticular zones. All phases display undulatory extinction. In some thin sections, microcline porphyroblasts were observed to crosscut the shear fabric.

Fig. 17 is a stereoplot of the $S_3$ shear foliation in the Pioneer Intrusive Suite within the Hyndman Shear Zone. It shows a mean dip of 33° to the southwest (2 sigma uncertainty= 4°). No mesoscopic folds of $D_3$ age were observed in the Pioneer Intrusive Suite.

Physical Conditions and Timing

Several observations suggest that the $S_3$ foliation of the early phases of the Pioneer Intrusive Suite is due to the superimposition of solid-state flow on magmatic flow. The orientation of the magmatic foliation and the high-temperature solid-state $S_3$ foliation are subparallel. This solid-state foliation is continuous with the $S_3$ shear foliation in the adjacent Pelitic Schist. Some of the early high-temperature porphyroblasts (sillimanite) in the adjacent pelitic mylonites are synkinematic with $S_3$ mylonitic fabrics. Reaction isograds wrap around the intrusives with grade dropping from sillimanite-orthoclase at the contact to andalusite at a distance of several hundred meters. Thus, the parallelism of the $D_3$ fabrics

in the intrusive suite and the pelitic schist, and the thermal connection between pelitic schist metamorphism and emplacement of the intrusives rather conclusively link these fabrics. The elongate shape of the western outcrop belt is consistent with emplacement in an active fault zone. The lack of any D3 fabric in the Wildhorse Gneiss Complex may be due to previous strain hardening associated with Mesozoic metamorphism and deformation.

The observation of megacrystic K-feldspars that crosscut the shear foliation in the Pioneer Intrusive Suite suggests that locally some amount of deformation occurred while final crystallization ensued. Dynamic recrystallization of feldspars requires temperatures above 725 K at natural strain rates. While D3 deformation of the immediately adjacent Pelitic Schist developed synchronously with sillimanite porphyroblast nucleation and growth, the garnets are largely late- to post-kinematic. Thus, garnet nucleation and growth post-dates that of sillimanite, and high temperature conditions persisted beyond movement in the D3 Hyndman Shear Zone. Despite this, deformation of the Pioneer Intrusive Suite mostly outlasted its own crystallization, at least at the contact margins.

Injection of the granodiorite phase caused localized melting of the Pelitic Schist. The Pelitic Schist is locally both an injection and partial melt migmatite. Rarely, leucosomes are observed to crosscut the D3 shear fabric. This indicates that heating and minor partial melting outlasted shear deformation, consistent with the observation of post-kinematic garnet porphyroblasts.

The Pioneer Intrusive Suite was emplaced at a depth of 11-14 km (Silverberg, in preparation). Hornblende barometry of the intrusives (both western granodiorite phase and eastern quartz monzonite phase) is consistent with geothermobarometry of pelitic hanging wall and footwall rocks relative to the Hyndman Shear Zone (Silverberg, in preparation). This suggests that the infrastructure was "locked" at the time of final equilibration of the samples. Given the post-kinematic nature of the garnets, little actual displacement could

have occurred along the Hyndman Shear Zone following the emplacement of the Pioneer Intrusive Suite. Final equilibration of pelitic schists and the granodiorite occurred at roughly 240 MPa and 840 K. Thus, assuming an average overburden density of 2750 $kg/m^3$, the petrologic data suggests a decompressional pressure-temperature path with a nominal slope of 1.3 MPa/K. This implies roughly 4.4 km of unroofing during the 48 - 45 Ma interval at a rate of 1.5 km/my.

The heterogeneity of fabric development in the Pioneer Intrusive Suite is partly controlled by the time in which a particular magmatic phase was emplaced. Since the $S_3$ fabric in the Hyndman Shear Zone apparently cuts across that of the Paymaster Fault, it follows that the bulk of $D_3$ extensional faulting occurred *before* emplacement of the Pioneer Intrusive Suite. The presence of extension that pre-dates intrusion of the Pioneer Intrusive Suite is consistent with Skipp's (1986) observations of pre-Challis extension in the Pioneer and nearby Lost River Mountains.

*Interpretive Structural Geology*

At the head of several valleys just south of the Pioneer Crest (West Fork of Hyndman Creek, Wilson Creek, Corral Creek, Zanskar Creek) a lineation within the $S_3$ shear fabric is defined by a preferred orientation of prismatic sillimanite needles. The lineations generally plunge to the south (Fig. 18).

The sense of shear was determined by observation of $D_3$ proto-mylonites in thin section. Detailed petrographic observations were made of thin sections cut parallel to the XZ plane and normal to the XY plane of the strain ellipse. Mica fish in psammitic interlayers and asymmetric feldspar porphyroclasts indicate normal-sense shear. The data suggests components of both dip-slip and oblique-slip displacement.

Minor intraformational shear zones that are sub-parallel to the Hyndman Shear Zone indicate normal-sense shear. Sense-of-shear indicators include intrafolial fold trains, asymmetric boudinage, meso- and megascopic displacement of lithologic horizons. These are consistent with the microstructural sense of shear indicators that also indicate dip-slip and oblique-slip displacement.

The amount of throw on the Hyndman fault is difficult to constrain. The pervasive high-grade metamorphism of the Wildhorse Gneiss Complex suggests a deep structural level during mid-Cretaceous metamorphism. Unfortunately, those rock units in the Wildhorse Gneiss Complex with appropriate mineral subassemblages for thermobarometry lie well within the contact aureole of the Pioneer Intrusive Suite.

## $D_4$

### *The Wildhorse Detachment Fault System*

The Wildhorse Detachment Fault System (Wust, 1987), separates unmetamorphosed suprastructure rocks from the igneous and metamorphic tectonites in the window (Fig. 2). The Wildhorse Detachment Fault System is comprised of numerous faults including: (1) the Wildhorse Shear Zone, (2) the Boulder Creek Fault of Holm (1962) and Dover (1966), (3) the Kane Creek Normal Fault of Dover (1966), (4) the Pioneer Fault of Dover (1966) where it bounds the window, (5) the White Mountain Fault (Dover, 1966); and (6) numerous unnamed brittle normal faults. Deformation progressed from ductile to brittle and structures will be discussed from oldest to youngest.

#### Wildhorse Shear Zone

The Wildhorse Shear Zone is a zone of non-coaxial laminar flow that clearly cuts across the older S-tectonite fabrics previously discussed. $D_4$ ductile deformation is present

from Summit Creek along the southwest margin of the core to Wildhorse Creek and Fall Creek along the core's northern margin. Ductile deformation within the Wildhorse Shear Zone is typified by Type II S-C mylonitic fabrics (Lister and Snoke, 1984) that crosscut the compositional layering and $S_2$ schistosity of the East Fork Formation and the upper portion of the Wildhorse Gneiss Complex including both quartzofeldspathic and mafic schist lithologies. It also crosscuts numerous aplitic dikes in pyroxenite and the $S_3$ shear foliation in granodiorite of the Eocene Pioneer Intrusive Suite. The width of the ductile shear zone ranges from a maximum of 200 to a minimum of 10 meters.

Along the western and northern portions of the shear zone, Type II S-C mylonites typify the ductile deformation. Distinctive S- and C- surfaces and a lineation are formed by a combination of both ductile and brittle deformation mechanisms. The degree of ductile deformation is a function of the modal percentage of minerals. Quartz and mica are dynamically recrystallized, whereas feldspar, pyroxene and amphibole display brittle deformation.

In pyroxenites, quartz diorites and quartz monzonites of the Pioneer Intrusive Suite, the $S_4$ shear foliation is defined by marginally chloritized biotite and the lineation is defined by trains of broken feldspar porphyroclasts. In contrast, the Kinnikinik Quartzite, psammitic schists of the Wildhorse Gneiss Unit and granodiorite and aplitic dikes of the Pioneer Intrusive Suite contain a mylonitic foliation defined by flattened elongate quartz and well-aligned variably chloritized mica. A distinctive stretched appearance and an asymmetry of feldspar porphyroclasts, as well as quartz deformation lamellae, are typical of the mylonitized granodiorite.

The variety of deformation styles is displayed well along the Wildhorse Shear Zone between Wildhorse Creek and Kane Creek. Aplitic dikes that intrude the Pioneer Intrusive

Suite pyroxenite are strongly mylonitic whereas the pyroxenite is intensely cataclastic. The pyroxenite is locally serpentinized and slickensides parallel the mylonitic lineations.

In quartzites the dominant megascopically visible mylonitic schistosity is defined by the $C_4$ surfaces (Fig. 19). $C_4$ surfaces are demarcated by ribbon aggregates of quartz. The $S_4$ surfaces are expressed by an alignment of elongate quartz subgrains and ribbon aggregates. The $S_4$ surfaces make an angle of 20-30° with the $C_4$ surfaces. Quartz subgrains range in size from 0.05-0.5 mm. Ribbon aggregates range in size from 0.2 to 2 mm. The subgrains have irregular form and display undulatory extinction, suggesting at least some component of low temperature plasticity. Feldspar porphyroclasts show no evidence of dynamic recrystallization.

The C-surfaces of psammitic schists of the Wildhorse Gneiss Complex and aplitic dikes of the Pioneer Intrusive Suite are defined by recrystallized quartz, white mica, biotite and chlorite. Along the Boulder Creek section of the Wildhorse Shear Zone, the $S_2$ foliation of the Wildhorse Gneiss Complex is transposed into the mylonitic C-surface. The prior orientation of the $S_2$ surfaces of the Wildhorse Gneiss Unit were sub-parallel to the WSZ and thus the transposition did not necessarily involve a great deal of displacement. In general, feldspar augen have asymmetric pressure shadows and tails that lie parallel to the dominant C-surfaces. Discontinuous microfolds are present.

In the vicinity of the west side of Kane Creek, strongly folded layers of psammitic schist (within the Wildhorse Mafic Gneiss) and calc-silicate schist (Ella Marble Formation) are interlayered with variably mylonitized hornblende granodiorite. $F_4$ axes strike N70°W with axial planes that are gently inclined to the northwest. These fold axes are parallel to the stretching lineation rather than the nearby $F_2$ fold axes. Outcrops that are roughly normal to $F_4$ fold axes display complete closure of F4 folds, suggesting a sheath geometry. Interlying zones of less strain are typified by NW trending $F_2$ axes. These $F_2$ folds are

overturned to the NE. As the Wildhorse Shear Zone is approached, the $S_2$ foliation and $F_2$ fold axes are highly variable due to movment along observable $D_4$ shear surfaces. Sheath folds are ubiquitous in this area and indicate high shear strain.

Fig. 20 is a series of equal area plots of poles to the $S_4$ mylonitic foliation in the Wildhorse Shear Zone. The foliation in the Wildhorse Shear Zone has a highly variable strike and dip. Along its N extent it strikes N72-88°E and dips 44-51° to the N. Along its southern extent it strikes N18°W and dips 39° to the SW. In the NW corner of the window it strikes N16°E and dips 30° to the NW. The change in strike is evenly transitional between these areas. The mylonitic lineation consistently plunges to the WNW (Fig. 21).

Related Minor Ductile Shear Zones

Discontinuous $D_4$ ductile shear zones ranging in width from 1 cm to 2 meters crosscut all rock types and previous fabrics in the footwall. The sparse occurrence and largely intraformational nature of these shear zones suggest that they do not account for a large amount of extension.

At Boulder Lake, the Eocene mafic dikes in the Wildhorse Gneiss Complex are cut by narrow shear zones with apparent normal displacements that range from centimeters to several meters.

In the headwater cirques of Hyndman Creek a discontinuous $D_4$ shear zone with maximum width of 2 m is entirely within the granodiorite of the Pioneer Intrusive Suite. This $D_4$ shear zone strikes N60°W with a dip of 32° to the northeast and crosscuts the $D_3$ shear fabric of the granodiorite. A lineation is defined by elongate feldspar porphyroclasts and quartz rods. The lineation is roughly horizontal, trending N60°W.

*Physical Conditions and Timing*

The fact that mylonitic deformation associated with the Wildhorse Shear Zone cuts through the middle quartzofeldspathic member, mafic member, and upper quartzofeldspathic member of the Wildhorse Gneiss, the Pioneer Intrusive Suite (granodiorite and late aplitic dikes), and the East Fork Formation suggests that localization of the D4 extensional shear zone was not controlled by pre-existing compression-related structures at mid-crustal depths. This finding is consistent with that of Wernicke and others (1985) for upper crustal extensional structures in the central Mormon Mountains of Nevada.

The temperature at which mylonitization occurred is not well constrained. Magnesio-hornblende phenocrysts display rim retrogression to actinolite. Chloritization of biotite, entirely cataclastic feldspar deformation, actinolitic alteration of fractured hornblende and thermochronometric data constrains mylonitization to have occurred under broadly defined greenschist facies conditions.

A non-actinolitic amphibole separate from a D4 shear-zone granodiorite yielded a $^{40}Ar/^{39}Ar$ plateau cooling age of 48 Ma , slightly older than hornblende plateau ages for the adjacent non-mylonitic granodiorite (45 Ma) and nearby Pelitic Schist Unit (45 Ma; Silverberg, 1988; Silverberg and others, in preparation). This supports the interpretation that temperatures attendant to D4 mylonitization were below roughly 800 K, the nominal closure temperature for Ar diffusion in amphibole. Unfortunately, it only provides a maximum age constraint for this shear zone. Biotite from this sample yields a $^{40}Ar/^{39}Ar$ fusion date of 35 Ma, consistent with the biotite ages for the Wildhorse Shear Zone.

D4 mylonitization appears to have occurred immediately before rapid cooling of shear zone rocks through the closure temperatures for argon diffusion in muscovite (36 Ma) , biotite (35 Ma) and orthoclase (33 Ma; Fig. 7; Silverberg and others, in preparation), roughly 625-475 K (McDougall and Harrison, 1988). During the Late Eocene, the rest of

the infrastructure had cooled at a moderate rate (20°/my) following emplacement of the Pioneer Intrusive Suite (Silverberg and others, in preparation). The infrastructure, outside of the intrusive thermal aureole, had cooled below the closure temperature of argon diffusion in K-feldspar by 44 Ma (Silverberg and others, in preparation). Rim thermobarometry suggests a maximum depth for the infrastructure in the Late Eocene of roughly 7.5-8.4 km. Any reasonable steady-state continental geotherm would probably have temperatures below 575 K at this depth. Thus a localized thermal event in the ductile shear zone is implied. It is plausible that the resetting of the argon isotopic sytem in the mylonites is due to a combination of advection of hot fluids into the shear zone, shear heating and possibly a reduction in the effective diffusion distance due to crystal-plastic deformation. The inferred cooling rate of 50 K/my is exceptionally rapid and is similar to the high dT/dt slopes of numerical models for extensional tectonic terranes (Ruppel and others, 1988). Although numerical models suggest that most of the conductive equilibration of the uplifted block occurs after extension, it is reasonable to interpret these cooling ages as dating the final stages of extension-related mylonitization.

The Oligocene age of ductile $D_4$ fabrics is consistent with the observation that Challis volcanics are not found in the infrastructure. Volcanic rocks are found at elevations in excess of 11,000 feet in the suprastructure and there are no recognized post-Challis normal faults with a large amount of throw. Thus we can not call on erosion to have removed all trace of Challis rocks from the infrastructure. Challis volcanism occurred before the final exposure of the core, and in fact, probably predated exposure of the core by a minimum of roughly 6 million years.

*Kinematics*

The Kinnikinik Quartzite Formation is the youngest footwall metasedimentary unit affected by the Wildhorse Shear Zone. In Kane Creek, Summit Creek, and Phi Kappa Creek, these quartzites display a well-developed Type II S-C mylonite fabric that grades, with distance from the detachment fault, to a non-mylonitic foliation more typical of the footwall metamorphic rocks. Quartz grains display undulose extinction and sutured grain boundaries. In the narrow S-surfaces, elongate subgrains of quartz have their long axes aligned at a 30° angle to the C-surface. Although the quartzite locally contains white mica and feldspar, three samples with relatively minor contaminants (P498 A and B, P48) were chosen for quartz crystallographic fabric study (Fig. 22). Despite the heterogeneous reorienting effects of the contaminant phases, the fabric patterns are likely to reflect the bulk shear sense.

The pole Figs. for quartz <a> axes were measured on sections oriented normal to C and containing the lineation with an automatic X ray texture goniometer operating in combined reflection and transmission mode at the ETH-Zurich, Switzerland. Measuring techniques and data processing routines are those reported in Schmidt and Casey (1986).

The a-pole Figs. for the three specimens are similar to one another and to the fabric plots of other quartzites with documented deformation histories of simple shearing (Schmidt and Casey, 1986; samples CC1 and R405). The presence of distinctly asymmetric fabrics in other lithologies cut by the Wildhorse Shear Zone and the constancy of the lineation regardless of the orientation of the cissailment surface is an argument against the role of a rotational component to the strain path in the context of pure shear.

For samples P498 A and B an angle of 18° separates the a-axis maximum and the c-surface. For sample P48 the equivelent angle is 11°. Following Schmidt and Casey (1986), the pole Fig. of P48 indicates a higher level of shear strain than those of P498AandB. The difference in a-axis maxima correlates to the transition from Type I c-

axis crossed girdles into single c-axis girdles (cf. Schmidt and Casey, 1986). Thus it is reasonable to conclude that this preferred alignment of a-axes reflects displacement that is parallel to the shear plane and in the shearing direction. The three quartz fabrics indicate a top-down-to-the-west sense of shear.

*Brittle Detachment Faulting*

A brittle detachment fault system consisting of multiple generations of oblique-slip and dip-slip normal faults bounds the core. The detachment fault is a zone of strictly brittle deformation. As it is approached from below, a fracture cleavage develops that is typically subparallel to the principle detachment surface. This fracture cleavage crosscuts all previously described fabrics. A breccia gradationally overlies all of the units cut by the Wildhorse detachment system. Brecciated $D_4$ mylonites are common. When ferromagnesian mineralogies are affected, the breccia is typically chloritic. The affected footwall units display curviplanar joints that anastomose around somewhat more coherent cataclastic pods. Joints and breccia zones have highly variable strikes.

The White Mountain Fault demarcates the eastern boundary of the Pioneer Metamorphic Core Complex (Dover, 1966). It strikes N30°E and dips 70° to the southeast. The fault places clastic rocks of the Copper Basin and Milligan Formations and andesites of the Challis volcanics over tectonites of the East Fork Group and the Pioneer Intrusive Suite. The White Mountain Fault is characterized by a 50 m wide zone of siliceous breccia composed of both footwall and hanging wall units. Numerous fractures parallel the fault trace. At the southern and northern limit of the White Mountain Fault, the fault truncates both the Wildhorse Shear Zone and the Wildhorse Detachment Fault System. The intersection of the faults is not exposed. The apparent displacement of geologic contacts within the suprastructure suggests a throw of less than 300 m.

Throughout the entire footwall, sparse brittle normal faults with small displacement strike N32°E with dip 64°NW. The surface of the fracture planes is often covered with chlorite and epidote; this indicates brittle failure under a broadly defined low-temperature variant of greenschist facies conditions. Slickenside lineations are downdip ranging from 30° to 60° toward N63-73°W. Along Pioneer Ridge, the Ella Marble Unit has calcite extension veins that strike N50-60°E and dip 70° to the SE and 80° to the NW. These brittle features suggest extension along a NW-SE axis.

The hanging wall of the Wildhorse Detachment Fault System does not display the degree of rotation associated with rollover that is observed in the hanging wall of many metamorphic core complexes. Nonetheless, along the northwest margin of the Pioneer Metamorphic Core Complex, Challis volcanics are observed to dip 10-25° to the east. It is difficult to discern the role of original depositional dip; however the relative consistency of the eastward dip suggests that some rollover of the hanging wall along the western edge of the infrastructure is present.

*Interpretive Structural Geology*

Recently, several workers have studied the brittle component of the Wildhorse Detachment Fault System. O'Neill (1985) studied the detachment where it crosscuts the quartz monzonite phase of the Pioneer Intrusive Suite along the north margin of the window in the Fall Creek area. He concurred with Dover's (1966) observations of a 20 m wide, moderately north-dipping zone of chloritic breccia. An Arnaud (1969) analysis of fault planes and slickenside orientations within the breccia indicated an oblique (sinistral and normal) northwest movement of the hanging wall for the latest displacement along the detachment in this area.

Kim (1986) conducted a similar study at several locations along the Wildhorse Detachment Fault System, including: (1) Boulder Creek, (2) Phi Kappa Creek, (3) Corral Creek, (4) Paymaster Gulch. Artaud analyses at these locations consistently indicate hanging wall vergence to the WNW. These data are consistent with the interpretation that brittle deformation in the Wildhorse Detachment Fault System developed along the same axis of extension as that of ductile deformation in the Wildhorse Shear Zone.

The White Mountain Fault does not significantly downdrop the Wildhorse Shear Zone. The orientation of the White Mountain Fault suggests it is an antithetic fault that is part of the Wildhorse Detachment Fault System. Since displacement is limited, the absence of the Wildhorse Shear Zone is enigmatic and suggests that the shear zone dips eastward along the eastern margin of the infrastructure.

The presence of a minor rollover structure along the western margin of the infrastructure suggests that the Wildhorse Detachment Fault System may be somewhat listric at depth. It is impossible to constrain the nature of the fault geometry at depth given the present data. Given the pre-$D_4$ 7.5-8.4 km maximum paleodepth of the infrastructure and the lack of any higher detachment fault systems yet recognized, it is reasonable to assume this to be a maximum throw on the Wildhorse Detachment Fault System. If the curviplanar Wildhorse Detachment Fault System dips 20° in the direction of transport, than a minimum displacement of 25 km is inferred. Given the probable listric nature of the Wildhorse Detachment Fault System, displacement would decrease at depth until it equaled the associated heave of 23 km. Thus, the Boulder Mountains to the northwest could be restored as the tectonically denuded roof of the Pioneer Mountain Metamorphic Core Complex. The extensive North Fork Lake quartz porphyry dike complex in the Boulder Mountains (Dover and others, 1976) is comprised of hypabyssal silicic intrusive rocks that range from aphanitic porphyritic hornblende quartz porphyry to porphyritic quartz

monzonite. Dated at 48.9+/-2.1 Ma (conventional K-Ar hornblende date; Zartman, unpublished); it is plausible that these dikes fed off of the Pioneer Intrusive Suite. Alternatively, Wust (1986) suggested that the Summit Creek Stock may be the beheaded cupola of the Pioneer Intrusive Suite. However, the cooling curves for the Pioneer Intrusive Suite and the Summit Creek Stock (Silverberg and others, in preparation) suggest a significant crustal section lay between them at the time of their contemporaneous emplacement; thereby invalidating the use of the intrusives as piercing points.

## $D_5$

*Old Hyndman Fault and Mount Cobb Fault*

There are numerous late faults, with attendent brittle deformation, that may be associated with Miocene to recent NE-SW extension. These faults have relatively minor displacment and do not significantly modify the post-$D_4$ structural framework. Two of these faults are described because of their spectacular exposure in the accessible Big Basin area.

The Old Hyndman Fault is best exposed in Big Basin on the ridge that connects Old Hyndman Peak to Mount Cobb separating the principle watersheds of the two main forks of Hyndman Creek (Fig. 11). The fault strikes N41°W and dips 67° to the SW. Here, it places the intensely folded Banded Calc-silicate unit on top of the Pelitic Schist unit, cutting out the Gneissose Quartzite unit. The fault is characterized by a high degree of cataclasis. Blocks of the Pelitic Schist unit and the Banded Calc-silicate unit are mixed incoherently.

A splay of this brittle fault, here called the Cobb Fault, strikes off the reactivated Hyndman Fault in Handwerk Creek. The fault strikes southeast cutting through Duncan Ridge and the south ridge of Hyndman Peak. It then continues southeast through the Mount Cobb-Old Hyndman ridge where it downdrops the Banded Calc-silicate unit against

the Gneissose Quartzite unit. The stratigraphic throw is less than 200 meters. Following the trace of the fault into Big Basin, the fault dies out into a single unit where the throw cannot be discerned.

*Discussion:*

*$D_2$*

The Middle Cretaceous was a time of extensive regional metamorphism, magmatism and deformation in the Idaho area (Fig. 1). Metamorphic cooling ages of suture-zone rocks of the Seven Devils Arc terrane, east of the Idaho batholith, yield ages of roughly 82 Ma (Lund and Snee, 1988). In the Albion Mountains, on the southern margin of the Snake River Plain, cooling ages range from 67 Ma to 80 Ma (Armstrong, 1975). Foliated granodiorites and quartz diorites of the Thompson Creek stock of the SE corner of the Idaho Batholith have been dated at between 82 and 95 Ma (Bennet, 1982). To the east, successive basal decollements were forming at deeper crustal levels during foreland propagation of the Sevier Thrust Belt (Royse and others, 1975).

It is noteworthy that the thermal and deformational effects of this mid-Cretaceous orogeny are present in south central Idaho. The kinematics of the $D_2$ event are somewhat obscured by $D_3$ faults and metamorphism. Nonetheless, the mid-crustal architecture which remained following mid-Cretaceous deformation comprised a complex structural framework. By the end of the Sevier orogeny, the intensely folded parautochthon formed a structural culmination with an antiform amplitude of roughly 4 km. The Hyndman and East Fork Groups had accomodated significant shortening that locally doubled the thickness of units.

The parautochthon and allochthonous sheets of the infrastructure responded somewhat differently to $D_2$ compression. The higher, cooler, and less ductile levels were subject to

folding and subsequent thrusting, similar in style to the thin-skinned tectonics of the foreland (Boyer and Eliot (1982), while the lower, hotter, and more ductile levels deformed more penetratively, with less focusing of shear strain. Nevertheless, even at these lower levels, strain is inhomogeneous, with the distribution of meso-scale structures largely dependent on varying rheologic parameters.

The infrastructure of the Pioneer Metamorphic Core Complex provides only a small window into the architecture of the Late Cretaceous middle crust. It is likely that a deep-seated ramp exists below the parautochthon and that uplift along this ramp and subsequent erosion contributed to setting the isotopic clocks in this region. The internal structures of the Big Basin, Paymaster and Southeast Corner Allochthons provide evidence of significant $D_2$ crustal shortening in the hinterland of the Sevier belt.

*$D_3$*

The lag-time between the end of the Sevier orogeny and the onset of $D_3$ extension of the central Idaho middle crust was a maximum of 30 million years. There are no recognized orogenic events or magmatic rocks emplaced between 79 Ma and the Challis episode in this region. Thus, we may hypothesize that if the onset of $D_3$ extension occurred before Challis age magmatism, but well after thermal re-equilibration of the Cretaceous event, barring any anomolous mantle heat flux, the crust had a somewhat elevated steady state geotherm. Alternatively, the emplacement of the extensional allochthons may well have occurred in the Cretaceous, with local reactivation along the Hyndman Shear Zone during Challis-age magmatism.

The Hyndman Fault System resulted in a series of allochthonous sheets that formed at depths of at least 11-14 km. It appears that the faults migrated down-section, propagating without regard to previously developed structures. The Eocene extensional event

culminated in the activation of the Hyndman Shear Zone, which decoupled the Hyndman and East Fork Groups from the parautochthon. When Tertiary magmatism began, it apparently followed the bulk of the D3 extensional event.

Late-kinematic emplacement of the early phases of the Pioneer Intrusive Suite at 48 Ma resulted in superposition of a solid-state shear fabric upon a magmatic foliation. The limited development of the S3 shear foliation in the Pioneer Intrusive Suite suggests that post-emplacement shear in the Hyndman Shear Zone was short-lived. Many of the early D3 fault zones were recrystallized. Prismatic sillimanite defines a lineation that plunges shallowly SSW. Asymmetric fabrics suggest normal fault motion along the Hyndman Shear Zone.

Plutonism resulted in a low pressure-high temperature metamorphism that reached the orthoclase-sillimanite zone of the amphibolite facies at the thermal culmination. Petrologic and thermochronometric data suggests a time-integrated uplift rate of roughly 1.5 km/million years. This rate is faster than that expected for simple erosion-controlled unroofing. Isostatic compensation has been suggested as a uplift mechanism during and following extensional tectonic denudation (Lister and Davis, 1989; Wernicke and Axon, 1988). It is difficult to imagine how tectonic unroofing itself should result in an isostatic rise of the region; instead, we might expect subsidence and basin development. Nevertheless, a thermal perturbation, perhaps only marginally indicated by the Pioneer Intrusive Suite, could cause a regional isostatic uplift of the crust. The widespread occurence of Eocene quartz monzonites from the Sawtooth Batholith to the Pioneer Mountains, part of the regional Challis volcanic-plutonic event, is consistent with a regionally elevated crustal geotherm. Rapid erosion-controlled unroofing could have resulted from an elevated topography following isostatic compensation of the south-central Idaho region. This "passive" unroofing mechanism should result in significant erosional

deposits. The Tertiary redbed conglomerate that underlies the Challis volcanics in this area is of the appropriate age, although its thickness and regional extent requires further study.

Alternatively, some moderate amount of "active" tectonic denudation could have occurred in the 48-45 Ma interval. The fault system along which this unroofing occurred would have been structurally higher than the presently exposed infrastructure. The orientation and geometry of this hypothetical fault system is unknown, therefore it is impossible to constrain a slip rate along this fault. Regardless of whether the unroofing is "passive" or "active", it is clearly related to extensional tectonic denudation.

The data unequivocally demonstrate an Eocene extensional event in southern Idaho. A curiosity lies in the differing relationships among compression, magmatism and extension along the length of the Eocene extensional zone. In the Shuswap Complex, extension follows compressional thickening of the crust by only a few million years (Brown and Journeay, 1987; Parrish, 1988). In the Bitterroot Mylonite (Garmezy and Sutter, 1983), this extension post-dates any known compressional event by almost 30 million years, however its age is similar to the strike-slip "Trans-Challis Fault System" (Bennett, 1985). Dickenson and others (1988) have suggested that a shallow dip and high rate of oblique convergence between the North American and Farallon plates in the Eocene resulted in mechanical coupling, an elevated regional heat flow and strike-slip faulting. The Eocene event in the Pioneers at first glance, appears to be similar to this latter event. However the vergence is different by almost 70°. Alternatively, Thorkelson and Taylor (1989) have suggested passage of a slab window beneath the west margin of North America at the latitude of central Idaho during the late Paleocene through the Middle Eocene. It is plausible that "edge effects" of a subducted Kula-Farallon spreading ridge could affect thermal and mechanical anomalies that would increase crustal elevation and contribute to tectonic denudation (Thorkelson and Taylor, 1989). The data suggest that although the

Pioneers region shared a somewhat similar Eocene magmatic and thermal evolution with the greater Idaho region which may be related to plate margin processes, the inboard structural and kinematic history is somewhat different, and without an obvious dynamic linkage to the regional strike slip fault system.

A potential caveat is the lack of clear evidence that all of the extensional allochthons in the infrastructure formed in the Eocene. The data in this paper constrain only the most recent movement on the Hyndman Shear Zone. It is entirely plausible for the Big Basin, Paymaster and Southeast Corner Allochthons to have been emplaced any time after $D_2$ and before the late-$D_3$ magmatic event. These allochthons may have been emplaced as a result of a Cretaceous collapse of an overthickened Sevier orogenic pile (e.g. as in the Himalayas, Burchfiel and Royden, 1985). There are numerous low-angle faults in the suprastructure which have younger rocks displaced over older rocks, strongly suggestive of low-angle normal faulting. These faults place the Pennsylvanian-Permian Wood River Formation over the Devonian Milligan Formation. Both of these units comprise the hanging wall of the Milligan-Wood River-Grand Prize thrust complex that is in fault contact with the Missisipian Copper Basin plate. These faults are overlain by the Challis volcanics. It is likely that the $D_3$ extensional faulting observed in the infrastructure bears some relation to this higher level pre-Challis deformational event. The cause and timing of this event may be better constrained by more field work to determine the regional extent of this extensional episode.

*$D_4$*

Post-Challis extension was common south of the Snake River Plain. The Albion-Raft River Core Complex displays Late Oligocene and younger WNW-ESE extension (Armstong, 1975; Saltzer and Hodges, 1987). East-directed extension along the Bitterroot

Mylonite Zone, well north of the Snake River Plain and the Pioneer Mountains (Fig. 1), has been dated at 42 Ma (Garmezy and Sutter, 1983). In the Pioneer Metamorphic Core Complex extension is diachronous. Ductile deformation within the core-bounding Wildhorse Detachment Fault System occurred at 36-33 Ma (Silverberg and others, in preparation). Thus, the age of post-Eocene extension does change abruptly at the Snake River Plain.

The Early Oligocene extensional event occurred roughly 10 million years after emplacement of the Pioneer Intrusive Suite. One-dimensional thermal models suggest that the middle crust would have equilibrated to a steady-state elevated geotherm within a few million years of the emplacement (Spear and Peacock, 1989) suggesting that the crust in south-central Idaho was thermally perturbed and had a non steady-state geotherm until at least 5 million years before the onset of extension. Prior to the onset of Oligocene extension, during the Latest Eocene, the middle crust was cooling at a rate of roughly 20°/million years (Silverberg and others, in preparation). The location of the ductile-brittle transition would be migrating downwards (possibly as much as 1 km/my), as well as, laterally, toward the cooling contact aureole of the Pioneer Intrusive Suite and any other Challis-related thermal perturbations.

Holm (1962) recognized that a portion of the core-bounding fault system had normal-sense displacement. Wust (1985) and O'Neill (1985) independently examined ductile deformation in the NW corner of the core and reported this shear to have WNW vergence. This study concurs with Wust's (1987) interpretation that the Wildhorse Detachment Fault System bounds the core. While most contemporary workers would agree that there is an episode of WNW-directed extension in the Wildhorse Detachment Fault System, the nature of ductile and brittle deformation is controversial.

In contrast to previous studies (Wust and Link, 1988; O'Neill, 1985; O'Neill and Pavlis, 1985, 1986, 1988), the present work documents ductile deformation within the Wildhorse Detachment Fault System to be much more extensive than a "mylonitic quartzite carapice." The mylonitic shear zone cuts through several of the units in the infrastructure. S-C and quartz fabrics suggest hanging-wall down-to-the-WNW transport.

The consistent orientation of the $D_4$ mylonitic lineation of N70°W along the entire Wildhorse Shear Zone has important implications. If the present domal geometry of the ductile shear zone were superimposed on an originally flat planar structure, we would expect a plot of the lineations to fall on a great circle. Instead, we find that the lineation varies from predominantly down-dip slip in the Kane Creek area to oblique-slip in both the Phi Kappa Creek area and the Boulder Creek area. Thus the mullion form of the $D_4$ mylonitic shear zone is most easily interpreted as an initially curviplanar zone of shear. Similar large-scale mullion structures have been found in middle crustal levels of compressional orogenic belts such as the Scandinavian Caledonides (Tilke, 1987), and have been described extensively in the Basin and Range province (Wright and others, 1974; John, 1987).

As proposed by O'Neill and Pavlis (1988), brittle deformation associated with the Wildhorse Detachment Fault System clearly overprints ductile fabrics in the footwall. Based on the work of O'Neill and Pavlis(1988) and Kim (1986), brittle deformation in the Wildhorse Detachment Fault System developed in response to extensional deviatoric stress along a WNW-ESE axis, coincident with the WNW-directed ductile extension.

The evolution of the brittle detachment fault system involved multiple generations of dip-slip and oblique-slip normal faults. The lack of any mylonitic fabric along the eastern segments of the northern and southern margins of the detachment fault system demands that the infrastructure be incised by the detachment fault system. New detachment faults

that incise into the infrastructure displace the former active detachment fault downward resulting in the superposition of brittle deformation on the relict mylonitic shear zone as the new detachment eventually cuts upward through the superstructure (Davis and Lister, 1988). The "shaved" mullion of the infrastructure is thereby uplifted and reduced in extent. When the infrastructure is finally exposed by erosion, all trace of a former ductile shear zone can be locally eliminated. Note that only excising the suprastructure will not accomplish the emplacement of a brittle $D_4$ suprastructure against a strictly brittle $D_4$ infrastructure. One distinction between this interpretation of the Pioneers and the Davis and Lister (1988) model is that the curviplanar geometry of the ductile shear zone in the Wildhorse Detachment Fault System is primary and was not "secondary" and isostatically induced.

It is difficult to constrain the length and time-scale of isostatic adjustment associated with the large volume of Eocene granitoids and tectonic denudation. If displacement rates were rapid along the Wildhorse Detachment Fault System, the infrastructure would continue to rise after the cessation of movement along the fault system. If broad isostatic adjustment occurred with a gentle warp along a roughly north-south axis, this may have activated the minor displacement along the White Mountain Fault.

The data presented are interpreted to indicate that a great variety of structural relations are to be expected in extensional orogens. Incisement and possible distal propagation of the detachment fault system and excisement or back-breaking of the detachment fault system may occur. While planar detachment fault systems seem more common, heterogeneous strain will result in curviplanar detachment fault systems. These latter may result in mullion-form infrastructures. The inherited pre-extension middle to upper-crust structural framework does not seem to localize the detachment fault system. As the core complex evolves, curviplanar faults incise and excise developing exceptionally complex

structural relations that do not always result in significant break up and rotation of the suprastructure.

If the infrastructure had a maximum paleodepth of 7.5-8.4 km at the onset of Oligocene extension (Silverberg, in preparation), then assuming an original 20° dip to the Wildhorse Shear Zone, the maximum dip-slip displacement along the fault is roughly 25 km. Calculations of the total Oligocene extension in the south-central Idaho region must accomodate the inferred maximum horizontal-slip (heave) displacement of roughly 23 km.

Documentation of Early Oligocene extension north of the Snake River Plain suggests that the plain does not represent a fundamental geologic break, but rather is superimposed on an Oligicene to Miocene extension corridor. The kinematics of this Oligocene event is similar to that reported for WNW-directed extension in the Albion Mountains [Saltzer and Hodges, 1988]. Based on current geochronological constraints, a minimum of roughly 8 million years separates the age of extension of these two regions. If Oligocene extension is associated with migration of a extensional regime southward, than with the Albion Mountains roughly 140 km south, that migration would have occurred at a rate not faster than roughly 20 km/million years.

*D5*

Brittle normal faulting along an ENE-WSW axis of extension is responsible for the more typical "basin and range" topography to the east in the Lost River Mountains. The domal form of the Pioneer mountains and the pervasive NNE-SSW drainage system suggest that the present topography is an artifact of early Oligocene extension. Northwest striking normal faults of relatively minor offset are no doubt related to the Miocene to Holocene extension that is typical of the northern Great Basin. The presence of these structures north of the Snake River Plain is significant in that it suggests that the Snake

River Plain does not represent a major Neogene stuctural discontinuity vis-a-vis extension of the Great Basin continental lithosphere.


## Acknowledgements

I wish to thank Gilles Wust, Ned Gates, Allison Macfarlane, Gregory Reller, Kip Hodges, Timothy East, Lawrence McKenna, Elaine Alberti, John Sutter and Elaine Padovani for their help in the field. Gilles, in particular, shared the joys and troubles of living in the mountain "pleasure dome". Kudos to Timothy and Patricia East for endless hospitality in Ketchum, Idaho. Gilles Wust kindly arranged for the quartz fabric analyses at the ETH-Zurich. Comments by Kip V. Hodges, John Grotzinger, Brad Hager and Roy Adams were very appreciated and greatly improved the text and figures. I thank The Geological Society of America for grant support that enabled my attendance at pertinent Penrose Conferences. This research was a part of my Ph.D. thesis research at the Massachusetts Institute of Technology and was financially supported by U.S. National Science Foundation grant EAR-8407730 to K.V. Hodges.

## References


Armstrong, R.L., Sevier orogenic belt in Nevada and Utah, *Geol. Soc. Amer. Bull., 79,* 429-458, 1968.

Armstrong. R.L., Low-angle (denudation) faults, hinterland of the Sevier orogenic belt, eastern Nevada and western Utah, *Geol. Soc. Amer. Bull., 83,* 1729-1754, 1972.

Armstrong, R.L., Geochronometry of the Eocene volcanic-plutonic episode in Idaho, *Northwest Geology, 3,* 1-15, 1974.

Armstrong, R.L., The geochronometry of Idaho (part1), *Isochron West, 14,* 1-50, 1975.

Armstrong, R.L., The geochronometry of Idaho (part 2), *Isochron West, 15,* 1-34, 1976.

Armstrong, R.L., Cordilleran metamorphic core complexes — From Arizona to southern Canada, *Ann. Rev. Earth Planet. Sci., 10,* 129-154, 1982.

Arthaud, F., A graphic method of determination of shortening, elongation, and intermediate directions from a population of faults, *Extraut du Bulletin de la Soc. Geol. de France, 7e serie, tXI,* 720-737, 1969.

Bennet, E.H. and Knowles, C.R., Tertiary plutons and related rocks in central Idaho,

Bennett, E.H., Relationship of the Trans-Challis fault system in central Idaho to Eocene basin and range extensions, *Geology, 14,* 481-484, 1986.

Boyer, S.E. and Elliott, D., Thrust systems, *Am. Assoc. Pet. Geol. Bull., 66,* 1196-1230, 1982.

Brown, R.L. and Journeay, J.M., Tectonic denudation of the Shuswap metamorphic terrain of southeastern British Columbia, *Geology, 15,* 142-146, 1987.

Brown, R.L., Journeay, J.M., Lane, L.S., Murphy, D.C. and Rees, C.J., Obduction, backfolding and piggyback thrusting in the metamorphic hinterland of the southeastern Canadian Cordillera, *Journal of Structural Geology, 8,* 255-268, 1986.

Burchfiel, B.C. and Royden, L.H., North-south extension within the convergent Himalayan region., *Geology, 13,* 679-682, 1985.

Churkin, M., Facies across Paleozoic miogeoclinal margin of central Idaho, *Am. Assoc. Petrol. Geol. Bull.46,* 569-591, 1962.

Coney, P.J., Cordilleran metamorphic core complexes: An overview, in *Cordilleran metamorphic core complexes*, edited by Crittenden, M.D., Coney, P.J. and Davis, G.H., pp. 7-34, The Geological Society of America, Boulder, 1980.

Coney, P.J., The regional tectonic setting and possible causes of Cenozoic extension in the North American Cordillera, in *Continental Extensional Tectonics*, edited by Coward, M.P., Dewey, J.F. and Hancock, P.L., pp. 177-186, The Geological Society, Oxford, 1987.

Coney, P.J. and Harms, T.A., Cordilleran metamorphic core complexes: Cenozoic extensional relics of Mesozoic compression., *Geology, 12,* 550-554, 1984.

Cook, E.F., Tungsten deposits of south-central Idaho, *Ida. Bur. Mines and Geol., 108,* 40, 1956.

Davis, G.A. and Lister, G.S., Detachment faulting in continental extension; Perspectives from the Southwestern U.S. Cordillera, in *Processes in Continental Lithospheric Deformation*, edited by Clark, S.P., Burchfiel, B.C., and Suppe, J., pp. 133-159, Geological Society of America, Boulder, CO, 1988.

Dickinson, W.R., Klute, M.A., Hayes, M.J., Janecke, S.U., Lundin, E.R., McKittrick, M.A. and Olivares, M.A., Paleogeographic and paleotectonic setting of Laramide sedimentary basins in the central Rocky Mountain region, *Geol. Soc. Am. Bull., 100,* 1023-1039, 1988.

Dover, J.H., Bedrock geology of the Pioneer Mountains, central Idaho, Ph.D. Thesis, University of Washington, 1966.

Dover, J.H., Bedrock geology of the Pioneer Mountains, Blaine and Custer counties, central Idaho, *Idaho Bureau of Mines and Geology Pamphlet 142, 66,* 1969.

Dover, J.H., Geology of the Boulder-Pioneer wilderness study area, Blaine and Custer counties, Idaho, *U. S. Geol. Surv. Bull., 1497-A,* 21-75, 1981.

Dover, J.H., Geologic map and sections of the central Pioneer mountains, Blaine and Custer counties, *United States Geological Survey Miscellaneous Investigation Series, I-1319,* 1983.

Engebretson, D.C., Cox, A. and Thompson, G.A., Correlations of plate motions with continental tectonics: Laramide to Basdin-Range, *Tectonics, 3,* 115-119, 1984.

England, P.C. and Thompson, A.B., Pressure-temperature-time paths of regional metamorphism I. Heat transfer during the evolution of regions of thickened continental crust., *J. Petrol., 25,* 894-928, 1984.

Garmezy, L. and Sutter, J.F., Mylonitization coincident with uplift in an extensional setting, Bitterroot Range, Montana-Idaho, *Geol. Soc. Amer. Abs. w. Prog., 15,* 578, 1983.

Gibbs, A.D., Structural evolution of extensional basin margins., *J. Geol. Soc. Lond., 141,* 609-620, 1984.

Hall, W.E., Stratigraphy of and mineral deposits in middle and upper Paleozoic rocks of the Black-Shale mineral belt, central Idaho, *1658-J,* 117-131, 1986.

Holm, R.F., Geology of the Wildhorse Creek area, Custer County, Idaho, M.S. Thesis, Idaho State University, 1962.

Kim, A.Y.H., The kinematics of brittle polyphase deformation within the Pioneer Metamorphic Core Complex, Pioneer Mountains, Idaho, M.S. Thesis, Lehigh University, 1986.

Lister, G.S. and Davis, G.A., The origin of metamorphic core complexes and detachment faults during Tertiary continental extension in the northern Colorado river region, U.S.A., *Journal of Structural Geology, 11,* 65-94, 1989.

Lister, G.S. and Snoke, A.W., S-C mylonites, *J. Struct. Geol., 6,* 617-638, 1984.

Lund, K. and Snee, L.W., *Metamorphism, structural development, and age of the continent-island arc juncture in west-central Idaho*,, pp. 297-331, 1988.

McDougall, I. and Harrison, T.M., *Geochronology and Thermochronology by the 40Ar/39Ar Method*,, pp. 212, Oxford University Press, New York, 1988.

Nilsen, Paleogeography of Mississippian turbidites in south-central Idaho, in Stewart, J.H., Stevens, C.H. , and Fritsche, A.E., eds., *Paleozoic paleogeography of the Western United States*: Soc. Econ. Paleon. and Mineral., Pacific Section, Pacific Coast Paleogeography Symposium 1, 275-299.

O'Neill, R.L., Superposition of Cenozoic extension on Mesozoic compressional structures of the Pioneer Mountains, central Idaho, M.S. Thesis, Lehigh University, 1985.

O'Neill, R.L. and Pavlis, T.L., Superposition of Cenozoic extension on Mesozoic compressional structures of the Pioneer Mountains, central Idaho, *17,* 397-398, 1985.

O'Neill, R.L. and Pavlis, T.L., Superposition of Cenozoic extension on Mesozoic compressional structures in the Pioneer mountains metamorphic core complex, central Idaho, *Geological Society of America Bulletin, 100,* 1833-1845, 1988.

Parrish, R.R., Metamorphic core complexes of southern B.C.-distictions between extensional or compressional origins [abs.], *Geological Society of America Abstracts with Programs, 17,* 399, 1985.

Parrish, R.R., Carr, S.D. and Parkinson, D., Metamorphic complexes and extensional tectonics, southern Shuswap complex, southeastern British Columbia, *Geological Society of America, Cordilleran Section, Field Trip Guidebook, Trip 12, 15,* 1985.

Parrish, R.R., Carr, S.D. and Parkinson, D.L., Eocene extensional tectonics and geochronology of the southern Omineca belt, British Columbia and Washington, *Tectonics, 7,* 181-212, 1988.

Parrish, R.R., Haugerud, R.A. and Price, R.A., Penrose Conference Report: The Eocene Tectonic Transition, Oregon to Alaska, *GSA News & Information, 12,* 124-125, 1990.

Platt, J.P., Dynamics of orogenic wedges and the uplift of high-pressure metamorphic rocks., *Geol. Soc. Amer. Bull., 97,* 1037-1053, 1986.

Poole, F.G., Flysch deposits of Antler foreland basin, western United States, in *Tectonics and sedimentation: Society of Economic Paleontologists and Mineralogists Special Publication*, edited by Dickenson, W.R., pp. 58-82, 1974.

Royse, F., Warner, M.A. and Reese, D.L., Thrust belt structural geometry and related stratigraphic problems, Wyoming-Idaho-northern Utah, in *Deep drilling frontiers of the central Rocky Mountains*, edited by Bolyard, D.W., pp. 41-54, Rocky Mountain Association of Geologists, Denver, Colorado, 1975.

Ruppel, C., Royden, L. and Hodges, K.V., Thermal modeling of extensional tectonics: application to pressure-temperature-time histories of metamorphic rocks., *Tectonics, 7,* 947-957, 1988.

Saltzer, S. and Hodges, K.V., The Middle Mountain shear zone, southern Idaho: Kinematic analysis of a Tertiary, high-temperature detachment, *Geol. Soc. Amer. Bull., 100,* 96-103, 1988.

Schmidt, S.M. and Casey, M., Complete fabric analysis of some commonly observed quartz C-axis patterns, in *Mineral and rock deformation: laboratory studies-The Paterson Volume*, edited by Hobbs, B.E. and Heard, H.C., pp. American Geophysical Union, Washington, D.C., 1986.

Silverberg, D.S., Petrologic constraints on the tectonic history of the Pioneer metamorphic core complex, south-central Idaho: depth-temperature-time paths in the upper amphibolite facies, in preparation.

Silverberg, D.S., Hodges, K.V., Kunk, M., and Sutter, J., Thermal evolution of the PPioneer Metamorphic Core Complex, south-central Idaho: diachronous Paleogene extension of the middle crust, Tectonics, in preparation.

Skipp, B., Basement thrust sheets in the Clearwater orogenic zone, central Idaho and western Montana, *Geology, 15,* 220-224, 1987.

Skipp, B. and Hait, M.H., Allochthons along the northeastern margin of the Snake River Plain, Idaho, in *Rocky Mountain thrust belt geology and resources: Wyoming Geological Association, 29th Field Conference, Guidebook*, edited by Heisey, E.L., pp. 499-515, 1977.

Stock, J.M. and Molnar, P., Uncertainties and implications of the Late Cretaceous and Tertiary position of North America relative to the Farallon, Kula, and Pacific plates, *Tectonics, 7,* 1339-1384, 1988.

Thorkelson, D.J. and Taylor, R.P., Cordilleran slab windows, *Geology, 17,* 833-836, 1989.

Tilke, P.G., Caledonian structure, metamorphism, geochronology, and tectonics of the Sitas-Singis area, Sweden, Ph.D. Thesis, M.I.T., 1987.

Umpleby, J.B., Westgate, L.G. and Ross, C.P., Geology and ore deposits of the Wood River region, Idaho, *U.S. Geol. Survey Bull., 814,* 1-80, 1930.

Wernicke, B. and Axen, G.J., On the role of isostacy in the evolution of normal fault systems, *Geology, 16,* 848-851, 1988.

Wernicke, B.P., Uniform-sense normal simple shear of the continental lithosphere, *Can. J. Earth Sci.,* 108-125, 1985.

Wernicke, B.P., Christiansen, R.L., England, P.C. and Sonder, L.J., Tectonomagmatic evolution of Cenozoic extension in the North American Cordillera., in *Continental Extensional Tectonics*, edited by Coward, M.P., Dewey, J.F. and Hancock, P.L., pp. 203-221, Geological Society of London, Oxford, 1987.

Wright, L.A., Troxel, B.W., Williams, E.G. and Roberts, M.T., Precambrian sedimentary environments of the Death Valley region, eastern California, in *Geological Society of America Cordilleran Section Field Trip Guidebook*, pp. 27-35, Death Valley Publishing Company, Shoshone, CA, 1974.

Wust, S.L., Tectonic development of the Pioneer Structural Complex, Pioneer Mountains, central Idaho, Ph.D. thesis, University of Arizona, 1986.

Wust, S.L. and Link, P.K., Geology of the Pioneer Mountains Core Complex, south central Idaho, *Northwest Geology, 16,* 85-94, 1987.

## Figure Captions

Fig. 1.1. Simplified regional tectonic map of the Idaho area. Rectangle shows the location of Fig. 1.2. lr = Lost River Range; sb = Sawtooth Batholith; gc = Goose Creek Mountains; am = Albion Mountains; rr = Raft River mountains.

Fig. 1.2. Simplified tectonic map of the Pioneer Metamorphic Core Complex, south-central Idaho (after published mapping of J. Dover, 1981 and unpublished mapping of D.S. Silverberg). Line A-A' show the cross-section transect of Fig. 1.4. kc = Kane Creek; whc = Wildhorse Canyon; fc = Fall Creek; cc = Corral Creek; pc = Pioneer Cabin; hc = Hyndman Creek; bb = Big Basin; wr = Wood River; bc = Boulder Creek; kce = East Kane Creek; wkc = West Kane Creek; sc = Summit Creek; ir = Imbricate Ridge.

Fig. 1.3. Tectonic stratigraphic column of the infrastructure in the Pioneer Metamorphic Core Complex. Lithostratigraphy as in Dover, 1983.

Fig. 1.4. Cross-section along the A-A' transect of Fig. 1.2. Unit abbreviations as in Figs. 1.2 and 1.3. pct = Pioneer Cabin Thrust; hsz = Hyndman Shear Zone; wdfs = Wildhorse Detachment Fault System.

Fig. 1.5. Synopsis of deformation events in the Pioneer Metamorphic Core Complex. Tc = cooling age as constrained by 40Ar-39Ar plateau ages (Silverberg et al., in preparation); MM = style and maximum grade of dynamothermal metamorphism (syn-K = syn-kinematic, post-K = post-kinematic); PIS = Pioneer Intrusive Suite

Fig. 1.6. Timing relationships between petrofabrics and principal porphyroblast growth in the pelitic schist of the Hyndman Group.

Fig. 1.7. Synoptic temperature-time paths for the Pioneer Intrusive Suite, the Summit Creek Stock, the Wildhorse Gneiss Complex, and the Wildhorse Detachment Fault system (from Silverberg and others, in preparation). PCwgc = Precambrian Wildhorse Gneiss Complex; Epis = Eocene Pioneer Intrusive Suite; Escs = Eocene Summit Creek Stock; Owdfs = Oligocene Wildhorse Detachment Fault System.

Fig. 1.8. Map of the Wildhorse Gneiss Complex. Legend as in Figs. 1.2, 1.3 and 1.4. wl = Wildhorse Lake, Kl = Kane Lake.

Fig. 1.9. Wildhorse Gneiss Complex, Wildhorse Creek Canyon, Plot of poles to $S_2$. N=186, contoured maxima = 1,2,3% per 1% area; cylindrical best fit = 149, 8. Plots are lower hemisphere, equal area projections.

Fig. 1.10. Wildhorse Gneiss Complex, Kane Creek, Plot of poles to $S_2$. N=44, contoured maxima = 1,2,3% per 1% area; cylindrical best fit = 290,13. Plots are lower hemisphere, equal area projections.

Fig. 1.11. Simplified geologic map of the western phase of the Pioneer Intrusive Suite, the Hyndman and East Fork Groups in the vicinity of the Hyndman Shear Zone (HSZ; D3). Deformational events keyed to Fig. 1.5. Note that some D4 and D5 trends are marked on the map; Gray lines delineate creek drainages; SC = Summit Creek; KC = Kane Creek; WC = Wilson Creek; IR = Imbricate Ridge; CC = Corral Creek; PCR = Pioneer Cabin Ridge; HP = Hyndman Peak; NFHC = North Fork of Hyndman Creek; DR = Duncan Ridge; OHP = Old Hyndman Peak; MC = Mount Cobb; HC = Hyndman Creek; PG = Paymaster Gulch; EFWR = East Fork of the Wood River; wdfs = Wildhorse Detachment Fault System; SECF = Southeast Corner Fault; PF = Paymaster Fault; OHF = Old Hyndman Fault; CF = Cobb Fault; Rock units as in Fig. 1.3. $L_3$ = Trend and plunge of sillimanite lineations in the Hyndman Shear Zone, synoptic plot in Fig. 1.18.

Fig. 1.12. Hyndman and East Fork Groups, Big Basin Allochthon, Plot of poles to $S_2$. N=129, contoured maxima = 1,2,3,4,5,6% per 1% area; cylindrical best fit = 135,2. Plots are lower hemisphere, equal area projections.

Fig. 1.13. Hyndman and East Fork Groups, Big Basin Allochthon, Plot of $F_2$. N=62, contoured maxima = 2,4,6,8% per 1% area. Plots are lower hemisphere, equal area projections.

Fig. 1.14. Hyndman and East Fork Groups, Paymaster Allochthon, Plot of poles to $S_2$. N=55, contoured maxima = 2,4,6,8% per 1% area. Plots are lower hemisphere, equal area projections.

Fig. 1.15. Cross-Section for Pioneer Cabin Thrust Nappe. Transect line C-C' keyed to Fig. 1.11. Rock units as in Fig. 1.3.

Fig. 1.16. Cross-Section for Extensional Nappe Pile. Transect line B-B' keyed to Fig. 1.11. Rock units as in Fig. 1.3.

Fig. 1.17. Pioneer Intrusive Suite, Plot of poles to $S_3$. N=43, contoured maxima = 1,2,3,4,6,8,10,12% per 1% area; mean dip = 33°±4°(2 s.d.); no apparent fold axis; best cylindrical fit = 189,29. Plots are lower hemisphere, equal area projections.

Fig. 1.18. Hyndman Group pelitic schist protomylonite; Plot of $L_3$ sillimanite. Plots are lower hemisphere, equal area projections.

Fig. 1.19. Photomicrograph of East Fork Group Kinnikinnik Quartzite, $D_4$ Type II S-C Mylonite. Sample P499. XZ section. Dextral shear indicated by S-C fabric. S = schistosite; C = cissailement. Field of View 2 mm x 1.2 mm.

Fig. 1.20. Plot of $S_4$ and $L_4$ in $D_4$ Mylonites. Keyed to Fig. 1.2. Plots are lower hemisphere, equal area projections. a: Boulder Creek area, N=13, contoured maxima 4,8% per 1% area, conical axis 300,44; 1/2 apical angle 11°, cissailment surface 252,51N. b: Kane Creek, east slope, N=17, contoured maxima 4,8,12% per 1%

area, conical axis 304,28; 1/2 apical angle 12°, cissailment surface 88,44N. c: Kane Creek, west slope, N = 40; contoured maxima 4,8, 12% per 1% area, conical axis 289,21; 1/2 apical angle 11°, cissailment surface 43,23W. d: Summit Creek area, N = 6; conical axis 293,24; 1/2 apical angle 7°, cissailment surface 196,30W. e: Imbricate ridge area, N = 6; conical axis 299,37; 1/2 apical angle 17°, cissailment surface 162,39SW.

Fig. 1.21. Synoptic plot of $L_4$ mylonitic lineations. N = 82; contoured maxima 4,6,8,10,11% per 1 % area, conical axis 296,32, 1/2 apical angle 17°. Plots are lower hemisphere, equal area projections.

Fig. 1.22. Quartz A reflections for $D_4$ quartzite mylonites of the East Fork Group (Kinnikinnik Quartzite formation). Collected from Wildhorse Shear Zone of Wildhorse Detachment Fault System in Summit Creek. All lineations N55W. XZ sections analyzed on textural goniometer at the ETH-Zurich, Switzerland. Shaded line indicates the rake of C. All samples indicate sinstral shear corresponding to hanging wall down to the WNW. a: Sample P48, contour values, 1, 2, 3, 4, 5, 6, 7, 8% per 1% area. b: Sample P498A, contour values, .5, 1, 1.5, 2, 2.5, 3, 3.5, 4, 4.5, 5, 5.5% per 1% area. c: Sample P498B, contour values, .5, 1, 1.5, 2, 2.5, 3, 3.5, 4, 4.5% per 1% area.

Figure 1.1

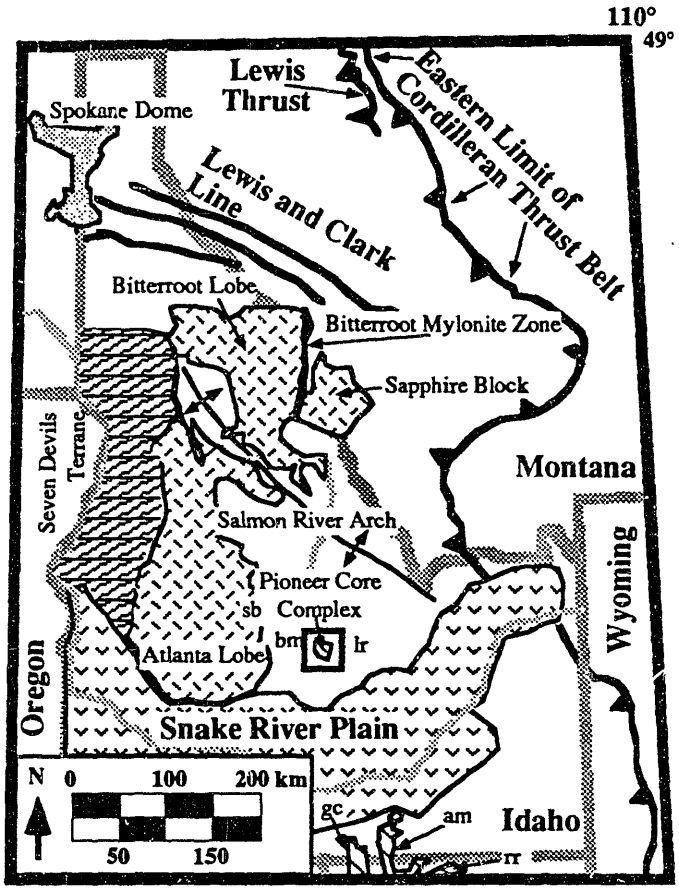
110°
49°
Lewis Thrust
Eastern Limit of Cordilleran Thrust Belt
Spokane Dome
Lewis and Clark Line
Bitterroot Lobe
Bitterroot Mylonite Zone
Sapphire Block
Seven Devils Terrane
Montana
Salmon River Arch
Pioneer Core
sb Complex
bm
lr
Atlanta Lobe
Wyoming
Oregon
Snake River Plain
N
0
100
200 km
50
150
gc
am
Idaho
rr

Figure 1.2

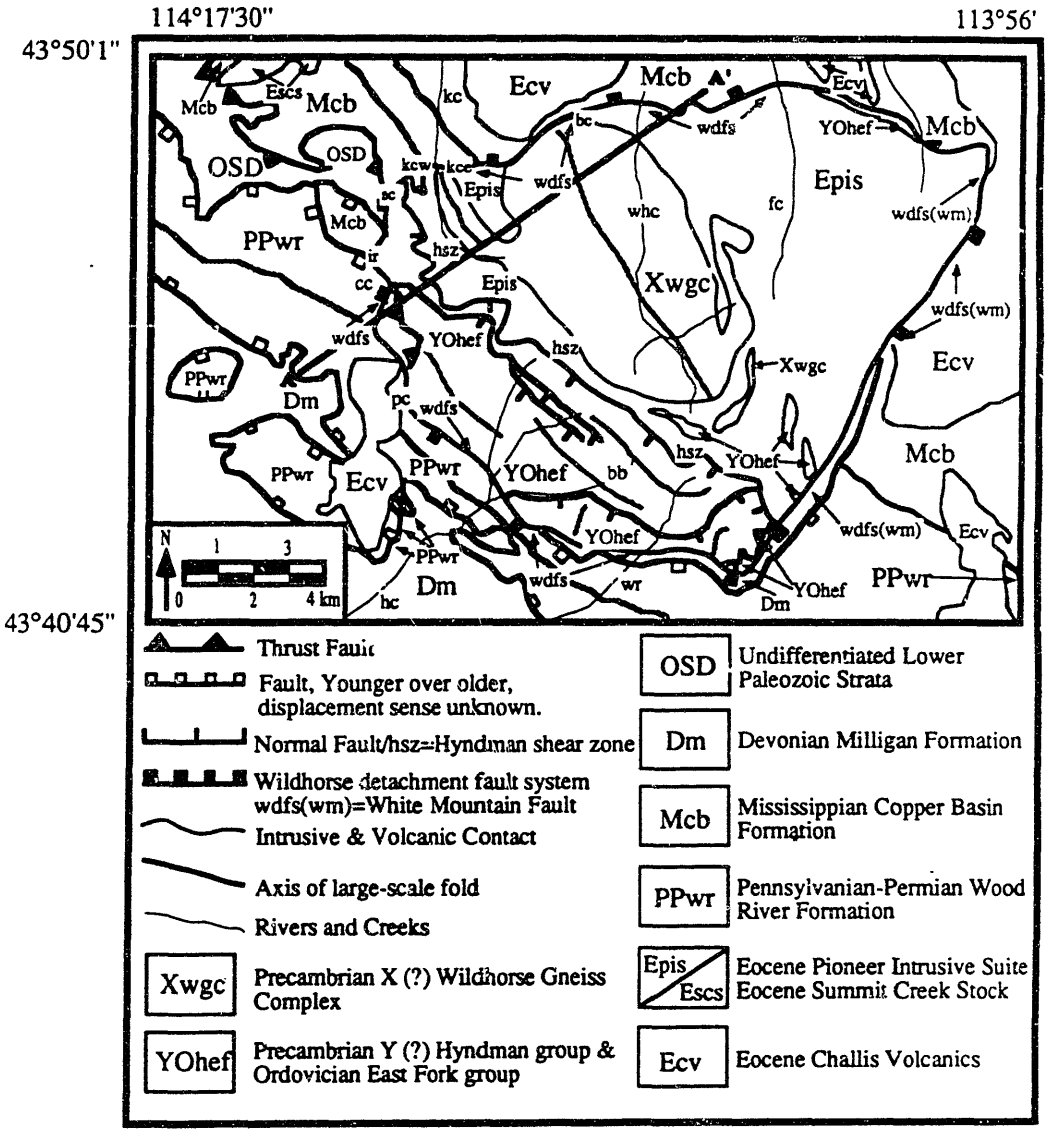
114°17'30"
113°56'
43°50'1"
43°40'45"
Mcb
Escs
Ecv
kc
bc
wdfs
A'
YOhef
OSD
kcw
kcc
Epis
ac
Epis
whc
fc
wdfs(wm)
PPwr
Mcb
ir
hsz
cc
Xwgc
wdfs
YOhef
hsz
Xwgc
Ecv
PPwr
Dm
pc
wdfs
hsz
YOhef
Mcb
PPwr
Ecv
PPwr
YOhef
bb
YOhef
wdfs(wm)
Ecv
N
1
3
0
2
4 km
PPwr
Dm
wdfs
wr
hc
YOhef
PPwr
Dm
Thrust Fault
Fault, Younger over older, displacement sense unknown.
Normal Fault/hsz=Hyndman shear zone
Wildhorse detachment fault system
wdfs(wm)=White Mountain Fault
Intrusive & Volcanic Contact
Axis of large-scale fold
Rivers and Creeks
Xwgc
Precambrian X (?) Wildhorse Gneiss Complex
YOhef
Precambrian Y (?) Hyndman group & Ordovician East Fork group
OSD
Undifferentiated Lower Paleozoic Strata
Dm
Devonian Milligan Formation
Mcb
Mississippian Copper Basin Formation
PPwr
Pennsylvanian-Permian Wood River Formation
Epis
Escs
Eocene Pioneer Intrusive Suite
Eocene Summit Creek Stock
Ecv
Eocene Challis Volcanics

Figure 1.3

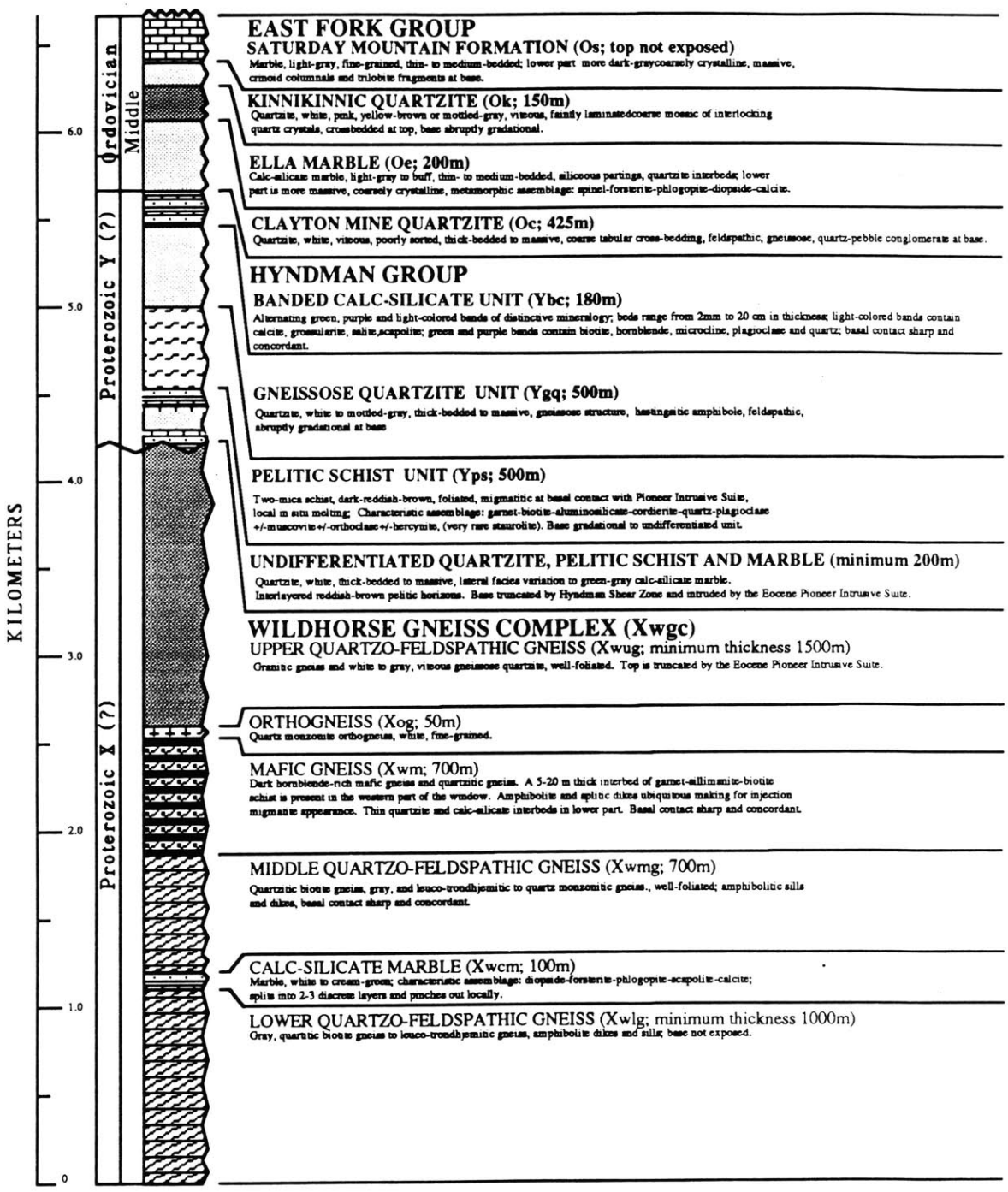
KILOMETERS
0
1.0
2.0
3.0
4.0
5.0
6.0
Proterozoic X (?)
Proterozoic Y (?)
Ordovician
Middle
EAST FORK GROUP
SATURDAY MOUNTAIN FORMATION (Os; top not exposed)
Marble, light-gray, fine-grained, thin- to medium-bedded; lower part more dark-gray coarsely crystalline, massive, crinoid columnals and trilobite fragments at base.
KINNIKINNIC QUARTZITE (Ok; 150m)
Quartzite, white, pink, yellow-brown or mottled-gray, vitreous, faintly laminated coarse mosaic of interlocking quartz crystals, crossbedded at top, base abrupdly gradational.
ELLA MARBLE (Oe; 200m)
Calc-silicate marble, light-gray to buff, thin- to medium-bedded, siliceous partings, quartzite interbeds; lower part is more massive, coarsely crystalline, metamorphic assemblage: spinel-forsterite-phlogopite-diopside-calcite.
CLAYTON MINE QUARTZITE (Oc; 425m)
Quartzite, white, vitreous, poorly sorted, thick-bedded to massive, coarse tabular cross-bedding, feldspathic, gneissose, quartz-pebble conglomerate at base.
HYNDMAN GROUP
BANDED CALC-SILICATE UNIT (Ybc; 180m)
Alternating green, purple and light-colored bands of distincave mineralogy; beds range from 2mm to 20 cm in thickness; light-colored bands contain calcite, grossularite, sahlite,scapolite; green and purple bands contain biotite, hornblende, microcline, plagioclase and quartz; basal contact sharp and concordant.
GNEISSOSE QUARTZITE UNIT (Ygq; 500m)
Quartzite, white to mottled-gray, thick-bedded to massive, gneissose structure, hastingsitic amphibole, feldspathic, abrupdly gradational at base
PELITIC SCHIST UNIT (Yps; 500m)
Two-mica schist, dark-reddish-brown, foliated, migmatitic at basal contact with Pioneer Intrusive Suite, local in situ melting; Characteristic assemblage: garnet-biotite-aluminosilicate-cordierite-quartz-plagioclase +/-muscovite+/-orthoclase+/-hercynite, (very rare staurolite). Base gradational to undifferentiated unit.
UNDIFFERENTIATED QUARTZITE, PELITIC SCHIST AND MARBLE (minimum 200m)
Quartzite, white, thick-bedded to massive, lateral facies variation to green-gray calc-silicate marble. Interlayered reddish-brown pelitic horizons. Base truncated by Hyndman Shear Zone and intruded by the Eocene Pioneer Intrusive Suite.
WILDHORSE GNEISS COMPLEX (Xwgc)
UPPER QUARTZO-FELDSPATHIC GNEISS (Xwug; minimum thickness 1500m)
Granitic gneiss and white to gray, vitreous gneissose quartzite, well-foliated. Top is truncated by the Eocene Pioneer Intrusive Suite.
ORTHOGNEISS (Xog; 50m)
Quartz monzonite orthogneiss, white, fine-grained.
MAFIC GNEISS (Xwm; 700m)
Dark hornblende-rich mafic gneiss and quartzitic gneiss. A 5-20 m thick interbed of garnet-sillimanite-biotite schist is present in the western part of the window. Amphibolite and aplitic dikes ubiquitous making for injection migmatite appearance. Thin quartzite and calc-silicate interbeds in lower part. Basal contact sharp and concordant.
MIDDLE QUARTZO-FELDSPATHIC GNEISS (Xwmg; 700m)
Quartzitic biotite gneiss, gray, and leuco-trondhjemitic to quartz monzonitic gneiss., well-foliated; amphibolitic sills and dikes, basal contact sharp and concordant.
CALC-SILICATE MARBLE (Xwcm; 100m)
Marble, white to cream-green; characteristic assemblage: diopside-forsterite-phlogopite-scapolite-calcite; splits into 2-3 discrete layers and pinches out locally.
LOWER QUARTZO-FELDSPATHIC GNEISS (Xwlg; minimum thickness 1000m)
Gray, quartzitic biotite gneiss to leuco-trondhjemitic gneiss, amphibolite dikes and sills; base not exposed.

Figure 1.4

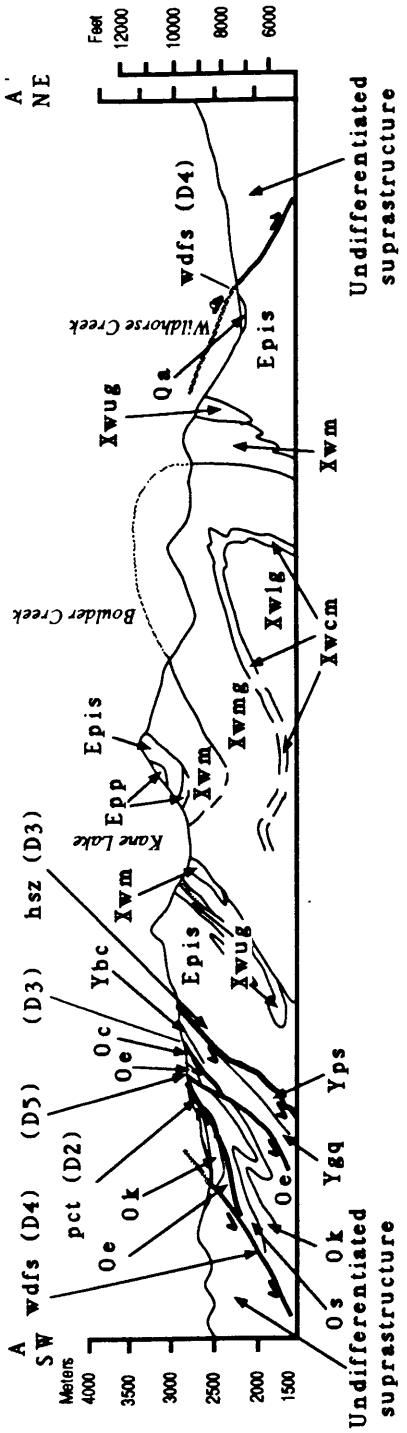
A
SW
A'
NE
Meters
4000
3500
3000
2500
2000
1500
Feet
12000
10000
8000
6000
Undifferentiated suprastructure
wdfs (D4)
pct (D2)
(D5)
(D3)
hsz (D3)
Oe
Ok
Os
Ygq
Yps
Ybc
Oc
Xwm
Xwug
Epis
Epp
Kane Lake
Boulder Creek
Xwmg
Xwlg
Xwcm
Wildhorse Creek
Qs

| ROCK UNIT | D1 | D2 | D3 | D4 | D5 |
|---|---|---|---|---|---|
| | | Tc (800K) = 79 ma | Tc (800K) = 46 ma | Tc (675-475K) = 36-33 ma | |
| Eocene Pioneer Intrusive Suite | | | S3: N65°W, 30°SW; L3: S10°W; Late D3 Emplacement | S4: variable; L4: N68W; MM: greenschist facies; brittle D4 superimposed on ductile | Local brittle extension along NE-SW axis of extension |
| Precambrian-Ordovician Hyndman and East Fork Groups | | F2: NW Trend, isoclinal, recumbent Axial Plane SW Dip MM: syn-kinematic amphibolite facies Post F2 Thrust Faults | Pre-PIS emplacment of allochthons; Syn-PIS Hyndman Shear Zone; protomylonite, S3: N65°W, 30°SW; MM: Syn-K: Sill, Cdt; post-K: Garnet | S4: variable; L4: N68W; MM: greenschist facies; brittle D4 superimposed on ductile | Local brittle extension along NE-SW axis of extension |
| Precambrian Wildhorse Gneiss Complex | Cryptic dome & basin interference patterns suggest an early deformation event. | F2: NW Trend, isoclinal, overturned Axial Plane: SW dip MM: syn-kinematic amphibolite facies | F3: Broad megascale folds, NNW-SSE trend; Minor Intraformational Faults | S4: variable; L4: N68W; MM: greenschist facies; brittle D4 superimposed on ductile | Local brittle extension along NE-SW axis of extension |

Figure 1.5

Figure 1.6

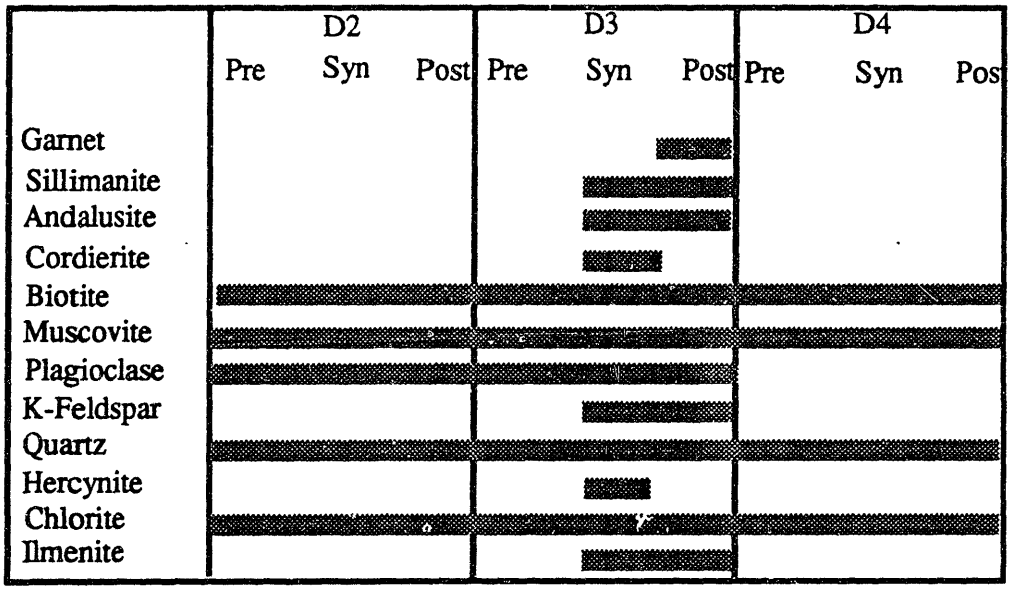
D2
D3
D4
Pre
Syn
Post
Pre
Syn
Post
Pre
Syn
Pos
Garnet
Sillimanite
Andalusite
Cordierite
Biotite
Muscovite
Plagioclase
K-Feldspar
Quartz
Hercynite
Chlorite
Ilmenite

Figure 1.7

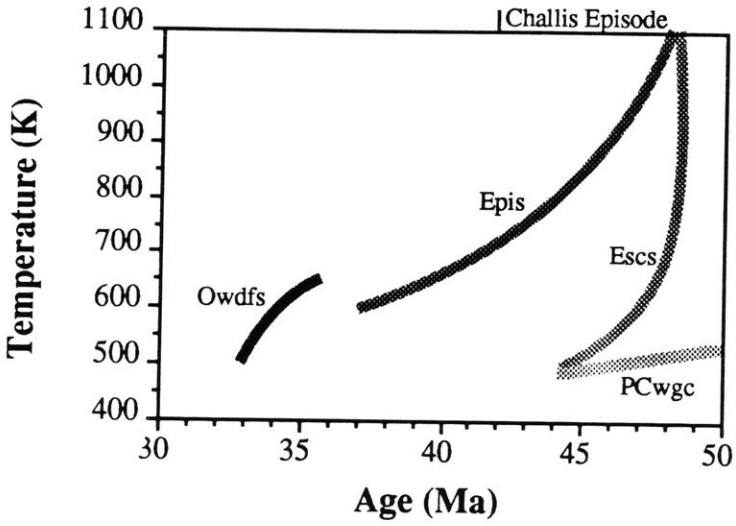
Challis Episode
Epis
Escs
Owdfs
PCwgc
Temperature (K)
1100
1000
900
800
700
600
500
400
30
35
40
45
50
Age (Ma)

Figure 1.8

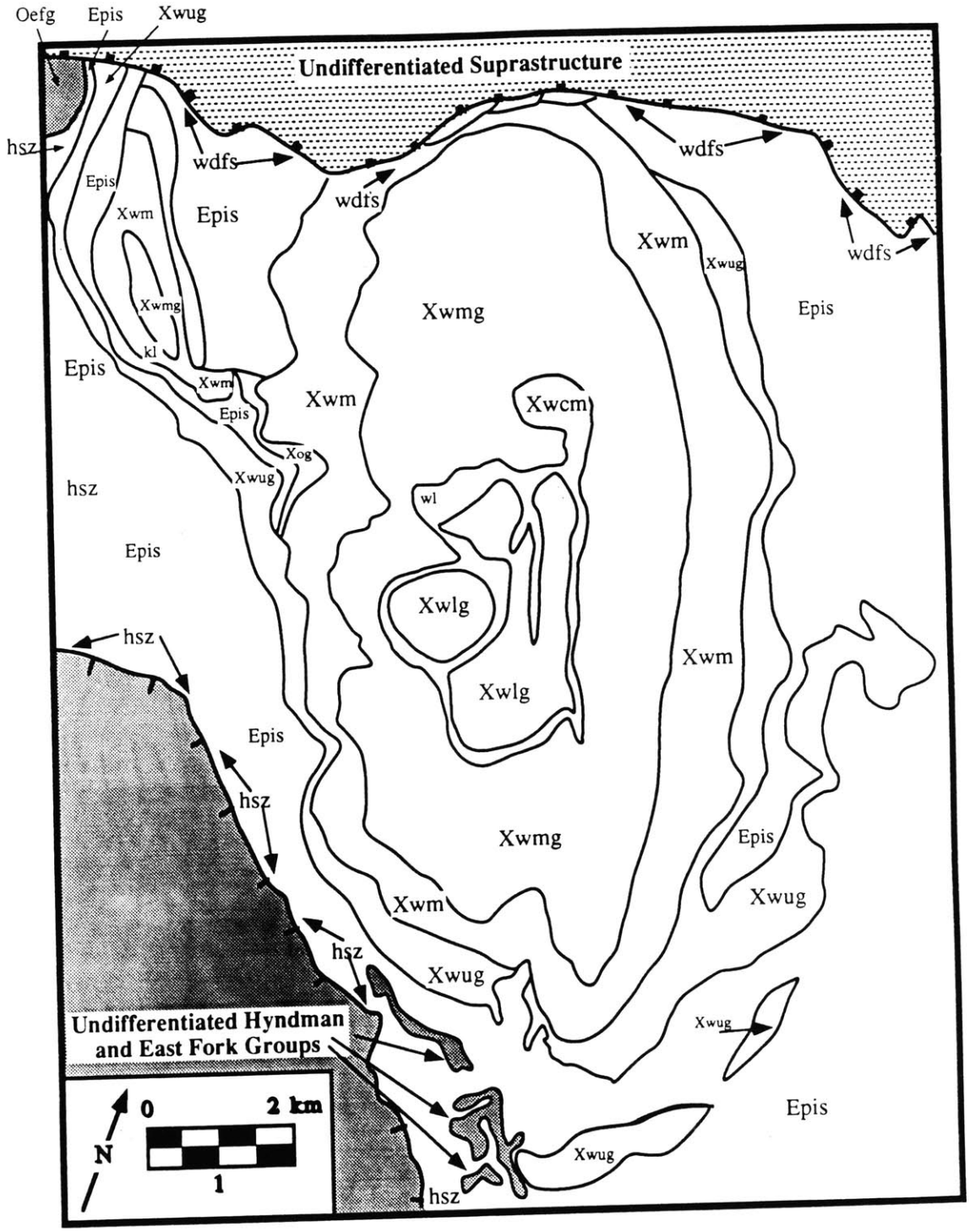
Oefg
Epis
Xwug
Undifferentiated Suprastructure
hsz
wdfs
Epis
Xwm
Xwmg
kl
Xwcm
Xog
wl
Xwlg
Undifferentiated Hyndman and East Fork Groups
0
2 km
1
N

Figure 1.9

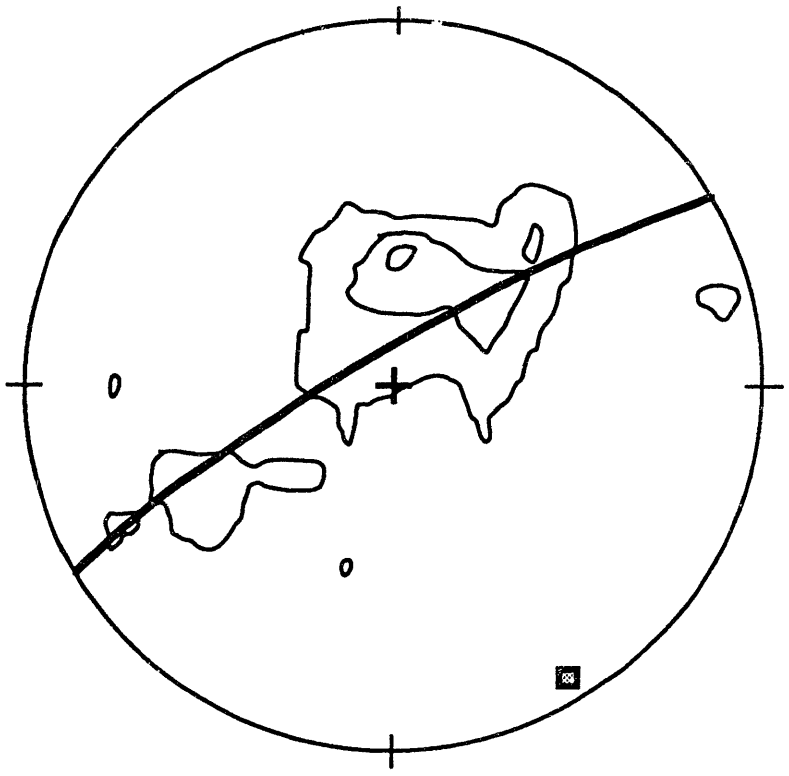

Figure 1.10

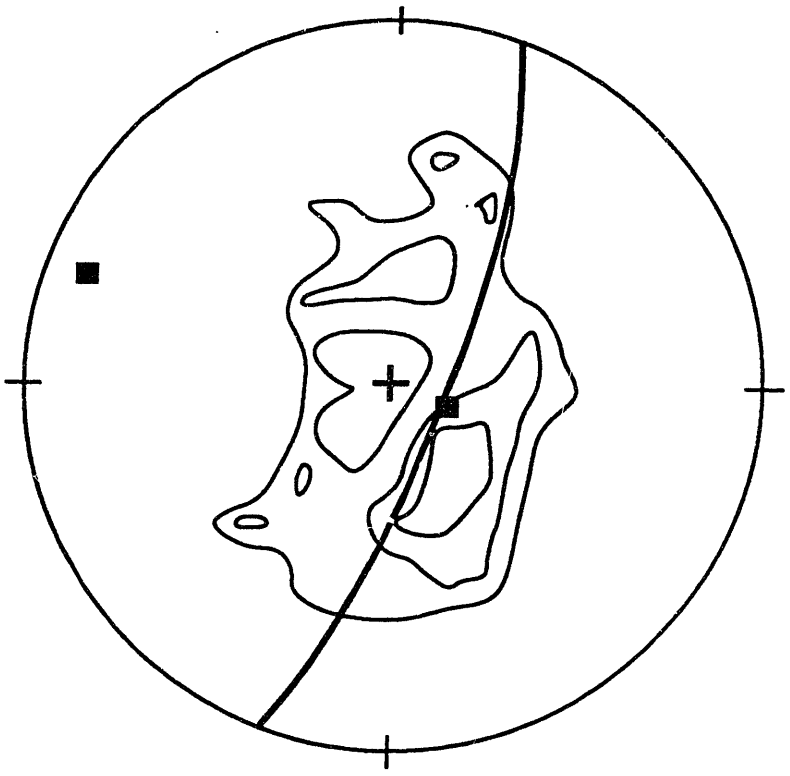

Figure 1.11

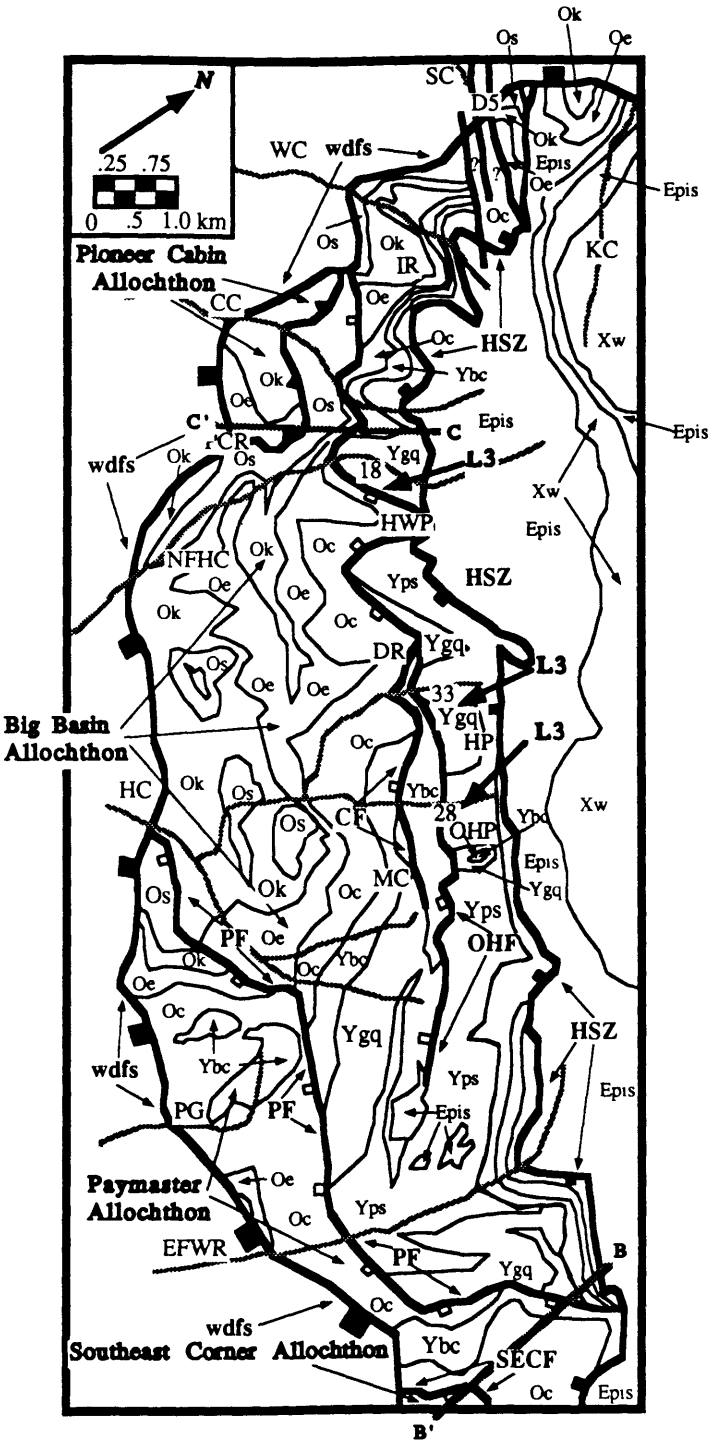
N
.25 .75
0 .5 1.0 km
Pioneer Cabin Allochthon
Big Basin Allochthon
Paymaster Allochthon
Southeast Corner Allochthon
WC
wdfs
SCV
D5
IR
CC
HSZ
KC
Xw
Epis
C'
C
CR
L3
HWP
NFHC
DR
HP
HC
CF
OHP
MC
PF
OHF
PG
EFWR
SECF
B
B'
Ok
Os
Oe
Oc
Ybc
Ygq
Yps
18
33
28

Figure 1.12

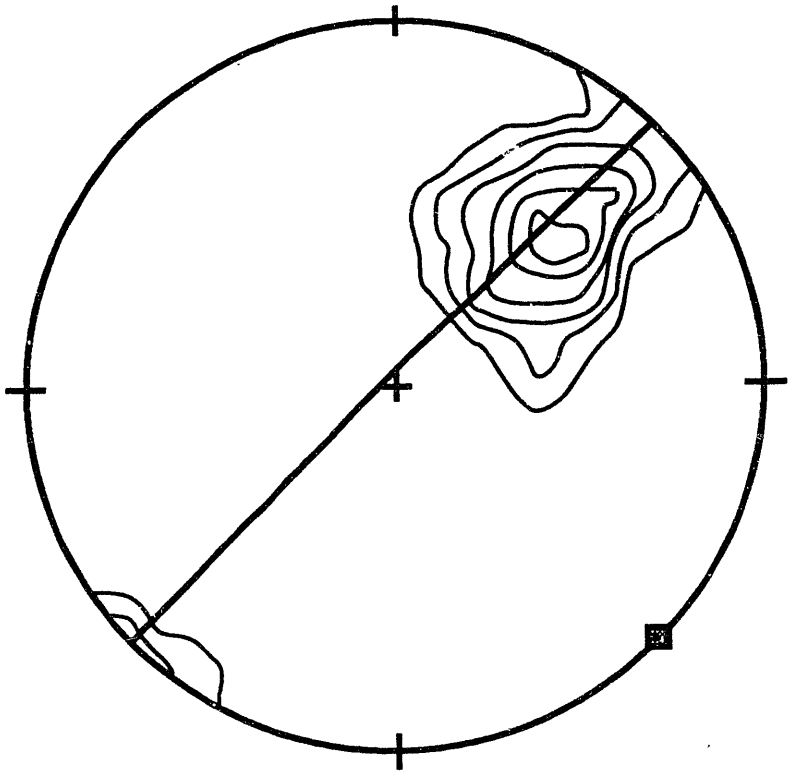

Figure 1.13

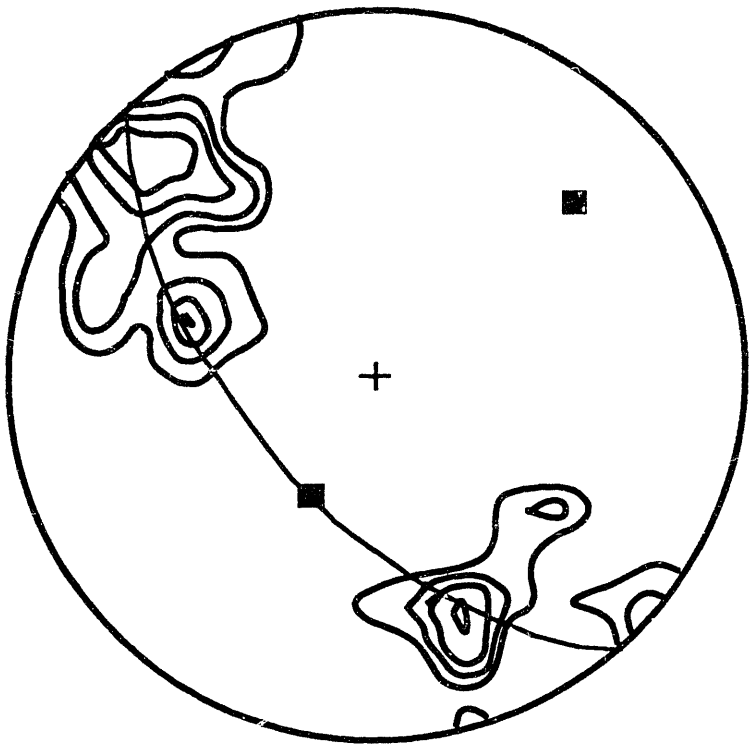

Figure 1.14

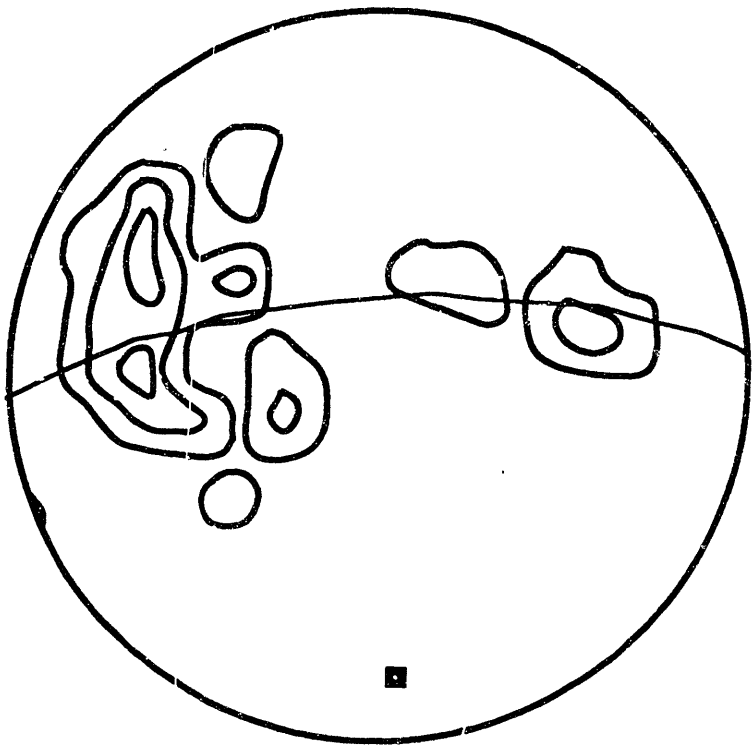

Figure 1.15

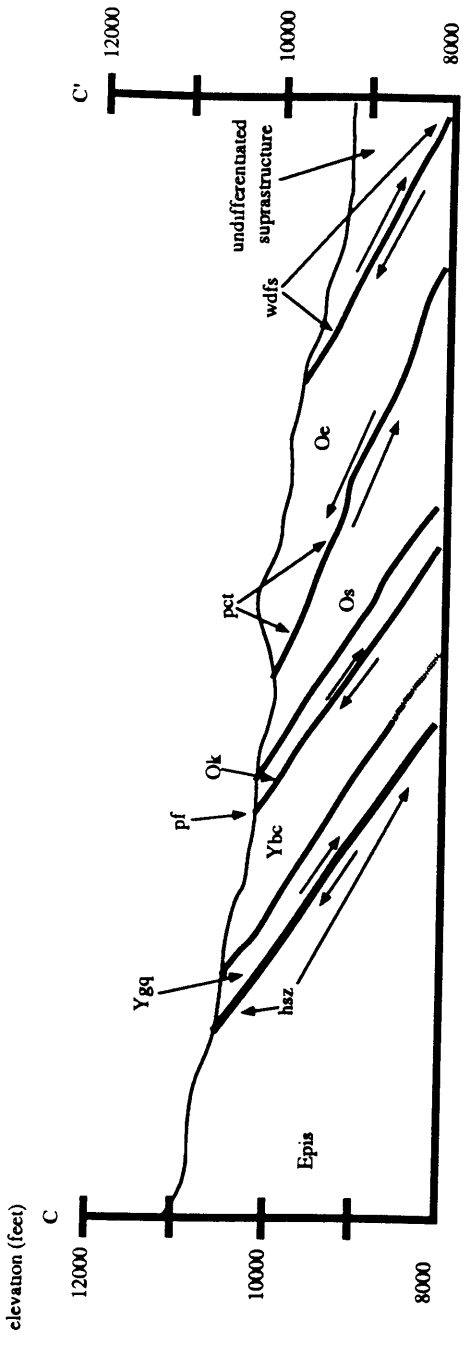
C'
12000
10000
8000
undifferentiated suprastructure
wdfs
Oe
Os
pct
Ok
pf
Ybc
Ygq
hsz
Epis
C
elevation (feet)
12000
10000
8000

Figure 1.16

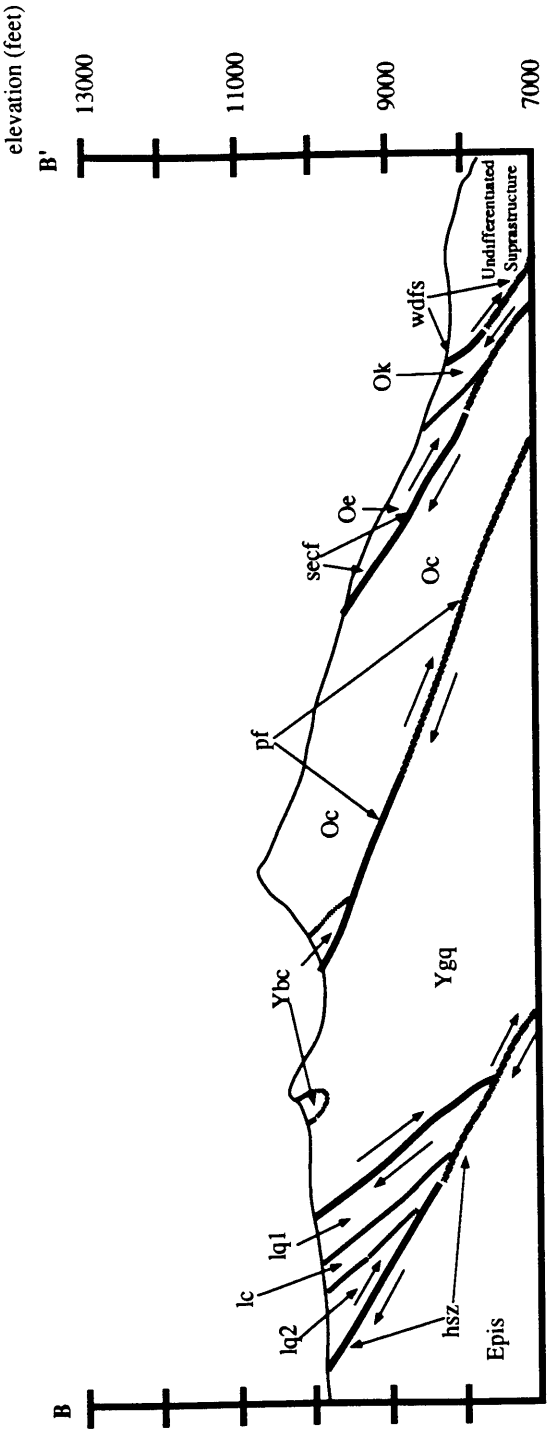
elevation (feet)
B'
13000
11000
9000
7000
Undifferentiated Suprastructure
wdfs
Ok
Oe
secf
Oc
pf
Oc
Ybc
Ygq
lq1
lc
lq2
hsz
Epis
B

Figure 1.17

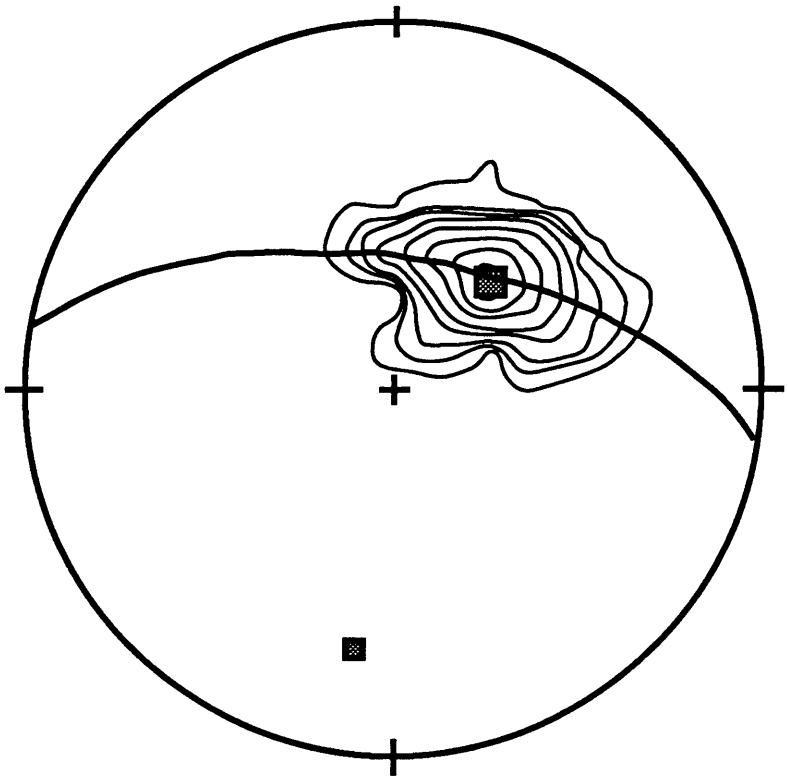

Figure 1.18

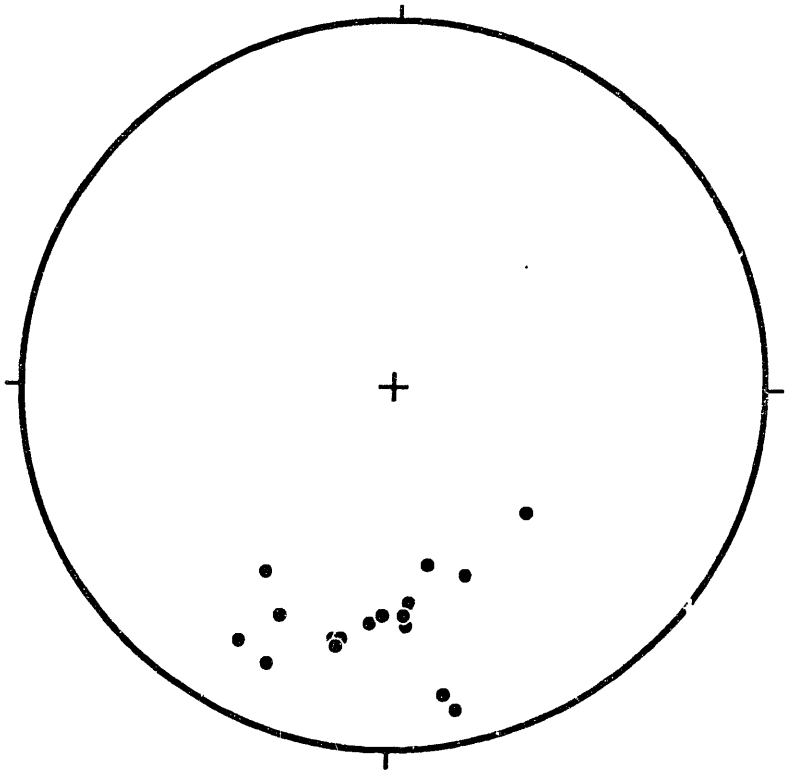

Figure 1.19

Figure 1.20

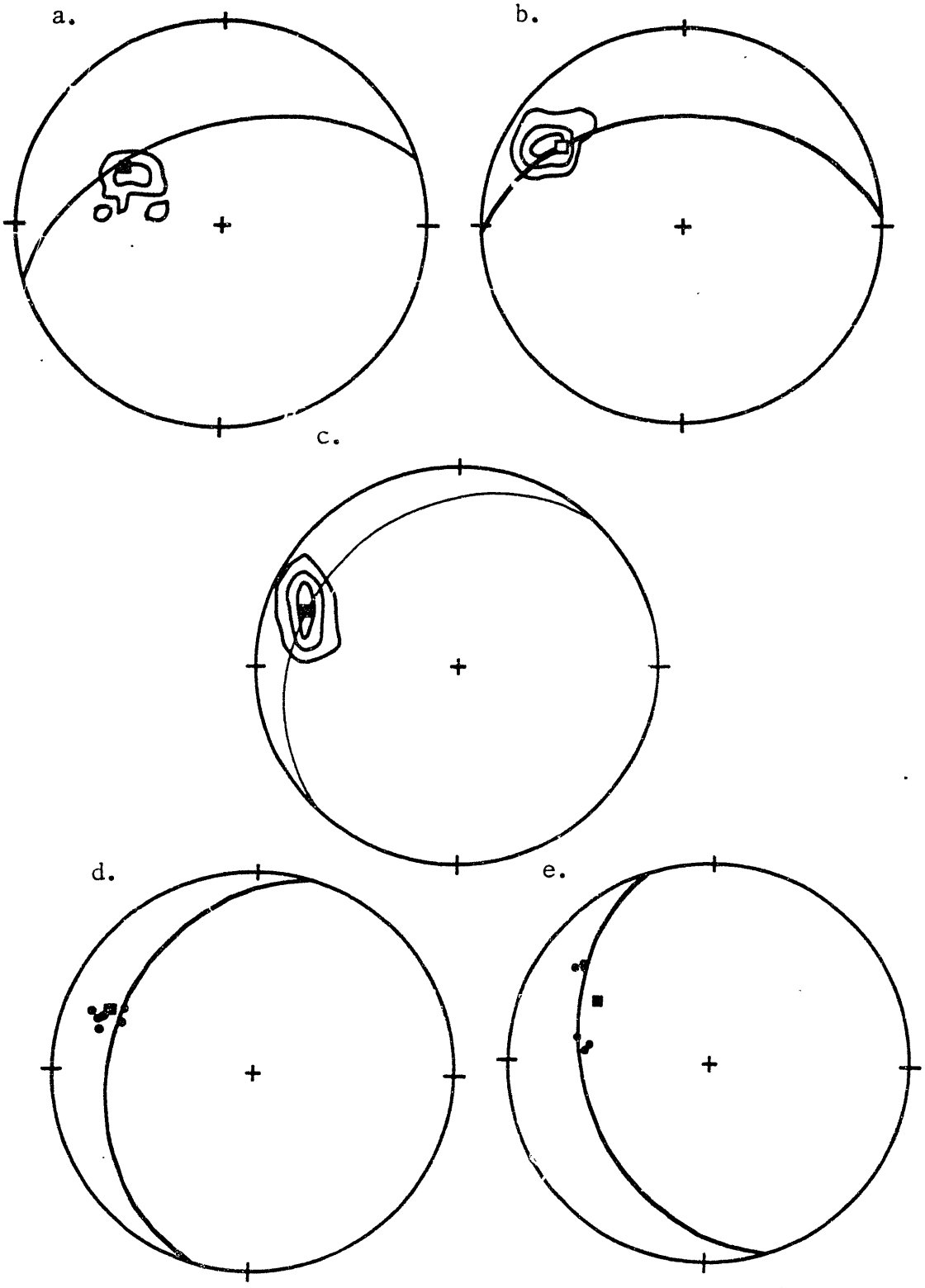

Figure 1.21

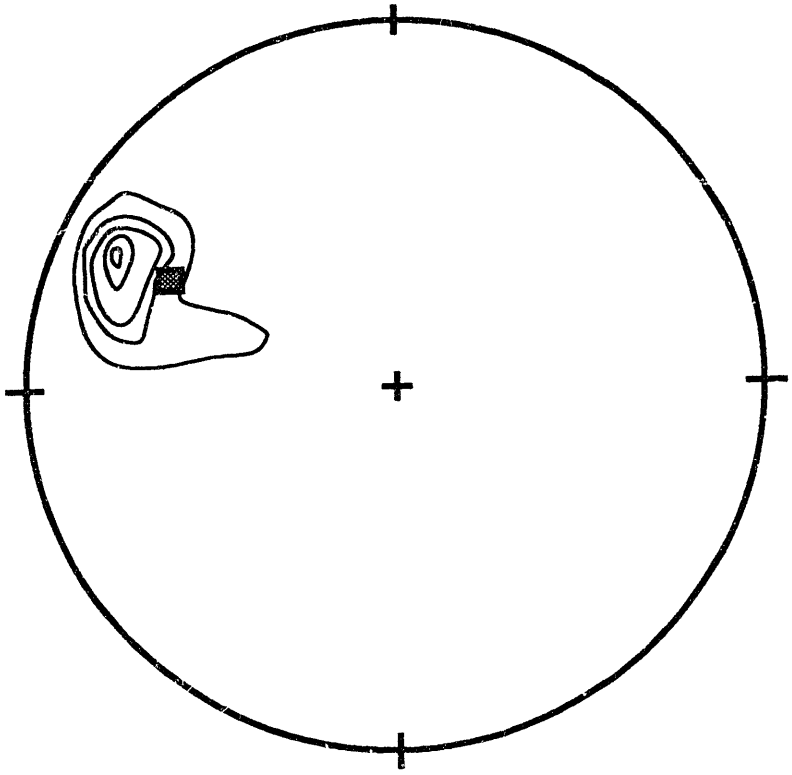

Figure 1.22

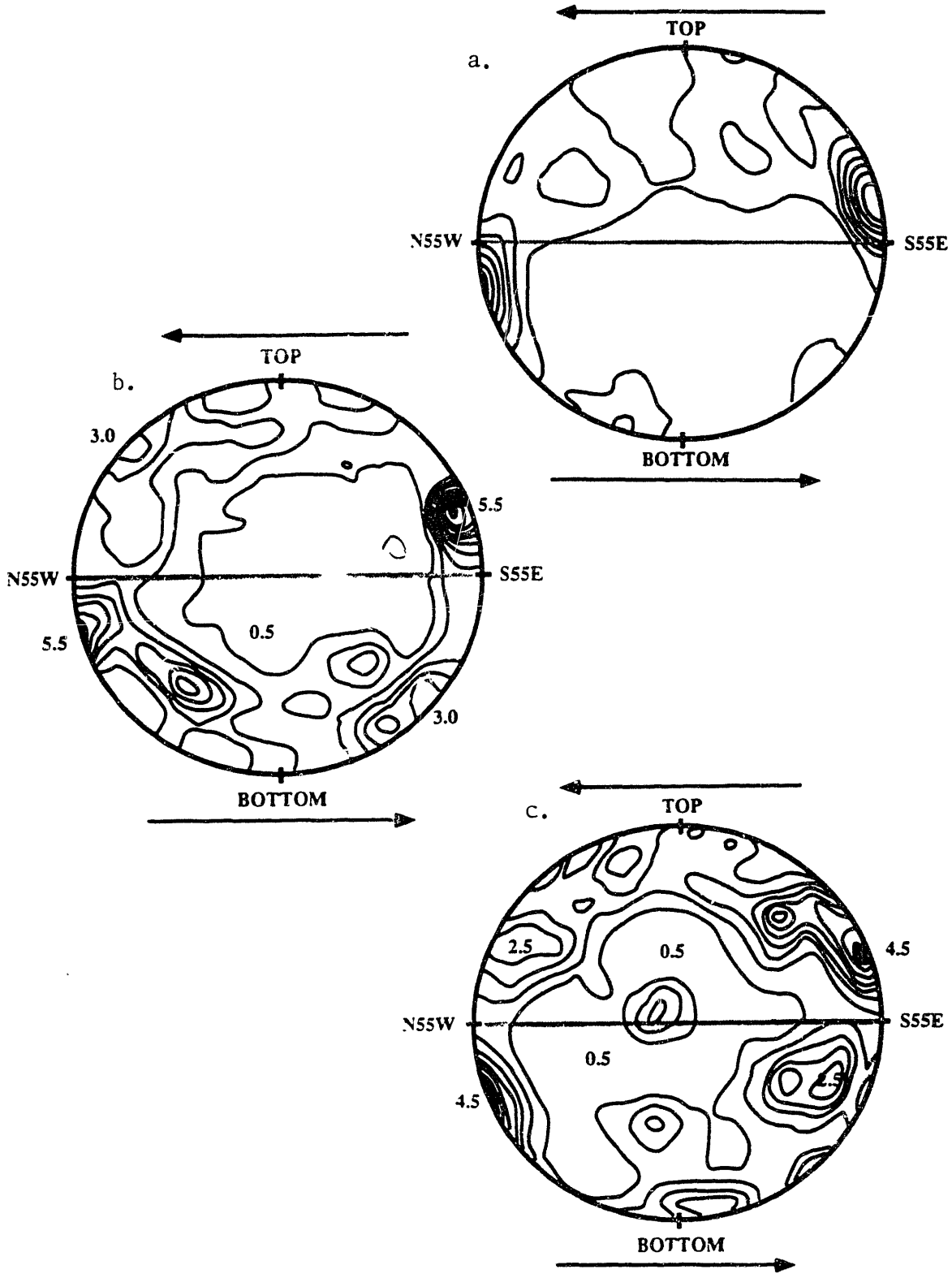
a.
TOP
N55W
S55E
BOTTOM
b.
TOP
3.0
5.5
N55W
S55E
0.5
5.5
3.0
BOTTOM
c.
TOP
2.5
0.5
4.5
N55W
S55E
0.5
4.5
2.5
BOTTOM

# CHAPTER 2: PETROLOGIC CONSTRAINTS ON THE TECTONIC EVOLUTION OF THE PIONEER METAMORPHIC CORE COMPLEX, SOUTH-CENTRAL IDAHO: DEPTH-TEMPERATURE-TIME PATHS IN THE UPPER AMPHIBOLITE FACIES

David S. Silverberg

**Abstract**

The infrastructure of the Pioneer metamorphic core complex in south-central Idaho exhibits the effects of a Middle Eocene low-pressure high-temperature (Abukumi-style) metamorphism with a fairly narrow distribution of reaction isograds which parallel the granodiorite phase of the Middle Eocene Pioneer Intrusive Suite. Structural and textural relationships in the intrusives and country rock indicate that metamorphism and plutonism occurred during the waning stages of south-directed normal-sense shear related to regional extension. Textural relationships in pelitic samples from the Hyndman Group suggest that garnet nucleation and growth is late-kinematic to this extensional episode. Projections onto planar A-F-M phase diagrams and into A-F-M-Ca tetrahedra suggest that garnet cores and rims equilibrated at different pressure and temperatures. Modeling of effective penetration distances for diffusing species into garnet using the available diffusion data indicates that flat garnet core compositional profiles may result from rapid growth rather than post-crystallization volume diffusion. Inclusion suites (cordierite+plagioclase+biotite+sillimanite+ hercynite) suggest significant temperature overstepping of reactions before garnet nucleation. Following nucleation within the 850-960K range, rapid growth resulted in a lack of zoning that is consistent with a model for disequilibrium diffusion-controlled growth. This local equilibrium model predicts the observed Mg-Fe depleted growth aureoles which surround garnet porphyroblasts, the apparent Al- and Si-saturation of the core domain and the reasonable core pressure-temperature ellipses. The infrastructure experienced peak metamorphic conditions of >950K and roughly 355 MPa (roughly 12.4 km depth).

Rim compositions of minerals in the sub-assemblage garnet-plagioclase-biotite-cordierite-quartz-sillimanite±muscovite±chlorite indicate late re-equilibration under

conditions of decreased pressure and temperature. Final equilibration of the matrix occurred at 815-855K and 215-240 MPa (roughly 7.5-8.4 km paleodepth).

Hornblende core and rim barometry and hornblende-plagioclase rim thermometry yielded similar calculated temperatures and pressures. The garnet-cordierite thermometer yielded final equilibration temperatures 150K to 200K lower than those calculated with the garnet-biotite thermometer.

The Middle to Late Eocene decompressional pressure-temperature path has a nominal slope of 1.3 MPa/Kelvin. It implies roughly 4.4 km of unroofing. When coupled with U-Pb ziron data and recent $^{40}Ar$-$^{39}Ar$ data, the petrologic data suggest a time-integrated unroofing rate of roughly 1.5 km/my from 48 Ma to 45 Ma, at the end of the Challis magmatic episode. This could be a result of a rapid erosion-controlled unroofing mechanism or some amount of tectonic unroofing. The final equilibration of the matrix at 7.5-8.4 km is interpreted as the maximum paleodepth at the onset of Oligocene extension. Tectonic models for regional Oligocene extension in south-central Idaho must accomodate the inferred 23 km maximum horizontal slip of the Wildhorse Detachment Fault System.

## Introduction

The use of equilibrium thermodynamics to constrain tectonic processes and their rates may be divided into four fundamental approaches: rim themobarometry (Essene, 1982; 1989; Hodges & Royden, 1984; Spear & Peacock, 1989), garnet inclusion suite thermobarometry (Tracy et al., 1976; Ghent et al., 1979; St. Onge, 1987), the Gibbs method of thermodynamic modelling of garnet zonation (Spear & Selverstone, 1983; Selverstone et al., 1984) and fluid inclusion analysis (Roedder, 1984). Application of these techniques is predicated on the assumption of equilibrium between phases. For the garnet zoning and inclusion thermobarometry techniques, the preservation of equilibrium growth and retrograde re-equilibration compositions in garnet are also essential. In many previous studies essentially flat garnet compositional profiles were interpreted to result from post-crystallization diffusional homogenization (Hollister, 1969; Grant & Weiblen, 1971; Tracy et al., 1976, Woodsworth, 1977). The high temperatures and slow cooling rates associated with many Barrovian terranes may undoubtedly affect the compositional profile of garnet. However, the high temperatures and exceptionally rapid heating and cooling rates associated with Abukumi- or Buchan-style metamorphism may result in the preservation of equilibrium compositions. Field-based studies in a wide variety of metamorphic terranes offer the opportunity to test experimental calibrations of geothermobarometers and numerical models of tectonometamorphic processes.

The footwall of the Pioneer Metamorphic Core Complex provides the first exposure of mid-crustal level rocks north of the Snake River Plain in south-central Idaho (Figure 1; Dover, 1966; Coney, 1980). This region is characterized by the superimposition of significant Tertiary magmatism and extension upon the thermal and deformational effects of the Mesozoic Sevier orogeny (Armstrong, 1974; Silverberg *et al.*, in preparation). High-grade metamorphism associated with Eocene plutonic activity occurred in the core of the

Pioneer Mountains between two phases of extensional unroofing, providing the opportunity to constrain quantitatively the pressure-temperature history of the footwall during Tertiary extension. In this paper, the results of detailed thermobarometric studies of plutonic and metamorphic lithologies are integrated with recently obtained thermochronologic and structural data (Silverberg *et al.*, in preparation; Silverberg, in preparation) in order to examine the timing and thermal consequences of extensional unroofing in the Pioneer Mountains.

## Geologic Setting

The basic structure of the Pioneer Mountains is best described in terms of a metamorphic and plutonic infrastructure that is structurally overlain by a predominantly sedimentary and volcanic suprastructure (Figure 2; Dover, 1966, 1981). The infrastructure may be subdivided further into (Figures 3 & 4): 1) a parautochthon, consisting of the Precambrian (X?) Wildhorse Gneiss Complex; 2) a series of allochthonous sheets composed of the Precambrian-Ordovician, high-grade metasediments of the Hyndman and East Fork Groups; and 3) a predominantly granodioritic and quartz monzonitic intrusive complex (the Eocene Pioneer Intrusive Suite).

Five deformational events can be observed in the infrastructure of the Pioneer Metamorphic Core Complex (Figure 5; Silverberg, in preparation). $D_1$ structures are observed only in the parautochthon. Characterization of this event is difficult due to penetrative $D_2$ deformation. Isoclinal $F_2$ folds in the Wildhorse Gneiss Complex, the Hyndman Group and the East Fork Group are overturned to the east (Holm, 1962; Dover, 1966, 1981; O'Neill & Pavlis, 1988; Silverberg, in preparation). $F_2$ folds locally double the stratigraphic thickness of the Hyndman and East Fork Groups suggesting significant shortening in the hinterland of the Sevier orogenic belt at this latitude. High-grade

metamorphism of the basement and low greenschist facies metamorphism of the Hyndman and East Fork Groups accompanied this deformation. A single thrust nappe, the Pioneer Cabin Thrust, cuts across $F_2$ folds in its footwall. The basement cooled below 800K by 79 Ma (Silverberg *et al.*, 1989), an age similar to many other magmatic, metamorphic and deformational events in the hinterland south of the Snake River Plain (Miller & Gans, 1989) and northwest towards the Idaho Batholith (Barton *et al.*, 1988).

Tertiary extensional deformation is distinctly diachronous in the Pioneer Mountains as constrained by cross-cutting tectonite fabrics (Silverberg, in preparation) and the topology of temperature-time curves (Figure 6; Silverberg *et al.*, in preparation). Extension associated with $D_3$ resulted in the development of three extensional allochthons: the Southeast Corner Allochthon, the Paymaster Allochthon and the Big Basin Allochthon. Extensional faults propagated down-section until the Hyndman Shear Zone decoupled the Hyndman and East Fork Groups from the parautochthon. At roughly 48 Ma, the Pioneer Intrusive Suite (coeval with the Challis volcanic-plutonic episode in this region) was emplaced along the still-active Hyndman Shear Zone causing a low pressure-high temperature metamorphism of the country rocks. Metamorphic reaction isograds in the country rocks wrap around the intrusive suite, with metamorphic grade dropping from sillimanite-orthoclase at the contact to andalusite several hundred meters away. Thermal affects of the Pioneer Intrusive Suite resulted in recrystallization and overprinting of some $S_3$ fabrics. Despite this, low-angle normal-sense shear with hanging wall transport to the south is well-constrained by $D_3$ mylonitic lineations, S-C fabrics, and asymmetric porphyroclasts in the Hyndman Shear Zone (Silverberg, in preparation).

$D_4$ extension was characterized by motion along the Wildhorse Detachment Fault System (Wust, 1987; O'Neill and Pavlis, 1988; Silverberg, in preparation). This fault system has both a ductile and a brittle component. Ductile deformation is restricted to a less than 200

m-wide shear zone that cuts across older structures in the Wildhorse Gneiss Complex, the East Fork Group and the Pioneer Intrusive Suite (Silverberg, in preparation). Lineations are constant in trend along variously oriented segments of the shear zone, suggesting that the original shear zone geometry was curviplanar. Mylonites from the shear zone cooled at a time-integrated rate of 50 K/Ma from 36 to 33 Ma, effectively dating ductile deformation in the shear zone (Figure 6; Silverberg *et al.*, in preparation). As the infrastructure was uplifted through the ductile-brittle transition, brittle deformation overprinted the earlier ductile deformation and a series of detachment faults developed. Some of these incised the infrastructure, cutting out earlier $D_4$ ductile structures toward the east. The eastern margin of the infrastructure is bounded by the east-dipping White Mountain normal fault, probably a compensation structure related to late $D_4$ isostatic adjustment.

This study focuses on plutonic lithologies of the Pioneer Intrusive Suite, pelitic schists of the Hyndman Group in the immediate vicinity of the Hyndman Shear Zone, and pelitic schists in the mafic schist member of the Wildhorse Gneiss Complex. The Wildhorse Gneiss Complex displays evidence of only $D_1$ and $D_2$ deformation in the sample localities; however the thermal effects associated with late-$D_3$ emplacement of the Pioneer Intrusive Suite may have affected samples from this complex. The following observations suggest that emplacement of the Pioneer Intrusive Suite and related high-temperature metamorphism of the Hyndman Group were syn- to late-kinematic with respect to the $D_3$ Hyndman Shear Zone: 1) the western outcrop belt of the intrusive suite follows closely along the trace of the shear zone; 2) magmatic and high-temperature solid-state foliations in the intrusive suite are subparallel; 3) the solid-state foliation in the intrusive rocks is subparallel to $S_3$ foliation in the Hyndman Group; and 4) most of the high-temperature porphyroblasts in the pelitic rocks, with the exception of garnet, are synkinematic with $S_3$ protomylonitic fabrics.

Consequently, thermobarometric results for samples collected near the shear zone are interpeted as pertaining to late-$D_3$ extensional conditions.

## Sample Descriptions and Mineral Chemistry

Compositional transects and detailed evaluation of rim compositions were made using the JEOL 733 Superprobe at the Massachusetts Institute of Technology. Standardization with a combination of natural and synthetic phases was performed at the beginning of each run and rechecked at 5 hour intervals. Rim analyses were made just beyond any measurable edge effect, usually within 4 μm of the apparent rim in backscatter electron images. All phases were analyzed with a 2 μm electron beam. Tables 2-8 contain compositional data, with uncertainties reported at the 95% confidence level, for minerals used in thermobarometry. Figures 11 and 12 show representative phase composition profiles of the Hyndman Group pelitic schist and Pioneer Intrusive Suite, respectively.

### *Pelitic Schists of the Hyndman Group*

The pelitic schists often display a compositional banding that probably reflects graded bedding in the sample protolith with the siliceous/psammitic layers composed of biotite, plagioclase, quartz and ilmenite, and the aluminous/pelitic layers consisting of garnet, aluminum silicate, biotite, cordierite, quartz, plagioclase and muscovite. The relationship between crystallization and deformation events is illustrated in Figure 7.

At distances greater than 50 meters from the Hyndman Shear Zone, the predominant foliation ($S_2$) is subparallel to the compositional banding. Aluminum silicate polymorphs are randomly oriented and locally form 5-7 cm long porphyroblasts which splay within $S_2$.

Within 50 m of the Hyndman Shear Zone, the peltic schist is characterized by $S_3$, a discontinuously protomylonitic foliation. Prismatic sillimanite porphyroblasts define a

lineation, $L_3$, that plunges roughly 30° SSW. Quartz and plagioclase show undulatory extinction, with quartz occasionally displaying poorly developed deformation lamellae. In contrast certain quartz-rich horizons display a mosaic texture with interfacial angles of 120°, suggestive of high-temperature, post-kinematic strain relaxation. Feldspar porphyroclasts are usually pulled apart with biotite and quartz growing in fractures.

The distribution of metamorphic assemblages may be conveniently subdivided into three mineralogically distinct zones separated by the 1st and 2nd sillimanite reaction isograds. Assemblages characteristic of these facies place general constraints on the temperature structure and paleodepth during metamorphism. The facies series can be understood through examination of a petrogenetic grid for pelitic schists (Figure 10).

*High-Temperature Side of the 2nd Sillimanite Reaction Isograd*

Pelitic Schists from the high-temperature side of the 2nd sillimanite reaction isograd crop out within 25 meters of the contact with the Pioneer Intrusive Suite. Approaching the contact with the intrusive rocks, the pelitic schist is locally migmatitic. It is likely that these migmatites are a consequence of both igneous injection and minor anatectic melting. The absense of evidence for extensive in situ anatectic melting suggests maximum temperatures did not long exceed the granodiorite solidus. At pressures approaching the aluminum silicate triple point, the granodiorite solidus is at 935K (Manning & Pichavant, 1983), roughly 35K higher than that for granite (Piwinskii, 1968). The matrix assemblage includes K-feldspar, biotite with ilmenite exsolution lamellae, retrograde muscovite after sillimanite, retrograde pinnite after cordierite and retrograde muscovite, rutile and Fe-rich chlorite after biotite. The domain immediately around garnets is somewhat depleted in micas. Ilmenite is observed altered to rutile-rich leucoxene. Trace phases include monazite and apatite. The absence of prograde muscovite and the presence of sillimanite and K-

feldspar in these pelitic schists suggests that peak temperatures exceeded that associated with the 2nd sillimanite reaction isograd (Kerrick, 1972; Thompson, 1974):

$$Ms + Qtz = Kfs + Sill + H2O. \qquad [Reaction\ 1]$$

At pressures below the aluminum silicate triple point of Holdaway (1971) and $X_{H2O}=1$, this reaction isograd is located in the temperature interval of roughly 875-975K.

Garnets in the 2nd sillimanite zone contain the inclusion suite: sillimanite+hercynite+cordierite+biotite+plagioclase+quartz+ilmenite. In some cases, inclusions in these garnets have inclusions themselves: biotite, hercynite and ilmenite are found within sillimanite; plagioclase occurs in quartz; and cordierite inclusions contain plagioclase.

Experiments on the stability field of hercynite+cordierite+sillimanite in the absense of staurolite in low $f_{O2}$ and Mg-free systems have suggested a minimum stability temperature of roughly 960-1025K at pressures between 200-400 MPa (Richardson, 1968). A compilation of data on hercynite-cordierite pairs by Kars *et al.* (1980) suggests estimated temperature and pressure conditions that range from 925-1100K and 400-650MPa.

*High Temperature Side of the 1st Sillimanite Reaction Isograd*

Pelitic schists from the high temperature side of the 1st sillimanite reaction isograd are charaterized by an absence of matrix K-feldspar and the presense of main-phase matrix muscovite. All of the other matrix minerals from the 2nd sillimanite zone are present. Sillimanite occurs as randomly oriented prismatic needles that lie within the foliation and pseudomorphic fibrolitic mats after muscovite. The discontinuous reaction:

$$andalusite = sillimanite \qquad [reaction\ 2]$$

delineates the low-temperature boundary and constrains the pressure of this facies series to be below the aluminum silicate triple point (Holdaway, 1971). Although reaction 2 is likely not the actual overall reaction that accomodates the polymorph inversion, it is

nonetheless useful to use this univariant reaction to delineate the andalusite zone from that of the 1st sillimanite zone. Inclusions of hercynite in garnet are conspicuously absent.

*Low Temperature Side of the 1st Sillimanite Reaction Isograd*

Pelitic Schists on the low temperature side of the 1st sillimanite reaction isograd crop out at a map distance of greater than 0.4 km from the igneous contact. Toward the southeast, the pelitic schist is separated from the Pioneer Intrusive Suite by a gneissose quartzite unit. Pelitic intercalations within the gneissose quartzite formations of the Hyndman and East Fork Groups display spectacular splays of randomly oriented andalusite prisms. The main phase assemblage on the low temperature side of the 1st sillimanite reaction isograd is similar to that on the high temperature side of the 1st sillimanite reaction isograd except that garnet is conspicuously absent and staurolite is present but very rare. The lower temperature limit of the mineral assemblage is delineated by the kyanite-sillimanite univariant curve (Holdaway, 1971) and the breakdown of Mg-cordierite (Schreyer & Yoder, 1964) to approximately 775-825K.

The stability of cordierite-andalusite-staurolite, with the absence of almandine, suggests conditions between 775-975 K and 200-600 MPa.(Ganguly, 1972) Nonetheless, staurolite was only rarely observed suggesting that its localized presence may be due to the existence of a trace system component such as zinc that expands its stability field. The general absence of staurolite suggests that the facies series in the Pioneer Mountains Core Complex is similar to that developed typically in the Abukuma Plateau of Japan (Miyashiro, 1958, 1961; Shido, 1958; Shido & Miyashiro, 1959), a distinctly *low-pressure facies series*.

*Mineral Chemistry*

Ten samples were studied in detail from the high-grade side of the 1st sillimanite reaction isograd. Reasonable projection of the Pioneer Intrusive Suite granodiorite-Hyndman Group pelitic schist contact at a constant dip of 30° indicates that all of the samples were collected within roughly 100 meters of the intrusion. These 10 samples are: P5B, P151, P213A, P225A, P225B, P230, P243B, P248B, P317, and P335. Textural and compositional descriptions of the mineralogy are given below (see also Dover, 1966, 1969). Mineral assemblages of selected schists and analyses are presented in Tables 1 through 10.

*Garnet* porphyroblasts are 1-5 mm in diameter, subhedral and poikiloblastic (Figure 9) containing inclusions of sillimanite, biotite, cordierite, hercynite, plagioclase, quartz and less commonly muscovite. Syntectonic fabrics are absent and the matrix foliation, as defined by aligned biotite and sillimanite, is truncated by the garnet edge suggesting that final growth of garnet post-dated development of the $S_3$ fabric. The area immediately around the garnet is sometimes depleted in biotite suggesting garnet growth at the expense of biotite. Porphyroblasts display rim resorption textures (Tracy, 1982) and are sometimes fractured.

Several samples displayed depletion halos at garnet rims adjacent to biotite. In this case, garnet rim compositions were measured adjacent to plagioclase or quartz. The garnet that surrounded biotite inclusions frequently displayed a minor depletion halo adjacent to the biotite inclusion, strongly suggestive of post-crystallization volume diffusion. There were no observed depletion halos in garnet adjacent to either matrix or inclusion plagioclase. With the exception of biotite-associated depletion halos, garnet compositional profiles reveal relatively little variation. The offset symmetry of P335 profile probably reflects a somewhat off-center transect. P335 garnet is rather homogeneous from the core area to within 100 μm of the rim. Beyond 100 μm, Mg/Mg+Fe decreases and Xsp increases,

implying rim resorption at a temperature lower than the thermal maximum. Although not present in sample P335, several other samples display minor positive and negative gradational changes in the grossular component at roughly 10 μm in from the rim, suggestive of a pressure sensitive net-transfer reaction that involves Ca.

*Biotite* occurs as 1-3 mm foliation-defining laths in the matrix and as inclusions less than 1 mm in length in garnet poikiloblasts. Within a given sample biotite composition is relatively uniform; however between samples the Fe/Fe +Mg ratios range from 0.40 to 0.49. The most annite-rich compositions in any sample occur where matrix biotite is in direct contact with garnet, reaching up to $X_{ann} = 0.60$. In two samples, $X_{ann}$ increases by as much as 0.02 at the mineral edge. These late diffusive effects were noted when a sample was analyzed for thermobarometry. Similar steep compositional gardients in biotite inclusions were noted. Most individual biotite inclusions in garnet poikiloblasts are homegeneous and the inclusion $X_{ann}$ may be as much as 0.08 lower than the matrix composition.

*Muscovite* is a part of the stable matrix assemblage and is rarely observed as an inclusion in garnet poikiloblasts. In a few samples the muscovite is found replacing sillimanite, suggesting a retrograde reaction consuming sillimanite and $H_20$ to produce muscovite and biotite. It was also observed in garnet fractures with chlorite as a retrograde phase.

*Plagioclase* , a ubiquitous matrix phase, occurs as anhedral (1-3 mm in diameter) relatively homogeneous porphyroblasts and is also present as rare, small (< 1 mm in diameter) inclusions in poikiloblastic garnet. Matrix plagioclase composition ranges from oligoclase to labradorite depending on the sample. Individual grains show a smooth zonation from anorthite-rich cores to more albite-rich rims with rims 1-4 mole % richer in

albite content than the cores. Inclusion plagioclase is homogeneous and 1-3 mole % richer in anorthite than matrix plagioclase edges.

*Cordierite* occurs as inclusions (0.1-0.3 mm in diameter) in garnet poikiloblasts and as isolated anhedral grains (0.1-0.5 mm in diameter) in the matrix. Matrix cordierite Mg/Mg+Fe ratios range from 0.6 to 0.7 depending on the sample, but have relatively uniform core composition. Individual samples are zoned within 15 μm of the matrix edge, and $X_{Mg}$ of the core may be 0.06 greater than that at the matrix edge. A single sample (P244) showed a reverse trend for $X_{Mg}$, in both cordierite and biotite. In general, cordierite inclusions in garnet poikiloblasts are unzoned and have similar composition to matrix cordierite cores.

*Sillimanite* occurs as abundant euhedral prismatic needles (0.6-2 mm in length) or as fine mats of fibrolite in the matrix. It is frequentlty observed as inclusions in garnet and is closely associated with hercynite in the core areas of garnet poikiloblasts.

*Hercynite* occurs as clusters of dark-green anhedral grains (.10-.25 mm in diameter) enclosed in garnet. It is usually associated with sillimanite and cordierite, sometimes intimately intergrown with euhedral sillimanite in the garnet core.

*Pelitic Schist of the Wildhorse Gneiss Complex*

A pelitic schist horizon in the Mafic Gneiss member of the Wildhorse Gneiss Complex occurs as 2-4 parallel discontinuous layers. They are 1-6 m in thickness and outcrop prominently at Kane Lake and in the headwater cirques of Boulder Creek (P120, P125; Figure 2). The predominant mesoscopic fabric in these garnet-biotite schists is $S_2$, parallel to the penetrative $S_2$ in the adjacent mafic and quartzofeldspathic gneisses.

*Garnet* is anhedral and intensely cracked so that the core areas may not have been isolated from the matrix. The cracking could be late- to post-kinematic to the $D_2$

metamorphism. Garnets are strongly zoned: Mg/Mg+Fe decreases from core to rim, while $X_{sp}$ increases. Xgr remains constant.

*Sillimanite* is present as prismatic crystals 2-10 mm in length and as fibrolitic mats intergrown with biotite.

The *Biotite*is a dark red-brown and has a modal abundance of roughly 50%. Biotite is homogeneous with a $X_{ann}$=0.404±0.011.

*Plagioclase* occurs as anhedral (1-2 mm in diameter) porphroblasts that are intensely cracked. They are apparently normally zoned; edge compositions, at $X_{an}$=.480, are more albitic by 0.07 to 0.13 than the cores.

*Cordierite* occurs rarely as small (2-4 mm in diameter) anhedral crystals in the matrix. It is relatively homogeneous with a $X_{Fe}$=0.33.

*Chlorite* sheafs fill garnet cracks which are roughly 8 μm wide.

*Pioneer Intrusive Suite:*

The $S_3$ foliation of the Pioneer Intrusive Suite (P92, P155 & P156) is defined by a preferred orientation of broken hornblende phenocrysts and a second generation of biotite (biotite II) that clearly post-dates the broken primary biotite (biotite I). In rocks with a well-developed $S_3$ fabric, plagioclase and microcline are broken. Recrystallized quartz and mica fill the fractures in feldspar and hornblende. The long length of oscillatory zones and albite law interfaces in the plagioclase porphyroclasts are sub-parallel to the shear foliation. All phases display undulatory extinction. In some cases, microcline porphyroblasts were observed to cross-cut the shear fabric.

Samples P155 and P156 were collected at the 2980 m level of the north fork of Hyndman Creek (Site 2 of Figure 2). Sample P155 is a well-foliated dioritic gneiss that contains the assemblage pyroxene, hornblende, biotite, plagioclase, K-feldspar, ilmenite

and quartz. Sample P156 is a granodiorite collected 20 m from sample P155. Sample P156 contains hornblende, biotite, K-feldspar, plagioclase, quartz, sphene, apatite and ilmenite. It is well-foliated and contains relict phenocrysts of clinopyroxene with reaction rims of hornblende.

Sample P92 was collected from the 3220 m level above Betty Lake in the eastern outcrop belt of the Pioneer Intrusive Suite (Site 1 of Figure 2). It is a fine-grained granodiorite with a directionless fabric. The predominant quartz monzonite phase of the Pioneer Intrusive Suite in this area contains cognate inclusions of similar rock. The quartz monzonite contact with the granodiorite is sharp; field observations suggest that this granodiorite predates emplacement of the quartz monzonite. The P92 granodiorite assemblage includes hornblende, biotite, K-feldspar, plagioclase, quartz, sphene and magnetite.

*Hornblende* grains , 0.5 to 2.5 cm long, are typically euhedral to subhedral porphyroblasts that lie in the $S_3$ foliation plane. In a few samples, rare remnants of clinopyroxene have been converted to a ferrohastingsitic hornblende. The hornblende in turn has undergone minor alteration to biotite. Hornblende analyses were recalculated and cations were assigned using the procedure described by Spear & Kimball (1984). The amount of $Fe^{3+}$ in the hornblende is critical in this study because both Na (M4) and Al (T) are very sensitive to this quantity. The preferred $Fe^{3+}/(Fe^{2+} + Fe^{3+})$ used in further calculations was the average of the least upper bound and the greatest lower bound of $Fe^{3+}/(Fe^{2+} + Fe^{3+})$ obtained from the different normalizations. Hornblende rims contain between 1.298 and 1.339 Al cations whereas the cores often range up to 1.7 Al cations. Si shows a corresponding decrease of 0.1-0.2 cations from rim to core. Amphiboles are largely unzoned with respect to Mg and Fe.

*Plagioclase* composition ranges from $An_{40}$ to $An_{22}$. Rims are generally 0.02 to 0.10 richer in $X_{ab}$ than the cores, although a few samples contain relatively homogeneous plagioclase. Individual grains display normal zoning with thin oscillations superimposed on the normal zoning trend. Seritization of the calcic cores is common.

*Potassium Feldspar* occurs as microcline, although perthitic orthoclase occurs locally. Both varieties of K-feldspar are usually poikilitic with inclusions of quartz. K-feldspars are unzoned and binary, with maximum $X_{ab} = 0.03$.

## Phase equilibria considerations

Phase relations in the Hyndman Group and Wildhorse Complex pelitic schists may be described in the major element model system $SiO_2$-$Al_2O_3$-MgO-FeO-CaO-$Na_2O$-$K_2O$-$H_2O$. The eight component sytem can be shown graphically in three and four component space by projection from ubiquitous phases. Crossing tie-lines or phase volumes can be construed to represent: a) non-uniform pressures and temperatures of equilibration; b) non-uniform composition of the phases through which projections were made; c) minor and trace element modification of phase relations, such as Mn stabilizing garnet, Ti stabilizing biotite, or Zn stabilizing staurolite.

*AFM*

Phase relations projected from quartz, muscovite and $H_2O$ into $Al_2O3$-FeO-MgO (AFM; Thompson, 1957) space for rim and host-garnet/entrapped-mineral compositions of the Hyndman Group and Wildhorse Gneiss Complex are shown in Figure 13. Samples with muscovite have been projected through muscovite; samples with K-feldspar have been projected through K-feldspar. The host-garnet/inclusion compositions have been plotted with the assumption that muscovite was stable. Given these assumptions, all projections are thermodynamically legal (Greenwood, 1975). The garnet-biotite-cordierite-sillimanite

final equilibration compositions from pelitic schists of the Hyndman Group and the Wildhorse Gneiss Complex have been simplified in projection to garnet-aluminum silicate-biotite triangles. These projections yield abundant crossing tie-line relationships.

*AFMC*

The appearance of intersecting phase volumes in AFMC plots of the three sets of data (Figure 14) suggests that the evidence for disequilibrium in AFM space is not an artifact of the projection. The presence of five Al-Fe-Mg-Ca phases (garnet-sillimanite-cordierite-biotite-plagioclase) in both matrix and inclusion assemblages suggests the stabilization of plagioclase by Na. The lack of systematic Fe-Mg partitioning among garnet-biotite-cordierite and Ca partitioning among garnet-plagioclase may reflect different conditions of nucleation and growth within and among the core and matrix compositions, or within sample non-equilibrium processes.

## Pressure and Temperature Determinations

### *Hyndman Group Pelitic Schists Geothermometry and Geobarometry*

The rationale for sample collection and quantitative analysis was to maximize the number of geothermobarometers that could be applied to a suite of rocks that have undergone a somewhat similar evolution of physical conditions. The physical conditions attendant during high-grade metamorphism of the Pelitic Schist Formation of the Hyndman Group and the Wildhorse Gneiss Complex were calculated using the garnet-biotite (GARB) geothermometer (Ferry & Spear, 1978; Hodges & McKenna, 1987) and the well-calibrated garnet-aluminum silicate-quartz-plagioclase geobarometer (GASP-Newton & Haselton, 1981; McKenna & Hodges, 1988), using the solution models described in Hodges & Royden (1984). A Monte Carlo technique (Hodges & McKenna, 1987) was used to propagate standard deviations of measured compositions through simultaneous solution of

the preferred pelitic thermobarometers in order to determine the precision of the calculated pressures and temperatures (Table 9); the resultant ellipses indicate 95% confidence fields (Figures 15, 16, 17). "Final equilibration" conditions refers to calculations made with rim or edge compositional data. "Core" conditions refer to calculations made with compositions measured in the homogeneous interior of garnets coupled with the compositions of entrapped minerals. These latter are sometimes refered to as "garnet-host/entrapped-mineral" calculations.

An attempt was made to apply equilbria which involve cordierite, but these are suspect due to: a) the present lack of consensus concerning the behaviour of $K_D$ for Mg-Fe exchange reactions which involve cordierite (for discussion see Van Bosse and A.E. Williams-Jones, 1988; Perchuk & Lavrent'eva, 1983); and b) the strong dependence on hydroxyl content for barometric calculations (Holdaway & Lee, 1977; Aranovich & Podlesskii, 1983).

Most of the pressure-temperature estimates plot within the sillimanite stability field of Holdaway (1971). P225B plots in the kyanite field and is considered spurious. P243B plots in the andalusite stability field. This could reflect the slow kinetics of the aluminum silicate polymorph transformation. Despite the reasonability of the calculated pressure, the documented disequilibrium obviates use of the calculated pressure and temperature. P248 plots at significantly higher pressure and temperatures than any of the samples and so is also considered spurious. The higher temperature of P248 may reflect the late crystallization of chlorite in the matrix which may have disturbed the equilibrium partitioning of Mg-Fe between garnet and biotite. With the exception of P151 and P225A, the ellipticity of the final equilibration plots indicates precisions of better than ±50K.and ±60MPa Five of the samples (P5B, P151, P225A, P230E, P335) are statistically

indistinguishable at conditions of 210 MPa and 850K. P213A lies just out of this range with a minimum pressure of 235MPa at 850K.

*Wildhorse Gneiss Complex Pelitic Schists Geothermometry and Geobarometry*

The two samples, P120 and P125, yielded significantly different final equilibration pressures and temperatures (Table 9; Figure 17). P120 contains a great amount of compositional variance and this is reflected in the enormous calculated uncertainties. In contrast, P125 yielded final equilibration conditions of 342±75 MPa and 848±48 K.

*Pioneer Intrusive Suite*

*Hornblende Barometry*

The Pioneer Intrusive Suite was sampled in order to determine the emplacement pressure and temperature using the hornblende barometer (Hammarstrom & Zen, 1986; Hollister *et al.*, 1987; Johnson & Rutherford, 1989), and the plagioclase-hornblende thermometer (Spear, 1980). Solidus hornblende equilibrium compositions were assumed when textural features did not suggest post-crystallization re-equilibration (well-defined phase rims, smooth continuous compositional profiles, a lack of $D_3$ deformation at the hornblende-quartz interface). Despite these safeguards, a range in hornblende rim compositions was frequently identified that probably reflects a variability beyond that expected of mere analytical imprecision. In this case, numerous analyses of hornblende rims adjacent to quartz were made for each sample. The reported rim compositions are averages of all rim analyses of hornblende in a thin section selected by the aforementioned criteria (Table 7)

The hornblende geobarometer relates the total alumina content of hornblende to crystallization pressure (Hammarstrom & Zen, 1986, Hollister *et al.*, 1987). It affords the potential of determining depths of emplacement of metaluminous intrusive rocks like those

of the Pioneer Intrusive Suite, but the assumptions inherent in its empirical calibration suggest caution in its use. Theoretically, a sample used for hornblende geobarometry should have the following characteristics: 1) it must be reasonably described by the model system $K_2O$-CaO-FeO-$Fe_2O_3$-$Na_2O$-$TiO_2$-MgO-$Al_2O_3$-$SiO_2$-$H_2O$; 2) it must have contained the phase assemblage plag-qtz-hb-bt-kspar-mag-sphene-melt-$H_2O$ at the time of crystallization; 3) it must have plagioclase composition in the range $An_{25}$-$An_{35}$; and 4) the solidus for the sample must have been similar to that of the samples used for empirical calibration. Samples P92, P155 and P156 contain the necessary assemblage and appear to have the appropriate chemistry. Plagioclase compositions are sightly different from those in the calibration set of Hollister *et al* (1987). The Pioneer samples are quite similar mineralogically to the calibration suite of Hollister *et al* (1987) and there is no reason to believe that their solidii would be substantially different. The empirical calibration of Hollister et al. (1987) yielded the following linear relationship between pressure and total Al:

$$P\ (MPa) = 564Al^T - 476 \qquad r^2=0.97 \qquad \text{[equation 1]}$$

The recent experimental calibration of the hornblende geobarometer (Johnson & Rutherford, 1989) yields a somewhat different regression .

$$P\ (MPa) = 423\ (Al^T) - 346 \qquad r^2=0.99 \qquad \text{[equation 2]}$$

The final equilibration pressures of the three samples ranges from 256-279 MPa by equation 1, and 203-220 MPa by equation 2 (Table 9). Sample P92 consistently gives the lowest pressure; however, all final equilibration pressures lie within the uncertainty of the calibration.

*The Plagioclase-Amphibole Thermometer.*

The partition coefficient, $K_D$, for the exchange reaction

2 albite + tschermakite = 2 anorthite + glaucophane [Reaction 3]

has been calibrated empirically and shown to be moderately sensitive to temperature (Spear,1980). At an $X_{An}$=.25, two linear regressions were calculated on the four points of the original data set (765±20K, 805±20K, 925±25K, 1000±25K). The first regression, which includes all four points yielded:

$$\ln K_D = -11{,}500/T + 11.14 \quad r^2=0.96 \qquad \text{[Equation 3]}$$

The second regression included only the three high temperature points and yielded:

$$\ln K_D = -8{,}600/T + 8.04 \quad r^2=0.98 \qquad \text{[Equation 4]}$$

where $K_D = (X_{An}/X_{Ab})_{plag} \times (X_{Na}/X_{Ca})_{M4,am}$

The sources of error in this calibration include analytical precision, uncertainties in calculating the amphibole formula from the microprobe analysis, divergence in sample composition from the calibration set, and a pressure dependence of the net transfer reaction.

The final equilibration temperatures for samples P92 and P156 were calculated using both sets of coefficients. By equation 3, the temperature range is 889-910K. The temperature range calculated using equation 4 is 874-901K. Given the copious uncertainties in this thermometer, both of these temperature sets are indistinguishable. The calculated solidus temperatures are remarkably similar to those of a granite in the 200-400 MPa range (Figure 20; Piwinskii, 1968); however due to the more mafic composition of the granodiorite and quartz diorite we might expect the solidus to be somewhat higher than that for granite. The temperatures may reflect a minor amount of sub-solidus re-equilibration.

*GARB-GASP-GMBP-Solidus Equilibria*

A single sample of the granodiorite, P153, collected adjacent to the contact with the Hyndman Group pelitic schist, contained garnet and sillimanite. This rather singular

observation of garnet and sillimanite in the granodiorite suggests that they are either xenocrystic or the result of very local metasomatism. In either case, their compostions may not have achieved equilbrium with other matrix phases. With the above caveats in mind, this sample was analyzed for thermobaromtetry by simultaneous solution of the GB and GASP thermobarometers (Table 9; Figure 20). The calculated final equilibration conditions of 420±49MPa and 957±25K are at significantly higher pressure than any of the pelite samples. Alternatively, we may use the intersection of the granodiorite solidus with the GASP $K_D$. This results in a pressure and temperature of 350 MPa and 910K.

## Post-Crystallization Volume Diffusion

The homogeneous garnet profiles imply that intragranular volume diffusion may have modified the chemical composition of early garnet (Hollister, 1966; Grant & Weiblen, 1971; Tracy et al., 1976; Woodsworth, 1977; Spear & Peacock, 1989). If this were the case, certain inclusion phases may not be in equilibrium with the measured garnet composition. However, given the unusually rapid heating and cooling of this style of metamorphism, it may not be wise to jump to a conclusion based on the morphology of the compositional profile alone. For example, exceptionally rapid garnet growth at a restricted range of pressure and temperature, may result in a flat compositional profile (Hodges & Silverberg, 1988). This latter scenario may be further explored by consideration of current garnet diffusion data and the pressure-temperature facies series observed in the field. Although there is a general void in accurate diffusion data for cations under crustal metamorphic conditions, recent experiments have refined our understanding of interdiffusion and self diffusion coefficients for Fe, Mg, Mn and Ca in garnet (Lasaga, et al., 1977; Freer and Dennis, 1982; Cygan and Lasaga, 1985). Edge thermobarometric data for the Hyndman Group suggests that most of the samples may have passed through the

900-925K temperature range which many others have suggested could result in complete diffusional homogenization of mm-sized garnets (Woodsworth, 1977; Tracy, 1982). A minimum homogenization time for garnet can be calculated from Mg self-diffusion data (Cygan and Lasaga, 1985) if one assumes: 1) that Mg transport is the rate determining step for garnet homogenization; and 2) that the kinetic data collected at high temperature is applicable in the temperature range of interest. Assuming constant temperature, an unrealistic but end-member scenario, the approximate penetration distance of a diffusing species is given by Crank (1975) as:

$$x \sim (4Dt)^{.5} \qquad \text{[Equation 5]}$$

Figure 18 illustrates the time needed to homogenize a garnet as a function of temperature and radius. The 800K, 850K, and 900K curves suggest that garnets of diameter greater than 1 mm would need greater than 10 million years to homogenize. Thermal models for rocks subject to a Barrovian-style compression-heating pressure-temperature trajectory, followed by erosion controlled uplift, suggest that rocks remain within 50K of their peak temperature for almost 50% of the orogenic cycle (England and Thompson, 1984). Therefore, with a temperature maximum of 900K or greater, we may expect significant alteration of growth compositions in garnets with diameter 1-4 mm. In contrast, the perturbed geotherm associated with a Buchan or Abukumi-style dynamothermal metamorphism probably cannot be sustained for more than a few million years (England and Thompson, 1984). In reality, the temperature following intrusive emplacement drops rapidly and we might expect a shorter effective penetration distance. Applying these calculations to rocks of the Hyndman Group, we may expect significant diffrences in the compositional profiles that would reflect distance from the intrusive contact and size of the garnet. The fact that garnets of radius greater than 4 mm in the Pioneer Mountains show

homogeneous compositions suggests that the profiles reflect growth processes rather than diffusive homogenization.

If this assumption is made, we may consider application of inclusion suite thermobarometry (St. Onge, 1987) and Gibbs method modeling (Spear and Selverstone, 1983; Selverstone et al., 1984; Spear and Peacock, 1989) only if inclusion phases and monitor parameters other than garnet behaved in a refractory manner since growth. Biotites are almost universally homogeneous in amphibolite facies pelites suggesting that it is not a refractory phase, but rather remains in its entirety in equilibrium with the garnet edge until the ion exchange reaction shuts down. Reaction shutdown may reflect either cessation of garnet binary Mg-Fe diffusion, or possibly, shutdown of a different rate-limiting transfer process such as interface kinetics or intercrystalline transport. If garnet binary diffusion were rate-limiting, we might expect all inclusion garnet-biotite temperatures from the upper amphibolite facies to be identical. A perusal of the literature (Hodges and Silverberg, 1988) and the results of this study indicates that high-grade garnet-host/entrapped-mineral temperatures from different areas vary greater than analytical precision . Although this may result from different cooling rates, variations in core temperatures from intra-unit studies suggest that nucleation or intercrystalline transport rates may be rate limiting. The availibility of water may have profound affects on reaction rates (Walther & Wood, 1984); similiar to the affect of water on order-disorder reaction rates in feldspar (Yund & Tullis, 1980). Thus, if flat growth profile garnets do not display a diffusion halo around biotite inclusions, and the biotite is homogeneous or steeply zoned near its edge, it may be reasonable to use the biotite composition as a monitor parameter for thermobarometric calculations. A minor diffusion halo around a biotite may indicate a post-crystallization compositional change. In this case, it may be plausible to use the garnet core composition away from the biotite inclusion. This latter approach is more reasonable if the biotite

inclusion itself is large and sharply zoned suggesting very rapid cooling and a lack of significant penetration of the binary diffusional equilibrium gradient into the biotite core. A $K_D$ calculated from the biotite core and the garnet core away from the inclusion may reflect growth equilibrium compositions and temperatures. If garnet-biotite thermometry is reasonable for flat growth profile garnets, than simultaneous solution of the GARB geothermometer with the GASP geobarometer or use of the plagioclase as a monitor in garnet zoning modeling is probably safe because of the exceptionally slow coupled substitution of (Na,Ca) and (Al,Si) necessary for the GASP net transfer reaction to occur (Grove et al., 1984).

If the garnet cores are not significantly affected by post-crystallization volume diffusion, then it is worthwhile to consider whether the garnet-host and entrapped mineral compositions reflect some extent of equilibrium. Clearly, the presense of even minor zoning in garnet, cordierite, biotite and plagioclase suggest that complete equilibrium can be ruled out. Despite this, it is plausible that local or partial equilibrium for individual samples was achieved.

## Core Thermobarometry

*GASP-GARB simultaneous solutions: Hyndman Group pelitic schists*

Garnet-host/entrapped-mineral compositions were chosen in regard to those which most likely reflected equilibrium compositions for the individual sample. Thus, garnet core compositions outside of depletion halos and biotite inclusion core compositions, coupled with plagioclase inclusion rim compositions were frequently utilized. The lack of any textural signiture for GASP back reaction in the inclusion suites is consistent with this approach. The five samples with appropriate inclusions yielded temperatures in the range 863-960 K (Figure 16; Table 9). This is more or less within the range of rim calculations,

although two cores are statistically higher (P213A, P225B) with temperature in excess of 920K. Mean core equilibration pressures are statistically indistinguishable between samples, with an average pressure of 355 MPa (Figure 16; Table 9). The AFM and AFMC plots for P248B and P230E do not show crossing tie-lines or phase volumes (Figure 13 & 14). Their 95% confidence fields are largely coincident, consistent with the interpretation of sustained equilibrium under identical physical conditions for these two samples. P335 plots mostly outside the overlap of the P248B and P230E ellipses. P335 crosses tie-lines and tie-planes with P248B and P230E, consistent with nucleation and growth under slightly higher temperatures. P213A and P225 plot at even higher temperatures than P335 and their tie-planes and phase volumes cross those of the lower temperature samples. This distribution of ellipses suggests variable nucleation temperatures of garnet at essentially similar pressures among the sample suite.

*Hornblende Core Barometry: Pioneer Intrusive Suite*

The relatively higher $Al^T$ cation totals for hornblende cores may reflect higher temperatures and a possible lack of $SiO_2$ saturation during crystal nucleation and initial growth. The profiles of all the samples indicate an inverse correlation between Si and Al (Figure 12). P155 displays quartz intimately intergrown with small hornblende phenocrysts and a few quartz inclusions toward the margin of the hornblende grains. Thus, it is plausible that the melt was silica-saturated before final crystallization. It is more difficult to evaluate the effect of higher temperature on Al partitioning. However, the amphibole liquidus temperature is probably no more than 75-100K higher than the likely range in solidus temperature (975-1025K) at pressures below the aluminum silicate triple point (Clemens & Wall, 1981). Although not theoretically rigorous, it is intriguing to consider the possibility that core $Al^T$composition can be used to estimate the pressure at

which the granodioritic magma originally intruded the country rock. This approach yields pressures of 296-315 MPa by equation 1, and 233-247 MPa by equation 2 (Table 9; Figure 20). The core equilibration pressures of all three samples lie within the uncertainty of the respective calibrations. These pressures are remarkably similar to those calculated for the garnet inclusion suites of the Hyndman Group.

## Garnet Growth Models and Element Partitioning

From the mineral compositional profiles and the textural distribution of the constituent inclusion and matrix minerals, as well as the results of core and rim thermobarometry, we may deduce the processes which resulted in the garnet compositional profiles.

Loomis (1983) has provided an overview of three different models for garnet growth:

1) the "equilibrium growth" model.

2) the "diffusion-controlled growth" model.

3) the "reaction-controlled growth" model.

Numerical simulations of these growth models are presented in Loomis (1982) and Loomis & Nimick (1982). The models suggest that we can expect a characteristic garnet compositional and textural morphology for a particular growth process (Figure 21). The value of such models lies beyond the curiosity of growth processes. A comparison of natural occurences of garnet assemblages and compositional profiles to those modeled numerically provides a test for both the assumption of equilibrium as well as the reasonability of the model.

*The Equilibrium Growth Model* (KFMnMASH system) assumes that equilbrium is maintained between the garnet matrix edge and all the crystals in the matrix assemblage (Loomis & Nimick, 1982). Garnet is the only refractory phase. The growth-temperature history is one of continuous progressive metamorphism. Transport of the components in the matrix keeps up with any reaction required to maintain partial equilibrium. Thus, the reaction rate is controlled by the rate of change of pressure, temperature and other intensive parameters. The model indicates early stabilization of garnet by manganese and the onset of rapid growth only beyond the almandine reaction isograd. The simulated profiles closely match those from garnets collected in the upper-greenschist to lower- and middle amphibolite facies. The bell-shaped spessartine curve, increase in almandine and pyrope,

and relatively flat grossular morphologies are also similar to those modelled by Rayleigh fractionation (Hollister, 1966, 1969). Loomis (1982) effectively argues that simple Rayleigh fractionation is not a reasonable model for major elements because the partitioning coefficient must be a function of bulk composition, sample grade, and the majority of garnets which display this type of morphology are probably not isothermal.

There are several observations that rule out equilibrium growth of garnet in the Hyndman Group pelitic schists. Firstly, the presense of a high-temperature inclusion suite which includes sillimanite, cordierite and hercynite constrains the bulk of garnet growth to have occured at temperatures in excess of 850K. This lies well beyond the temperature required for the first appearance of almandine and indicates a nominal temperature overstep of 50-75K. Secondly, garnet core profiles are flat. In the equilibrium growth models, the only input parameter values which result in a flat core profile occurs when $X_{sp}$=0.0. Hyndman Group schists contain garnets with 2-8 mole percent spessartine, well within the range of phase compositions used to derive thermodynamic data in the Loomis (1982) model. It appears that this growth equilibrium model does not describe the core region in garnets of the Hyndman schist. However, the zoned rim region may have grown by an equilibrium growth process if temperature stabilized and the element partitioning caught up with the temperature overstep. If the temperature trajectory was then retrograde, the observed compositional shift to a lower Mg/Mg+Fe ratio, as well as the increase in spessartine, could be a growth process. This unusual reaction has been observed by Spear & Rumble (1986) and Selverstone et al.(in preparation) in the Ordordville Belt of west-central New Hampshire and the Rapid River Plate of the Salmon River Suture Zone, respectively. Retrograde growth of garnet has been explained by a continuous lowering of a $H_2O$ with declining temperature. The observation of apparent resorption textures at the

garnet rims suggests operation of a garnet consuming net transfer reaction and argues somewhat against equilibrium retrograde growth, but does not eliminate the possibility.

*The Diffusion-Controlled Growth Model* assumes that the rate of reaction is limited only by the rate at which components are transfered among reaction sites which are determined by nucleation processes (Loomis and Nimick, 1982). For garnet growth, the diffusing cations that determine compositional zoning are Mg, Fe, Mn, and Ca. A continuous chemical potential gradient for each of these components would occur from the matrix to the growing crystal edge where local equilibrium persists. Thus, if temperature varies only slightly, the equilibration partitioning is constant and the rate of growth is limited only by cation diffusivity. The resultant crystal may be homogeneous if the cations have similar diffusion rates. The distant matrix is in disequilibrium with the growing crystal; however, phases near the garnet crystal edge may experience a similar chemical potential environment. If temperatures are high, steep gradients and exceptionally rapid intergranular diffusion could result in rapid crystal growth. The advection of a fluid through the intergranular region, perhaps derived from dehydration reactions, may significantly enhance transport rates. Its effect would be proportional to the length-scale of the diffusion gradient and the diffusion transport rate. Nevertheless, it would probably result in a "mixing" effect that may expand the equilibrium domain. Thus, unzoned inclusion phases such as cordierite, biotite, and plagioclase may be in equilibrium with the garnet core composition and collectively define a state of local equilibrium. Bell-shaped curves could result from varying diffusion rates among the cations as temperature changes. The diffusion rate and equilibration range of various cations are poorly understood, thus this possibility can not be evaluated. Nonetheless, the morphology of compositional profiles of garnet cores and the inclusion phases in garnets are consistent with the diffusion-controlled growth model. The observation of a quartz halo around garnets

suggests a metasomatic domain resulting from local depletion of ferromagnesian components. This is what we would expect to find in a sample which developed chemical potential gradients consistent with the diffusion-controlled growth model. The discordant temperatures at relatively constant pressure of the core 95% confidence fields indicate a range in nucleation temperatures during reaction overstepping.

*The Disequilibrium-Partitioning or Reaction-Controlled Growth Model* assumes that the rate of reaction is limited by the diffusion of Si or Al in addition to the diffusion of the octohedrally coordinated cations. It is equally applicable to reactions with rate limited by dissolution kinetics and/or most aspects of interface kinetics (Kirkpatrick, 1975). In the Loomis & Nimick (1982) numerical model (KFMnMASH system), the rate of garnet growth was slow enough that divalent cations had no chemical potential gradient in the matrix. The principle consequence of the reaction-controlled model is that local equilibrium is not maintained at the crystal face. Disequilibrium at the crystal interface adds considerable uncertainty to element partitioning, particularly because we do not know the compositional dependence of $K_D$ values in a system out of equilibrium. In an equilibrium system, the partition coefficient for a trace component between two ideal solution phases changes as a function of temperature. However, the partition coefficient for a major component in a disequilibrium system is primarily a function of composition; that is, the effective bulk composition with which the crystal "chemically communicates", even for isothermal growth. The matrix comprises an effective bulk composition that has not achieved an equilibrium state. This growth scenario assumes that the free energy of the system will be reduced a maximum amount for a given amount of reaction. If temperature overstepping occurs, the composition of the growing crystal will lie between the equilibrium composition expected at the overstepped temperature and the composition expected at the temperature of nucleation in a continuous equilibrium growth model.

The flat morphology of the compositional profiles for garnet, cordierite and plagioclase in the Hyndman schists do not resemble the curves produced in the reaction-controlled growth model. Indeed, inclusions of quartz and sillimanite in garnet cores suggest that the local equilibration domain was saturated with respect to Si and Al. The consistency of an individual sample's mineral core compositions and the apparent overall equilibration on a thin-section scale is consistent with the lack of significant chemical potential gradients as predicted by this model. The suggested overstepping may contribute to any profile relaxation effect of post-crystallization volume diffusion, because the original compositional gradient would not be as pronounced as that in the equilibrium growth model. However, taking the penetration distance calculations presented in the previous section at face value, the core regions of garnet and possibly other phases do not resemble those predicted by the reaction-controlled growth model.

In summary garnet core compositional profiles most closely match those calculated by the diffusion-controlled growth model. This model allows for very localized equilibrium growth. The compositional gradients observed approaching the garnet rims match the morphology of profiles produced by retrograde volume diffusion, retrograde reaction-controlled diffusion, retrograde diffusion-controlled diffusion and equilibrium growth models. It is difficult to distinguish which mechanism is responsible for the present compositional gradient. It seems highly likely, that different mechanisms may be operative under a single evolution of physical conditions.

## Gibbs Method Trends: Constraints on Disequilibria

The Gibbs method technique (Spear and Selverstone, 1983; Selverstone et al., 1984; Spear and Peacock, 1989) may help constrain pressure-temperature conditions prior to the final equilibration of a particular sample. This technique requires the input of a pressure

and temperature of final equilibration, edge compositions of all phases in the sample, and $n$ independent compositional monitoring parameters for samples with a variance of $n$. In the quadravariant subassemblages of the Hyndman Group which were modeled, I tried three different combinations of the compositional monitors $\Delta X_{alm}$, $\Delta X_{gros}$, $\Delta X_{spes}$, $\Delta X_{ann}$, and $\Delta X_{an}$, where $\Delta X$ terms refer to changes in composition from garnet edge to garnet core or from matrix edge to inclusion edge. The output parameters of the technique are the calculated pressure and temperature change for the single step and the calculated compositions of phases in the subassemblage that were in equilibrium with the garnet core.

The assumptions of the technique include: 1) that there was no change in the assemblage during garnet growth or re-equilibration; and 2) the compositions of the garnet-host and entrapped minerals used as monitor parameters reflect equilibrium partitioning and do not represent disequilibrium which may result from post-crystallization homogenization.

Table 10 lists the monitor parameters and results of three garnets modelled by this technique. Figure 19 shows the results plotted in pressure-temperature space. The $\Delta P$ and $\Delta T$ values are strongly dependent on the particular compositional monitors chosen for the model. The three trends calculated for a particular sample are completely inconsistent. However, there is a strong similarity among the calculated trends for a particular set of monitor parameters.

The data can not be simply interpreted in terms of actual pressure-temperature trends. Rather, the consistency of the "monitor trajectories" suggest that we are modelling disequilibrium partitioning for these particular samples. The very small value of the $\Delta X_{gros}$ monitor parameter results in the trend "sliding down" the $K_D$ of the GASP net transfer reaction, highly suggestive of a reaction-controlled rate limiting mechanism for these samples.

The general absense of muscovite and the presence of hercynite as inclusion phases suggests that the pressure-temperature trajectory probably crossed a discontinuous reaction boundary. This violates a basic assumption of the model and would result in spurious $\Delta P$ and $\Delta T$. The models suggests that great care must be used in applying the Gibbs technique to upper amphibolite facies garnets and the practioner must document the applicability of the technique by using several different combinations montior parameters before a unique pressure-temperature trend is constrained.

## Interpretation of the Petrologic Data

The pressure-temperature-time evolution of the infrastructure during the Middle to Late Eocene is illustrated in Figure 22. The emplacement of the Pioneer Intrusive Suite at roughly 48 Ma resulted in the metamorphism of the Hyndman Group pelitic schists. The emplacement temperature was in excess of 960K, the core temperature of P225. The P151 GARB temperature is consistent with this interpretation. The pressure of intrusion is constrained at roughly 355 MPa by the locus of calculated core pressures in Hyndman Group samples. This corresponds to a depth of 12.4 km, assuming a crustal density of 2850 $kg/m^3$. The isobaric distribution of core ellipses suggest that garnet nucleated at temperatures from 850K (P248B) to 950K (P225). AFM and AFMC relations among P248B and P230E suggest that these samples may have nucleated and grown under similar conditions (no crossing tie-lines or phase volumes); thus it is not a surprise to find their 95% confidence fields largely overlap. In contrast P335, P213A and P225 show crossing tie-lines and tie-planes, indicating different physical conditions of nucleation and growth. Hornblende core thermobarometry yields results consistent with the pelitic inclusion thermobarometry.

The pelitic schist of the Wildhorse Gneiss Complex (P125) achieved final equilibrium at conditions comparable with the granodiorite emplacement (342±75 MPa & 848±48K), suggesting little displacment between the parautochthon and the allochthons along the Hyndman Shear zone at this time.

Phase equilibria considerations indicate that the final equilibration of the ten pelitic samples from the Hyndman Group may have occurred at different times under different physical conditions. Disregarding for the moment the three spurious outliers to the final equilibration data (P225B, P243B & P248), the rim pressure-temperature ellipses can be interpreted as representative of different physical conditions along the retrograde path (Hodges and Royden,1984). The final equilibration of P335, P225A, P230E, P5B, and P151 at pressures of 215-240 MPa and temperatures of 815-855K indicates moderate unroofing with a significant amount of cooling. Samples P5B, P230E and P335 yield pressures that are statistically distinguishable from any of the core ellipses. The 95% confidence fields of P213A and P225A overlap the pressure-temperature conditions of core ellipses, however their mean pressure values are lower than those of core ellipses. Final equilibration pressures calculated by hornblende barometry of the Pioneer Intrusive Suite (P92, P155, P156) indicates pressures 203-220 MPa or 256-279 MPa depending on whether the experimental or empirical calibrations are used, respectively. These hornblende final equilibration data are in good agreement with the rim thermobarometry from the pelitic schists. This corresponds to a 7.5 to 8.4 km paleodepth, assuming a crustal density of 2850 kg/m$^3$. Thus, the decompressional pressure-temperature path has a nominal slope of 1.3 MPa/Kelvin. It implies 4.4 km of unroofing.

Within the contact aureole, the footwall was at 800K at roughly 45 Ma (Silverberg et al., in preparation). Therefore, the petrologic data suggests a time-integrated uplift rate of roughly 1.5 km/million years. This rate is faster than that expected for simple erosion-

controlled unroofing. Isostatic compensation has been suggested as a uplift mechanism during and following extensional tectonic denudation (Lister & Davis, 1989; Wernicke & Axon, 1989). Rapid erosion-controlled unroofing could have resulted from an elevated topogragraphy following isostatic compensation of the south-central Idaho region. Alternatively, some moderate amount of tectonic denudation could have occurred in the 48-45 ma interval. Regardless of whether the unroofing is "passive" or "active", it is clearly related to extensional tectonic denudation.

Thus, it appears that rapid extensional tectonic unroofing had ceased in this region at the close of the Challis magmatic episode. The infrastructure was at a maximum depth of 7.5-8.4 km before the onset of west-northwest directed extension at roughly 35 Ma (Silverberg et al., in preparation). If the initial dip of the Wildhorse Detachment Fault System was 20° (Silverberg, in preparation), then the maximum amount of dip-slip on the fault was 25 km. Tectonic models for regional Oligocene extension in south-central Idaho must accomodate the inferred 23 km maximum horizontal slip of the Wildhorse Detachment Fault System.

## Conclusions

Twelve pelitic schist and three granodiorite samples collected from the footwall of the Pioneer Metamorphic Core Complex, south-central Idaho, constrain the pressure-temperature evolution of a low-pressure high-temperature metamorphic facies series. The distribution of reaction isograds and geochronologic constraints suggests that the granodiorite provided the heat required for metamorphism contemporaneous with the Eocene Challis magmatic episode at 48 ma. Pressures and temperatures derived from inclusion equilibria of garnet suggests garnet nucleation and growth at a depth of roughly 11-13 km under essentially isobaric conditions. Overstepping of reaction obviates the equilibrium garnet growth model and suggests diffusion-controlled garnet growth following nucleation over a 150K interval. Final equilibration conditions of most samples are consistent suggesting that the infrastructure paleodepth was approximately 7.5-8.4 km at the Eocene-Oligocene boundary. A combination of garnet volume diffusion and reaction-controlled re-equilibration for matrix minerals was the likely mechanism for final equilibration of the matrix. Thermodynamic modeling of garnet zonation (Gibbs method) yielded widely ranging mutually exclusive pressure-temperature trajectories depending on which monitor is used in addition to garnet. The possibility of crossing a discontinuous reaction space and/or disequilibrium partitioning makes such calculations unreliable.

The unroofing rate, 1.5 km/my in the Late Eocene (48-45 Ma), may be explained by a passive or active unroofing mechanism that is related to tectonic denudation. The passive model suggests that isostatic adjustment following extensional unroofing could result in an elevated topography. It is possible that this could contribute to rapid erosion. Alternatively, the active model calls for a moderate amount of tectonic denudation in the 48-45 Ma interval. The infrastructure was at a paleodepth of not more than 7.5-8.4 km at the onset of west-northwest directed extension in the Oligocene (35 Ma). The calculated

paleodepth suggests a maximum dip-slip displacement of 25 km along the Wildhorse Detachment Fault System.

The results of this study place constraints on processes of metamorphism incumbent to a primarily advectively heated dynamothermal metamrophism, as well as the Eocene to Oligocene tectonic evolution of the south-central Idaho region. The judicious application of geothermobarometry to samples from the upper amphibolite facies in a rapidly heated and cooled low-pressure high-temperature facies series may yield important constraints on the rates of petrologic and tectonic processes.

## Acknowledgements

I wish to thank Gilles Wust, Ned Gates, Allison Macfarlane, Gregory Reller, Kip Hodges, Timothy East, Lawrence McKenna, Elaine Alberti, John Sutter and Elaine Padovani for their help in the field. Kudos to Timothy and Patricia East for endless hospitality in Ketchum, Idaho. Steve Recca is thanked for his help running the electron microprobe used in this study. Comments by Kip V. Hodges greatly improved the text. I thank The Geological Society of America for grant support that enabled my attendance at pertinent Penrose Conferences. This research was a part of my Ph.D. studies at the Massachusetts Institute of Technology and was financially supported by U.S. National Science Foundation grant EAR-8407730 to K.V. Hodges.

## References


Aranovich, L. Y. & Podlesskii, K. K., 1983. The cordierite - garnet - sillimanite - quartz equilibrium: experiments and applications. In: Saxena, S. K. *Kinetics and equilibrium in mineral reactions*. New York: Springer-Verlag, 173-198.

Armstrong, R. L., 1974. Geochronometry of the Eocene volcanic-plutonic episode in Idaho. *Northwest Geology* **3**, 1-15.

Atkin, B. P., 1978. Hercynite as a breakdown product of staurolite from within the aureole of the Ardara Pluton, Co. Donegal, Eire. *Mineral. Mag.* **42**, 237-239.

Barton, M. D., Battles, D. A., Bebout, G. E., Capo, R. C., Christensen, J. N., Davis, S. R., Hanson, R. B., Michelsen, C. J. & Trim, H. E., 1988. Mesozoic contact metamorphism in the western United States. In: Ernst, W. G. *Metamorphism and Crustal Evolution of the Western United States*. Englewood Cliffs, NJ: Prentice Hall, 110-178.

Clemens, J. D. & Wall, V. J., 1981. Origin and crystallization of some peraluminous (S-type) granitic magmas. *Can. Mineral.* **19**, 111-132.

Coney, P. J., 1980. Cordilleran metamorphic core complexes: An overview. In: Crittenden, M. D., Coney, P. J. & Davis, G. H. *Cordilleran metamorphic core complexes*. Boulder: The Geological Society of America, 7-34.

Crank, J., 1975. The mathematics of diffusion. Oxford: Oxford University Press, 414.

Cygan, R. T. & Lasaga, A. C., 1985. Self-diffusion of magnesium in garnet at 750° to 900°C. *Am. J. Sci.* **285**, 328-350.

Dover, J. H., 1966, Geology of the Pioneer Mountains, PhD thesis, University of Washington.

Dover, J. H., 1969. Bedrock geology of the Pioneer Mountains, Blaine and Custer counties, central Idaho. *Idaho Bureau of Mines and Geology Pamphlet 142* **66,**

Dover, J. H., 1981. Geology of the Boulder-Pioneer wilderness study area, Blaine and Custer counties, Idaho. *U. S. Geol. Surv. Bull.* **1497-A,** 21-75.

England, P. C. & Thompson, A. B., 1984. Pressure-temperature-time paths of regional metamorphism I. Heat transfer during the evolution of regions of thickened continental crust. *J. Petrol.* **25,** 894-928.

Essene, E. J., 1982. Geologic thermometry and barometry. In: Ferry, J. M. *Mineralogical Society of America Reviews in Mineralogy.* 153-206.

Essene, E. J., 1989. The current statis of thermobarometry in metamorphic rocks. In: Daly, J. S., Cliff, R. A. & Yardley, B. W. *Evolution of metamorphic belts.* Geological Society Special Publication, 1-44.

Ferry, J. M. & Spear, F. S., 1978. Experimental calibration of the partitioning of Fe and Mg between biotite and garnet. *Contrib. Mineral. Petrol.* **66,** 113-117.

Ganguly, J., 1972. Staurolite stability and related parageneses: theory, experiments, and applications. *Jour. Petrol.* **13,** 335-365.

Ghent, E. D., Robbins, D. B. & Stout, M. Z., 1979. Geothermometry, geobarometry and fluid compositions of metamorphosed calc-silicates and pelityes, Mica Creek, British Columbia. *Am. Mineral.* **64,** 874-885.

Grant, J. A. & Weiblen, P. W., 1971. Retrograde zoning in garnet near the second sillimanite isograd. *Amer. J. Sci.* **270,** 281-296.

Greenwood, H. J., 1875. Thermodynamically valid projections of extensive phase relationships. *Am. Mineral.* **60,** 1-8.

Grove, T. L., Baker, M. B. & Kinzler, R. J., 1984. Coupled CaAl-NaSi diffusion in plagioclase feldspar: Experiments and applications to cooling rate speedometry. *Geochim. Cosmochim. Acta* **48,** 2113-2121.

Hammarstrom, J. M. & Zen, E.-a., 1986. Aluminum in hornblende: An empirical igneous geobarometer. *Am. Mineral.* **71,** 1297-1313.

Hodges, K. V., Hubbard, M. S. & Silverberg, D. S., 1988. Metamorphic constraints on the thermal evolution of the central Himalayan Orogen. *Phil. Trans. R. Soc. Lond.* A **326,** 257-280.

Hodges, K. V. & McKenna, L. W., 1987. Realistic propagation of uncertainties in geologic thermobarometry. *Am. Mineral.* **72,** 671-680.

Holdaway, M. J., 1971. Stability of andalusite and the aluminosilicate phase diagram. *Am. J. Sci.* **271,** 97-131.

Holdaway, M. J. & Lee, S. M., 1977. Fe-Mg cordierite stability in high-grade pelitic rocks based on experimental, theoretical, and natural observations. *Contrib. Mineral. Petrol.* **63,** 175-198.

Hollister, L. S., 1966. Garnet zoning: an interpretation based on the Rayleigh fractionation model. *Science* **154,** 1647-1651.

Hollister, L. S., 1969. Contact metamorphism in the Kwoiek area of British Columbia: an end member of the metamorphic process. *Geol. Soc. Amer. Bull.* **80,** 2465-2494.

Hollister, L. S., Grissom, G. C., Peters, E. K., Stowell, H. H. & Sisson, V. B., 1987. Confirmation of the empirical correlation of Al in hornblende with pressure of solidification of calc-alkaline plutons. *Am. Mineral.* **72,** 231-239.

Holm, R. F., 1962, Geology of the Wildhorse Canyon area, M.S. thesis: Idaho State University.

Johnson, M. C. & Rutherford, M. J., 1989. Experimental calibration of the aluminum-in-hornblende geobarometer with application to Long Valley caldera (California) volcanic rocks. *Geology* **17,** 837-841.

Kars, H., Jansen, J. B. H., Tobi, A. C. & Poorter, R. P. E., 1980. The metapelitic rocks of the polymetamorphic Precambrian of Rogaland, SW Norway. *Contrib. Mineral. Petrol.* **74,** 235-244.

Kerrick, D. M., 1972. Experimental determination of muscovite + quartz stability with PH2)<PTotal. *Am. Jour. Sci.* **272,** 946-958.

Kirkpatrick, R. J., 1975. Crystal growth from the melt: a review. *Amer. Mineral.* **60,** 798-814.

Lasaga, A. C., Richardson, S. M. & Holland, H. D., 1977. The mathematics of cation diffusion and exchange between silicate minerals during retrograde metamorphism. In: Saxena, S. K. & Bhattacharji, S. *Energetics of Geological Processes.* New York: Springer-Verlag, 353-388.

Loomis, T. P., 1982. Numerical simulation of the disequilibrium growth of garnet in chlorite-bearing aluminous pelitic rocks. *Can. Min.* **20,** 411-423.

Loomis, T. P., 1983. Compositional zoning of crystals: a record of growth and reaction history. In: Saxena, S. K. *Kinetics and equilibrium in mineral reactions.* New York: Springer-Verlag, 1-60.

Loomis, T. P. & Nimick, F. B., 1982. Equilibrium in Mn-Fe-Mg- aluminous pelitic compositions and the equilibrium growth of garnet. *Can. Min.* **20,** 393-410.

Manning, D.A. & Pichavant, M., 1983. The role of fluorine and boron in the generation of granitic melts. In: Atherton, M.P. & Gribble, C.D.. *Migmatites, melting and metamorphism.* Nantwick, Cheshire U.K.: Shiva, 94-109.

McKenna, L. W. & Hodges, K. V., 1988. Accuracy versus precision in locating reaction boundaries: Implications for the garnet-plagioclase-aluminum silicate-quartz geobarometer. *Am. Mineral.* **73,** 1205-1208.

Miller, E. L. & Gans, P. B., 1989. Cretaceous crustal structure and metamorphism in the hinterland of the Sevier thrust belt, western U.S. Cordillera. *Geology* **17,** 59-62.

Miyashiro, A., 1961. Evolution of metamorphic belts. *Jour. Petrol.* **2,** 277-311.

Newton, R. C. & Haselton, H. T., 1981. Thermodynamics of the garnet - plagioclase - Al2SiO5 - quartz geobarometer. In: Newton, R. C. *Thermodynamics of minerals and melts*. New York: Springer-Verlag,

O'Neill, R. L. & Pavlis, T. L., 1988. Superposition of Cenozoic extension on Mesozoic compressional structures in the Pioneer mountains metamorphic core complex, central Idaho. *Geological Society of America Bulletin* **100,** 1833-1845.

Perchuk, L. L. & Lavrent'eva, I. V., 1983. Experimental investigation of excvhange equilibria in the system cordierite- - garnet - biotite. In: Saxena, S. K. *Kinetics and equilibrium in mineral reactions*. New York: Springer-Verlag, 199-240.

Piwinskii, A.J., 1968, Experimental studies of igneous rock series, central Sierra Nevada Batholith, California. Jour. Geology **76**, 548-570.

Richardson, S. W., 1968. Staurolite stability in a part of the system Fe-Al-Si-O-H. *Jour. Petrol.* **9,** 467-468.

Schreyer, W. & Yoder, H.S., 1964. The sytem Mg-cordierite-H2O and related rocks. Neues Jb. Miner. **101,** 271-342.

Seifert, F., 1970. Low temperature compatibility relations of cordierite in haplopelites of the system K2O-MgO-Al2O3-SiO2-H2O. *Journal of Petrology* **11,** 73-99.

Selverstone, J., Spear, F. S., Franz, G. & Morteani, G., 1984. High pressure metamorphism in the SW Tauern window, Austria: P-T paths from hornblende-kyanite-staurolite schists. *J. Petrol.* **25,** 501-531.

Silverberg, D. S., in preparation. Multiphase extension in the south-central Idaho region: Structural evolution of the Pioneer Metamorphic Core Complex. *Geological Society of America Bulletin*

Silverberg, D.S., Hodges, K.V., Kunk, M. & Sutter J., in preparation, Thermal evolution of the Pioneer Metamorphic Core Complex, south-central Idaho: Diachronous Paleogene extension of the mid-crust. *Tectonics.*

Spear, F. S., 1980. NaSi-CaAl exchange equilibrium between plagioclase and amphibole: An empirical model. *Contrib. Mineral. Petrol.* **72,** 33-41.

Spear, F. S. & Kimball, K. L., 1984. RECAMP-a FORTRAN IV program for estimating Fe3+ contents in amphiboles. **10,** 317-325.

Spear, F. S. & Peacock, S. M., 1989. Metamorphic Pressure-Temperature-Time Paths. Washington: American Geophysical Union, 102.

Spear, F. S. & Rumble, D., 1986. Pressure, temperature, and structural evolution of the Ordordville Belt, west-central New Hampshire. *J. Petrol.* **27,** 1071-1093.

Spear, F. S. & Selverstone, J., 1983. Quantitative P-T paths from zoned minerals: theory and tectonic applications. *Contr. Miner. Petrol.* **83,** 348-357.

Spear, F. S., Selverstone, J., Hickmott, D., Crowley, P. & Hodges, K. V., 1984. P-T paths from garnet zoning: A new technique for deciphering tectonic processes in crystalline terrains. *Geology* **12,** 87-90.

St-Onge, M. R., 1987. Zoned poikiloblastic garnets: P-T paths and synmetamorphic uplift through 30km of structural depth, Wopmay Orogen, Canada. *J. Petrol.* **28,** 1-27.

Stoddard, E. F., 1979. Zinc-rich hercynite in high-grade metamorphic rocks: a product of the dehydration of staurolite. *Am. Mineral.* **64,** 736-741.

Thompson, J. B., 1957. The graphical analysis of mineral assemblages in pelitic schists. *Am. Mineral.* **42,** 842-858.

Thompson, A. B., 1974. Recalculation of muscovite-paragonite-alkali feldspar relations. *Contr. Miner. Petrol.* **44,** 173-194.

Tracy, R. J., 1982. Compositional zoning and inclusions in metamorphic minerals. In: Ferry, J. M. *Characterization of Metamorphism through Mineral Equilibria.* Washington, DC: Mineralogical Society of America, 355-397.

Tracy, R. J., Robinson, P. & Thompson, A. B., 1976. Garnet composition and zoning in the determination of temperature and pressure of metamorphism, central Massachusetts. *Am. Mineral.* **61,** 762-775.

Van Bosse, J. Y. & Williams-Jones, A. E., 1988. Chemographic relationships of biotite and cordierite in the McGerrigle thermal aureole, Gaspe, Quebec. *J. metamorphic Geol.* **6,** 65-75.

Walther, J. V. & Wood, B. J., 1984. Rate and mechanism in prograde metamorphism. *Contrib. Mineral. Petrol.* **88,** 246-259.

Woodsworth, G. J., 1977. Homogenization of zoned garnets from pelitic schists. *Can. Mineral.* **15,** 230-242.

Wust, S. L. & Link, P. K., 1987. Geology of the Pioneer Mountains Core Complex, south central Idaho. *Northwest Geology* **16,** 85-94.

## Figure Captions

Figure 2.1. Simplified regional tectonic map of the Idaho area. Rectangle shows the location of Figure 2.2.

Figure 2.2. Simplified tectonic map of the Pioneer Metamorphic Core Complex, south-central Idaho (after published mapping of J. Dover, 1981 and unpublished mapping of D.S. Silverberg). Points A-A' show the cross-section transect of Figure 2.4. Unit abbreviations as in Figure 2.3. kc = Kane Creek; whc = Wildhorse Canyon; fc = Fall Creek; cc = Corral Creek; pc = Pioneer Cabin; hc = Hyndman Creek; bb = Big Basin; wr = Wood River.

Figure 2.3. Tectonic stratigraphic column of the infrastructure in the Pioneer Metamorphic Core Complex. Lithostratigraphy of Dover, 1983.

Figure 2.4. Cross-section along the A-A' transect of Figure 2.2. Unit abbreviations as in Figures 2.2 & 2.3. pct = Pioneer Cabin Thrust; hsz = Hyndman Shear Zone; wdfs = Wildhorse Detachment Fault System.

Figure 2.5. Synoptic of deformation events in the Pioneer Metamorphic Core Complex (Silverberg, in preparation). Tc = cooling age as constrained by $^{40}Ar$-$^{39}Ar$ plateau ages (Silverberg et al., in preparation); MM = style & maximum grade of dynamothermal metamorphism (syn-K = syn-kinematic, post-K = post-kinematic)..

Figure 2.6. Synoptic temperature-time paths for the Pioneer Intrusive Suite, the Wildhorse Gneiss Complex, and the Wildhorse Detachment Fault system (from Silverberg et al., in preparation). PCwgc = Precambrian Wildhorse Gneiss Complex; Epis = Eocene Pioneer Intrusive Suite; Owdfs = Oligocene Wildhorse Detachment Fault System.

Figure 2.7. Timing relationships between petrofabrics and principal porphyroblast growth in the pelitic schist of the Hyndman Group.

Figure 2.8. Simplified geologic map of the western phase of the Pioneer Intrusive Suite, the Hyndman and East Fork Groups in the vicinity of the Hyndman Shear Zone (HSZ; D3). Deformational events keyed to Figure 2.5. SC = Summit Creek; KC = Kane Creek; WC = Wilson Creek; IR = Imbricate Ridge; CC = Corral Creek; PCTN = Pioneer Cabin Thrust Napped; PCR = Pioneer Cabin Ridge; HP = Hyndman Peak; NFHC = North Fork of Hyndman Creek; DR = Duncan Ridge; OHP = Old Hyndman Peak; MC = Mount Cobb; HC = Hyndman Creek; PG = Paymaster Gulch; EFWR = East Fork of the Wood River; wdfs = Wildhorse Detachment Fault System; SECF = Southeast Corner Fault; PF = Paymaster Fault; OHF = Old Hyndman Fault; CF = Cobb Fault; Rock units as in Figure 2.3. Arrows with $L_3$ indicate trend and plunge of sillimanite lineations. Sample localities keyed to Table 2.9.

Figure 2.9. Photomicrograph of poikiloblastic garnet in sample P335. G = garnet host. S = sillimanite inclusion. H = hercynite inclusion. B = biotite inclusion. Field of view 2 mm by 1.2 mm.

Figure 2.10. Petrogenetic grid for pelitic schists of the Hyndman Group. Aluminum silicate stability fields are shown (Holdaway, 1971). Reactions: 1, granite solidus (natural reactants; Piwinskii, 1968); 2, muscovite+quartz=aluminum silicate+K-feldpsar+H2O (natural reactants; Kerrick, 1972); Mg-cordierite breakdown (MASH-system; Schreyer & Yoder, 1964).

Figure 2.11. Representative major element zoning profiles for garnet, cordierite, biotite and plagioclase in samples of the Hyndman Group pelitic schists.

Figure 2.12. Representative major element zoning profiles for amphibole and plagioclase in samples of the Pioneer Intrusive Suite.

Figure 2.13. Ternary phase diagrams. a. A-F-M projection from quartz, muscovite and $H_2O$ of garnet-biotite assemblage for edge compositions from the Hyndman Group Pelitic schists. b. A-F-M projection from quartz, muscovite and $H_2O$ of garnet-biotite assemblage for garnet core and inclusion edge compositions from the Hyndman Group Pelitic schists (P213A, P225B, P230E, P248B and P335). c. A-F-M projection from quartz, K-feldspar and $H_2O$ of garnet-biotite-siilimanite assemblage for edge compositions from the Wildhorse Gneiss Complex pelitic schists (P120 & P125).

Figure 2.14. Phase Diagrams. a. Ca-A-F-M projection from muscovite and quartz of garnet-sillimanite-plagioclase-biotite assemblages for inclusion suite compositions of the Hyndman Group pelitic schist. Sillimanite plots at A apex, biotite plots outside of tetrahedron due to muscovite projection, plagioclase plots along Ca-Al join . b. Ca-A-F-M projection from muscovite and quartz of garnet-sillimanite-plagioclase-biotite assemblages for matrix edge compositions of the Hyndman Group pelitic schists (P213A, P225B, P230E, P248B and P335). Sillimanite plots at A apex, biotite plots outside of tetrahedron due to muscovite projection, plagioclase plots along Ca-Al join. c. Ca-A-F-M projection from K-feldspar and quartz of garnet-sillimanite-plagioclase-biotite assemblages for matrix edge compositions of the Wildhorse Gneiss Complex pelitic schists (P120 & P125). Sillimanite plots at A apex, biotite plots outside of tetrahedron due to muscovite projection, plagioclase plots along Ca-Al join

Figure 2.15. Thermobarometric data for final equilibration in the Hyndman Group pelitic schist samples. Ellipses indicate 95% confidence fields for simultaneous solutions of the GB and GASP equilibria. Aluminum silicate stability fields are shown (Holdaway, 1971).

Figure 2.16 Inclusion suite thermobarometric data for the Hyndman Group pelitic schist samples. Ellipses indicate 95% confidence fields for simultaneous solutions of the GB and GASP equilibria. Aluminum silicate stability fields are shown (Holdaway, 1971).

Figure 2.17. Thermobarometric data for matrix equilibria in the Wildhorse Gneiss Complex pelitic schist samples P120 and P125. Ellipses indicate 95% confidence fields for simultaneous solutions of the GB and GASP equilibria. Aluminum silicate stability fields are shown (Holdaway, 1971).

Figure 2.18. Homogenization time for garnet. Assumed static temperatures of 800K, 850K, 900K, 950K and 1000K. Calculated from Mg self-diffusion data (Cygan & Lasaga, 1985). Activation energy = 239±16 kJ/mole, $D_0 = 9.8 \times 10^{-9}$ $m^2$/sec.

Figure 2.19. Thermodynamic modeling results for the Hyndman Group samples. Filled symbols indicate calculated equilibria conditions for mineral rims. Open symbols indicate points on the modelled pressure-temperature paths that are constrained by different mineral inclusion monitors. Arrows indicate progression from garnet interiors to rims. Pressures, temperatures and monitor parameters in Table 10.

Figure 2.20. Thermobarometric data for the Pioneer Intrusive Suite. HORB = hornblende barometer; HORP = hornblende-plagioclase thermometer (Spear, 1981); BARB = garnet-biotite thermometer (Hodges & McKenna, 1987); GASP = garnet-sillimanite-quartz-plagioclase barometer (McKenna & Hodges, 1988); ellipse indicates 95% confidence field for simultaneous solution for the GARB & GASP equilibria; aluminum silicate stability fields are shown (Holdaway, 1971); granite solidus (Piwinskii, 1968).

Figure 2.21. Computed zoning profiles for a typical pelitic bulk composition according to the following models: equilibrium growth (E) between 726.6 and 835 K, diffusion-controlled growth (DC) at 50K overstepping (775.6 K), and reaction-controlled

growth (RC) at 50K overstepping (775.6K). A. Mn profiles, B. Fe profiles, C. Mg profiles. (From Loomis, 1982).

Figure 2.22. Model for the pressure-temperature-time evolution of the infrastructure in the Pioneer Metamorphic Core Complex based on petrologic and isotopic data: 1, pro-grade metamorphic conditions caused by intrusion of the Pioneer Intrusive Suite; 2, peak metamorphic conditions achieved soon after intrusion; 3, rapid "erosion-controlled" or moderate tectonic unroofing with rapid cooling; 4, continued moderate cooling and slowed unroofing rate. Solid lines indicate portions of the pressure-temperature-time path constrained by petrologic and isotopic data, and shaded lines indicate hypothetical path segments. Aluminum silicate univariant curves of Holdaway (1971). And = andalusite; Kya = kyanite; Sill = sillimanite. Date of temperature maximum constrained by U-Pb zircon lower intercept age of Pioneer Intrusive Suite (Zartman, personal communication). 825K isotherm date constrained by hornblende $^{40}Ar$-$^{39}Ar$ plateau age. 700K isotherm constrained by time-integrated cooling rates calculated from hornblende and muscovite $^{40}Ar$-$^{39}Ar$ plateau dates given in Silverberg et al (in preparation).

## List of Tables

Table 1. Mineral assemblages of selected granodiorite and pelitic schists analyzed by the electron microprobe.

| Sample | Gar | Hbl | Bio | Chl | Mus | Plg | Kfs | Sil | Cdt | Herc | Qtz | Ilm | Sph | Other |
|---|---|---|---|---|---|---|---|---|---|---|---|---|---|---|
| *Pelitic Schists of the Hyndman Group* | | | | | | | | | | | | | | |
| P5b | X | | XI | R | T | X | | XI | X | | XI | | | |
| P151 | X | | X | | | X | | X | X | | X | | | |
| P212B | X | | X | R | TR | X | X | | | | X | X | | M,A |
| P213A | X | | XI | R | X | XI | | XI | X | | XI | X | | |
| P225A&B | X | | XI | | T | XI | X | X | X | | XI | XI | | |
| P230E | X | | XI | R | R | XI | | X | X | | XI | XI | | A,Z |
| P235* | X | | X | R | X | X | | | | | | X | | M |
| P243B | X | | XI | R | TR | X | | XI | XI | | XI | XI | | |
| P244 | X | | X | | | X | | X | X | | X | | | |
| P248 | X | | XI | | | XI | X | XI | XI | I | XI | XI | | M,A |
| P317 | X | | XI | R | XI | X | | X | X | | XI | X | | |
| P335 | X | | XI | R | R | XI | X | XI | XI | I | XI | XI | | |
| *Pelitic Schists of the Mafic Member of the Wildhorse Gneiss Complex* | | | | | | | | | | | | | | |
| P120 | X | | X | | | X | | X | X | | | | | |
| P125 | X | | X | | | X | | X | X | | | | | |
| *Granodiorite of the Pioneer Intrusive Suite* | | | | | | | | | | | | | | |
| P92 | | X | X | R | R | X | X | | | | | | | |
| P153 | X | | X | | | X | | X | X | | X | | X | E |
| P155 | | X | X | | R | X | X | | | | | X | | |
| P156 | | X | X | | T | X | X | | | | | | X | MT,CPX |
| | | | | | | | | | | | | | X | |

X = matrix phase, I = inclusion in garnet, R = retrograde, T = trace, M=monazite, A=apatite, z=zircon, E=epiote
MT=magnetite, CPX=clinopyroxene relict
*not analyzed by microprobe

Table 2a. Representative garnet analyses

| | P5b edge | P120 edge | P125 edge | P151 edge | P153 edge | P213A core | P213A edge |
|---|---|---|---|---|---|---|---|
| SiO | 37.15 ± 0.36 | 37.47 ± 0.49 | 37.77 ± 0.37 | 37.58 ± 0.12 | 37.88 ± 0.27 | 37.73 ± 0.23 | 37.54 ± 0.01 |
| AlO | 20.62 ± 0.06 | 20.71 ± 0.47 | 21.16 ± 0.27 | 20.87 ± 0.22 | 20.83 ± 0.22 | 21.11 ± 0.13 | 21.07 ± 0.06 |
| MgO | 3.06 ± 0.10 | 3.76 ± 0.54 | 3.31 ± 0.21 | 3.59 ± 0.33 | 2.95 ± 0.07 | 3.64 ± 0.03 | 2.88 ± 0.15 |
| Fe | 35.93 ± 0.78 | 34.66 ± 0.93 | 33.10 ± 0.54 | 35.06 ± 0.57 | 32.31 ± 0.45 | 36.52 ± 0.22 | 36.26 ± 0.25 |
| Mn | 2.00 ± 0.14 | 1.12 ± 0.11 | 3.67 ± 0.78 | 1.66 ± 0.47 | 4.52 ± 0.08 | 1.97 ± 0.11 | 3.10 ± 0.14 |
| Ca | 0.95 ± 0.04 | 2.16 ± 0.13 | 1.43 ± 0.06 | 1.10 ± 0.02 | 1.21 ± 0.05 | 0.97 ± 0.04 | 0.92 ± 0.00 |
| Total | 99.73 ± 0.48 | 99.88 ± 1.48 | 100.45 ± 0.49 | 99.86 ± 0.54 | 99.70 ± 0.54 | 101.95 ± 0.33 | 101.82 ± 0.18 |
| | | | | *cations per 12 oxygens* | | | |
| Si | 3.010 ± 0.018 | 3.009 ± 0.014 | 3.017 ± 0.013 | 3.020 ± 0.022 | 3.048 ± 0.013 | 2.989 ± 0.009 | 2.990 ± 0.001 |
| Al | 1.969 ± 0.009 | 1.960 ± 0.031 | 1.992 ± 0.013 | 1.977 ± 0.012 | 1.975 ± 0.024 | 1.971 ± 0.005 | 1.978 ± 0.005 |
| Mg | 0.370 ± 0.011 | 0.451 ± 0.068 | 0.394 ± 0.024 | 0.430 ± 0.038 | 0.354 ± 0.009 | 0.429 ± 0.004 | 0.341 ± 0.018 |
| Fe | 2.435 ± 0.056 | 2.328 ± 0.039 | 2.211 ± 0.032 | 2.356 ± 0.030 | 2.174 ± 0.023 | 2.420 ± 0.019 | 2.416 ± 0.017 |
| Mn | 0.137 ± 0.009 | 0.076 ± 0.007 | 0.248 ± 0.054 | 0.113 ± 0.033 | 0.308 ± 0.006 | 0.132 ± 0.007 | 0.209 ± 0.010 |
| Ca | 0.082 ± 0.003 | 0.186 ± 0.011 | 0.123 ± 0.006 | 0.095 ± 0.001 | 0.104 ± 0.004 | 0.082 ± 0.003 | 0.079 ± 0.000 |
| Total | 8.004 ± 0.019 | 8.011 ± 0.010 | 7.986 ± 0.015 | 7.991 ± 0.018 | 7.964 ± 0.007 | 8.024 ± 0.010 | 8.017 ± 0.003 |
| Pyr | 0.122 ± 0.004 | 0.150 ± 0.001 | 0.132 ± 0.008 | 0.144 ± 0.011 | 0.120 ± 0.003 | 0.140 ± 0.001 | 0.112 ± 0.005 |
| Alm | 0.805 ± 0.005 | 0.655 ± 0.003 | 0.743 ± 0.015 | 0.787 ± 0.013 | 0.739 ± 0.004 | 0.790 ± 0.003 | 0.793 ± 0.005 |
| Spes | 0.045 ± 0.001 | 0.147 ± 0.001 | 0.084 ± 0.017 | 0.038 ± 0.011 | 0.105 ± 0.002 | 0.043 ± 0.002 | 0.069 ± 0.003 |
| Gros | 0.027 ± 0.001 | 0.048 ± 0.002 | 0.041 ± 0.002 | 0.032 ± 0.001 | 0.035 ± 0.001 | 0.027 ± 0.001 | 0.026 ± 0.000 |

Table 2b. Representative garnet analyses

| | P225 core | P225 edge | P230E core | P230E edge | P248 core | P248 edge | P317 edge |
|---|---|---|---|---|---|---|---|
| SiO | 38.33 ± 0.19 | 36.58 ± 0.26 | 36.85 ± 0.22 | 36.49 ± 0.05 | 37.54 ± 1.23 | 37.26 ± 0.18 | 37.11 ± 0.18 |
| AlO | 21.48 ± 0.04 | 20.28 ± 0.23 | 20.63 ± 0.11 | 20.52 ± 0.10 | 20.71 ± 0.23 | 20.88 ± 0.19 | 20.61 ± 0.10 |
| MgO | 3.79 ± 0.02 | 1.76 ± 0.03 | 2.91 ± 0.10 | 2.50 ± 0.02 | 4.03 ± 0.09 | 4.18 ± 0.07 | 2.13 ± 0.14 |
| Fe | 29.42 ± 0.38 | 29.27 ± 0.45 | 30.68 ± 0.23 | 29.31 ± 0.02 | 35.37 ± 0.38 | 35.33 ± 0.41 | 32.61 ± 0.42 |
| Mn | 6.51 ± 0.05 | 9.05 ± 0.07 | 6.81 ± 0.06 | 8.19 ± 0.31 | 1.31 ± 0.08 | 1.17 ± 0.03 | 6.72 ± 0.16 |
| Ca | 1.70 ± 0.06 | 2.20 ± 0.08 | 1.55 ± 0.07 | 1.59 ± 0.06 | 0.76 ± 0.08 | 0.71 ± 0.04 | 1.11 ± 0.04 |
| Total | 101.22 ± 0.43 | 99.12 ± 0.78 | 99.44 ± 0.22 | 98.60 ± 0.11 | 99.74 ± 1.22 | 99.53 ± 0.71 | 100.29 ± 0.21 |
| | | | | *cations per 12 oxygens* | | | |
| Si | 3.022 ± 0.008 | 3.004 ± 0.017 | 2.995 ± 0.017 | 2.996 ± 0.003 | 3.018 ± 0.049 | 3.002 ± 0.009 | 3.009 ± 0.013 |
| Al | 1.995 ± 0.005 | 1.963 ± 0.011 | 1.977 ± 0.012 | 1.986 ± 0.008 | 1.963 ± 0.024 | 1.982 ± 0.009 | 1.970 ± 0.009 |
| Mg | 0.445 ± 0.002 | 0.215 ± 0.003 | 0.353 ± 0.013 | 0.305 ± 0.003 | 0.483 ± 0.012 | 0.502 ± 0.006 | 0.257 ± 0.017 |
| Fe | 1.940 ± 0.024 | 2.010 ± 0.020 | 2.086 ± 0.013 | 2.013 ± 0.003 | 2.379 ± 0.049 | 2.381 ± 0.020 | 2.211 ± 0.029 |
| Mn | 0.435 ± 0.003 | 0.629 ± 0.005 | 0.469 ± 0.005 | 0.570 ± 0.022 | 0.089 ± 0.006 | 0.080 ± 0.002 | 0.462 ± 0.012 |
| Ca | 0.144 ± 0.005 | 0.193 ± 0.008 | 0.135 ± 0.006 | 0.140 ± 0.005 | 0.066 ± 0.007 | 0.061 ± 0.004 | 0.096 ± 0.004 |
| Total | 7.980 ± 0.009 | 8.015 ± 0.012 | 8.015 ± 0.014 | 8.010 ± 0.006 | 7.999 ± 0.038 | 8.007 ± 0.009 | 8.006 ± 0.015 |
| | | | | | | | |
| Pyr | 0.150 ± 0.001 | 0.071 ± 0.001 | 0.116 ± 0.004 | 0.101 ± 0.001 | 0.160 ± 0.004 | 0.166 ± 0.002 | 0.085 ± 0.005 |
| Alm | 0.655 ± 0.003 | 0.660 ± 0.003 | 0.686 ± 0.004 | 0.665 ± 0.005 | 0.789 ± 0.005 | 0.787 ± 0.002 | 0.731 ± 0.006 |
| Spes | 0.147 ± 0.001 | 0.206 ± 0.002 | 0.154 ± 0.002 | 0.188 ± 0.006 | 0.030 ± 0.002 | 0.026 ± 0.001 | 0.153 ± 0.004 |
| Gros | 0.048 ± 0.002 | 0.063 ± 0.002 | 0.044 ± 0.002 | 0.046 ± 0.002 | 0.022 ± 0.002 | 0.020 ± 0.001 | 0.032 ± 0.001 |

Table 2c. Representative garnet analyses

| | P335 core | P335 edge |
|---|---|---|
| SiO | | 37.19 ± 0.30 |
| AlO | | 21.06 ± 0.13 |
| MgO | | 2.88 ± 0.01 |
| Fe | | 37.08 ± 0.06 |
| Mn | | 2.43 ± 0.24 |
| Ca | | 0.73 ± 0.01 |
| Total | | 101.55 ± 0.17 |
| | *cations per 12 oxygens* | |
| Si | 2.891 ± 0.164 | 2.987 ± 0.022 |
| Al | 1.921 ± 0.080 | 2.004 ± 0.012 |
| Mg | 0.516 ± 0.014 | 0.312 ± 0.022 |
| Fe | 2.382 ± 0.041 | 2.449 ± 0.023 |
| Mn | 0.059 ± 0.008 | 0.169 ± 0.021 |
| Ca | 0.080 ± 0.006 | 0.083 ± 0.002 |
| Total | 7.848 ± 0.047 | 8.023 ± 0.013 |
| | | |
| Pyr | 0.170 ± 0.004 | 0.103 ± 0.007 |
| Alm | 0.784 ± 0.005 | 0.813 ± 0.008 |
| Spes | 0.019 ± 0.003 | 0.056 ± 0.007 |
| Gros | 0.026 ± 0.002 | 0.028 ± 0.001 |

Table 3a. Representative Biotite Analyses

| | P5b matrix | P120 matrix | P125 matrix | P151 matrix | P153 matrix | P213A inclusion | P213A matrix |
|---|---|---|---|---|---|---|---|
| SiO | 35.06 ± 2.24 | 35.28 ± 0.57 | 35.96 ± 0.84 | 35.55 ± 0.45 | 35.40 ± 2.19 | 34.84 ± 0.27 | 34.91 ± 0.89 |
| AlO | 19.97 ± 0.29 | 17.18 ± 0.34 | 20.44 ± 0.40 | 19.44 ± 0.20 | 19.87 ± 0.26 | 18.95 ± 0.14 | 19.36 ± 0.52 |
| TiO | 1.36 ± 0.16 | 1.89 ± 0.37 | 1.96 ± 0.06 | 1.69 ± 0.05 | 1.05 ± 0.24 | 2.34 ± 0.17 | 1.92 ± 0.18 |
| MgO | 9.82 ± 0.21 | 7.72 ± 0.47 | 10.00 ± 0.19 | 9.71 ± 0.33 | 8.65 ± 0.01 | 8.99 ± 0.07 | 8.18 ± 0.69 |
| FeO | 21.06 ± 2.72 | 24.31 ± 0.59 | 18.81 ± 0.58 | 20.23 ± 0.38 | 23.35 ± 1.42 | 21.33 ± 0.58 | 21.93 ± 0.89 |
| MnO | 0.06 ± 0.04 | 0.12 ± 0.04 | 0.09 ± 0.02 | 0.14 ± 0.05 | 0.32 ± 0.10 | 0.04 ± 0.03 | 0.07 ± 0.04 |
| CaO | 0.03 ± 0.03 | 0.05 ± 0.04 | 0.00 ± 0.00 | 0.07 ± 0.02 | 0.08 ± 0.05 | 0.00 ± 0.00 | 0.02 ± 0.02 |
| NaO | 0.16 ± 0.06 | 0.09 ± 0.06 | 0.21 ± 0.01 | 0.24 ± 0.01 | 0.11 ± 0.07 | 0.35 ± 0.03 | 0.14 ± 0.05 |
| KO | 8.05 ± 2.01 | 8.85 ± 0.32 | 7.28 ± 0.68 | 8.61 ± 0.47 | 6.17 ± 0.13 | 8.49 ± 0.23 | 7.88 ± 0.55 |
| Total | 95.55 ± 1.87 | 95.49 ± 1.21 | 94.74 ± 1.92 | 95.68 ± 0.52 | 94.99 ± 1.17 | 95.33 ± 0.34 | 94.39 ± 0.98 |
| | | | | *cations per 11 oxygens* | | | |
| Si | 2.656 ± 0.099 | 2.743 ± 0.013 | 2.699 ± 0.021 | 2.691 ± 0.016 | 2.697 ± 0.095 | 2.666 ± 0.015 | 2.691 ± 0.065 |
| Al | 1.785 ± 0.034 | 1.574 ± 0.042 | 1.808 ± 0.021 | 1.734 ± 0.016 | 1.785 ± 0.024 | 1.709 ± 0.011 | 1.759 ± 0.040 |
| Ti | 0.077 ± 0.007 | 0.110 ± 0.020 | 0.111 ± 0.001 | 0.096 ± 0.002 | 0.060 ± 0.012 | 0.134 ± 0.010 | 0.111 ± 0.009 |
| Mg | 1.110 ± 0.049 | 0.894 ± 0.052 | 1.119 ± 0.023 | 1.095 ± 0.037 | 0.983 ± 0.028 | 1.026 ± 0.009 | 0.941 ± 0.082 |
| Fe | 1.339 ± 0.211 | 1.581 ± 0.047 | 1.181 ± 0.046 | 1.281 ± 0.033 | 1.490 ± 0.131 | 1.365 ± 0.039 | 1.414 ± 0.056 |
| Mn | 0.004 ± 0.003 | 0.008 ± 0.003 | 0.006 ± 0.001 | 0.009 ± 0.003 | 0.021 ± 0.007 | 0.003 ± 0.002 | 0.004 ± 0.002 |
| Ca | 0.002 ± 0.002 | 0.005 ± 0.004 | 0.000 ± 0.000 | 0.005 ± 0.001 | 0.006 ± 0.004 | 0.000 ± 0.000 | 0.001 ± 0.001 |
| Na | 0.023 ± 0.008 | 0.014 ± 0.009 | 0.031 ± 0.001 | 0.036 ± 0.001 | 0.016 ± 0.011 | 0.052 ± 0.004 | 0.021 ± 0.008 |
| K | 0.775 ± 0.177 | 0.877 ± 0.023 | 0.696 ± 0.053 | 0.831 ± 0.043 | 0.600 ± 0.004 | 0.829 ± 0.023 | 0.775 ± 0.052 |
| Total | 7.773 ± 0.021 | 7.805 ± 0.018 | 7.650 ± 0.044 | 7.779 ± 0.016 | 7.659 ± 0.102 | 7.785 ± 0.022 | 7.717 ± 0.053 |
| Xann | 0.450 ± 0.043 | 0.436 ± 0.007 | 0.404 ± 0.011 | 0.441 ± 0.009 | 0.491 ± 0.027 | 0.470 ± 0.008 | 0.484 ± 0.021 |
| Xphl | 0.374 ± 0.031 | 0.399 ± 0.007 | 0.383 ± 0.009 | 0.377 ± 0.010 | 0.324 ± 0.019 | 0.353 ± 0.006 | 0.322 ± 0.022 |
| Xmnbi | 0.001 ± 0.001 | 0.003 ± 0.001 | 0.002 ± 0.000 | 0.003 ± 0.001 | 0.007 ± 0.002 | 0.001 ± 0.001 | 0.001 ± 0.001 |

Table 3b. Representative Biotite Analyses

| | P225 inclusion | P225 matrix | P230E inclusion | P230E matrix | P248 inclusion | P248 matrix | P317 matrix |
|---|---|---|---|---|---|---|---|
| SiO | 36.15 ± 0.25 | 35.92 ± 0.38 | 34.82 ± 0.30 | 34.69 ± 0.02 | 35.52 ± 0.25 | 34.84 ± 0.18 | 34.80 ± 0.19 |
| AlO | 17.22 ± 0.09 | 19.04 ± 0.77 | 18.76 ± 0.11 | 18.40 ± 0.14 | 17.50 ± 0.15 | 18.46 ± 0.12 | 19.12 ± 0.08 |
| TiO | 3.03 ± 0.03 | 3.09 ± 0.15 | 2.78 ± 0.04 | 2.57 ± 0.02 | 4.43 ± 0.20 | 3.31 ± 0.07 | 2.16 ± 0.06 |
| MgO | 10.06 ± 0.29 | 9.32 ± 0.49 | 9.40 ± 0.09 | 8.90 ± 0.09 | 10.11 ± 0.20 | 8.53 ± 0.05 | 8.48 ± 0.14 |
| FeO | 19.54 ± 0.32 | 18.03 ± 0.77 | 20.16 ± 0.14 | 21.37 ± 0.13 | 17.59 ± 0.22 | 20.34 ± 0.12 | 21.73 ± 0.19 |
| MnO | 0.15 ± 0.04 | 0.16 ± 0.07 | 0.00 ± 0.00 | 0.21 ± 0.20 | 0.03 ± 0.02 | 0.02 ± 0.03 | 0.08 ± 0.03 |
| CaO | 0.02 ± 0.01 | 0.02 ± 0.02 | 0.02 ± 0.02 | 0.03 ± 0.02 | 0.02 ± 0.02 | 0.03 ± 0.02 | 0.00 ± 0.00 |
| NaO | 0.08 ± 0.02 | 0.15 ± 0.04 | 0.12 ± 0.03 | 0.10 ± 0.05 | 0.36 ± 0.04 | 0.08 ± 0.02 | 0.18 ± 0.02 |
| KO | 9.37 ± 0.14 | 9.43 ± 0.19 | 9.50 ± 0.02 | 9.32 ± 0.04 | 9.03 ± 0.19 | 9.37 ± 0.25 | 9.48 ± 0.02 |
| Total | 95.62 ± 0.41 | 95.16 ± 0.34 | 95.55 ± 0.54 | 95.58 ± 0.51 | 94.58 ± 0.50 | 94.97 ± 0.46 | 96.03 ± 0.29 |
| | | | | *cations per 11 oxygens* | | | |
| Si | 2.746 ± 0.008 | 2.716 ± 0.018 | 2.659 ± 0.005 | 2.665 ± 0.012 | 2.702 ± 0.006 | 2.678 ± 0.007 | 2.663 ± 0.013 |
| Al | 1.542 ± 0.010 | 1.697 ± 0.061 | 1.689 ± 0.004 | 1.666 ± 0.006 | 1.569 ± 0.007 | 1.672 ± 0.009 | 1.724 ± 0.010 |
| Ti | 0.173 ± 0.001 | 0.176 ± 0.008 | 0.160 ± 0.002 | 0.149 ± 0.001 | 0.254 ± 0.010 | 0.191 ± 0.004 | 0.124 ± 0.003 |
| Mg | 1.138 ± 0.028 | 1.051 ± 0.058 | 1.070 ± 0.004 | 1.020 ± 0.007 | 1.147 ± 0.026 | 0.977 ± 0.004 | 0.968 ± 0.013 |
| Fe | 1.241 ± 0.026 | 1.140 ± 0.053 | 1.287 ± 0.011 | 1.373 ± 0.009 | 1.119 ± 0.018 | 1.307 ± 0.006 | 1.390 ± 0.010 |
| Mn | 0.010 ± 0.002 | 0.010 ± 0.004 | 0.000 ± 0.000 | 0.013 ± 0.013 | 0.002 ± 0.002 | 0.001 ± 0.002 | 0.005 ± 0.002 |
| Ca | 0.001 ± 0.001 | 0.002 ± 0.002 | 0.001 ± 0.001 | 0.002 ± 0.002 | 0.002 ± 0.001 | 0.002 ± 0.002 | 0.000 ± 0.000 |
| Na | 0.012 ± 0.002 | 0.023 ± 0.006 | 0.018 ± 0.005 | 0.015 ± 0.007 | 0.053 ± 0.006 | 0.012 ± 0.003 | 0.027 ± 0.003 |
| K | 0.908 ± 0.010 | 0.910 ± 0.020 | 0.925 ± 0.007 | 0.914 ± 0.000 | 0.877 ± 0.016 | 0.918 ± 0.023 | 0.925 ± 0.003 |
| Total | 7.770 ± 0.008 | 7.726 ± 0.040 | 7.809 ± 0.011 | 7.817 ± 0.012 | 7.724 ± 0.016 | 7.760 ± 0.014 | 7.827 ± 0.010 |
| Xann | 0.436 ± 0.007 | 0.409 ± 0.017 | 0.449 ± 0.002 | 0.476 ± 0.004 | 0.401 ± 0.006 | 0.462 ± 0.002 | 0.484 ± 0.004 |
| Xphl | 0.399 ± 0.007 | 0.377 ± 0.017 | 0.373 ± 0.002 | 0.353 ± 0.003 | 0.411 ± 0.006 | 0.346 ± 0.002 | 0.337 ± 0.004 |
| Xmnbio | 0.003 ± 0.001 | 0.004 ± 0.002 | 0.000 ± 0.000 | 0.005 ± 0.005 | 0.001 ± 0.001 | 0.001 ± 0.001 | 0.002 ± 0.001 |

Table 3c. Representative Biotite Analyses

| | P335 inclusion | P335 matrix |
|---|---|---|
| SiO | | 34.83 ± 0.22 |
| AlO | | 19.19 ± 0.01 |
| TiO | | 1.50 ± 0.01 |
| MgO | | 9.14 ± 0.23 |
| FeO | | 22.14 ± 0.17 |
| MnO | | 0.07 ± 0.00 |
| CaO | | 0.01 ± 0.01 |
| NaO | | 0.21 ± 0.01 |
| KO | | 8.68 ± 0.35 |
| Total | | 95.77 ± 0.19 |
| | *cations per 11 oxygens* | |
| Si | 2.700 ± 0.023 | 2.664 ± 0.013 |
| Al | 1.714 ± 0.005 | 1.730 ± 0.004 |
| Ti | 0.080 ± 0.004 | 0.086 ± 0.001 |
| Mg | 1.226 ± 0.013 | 1.042 ± 0.027 |
| Fe | 1.199 ± 0.026 | 1.417 ± 0.013 |
| Mn | 0.003 ± 0.001 | 0.005 ± 0.000 |
| Ca | 0.002 ± 0.001 | 0.001 ± 0.001 |
| Na | 0.047 ± 0.001 | 0.031 ± 0.001 |
| K | 0.833 ± 0.014 | 0.847 ± 0.033 |
| Total | 7.803 ± 0.019 | 7.823 ± 0.005 |
| Xann | 0.411 ± 0.007 | 0.481 ± 0.005 |
| Xphl | 0.420 ± 0.006 | 0.354 ± 0.006 |
| Xmnbi | 0.001 ± 0.000 | 0.002 ± 0.000 |

Table 4a. Representative Muscovite Analyses

| | P5b matrix | P125 matrix | P151 matrix | P153 matrix | P213A matrix | P225 matrix | P317 matrix |
|---|---|---|---|---|---|---|---|
| SiO | 46.96 ± 0.05 | 45.97 ± 0.15 | 49.76 ± 3.70 | 47.19 ± 0.48 | 47.71 ± 0.71 | 47.98 ± 0.35 | 48.24 ± 0.89 |
| AlO | 37.08 ± 0.21 | 36.24 ± 0.10 | 35.49 ± 1.25 | 35.23 ± 0.13 | 35.87 ± 0.09 | 35.10 ± 0.07 | 34.68 ± 0.39 |
| TiO | 0.04 ± 0.05 | 0.41 ± 0.02 | 0.17 ± 0.08 | 0.64 ± 0.02 | 0.34 ± 0.04 | 0.22 ± 0.04 | 0.35 ± 0.01 |
| MgO | 0.68 ± 0.04 | 0.33 ± 0.03 | 0.62 ± 0.04 | 0.64 ± 0.00 | 0.45 ± 0.03 | 0.57 ± 0.08 | 0.48 ± 0.03 |
| FeO | 1.29 ± 0.06 | 0.74 ± 0.02 | 1.28 ± 0.08 | 1.33 ± 0.03 | 1.59 ± 0.09 | 1.87 ± 0.10 | 1.84 ± 0.12 |
| MnO | 0.00 ± 0.00 | 0.00 ± 0.00 | 0.00 ± 0.00 | 0.00 ± 0.00 | 0.00 ± 0.00 | 0.05 ± 0.03 | 0.00 ± 0.00 |
| CaO | 0.00 ± 0.00 | 0.01 ± 0.01 | 0.02 ± 0.02 | 0.02 ± 0.00 | 0.01 ± 0.01 | 0.01 ± 0.01 | 0.00 ± 0.00 |
| NaO | 1.03 ± 0.06 | 1.28 ± 0.08 | 0.55 ± 0.13 | 0.59 ± 0.09 | 1.13 ± 0.06 | 0.55 ± 0.08 | 0.99 ± 0.11 |
| KO | 9.48 ± 0.13 | 8.39 ± 0.16 | 6.70 ± 3.25 | 7.75 ± 0.89 | 9.09 ± 0.26 | 9.91 ± 0.08 | 9.64 ± 0.23 |
| Total | 96.53 ± 0.59 | 93.37 ± 0.13 | 94.56 ± 1.75 | 93.38 ± 1.54 | 96.17 ± 0.38 | 96.26 ± 0.55 | 96.21 ± 0.78 |
| | | | *cations per 11 oxygens* | | | | |
| Si | 3.063 ± 0.011 | 3.077 ± 0.010 | 3.231 ± 0.095 | 3.142 ± 0.002 | 3.119 ± 0.025 | 3.148 ± 0.010 | 3.165 ± 0.027 |
| Al | 2.850 ± 0.003 | 2.859 ± 0.008 | 2.718 ± 0.027 | 2.765 ± 0.020 | 2.764 ± 0.015 | 2.714 ± 0.013 | 2.681 ± 0.027 |
| Ti | 0.002 ± 0.002 | 0.021 ± 0.001 | 0.008 ± 0.003 | 0.032 ± 0.001 | 0.017 ± 0.002 | 0.011 ± 0.002 | 0.017 ± 0.001 |
| Mg | 0.066 ± 0.003 | 0.033 ± 0.003 | 0.060 ± 0.001 | 0.064 ± 0.001 | 0.044 ± 0.003 | 0.056 ± 0.008 | 0.047 ± 0.003 |
| Fe | 0.070 ± 0.003 | 0.042 ± 0.001 | 0.069 ± 0.001 | 0.074 ± 0.002 | 0.087 ± 0.005 | 0.103 ± 0.005 | 0.101 ± 0.007 |
| Mn | 0.000 ± 0.000 | 0.000 ± 0.000 | 0.000 ± 0.000 | 0.000 ± 0.000 | 0.000 ± 0.000 | 0.003 ± 0.002 | 0.000 ± 0.000 |
| Ca | 0.000 ± 0.000 | 0.001 ± 0.001 | 0.001 ± 0.002 | 0.001 ± 0.000 | 0.000 ± 0.001 | 0.001 ± 0.001 | 0.000 ± 0.000 |
| Na | 0.131 ± 0.007 | 0.166 ± 0.010 | 0.070 ± 0.019 | 0.076 ± 0.011 | 0.143 ± 0.008 | 0.070 ± 0.010 | 0.126 ± 0.014 |
| K | 0.788 ± 0.008 | 0.716 ± 0.014 | 0.562 ± 0.294 | 0.658 ± 0.069 | 0.758 ± 0.027 | 0.829 ± 0.005 | 0.807 ± 0.027 |
| Total | 6.970 ± 0.014 | 6.914 ± 0.013 | 6.718 ± 0.241 | 6.811 ± 0.053 | 6.933 ± 0.032 | 6.934 ± 0.007 | 6.944 ± 0.025 |
| K/Alk | 0.858 ± 0.006 | 0.811 ± 0.009 | 0.888 ± 0.059 | 0.895 ± 0.017 | 0.841 ± 0.009 | 0.922 ± 0.010 | 0.864 ± 0.013 |
| Al/VI | 0.933 ± 0.002 | 0.953 ± 0.002 | 0.934 ± 0.004 | 0.918 ± 0.001 | 0.927 ± 0.003 | 0.915 ± 0.004 | 0.918 ± 0.004 |

Table 4b. Representative Muscovite Analyses

| | P335 matrix | |
|---|---|---|
| SiO | | |
| AlO | | |
| TiO | | |
| MgO | | |
| FeO | | |
| MnO | | |
| CaO | | |
| NaO | | |
| KO | | |
| Total | | |
| | *cations per 11 oxygens* | |
| Si | 3.110 ± 0.012 | |
| Al | 2.763 ± 0.012 | |
| Ti | 0.007 ± 0.002 | |
| Mg | 0.051 ± 0.005 | |
| Fe | 0.106 ± 0.007 | |
| Mn | 0.002 ± 0.001 | |
| Ca | 0.001 ± 0.001 | |
| Na | 0.140 ± 0.014 | |
| K | 0.782 ± 0.020 | |
| Total | 6.962 ± 0.020 | |
| K/Alk | 0.848 ± 0.013 | |
| Al/VI | 0.918 ± 0.004 | |

Table 5a. Representative Plagioclase Analyses

| | P5b matrix | P120 matrix | P125 matrix | P151 matrix | P153 matrix | P213A inclusion | P213A matrix |
|---|---|---|---|---|---|---|---|
| SiO | 61.58 ± 0.32 | 57.44 ± 0.87 | 59.96 ± 0.40 | 60.95 ± 0.64 | 59.66 ± 0.32 | 61.08 ± 0.24 | 61.22 ± 0.20 |
| AlO | 24.42 ± 0.18 | 27.10 ± 0.45 | 25.91 ± 0.15 | 24.27 ± 0.43 | 25.86 ± 0.55 | 24.61 ± 0.07 | 24.07 ± 0.31 |
| FeO | 0.08 ± 0.02 | 0.11 ± 0.11 | 0.15 ± 0.13 | 0.04 ± 0.06 | 0.08 ± 0.06 | 0.09 ± 0.01 | 0.27 ± 0.01 |
| CaO | 5.67 ± 0.17 | 8.71 ± 0.32 | 7.07 ± 0.23 | 5.84 ± 0.36 | 7.09 ± 0.19 | 5.73 ± 0.04 | 5.46 ± 0.05 |
| NaO | 8.60 ± 0.09 | 6.33 ± 0.67 | 7.51 ± 0.13 | 7.63 ± 0.56 | 7.30 ± 0.24 | 8.46 ± 0.06 | 8.63 ± 0.10 |
| KO | 0.04 ± 0.01 | 0.12 ± 0.02 | 0.09 ± 0.02 | 0.08 ± 0.03 | 0.06 ± 0.02 | 0.07 ± 0.01 | 0.06 ± 0.01 |
| Total | 100.41 ± 0.23 | 99.80 ± 0.87 | 100.69 ± 0.25 | 98.79 ± 0.38 | 100.10 ± 0.21 | 100.02 ± 0.33 | 99.70 ± 0.66 |
| | | | | *cations per 8 oxygens* | | | |
| Si | 2.723 ± 0.009 | 2.575 ± 0.024 | 2.653 ± 0.014 | 2.717 ± 0.019 | 2.653 ± 0.019 | 2.713 ± 0.003 | 2.729 ± 0.008 |
| Al | 1.273 ± 0.009 | 1.432 ± 0.026 | 1.351 ± 0.010 | 1.301 ± 0.027 | 1.356 ± 0.027 | 1.288 ± 0.003 | 1.264 ± 0.009 |
| Fe | 0.003 ± 0.001 | 0.004 ± 0.004 | 0.006 ± 0.005 | 0.003 ± 0.002 | 0.003 ± 0.002 | 0.003 ± 0.000 | 0.010 ± 0.000 |
| Ca | 0.269 ± 0.009 | 0.418 ± 0.018 | 0.335 ± 0.011 | 0.293 ± 0.018 | 0.338 ± 0.009 | 0.273 ± 0.002 | 0.260 ± 0.001 |
| Na | 0.740 ± 0.008 | 0.552 ± 0.056 | 0.647 ± 0.011 | 0.632 ± 0.046 | 0.631 ± 0.021 | 0.731 ± 0.004 | 0.748 ± 0.004 |
| K | 0.002 ± 0.001 | 0.007 ± 0.001 | 0.005 ± 0.001 | 0.003 ± 0.002 | 0.004 ± 0.001 | 0.004 ± 0.000 | 0.003 ± 0.000 |
| Total | 5.012 ± 0.008 | 4.988 ± 0.036 | 4.997 ± 0.015 | 4.950 ± 0.019 | 4.986 ± 0.012 | 5.011 ± 0.003 | 5.015 ± 0.005 |
| An | 0.266 ± 0.007 | no ± 0.013 | 0.340 ± 0.008 | 0.316 ± 0.021 | 0.347 ± 0.010 | 0.271 ± 0.002 | 0.257 ± 0.001 |
| Ab | 0.732 ± 0.000 | 0.386 ± 0.000 | 0.655 ± 0.000 | 0.681 ± 0.000 | 0.649 ± 0.000 | 0.726 ± 0.000 | 0.739 ± 0.000 |

Table 5b. Representative Plagioclase Analyses

| | P225 inclusion | P225 matrix | P230E inclusion | P230E matrix | P248 inclusion | P248 matrix | P317 matrix |
|---|---|---|---|---|---|---|---|
| SiO | 53.65 ± 0.42 | 65.02 ± 0.64 | 57.84 ± 0.09 | 58.03 ± 1.15 | 62.91 ± 0.46 | 63.71 ± 0.51 | 62.24 ± 0.27 |
| AlO | 30.26 ± 0.19 | 22.89 ± 0.30 | 25.43 ± 0.17 | 26.53 ± 0.33 | 23.15 ± 0.36 | 23.01 ± 0.15 | 23.99 ± 0.21 |
| FeO | 0.17 ± 0.01 | 0.69 ± 0.07 | 0.05 ± 0.05 | 0.09 ± 0.06 | 0.28 ± 0.19 | 0.22 ± 0.12 | 0.26 ± 0.02 |
| CaO | 12.54 ± 0.28 | 3.63 ± 0.45 | 7.93 ± 0.09 | 8.23 ± 0.25 | 4.24 ± 0.34 | 3.82 ± 0.14 | 4.93 ± 0.18 |
| NaO | 4.38 ± 0.23 | 9.40 ± 0.22 | 7.08 ± 0.11 | 7.05 ± 0.18 | 9.29 ± 0.16 | 9.45 ± 0.13 | 9.20 ± 0.17 |
| KO | 0.10 ± 0.01 | 0.09 ± 0.02 | 0.11 ± 0.02 | 0.07 ± 0.05 | 0.21 ± 0.02 | 0.15 ± 0.03 | 0.13 ± 0.02 |
| Total | 101.11 ± 0.12 | 101.73 ± 0.19 | 98.46 ± 0.14 | 100.03 ± 1.43 | 100.09 ± 0.24 | 100.44 ± 0.78 | 100.78 ± 0.15 |
| | | | | *cations per 8 oxygens* | | | |
| Si | 2.402 ± 0.014 | 2.824 ± 0.020 | 2.627 ± 0.006 | 2.596 ± 0.013 | 2.785 ± 0.017 | 2.804 ± 0.005 | 2.744 ± 0.010 |
| Al | 1.596 ± 0.013 | 1.172 ± 0.019 | 1.361 ± 0.008 | 1.399 ± 0.011 | 1.208 ± 0.020 | 1.194 ± 0.008 | 1.247 ± 0.012 |
| Fe | 0.007 ± 0.000 | 0.025 ± 0.002 | 0.002 ± 0.002 | 0.003 ± 0.002 | 0.010 ± 0.007 | 0.008 ± 0.004 | 0.010 ± 0.001 |
| Ca | 0.601 ± 0.015 | 0.169 ± 0.022 | 0.386 ± 0.004 | 0.395 ± 0.016 | 0.201 ± 0.016 | 0.180 ± 0.007 | 0.233 ± 0.009 |
| Na | 0.382 ± 0.020 | 0.794 ± 0.016 | 0.625 ± 0.010 | 0.613 ± 0.015 | 0.800 ± 0.012 | 0.809 ± 0.008 | 0.789 ± 0.014 |
| K | 0.006 ± 0.001 | 0.005 ± 0.001 | 0.007 ± 0.001 | 0.004 ± 0.003 | 0.012 ± 0.001 | 0.008 ± 0.002 | 0.007 ± 0.001 |
| Total | 4.994 ± 0.010 | 4.990 ± 0.002 | 5.009 ± 0.006 | 5.013 ± 0.010 | 5.016 ± 0.004 | 5.008 ± 0.004 | 5.031 ± 0.004 |
| An | 0.608 ± 0.013 | 0.174 ± 0.019 | 0.379 ± 0.004 | 0.390 ± 0.011 | 0.199 ± 0.013 | 0.181 ± 0.006 | 0.226 ± 0.007 |
| Ab | 0.386 ± 0.000 | 0.820 ± 0.000 | 0.614 ± 0.000 | 0.606 ± 0.000 | 0.790 ± 0.000 | 0.811 ± 0.000 | 0.767 ± 0.000 |

Table 5c. Representative Plagioclase Analyses

| | P335 inclusion | P335 matrix |
|---|---|---|
| SiO | | 60.63 ± 0.21 |
| AlO | | 25.21 ± 0.01 |
| FeO | | 0.33 ± 0.05 |
| CaO | | 6.49 ± 0.18 |
| NaO | | 7.99 ± 0.01 |
| KO | | 0.07 ± 0.01 |
| Total | | 100.71 ± 0.10 |
| | *cations per 8 oxygens* | |
| Si | 2.747 ± 0.006 | 2.682 ± 0.005 |
| Al | 1.253 ± 0.004 | 1.314 ± 0.002 |
| Fe | 0.007 ± 0.001 | 0.012 ± 0.002 |
| Ca | 0.244 ± 0.002 | 0.307 ± 0.009 |
| Na | 0.748 ± 0.019 | 0.685 ± 0.002 |
| K | 0.004 ± 0.000 | 0.004 ± 0.000 |
| Total | 5.003 ± 0.014 | 5.005 ± 0.005 |
| An | 0.245 ± 0.005 | 0.309 ± 0.006 |
| Ab | 0.751 ± 0.000 | 0.688 ± 0.000 |

Table 6. Representative cordierite analyses.

| | P125 matrix edge | P213A matrix edge | P213A Inclusion | P243b matrix edge | P248 matrix edge | P248 inclusion |
|---|---|---|---|---|---|---|
| SiO | 48.608 ± 0.191 | 49.783 ± 1.211 | 48.520 ± 0.140 | 48.240 ± 0.441 | 48.198 ± 0.195 | 48.563 ± 0.248 |
| AlO | 32.567 ± 0.122 | 32.000 ± 0.701 | 32.210 ± 0.050 | 32.542 ± 0.252 | 32.655 ± 0.111 | 32.843 ± 0.239 |
| TiO | 0.018 ± 0.012 | 0.028 ± 0.013 | 0.030 ± 0.030 | 0.000 ± 0.000 | 0.005 ± 0.010 | 0.023 ± 0.017 |
| MgO | 8.065 ± 0.084 | 7.703 ± 0.262 | 7.343 ± 0.065 | 8.112 ± 0.155 | 8.478 ± 0.050 | 8.925 ± 0.045 |
| FeO | 7.235 ± 0.106 | 8.390 ± 0.211 | 9.237 ± 0.124 | 8.210 ± 0.221 | 7.945 ± 0.090 | 7.690 ± 0.106 |
| MnO | 0.265 ± 0.010 | 0.165 ± 0.029 | 0.187 ± 0.021 | 0.078 ± 0.025 | 0.055 ± 0.039 | 0.090 ± 0.042 |
| CaO | 0.027 ± 0.015 | 0.005 ± 0.006 | 0.003 ± 0.006 | 0.030 ± 0.018 | 0.005 ± 0.006 | 0.010 ± 0.008 |
| NaO | 0.622 ± 0.016 | 0.438 ± 0.051 | 0.410 ± 0.050 | 0.383 ± 0.030 | 0.210 ± 0.008 | 0.320 ± 0.042 |
| Total | 97.430 ± 0.219 | 98.533 ± 0.741 | 97.940 ± 0.166 | 97.598 ± 0.636 | 97.553 ± 0.324 | 98.460 ± 0.408 |
| | | | *cations per 18 oxygens* | | | |
| Si | 5.035 ± 0.016 | 5.113 ± 0.101 | 5.040 ± 0.004 | 5.006 ± 0.017 | 4.995 ± 0.006 | 4.985 ± 0.008 |
| Al | 3.976 ± 0.014 | 3.873 ± 0.098 | 3.944 ± 0.006 | 3.980 ± 0.009 | 3.989 ± 0.014 | 3.973 ± 0.015 |
| Ti | 0.001 ± 0.001 | 0.002 ± 0.001 | 0.002 ± 0.002 | 0.000 ± 0.000 | 0.000 ± 0.001 | 0.002 ± 0.001 |
| Mg | 1.246 ± 0.013 | 1.350 ± 0.348 | 1.137 ± 0.008 | 1.255 ± 0.025 | 1.310 ± 0.008 | 1.366 ± 0.006 |
| Fe | 0.627 ± 0.009 | 0.721 ± 0.019 | 0.802 ± 0.012 | 0.713 ± 0.021 | 0.688 ± 0.006 | 0.660 ± 0.011 |
| Mn | 0.023 ± 0.001 | 0.014 ± 0.002 | 0.016 ± 0.002 | 0.007 ± 0.002 | 0.005 ± 0.003 | 0.008 ± 0.004 |
| Ca | 0.003 ± 0.001 | 0.001 ± 0.001 | 0.001 ± 0.001 | 0.003 ± 0.002 | 0.001 ± 0.001 | 0.001 ± 0.001 |
| Na | 0.125 ± 0.003 | 0.088 ± 0.009 | 0.083 ± 0.010 | 0.077 ± 0.006 | 0.042 ± 0.002 | 0.064 ± 0.009 |
| Total | 11.039 ± 0.011 | 10.992 ± 0.056 | 11.026 ± 0.005 | 11.042 ± 0.017 | 11.030 ± 0.003 | 11.058 ± 0.008 |
| XFe | 0.334 ± 0.003 | 0.379 ± 0.005 | 0.413 ± 0.005 | 0.361 ± 0.007 | 0.345 ± 0.002 | 0.326 ± 0.005 |
| XMg | 0.664 ± 0.002 | 0.621 ± 0.004 | 0.586 ± 0.005 | 0.637 ± 0.008 | 0.655 ± 0.002 | 0.674 ± 0.004 |
| XCa | 0.002 ± 0.001 | 0.001 ± 0.001 | 0.000 ± 0.001 | 0.002 ± 0.001 | 0.001 ± 0.001 | 0.001 ± 0.001 |

Table 7. Representative microprobe analyses of amphiboles from the Pioneer Intrusive Suite.

| | P92 edge | P92 core | P155 edge | P155 core | P156 edge | P156 core |
|---|---|---|---|---|---|---|
| SiO2 | 45.74 | 44.47 | 48.39 | 48.23 | 49.03 | 44.06 |
| Al2O3 | 7.36 | 7.92 | 7.88 | 8.09 | 7.67 | 9.64 |
| TiO2 | 0.94 | 1.28 | 0.76 | 0.77 | 0.78 | 1.34 |
| MgO | 11.92 | 11.71 | 14.90 | 15.06 | 11.11 | 10.85 |
| FeO | 16.75 | 17.24 | 12.42 | 12.53 | 15.24 | 17.14 |
| MnO | 0.54 | 0.52 | 0.18 | 0.17 | 0.35 | 0.41 |
| CaO | 11.65 | 11.62 | 11.45 | 11.34 | 11.20 | 11.54 |
| Na2O | 1.39 | 1.46 | 0.84 | 1.05 | 1.04 | 1.45 |
| K2O | 0.78 | 0.92 | 0.61 | 0.75 | 0.74 | 1.18 |
| Total | 97.07 | 97.13 | 97.43 | 98.10 | 97.16 | 97.60 |
| | | | | | | |
| Si | 6.839 | 6.670 | 6.974 | 6.921 | 7.228 | 6.597 |
| Al iv | 1.161 | 1.330 | 1.026 | 1.079 | 0.772 | 1.403 |
| Al vi | 0.137 | 0.071 | 0.313 | 0.290 | 0.561 | 0.299 |
| Ti | 0.106 | 0.144 | 0.082 | 0.083 | 0.086 | 0.151 |
| *Fe3+ | 0.403 | 0.512 | 0.436 | 0.466 | 0.040 | 0.315 |
| Mg | 2.656 | 2.618 | 3.200 | 3.221 | 2.441 | 2.421 |
| Fe2+ | 1.691 | 1.651 | 1.061 | 1.037 | 1.839 | 1.831 |
| Mn | 0.068 | 0.066 | 0.022 | 0.021 | 0.044 | 0.052 |
| Ca | 1.867 | 1.868 | 1.768 | 1.744 | 1.769 | 1.851 |
| Na(M4) | 0.071 | 0.071 | 0.117 | 0.137 | 0.219 | 0.080 |
| Na(A) | 0.332 | 0.354 | 0.117 | 0.155 | 0.078 | 0.341 |
| K | 0.149 | 0.176 | 0.112 | 0.138 | 0.139 | 0.225 |

*Fe3+ calculated according to the method of Spear & Kimball (1984).

Table 8. Representative microprobe analyses of feldspar from the Pioneer Intrusive Suite.

| | P92 plagioclase edge | P92 K-feldpsar edge | P156 plagioclase edge | P156 K-feldspar edge |
|---|---|---|---|---|
| SiO2 | 64.83 ± 4.72 | 64.10 ± 1.93 | 63.52 ± 2.48 | 64.24 ± 0.12 |
| Al2O | 21.90 ± 2.39 | 18.04 ± 0.50 | 23.56 ± 1.56 | 18.65 ± 0.38 |
| FcO | 0.06 ± 0.10 | 0.19 ± 0.53 | 0.07 ± 0.06 | 0.04 ± 0.06 |
| MgO | 0.02 ± 0.03 | 0.00 ± 0.01 | 0.00 ± 0.00 | 0.00 ± 0.00 |
| CaO | 3.57 ± 1.39 | 0.01 ± 0.03 | 3.45 ± 2.15 | 0.02 ± 0.04 |
| Na2O | 9.39 ± 0.75 | 0.38 ± 0.16 | 9.28 ± 1.19 | 1.29 ± 0.03 |
| K2O | 0.12 ± 0.03 | 15.84 ± 0.23 | 0.17 ± 0.01 | 14.39 ± 0.31 |
| Total | 99.89 ± 0.83 | 98.55 ± 0.85 | 100.82 ± 0.27 | 98.62 ± 0.35 |
| | | *cations per 8 oxygens* | | |
| Si | 2.858 ± 0.152 | 3.003 ± 0.046 | 2.786 ± 0.088 | 2.989 ± 0.012 |
| Al | 1.139 ± 0.145 | 0.996 ± 0.042 | 1.218 ± 0.090 | 1.023 ± 0.019 |
| Fe | 0.002 ± 0.004 | 0.007 ± 0.021 | 0.002 ± 0.002 | 0.001 ± 0.002 |
| Mg | 0.001 ± 0.002 | 0.000 ± 0.001 | 0.000 ± 0.000 | 0.000 ± 0.000 |
| Ca | 0.169 ± 0.069 | 0.001 ± 0.002 | 0.198 ± 0.089 | 0.001 ± 0.002 |
| Na | 0.802 ± 0.069 | 0.034 ± 0.015 | 0.789 ± 0.096 | 0.116 ± 0.003 |
| K | 0.007 ± 0.002 | 0.947 ± 0.026 | 0.010 ± 0.000 | 0.854 ± 0.019 |
| Total | 4.977 ± 0.105 | 4.989 ± 0.045 | 5.004 ± 0.014 | 4.985 ± 0.012 |
| An | 0.172 ± 0.058 | 0.001 ± 0.002 | 0.199 ± 0.090 | 0.001 ± 0.002 |
| Ab | 0.821 ± 0.058 | 0.035 ± 0.014 | 0.792 ± 0.089 | 0.120 ± 0.002 |
| Or | 0.007 ± 0.001 | 0.965 ± 0.014 | 0.010 ± 0.000 | 0.879 ± 0.004 |

Table 9. Calculated pressures and temperatures.

| Sample number | edge/core | GTB | Temperature (Kelvin) | precision (±2 s.d.) | Pressure MPa | precision (±2 s.d.) | Sample Locality |
|---|---|---|---|---|---|---|---|
| *Pelitic Schists of the Hyndman Group* | | | | | | | |
| P5B | edge | GARB/GASP | 835 | 30 | 260 | 50 | 1 |
| P151 | edge | GARB/GASP | 895 | 77 | 336 | 113 | 2 |
| P213A | edge | GARB/GASP | 890 | 42 | 321 | 54 | 3 |
| | edge | G-C | 769 | | | | 3 |
| P213A | core | GARB/GASP | 936 | 10 | 382 | 31 | 3 |
| | core | G-C | 855 | | | | 3 |
| P225A | edge | GARB/GASP | 840 | 83 | 219 | 123 | 4 |
| P225B | edge | GARB/GASP | 715 | 13 | 511 | 83 | 4 |
| P225B | core | GARB/GASP | 960 | 12 | 331 | 32 | 4 |
| P230E | edge | GARB/GASP | 872 | 28 | 230 | 51 | 4 |
| P230E | core | GARB/GASP | 880 | 32 | 374 | 64 | 4 |
| P243B | edge | GARB/GASP | 735 | 37 | 179 | 60 | 2 |
| P248B | edge | GARB/GASP | 1025 | 17 | 553 | 69 | 2 |
| | edge | G-C | 824 | | | | 2 |
| P248B | core | GARB/GASP | 863 | 29 | 325 | 134 | 5 |
| | core | G-C | 807 | | | | 6 |
| P317 | edge | GARB/GASP | 804 | 50 | 325 | 73 | 6 |
| P335 | edge | GARB/GASP | 811 | 46 | 180 | 62 | 5 |
| P335 | core | GARB/GASP | 891 | 27 | 359 | 64 | 5 |
| *Pelitic Schists of the Wildhorse Gneiss Complex* | | | | | | | |
| P120 | edge | GARB/GASP | 1178 | 176 | 874 | 296 | |
| P125 | edge | GARB/GASP | 848 | 48 | 342 | 75 | |
| | edge | G-C | 768 | | | | |
| *Pioneer Intrusive Suite* | | | | | | | |
| P92 | edge | H1 (H2) | | | 256 (203) | | |
| | edge | GP1 (GP2) | 889 (874) | | | | |
| P92 | core | H1 (H2) | | | 314 (246) | | |
| P153 | edge | GARB/GASP | 957 | 25 | 420 | 49 | 2 |
| P155 | edge | H1 (H2) | | | 279 (220) | | 2 |
| P155 | core | H1 (H2) | | | 296 (233) | | 2 |
| P156 | edge | H1 (H2) | | | 276 (218) | | 2 |
| | edge | GP1 (GP2) | 910 (901) | | | | 2 |
| P156 | core | H1 (H2) | | | 315 (247) | | 2 |

edge = final equilibration calculated with edges of matrix assemblage as described in text; core = calculated with garnet-host/entrapped mineral or hornblende cores as described in text; GTB = geothermobarometer; GASP = garnet-aluminum silicate-quartz-plagioclase barometer; GARB = garnet-biotite thermometer; G-C = garnet-cordierite thermometer (Perchuk & Lavrent'eva, 1987); H1 = hornblende aluminum barometer (Johnson et al., 1989); H2 = hornblende aluminum barometer (Hollister et al., 1987); GP1 = garnet-plagioclase thermometer (4-point regression, Spear, 1981); GP2 = garnet-plagioclase thermometer (3-point regression, Spear, 1981). Sample localities on Figure 8.

Table 10. Gibbs Method monitors and results.

| Sample | ΔX alm | ΔX grs | ΔX sps | bi incl. ΔX ann | pg incl. ΔX an | Core temperature (K) | Core pressure (MPa) |
|---|---|---|---|---|---|---|---|
| P213A | -0.003 | 0.001 | -0.026 | 0.056* | 0.014 | 1095 | 576 |
| | -0.003 | 0.001 | -0.026 | -0.014 | -0.033* | 955 | 478 |
| | -0.003 | 0.001 | 0.012* | -0.014 | 0.014 | 845 | 257 |
| P225 | -0.005 | -0.015 | -0.059 | 0.386* | 0.434 | 3514 | 3503 |
| P248 | 0.002 | 0.002 | 0.004 | -0.012* | 0.018 | 977 | 491 |
| | 0.002 | 0.002 | 0.004 | -0.060 | -0.014* | 910 | 477 |
| | 0.002 | 0.002 | 0.041* | -0.060 | 0.018 | 823 | 288 |
| P335 | -0.029 | -0.002 | -0.037 | 0.053* | -0.064 | 1130 | 646 |
| | -0.029 | -0.002 | -0.037 | -0.070 | -0.141* | 908 | 503 |
| | -0.029 | -0.002 | 0.032* | -0.070 | -0.064 | 742 | 149 |

* = calculated ΔX; not used as monitor parameter in quadravariant assemblage.
alm = almandine, grs = grossular, sps = spessartine, ann = annite, an = anorthite.

Figure 2.1

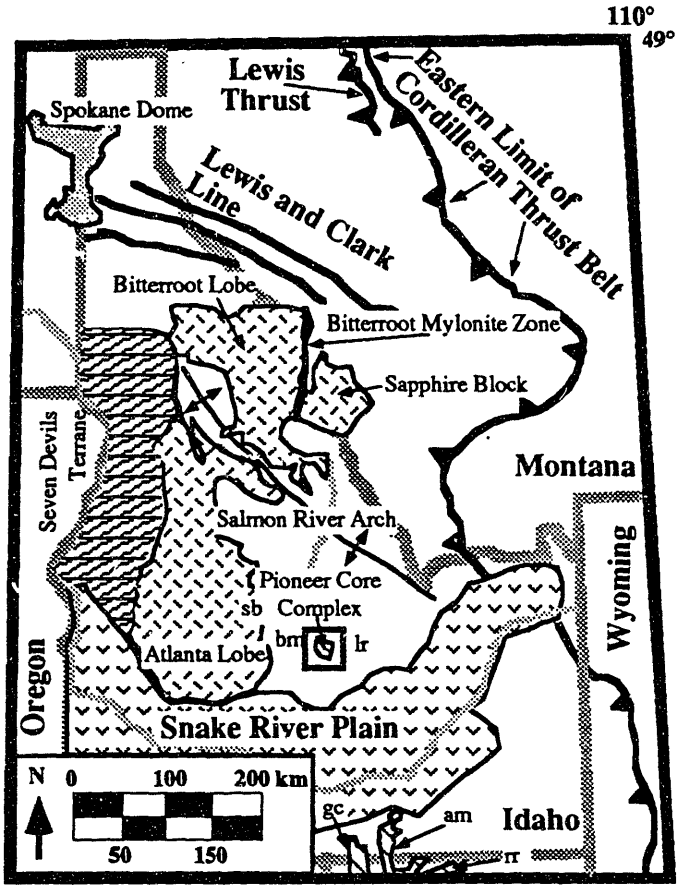
110°
49°
Lewis Thrust
Eastern Limit of Cordilleran Thrust Belt
Spokane Dome
Lewis and Clark Line
Bitterroot Lobe
Bitterroot Mylonite Zone
Sapphire Block
Seven Devils Terrane
Montana
Salmon River Arch
Pioneer Core
sb Complex
bm
lr
Atlanta Lobe
Wyoming
Oregon
Snake River Plain
N
0
100
200 km
50
150
gc
am
Idaho
rr

Figure 2.2

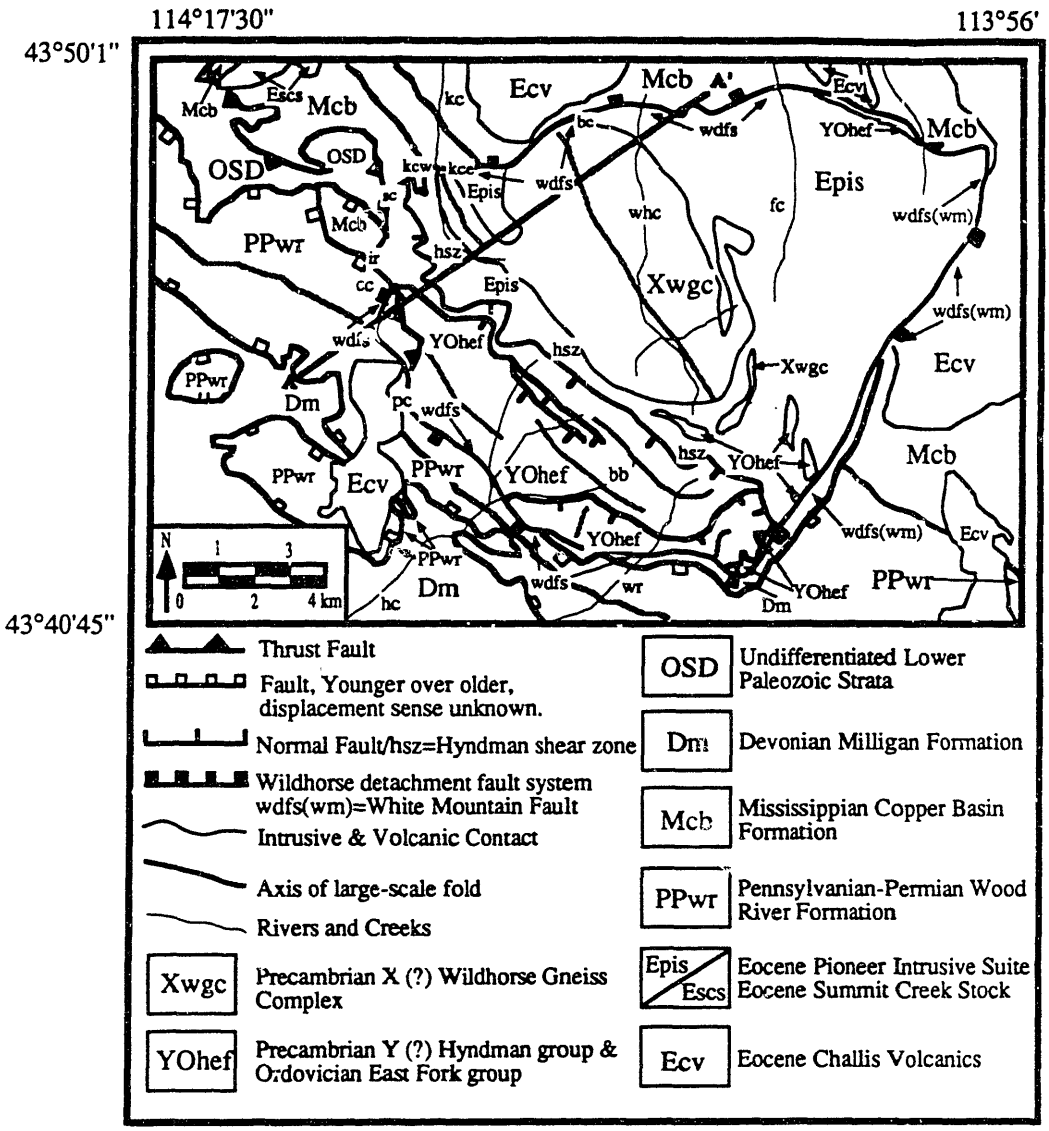
114°17'30"
113°56'
43°50'1"
43°40'45"
Mcb
Escs
Ecv
kc
bc
wdfs
A'
YOhef
OSD
kcw
kce
Epis
ac
whc
fc
wdfs(wm)
PPwr
Mcb
ir
hsz
cc
Xwgc
wdfs
YOhef
pc
Dm
bb
N
1
3
0
2
4 km
hc
wr
Thrust Fault
Fault, Younger over older, displacement sense unknown.
Normal Fault/hsz=Hyndman shear zone
Wildhorse detachment fault system
wdfs(wm)=White Mountain Fault
Intrusive & Volcanic Contact
Axis of large-scale fold
Rivers and Creeks
Xwgc
Precambrian X (?) Wildhorse Gneiss Complex
YOhef
Precambrian Y (?) Hyndman group & Ordovician East Fork group
OSD
Undifferentiated Lower Paleozoic Strata
Dm
Devonian Milligan Formation
Mcb
Mississippian Copper Basin Formation
PPwr
Pennsylvanian-Permian Wood River Formation
Epis
Escs
Eocene Pioneer Intrusive Suite
Eocene Summit Creek Stock
Ecv
Eocene Challis Volcanics

Figure 2.3

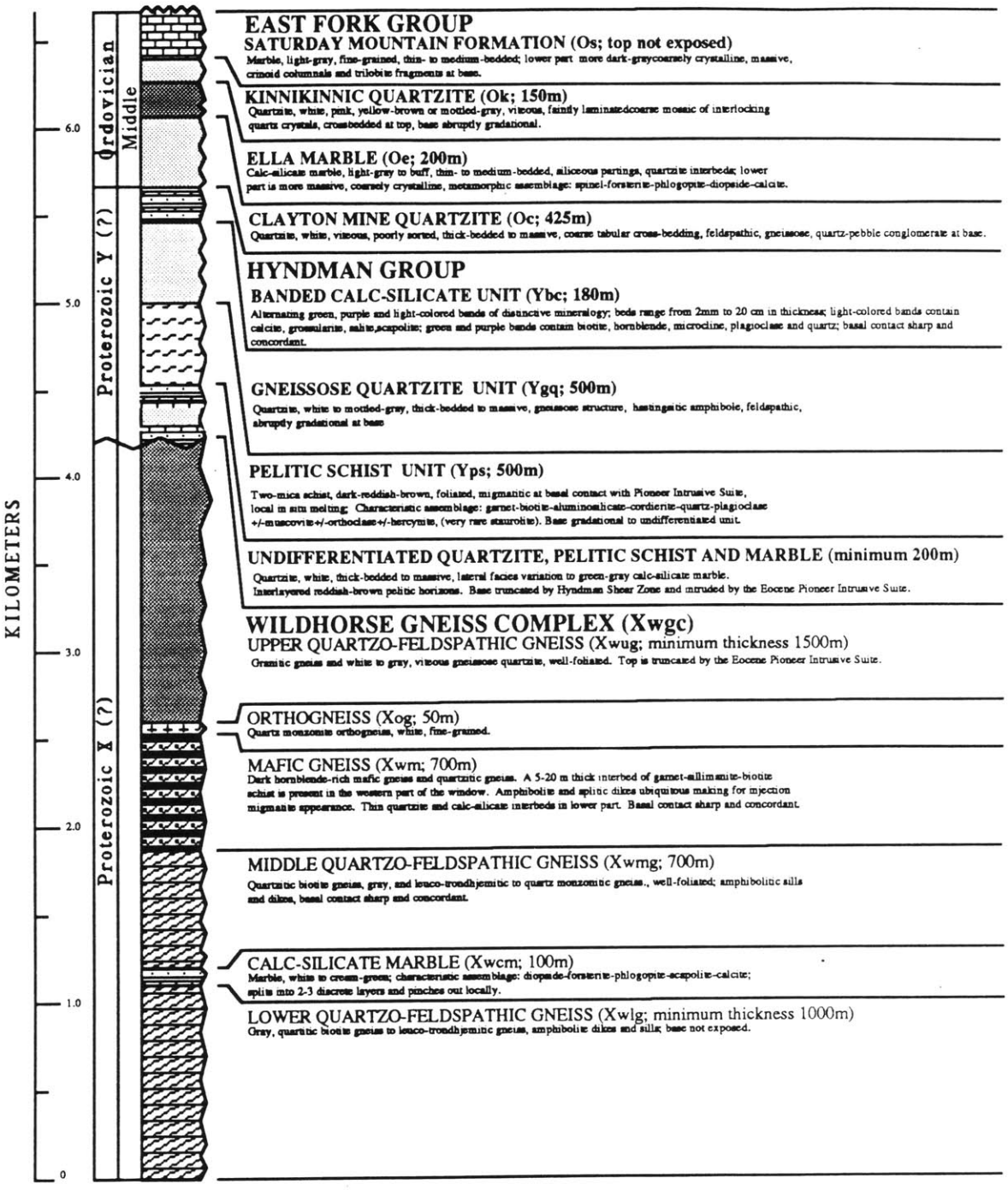
KILOMETERS
6.0
5.0
4.0
3.0
2.0
1.0
0
Ordovician
Middle
Proterozoic Y (?)
Proterozoic X (?)
EAST FORK GROUP
SATURDAY MOUNTAIN FORMATION (Os; top not exposed)
Marble, light-gray, fine-grained, thin- to medium-bedded; lower part more dark-gray coarsely crystalline, massive, crinoid columnals and trilobite fragments at base.
KINNIKINNIC QUARTZITE (Ok; 150m)
Quartzite, white, pink, yellow-brown or mottled-gray, vitreous, faintly laminated coarse mosaic of interlocking quartz crystals, crossbedded at top, base abruptly gradational.
ELLA MARBLE (Oe; 200m)
Calc-silicate marble, light-gray to buff, thin- to medium-bedded, siliceous partings, quartzite interbeds; lower part is more massive, coarsely crystalline, metamorphic assemblage: spinel-forsterite-phlogopite-diopside-calcite.
CLAYTON MINE QUARTZITE (Oc; 425m)
Quartzite, white, vitreous, poorly sorted, thick-bedded to massive, coarse tabular cross-bedding, feldspathic, gneissose, quartz-pebble conglomerate at base.
HYNDMAN GROUP
BANDED CALC-SILICATE UNIT (Ybc; 180m)
Alternating green, purple and light-colored bands of distinctive mineralogy; beds range from 2mm to 20 cm in thickness; light-colored bands contain calcite, grossularite, white scapolite; green and purple bands contain biotite, hornblende, microcline, plagioclase and quartz; basal contact sharp and concordant.
GNEISSOSE QUARTZITE UNIT (Ygq; 500m)
Quartzite, white to mottled-gray, thick-bedded to massive, gneissose structure, hastingsitic amphibole, feldspathic, abruptly gradational at base
PELITIC SCHIST UNIT (Yps; 500m)
Two-mica schist, dark-reddish-brown, foliated, migmatitic at basal contact with Pioneer Intrusive Suite, local in situ melting; Characteristic assemblage: garnet-biotite-aluminosilicate-cordierite-quartz-plagioclase +/-muscovite+/-orthoclase+/-hercynite, (very rare staurolite). Base gradational to undifferentiated unit.
UNDIFFERENTIATED QUARTZITE, PELITIC SCHIST AND MARBLE (minimum 200m)
Quartzite, white, thick-bedded to massive, lateral facies variation to green-gray calc-silicate marble. Interlayered reddish-brown pelitic horizons. Base truncated by Hyndman Shear Zone and intruded by the Eocene Pioneer Intrusive Suite.
WILDHORSE GNEISS COMPLEX (Xwgc)
UPPER QUARTZO-FELDSPATHIC GNEISS (Xwug; minimum thickness 1500m)
Granitic gneiss and white to gray, vitreous gneissose quartzite, well-foliated. Top is truncated by the Eocene Pioneer Intrusive Suite.
ORTHOGNEISS (Xog; 50m)
Quartz monzonite orthogneiss, white, fine-grained.
MAFIC GNEISS (Xwm; 700m)
Dark hornblende-rich mafic gneiss and quartzitic gneiss. A 5-20 m thick interbed of garnet-sillimanite-biotite schist is present in the western part of the window. Amphibolite and aplitic dikes ubiquitous making for injection migmatite appearance. Thin quartzite and calc-silicate interbeds in lower part. Basal contact sharp and concordant.
MIDDLE QUARTZO-FELDSPATHIC GNEISS (Xwmg; 700m)
Quartzitic biotite gneiss, gray, and leuco-trondhjemitic to quartz monzonitic gneiss., well-foliated; amphibolitic sills and dikes, basal contact sharp and concordant.
CALC-SILICATE MARBLE (Xwcm; 100m)
Marble, white to cream-green; characteristic assemblage: diopside-forsterite-phlogopite-scapolite-calcite; splits into 2-3 discrete layers and pinches out locally.
LOWER QUARTZO-FELDSPATHIC GNEISS (Xwlg; minimum thickness 1000m)
Gray, quartzitic biotite gneiss to leuco-trondhjemitic gneiss, amphibolite dikes and sills; base not exposed.

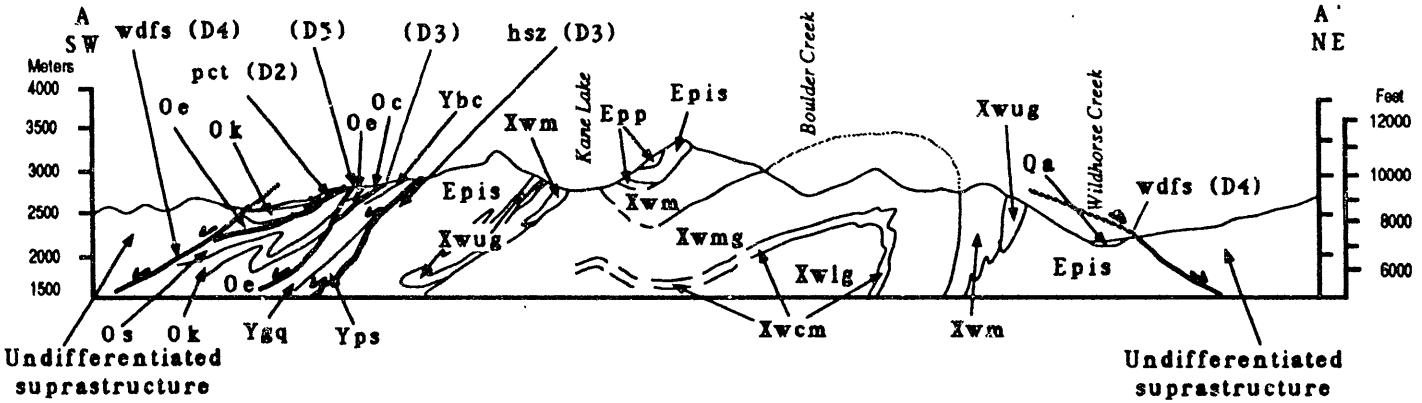
A
SW
A'
NE
Meters
4000
3500
3000
2500
2000
1500
Feet
12000
10000
8000
6000
wdfs (D4)
(D5)
(D3)
hsz (D3)
pct (D2)
Oe
Ok
Oc
Ybc
Xwm
Kane Lake
Epp
Epis
Boulder Creek
Xwug
Qa
Wildhorse Creek
wdfs (D4)
Epis
Xwm
Xwug
Xwmg
Xwlg
Os
Ok
Ygq
Yps
Xwcm
Xwm
Undifferentiated suprastructure
Undifferentiated suprastructure

Figure 2.4

| ROCK UNIT | D1 | D2 | D3 | D4 | D5 |
|---|---|---|---|---|---|
| | | Tc (800K) = 79 ma | Tc (800K) = 46 ma | Tc (675-475K) = 36-33 ma | |
| Eocene Pioneer Intrusive Suite | | | S3: N65°W, 30°SW; L3: S10°W; Late D3 Emplacement | S4: variable; L4: N68W; MM: greenschist facies; brittle D4 superimposed on ductile | Local brittle extension along NE-SW axis of extension |
| Precambrian-Ordovician Hyndman and East Fork Groups | | F2: NW Trend, isoclinal, recumbent Axial Plane SW Dip MM: syn-kinematic amphibolite facies Post F2 Thrust Faults | Pre-PIS emplacment of allochthons; Syn-PIS Hyndman Shear Zone; protomylonite, S3: N65°W, 30°SW; MM: Syn-K: Sill, Cdt; post-K: Garnet | S4: variable; L4: N68W; MM: greenschist facies; brittle D4 superimposed on ductile | Local brittle extension along NE-SW axis of extension |
| Precambrian Wildhorse Gneiss Complex | Cryptic dome & basin interference patterns suggest an early deformation event. | F2: NW Trend, isoclinal, overturned Axial Plane: SW dip MM: syn-kinematic amphibolite facies | F3: Broad megascale folds, NNW-SSE trend; Minor Intraformational Faults | S4: variable; L4: N68W; MM: greenschist facies; brittle D4 superimposed on ductile | Local brittle extension along NE-SW axis of extension |

Figure 2.5

Figure 2.6

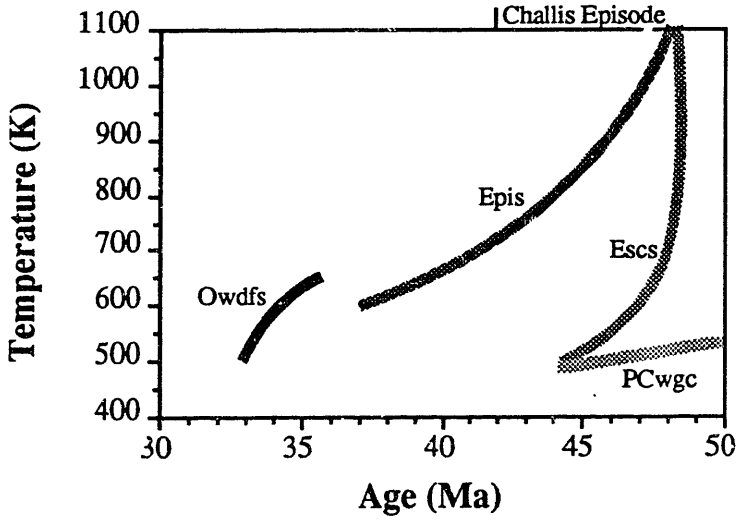
Challis Episode
1100
1000
900
800
700
600
500
400
Temperature (K)
Owdfs
Epis
Escs
PCwgc
30
35
40
45
50
Age (Ma)

Figure 2.7

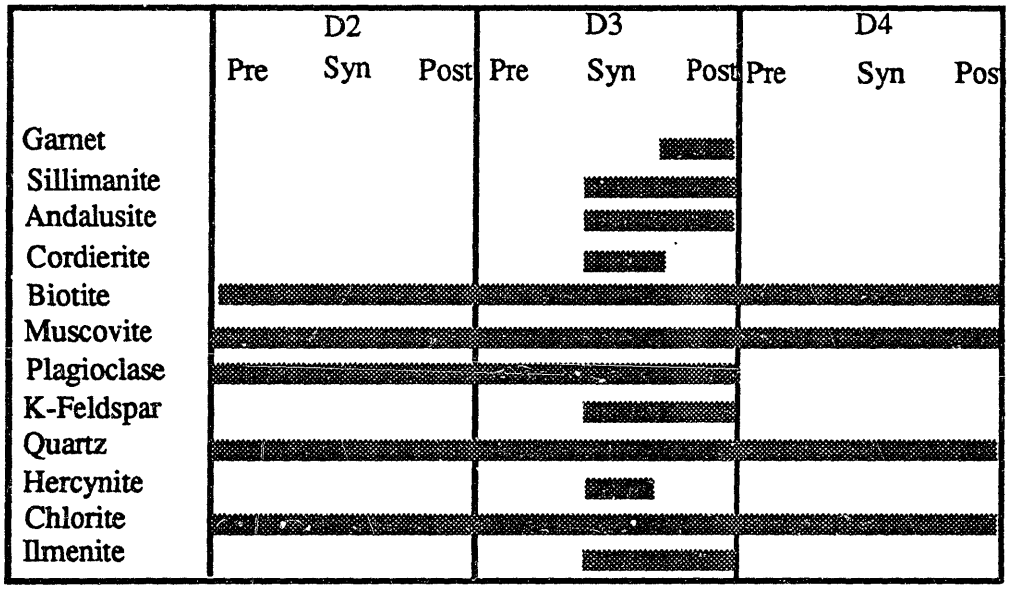
D2
D3
D4
Pre
Syn
Post
Pre
Syn
Post
Pre
Syn
Pos
Garnet
Sillimanite
Andalusite
Cordierite
Biotite
Muscovite
Plagioclase
K-Feldspar
Quartz
Hercynite
Chlorite
Ilmenite

Figure 2.8

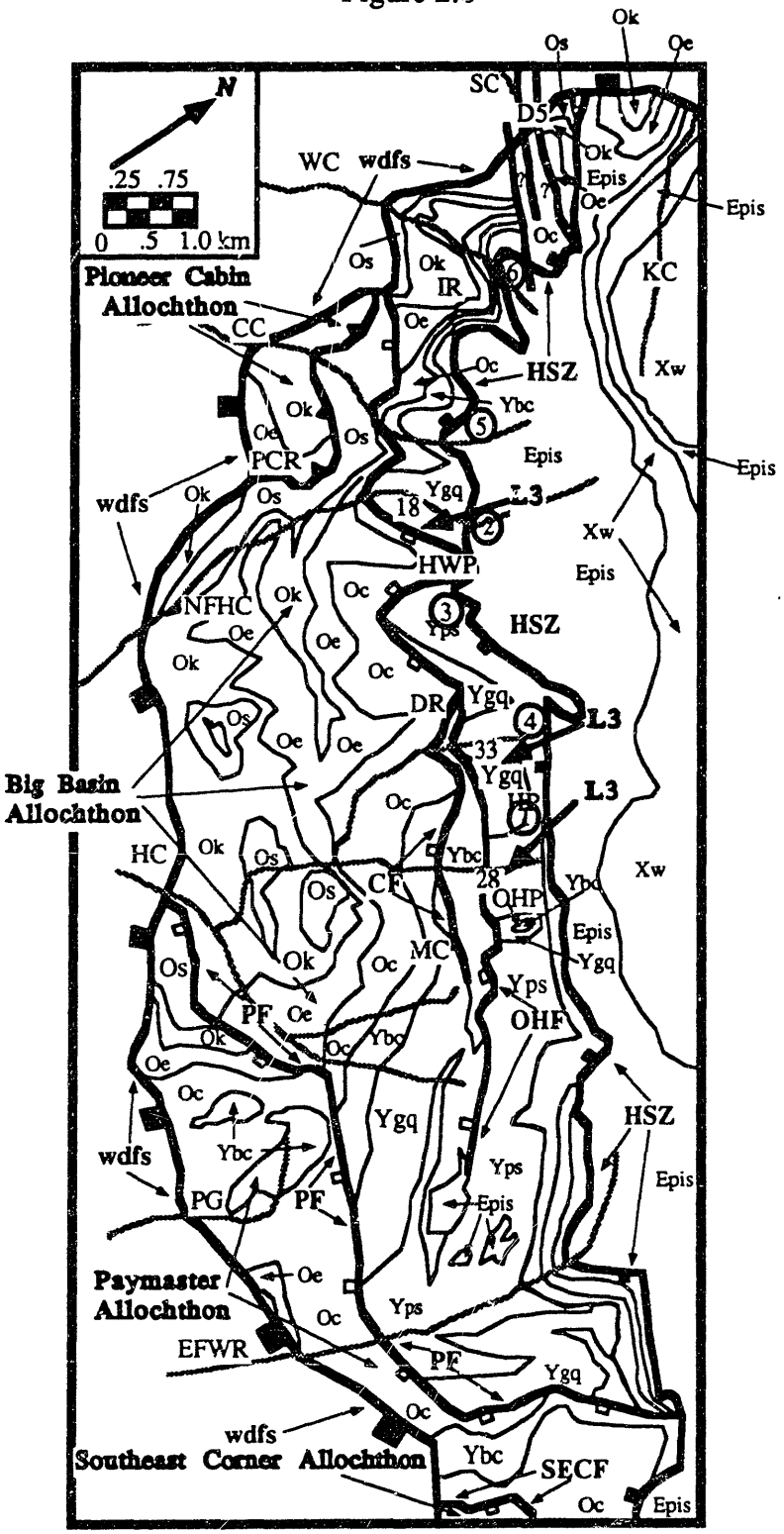
N
.25 .75
0 .5 1.0 km
Pioneer Cabin Allochthon
Big Basin Allochthon
Paymaster Allochthon
Southeast Corner Allochthon
SC
WC
wdfs
CC
PCR
NFHC
HC
PG
EFWR
SECF
IR
HSZ
HWP
DR
CF
MC
OHP
OHF
PF
KC
L3
Os
Ok
Oe
Oc
Epis
Xw
Ygq
Yps
Ybc
D5
18
33
28

Figure 2.9

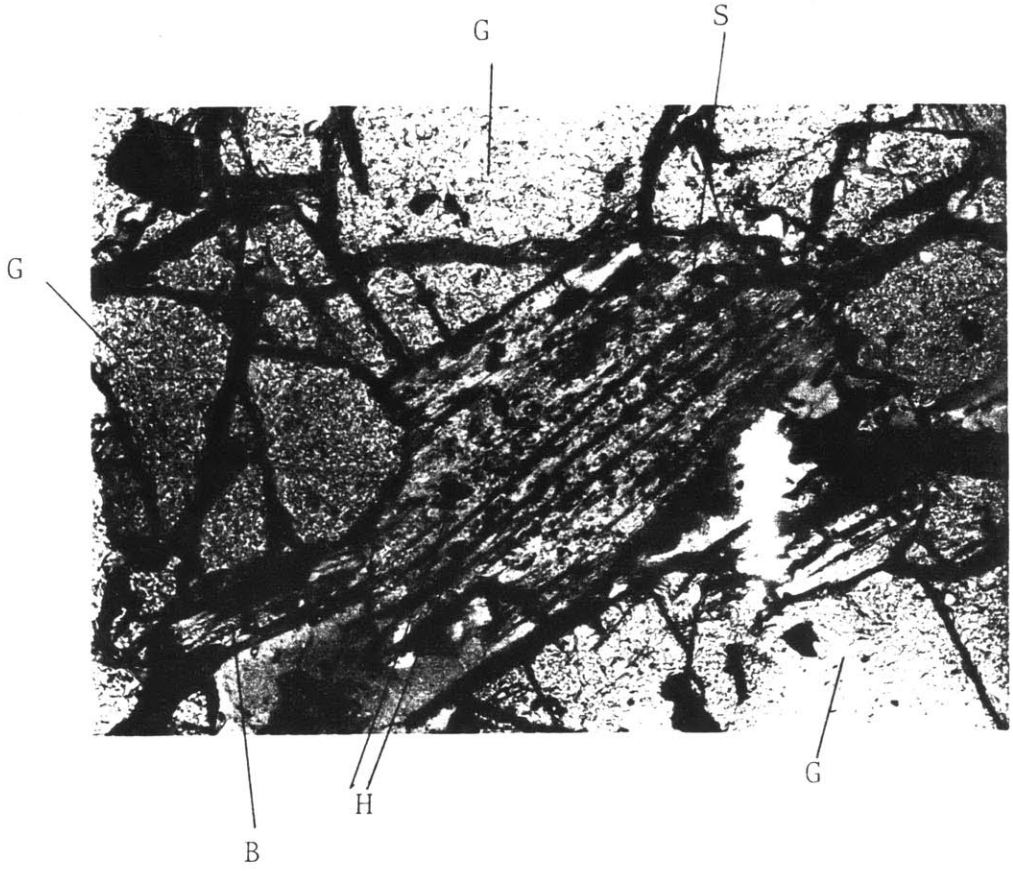

Figure 2.10

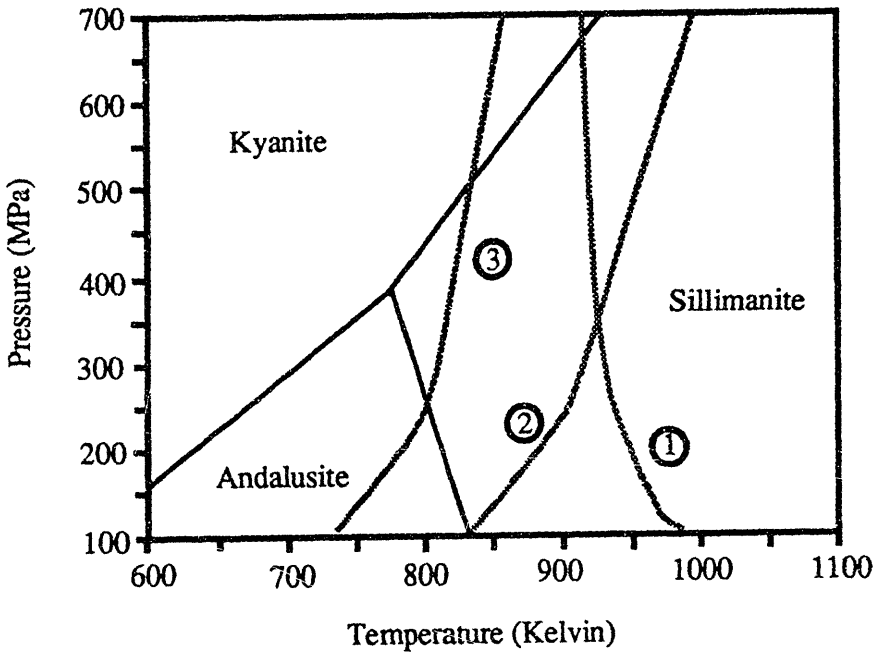
700
600
500
400
300
200
100
Pressure (MPa)
Kyanite
Andalusite
Sillimanite
3
2
1
600
700
800
900
1000
1100
Temperature (Kelvin)

Figure 2.11a

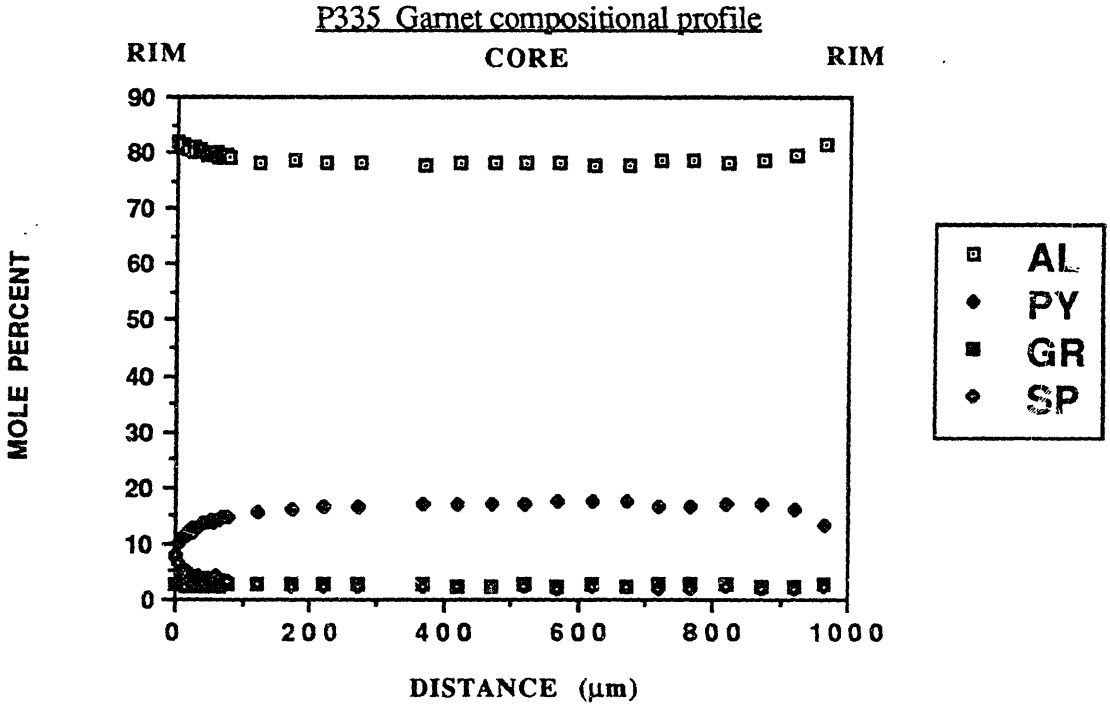
P335 Garnet compositional profile
RIM
CORE
RIM
MOLE PERCENT
90
80
70
60
50
40
30
20
10
0
0
200
400
600
800
1000
DISTANCE (μm)
AL
PY
GR
SP

Figure 2.11b

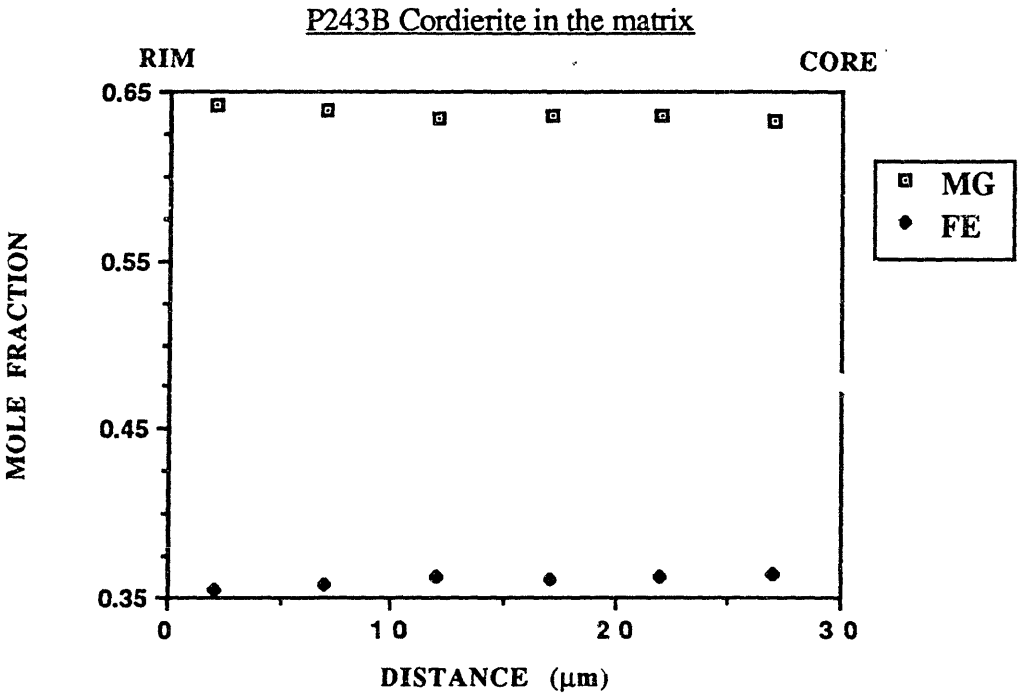
P243B Cordierite in the matrix
RIM
CORE
0.65
0.55
0.45
0.35
MOLE FRACTION
0
10
20
30
DISTANCE (μm)
MG
FE

Figure 2.11c

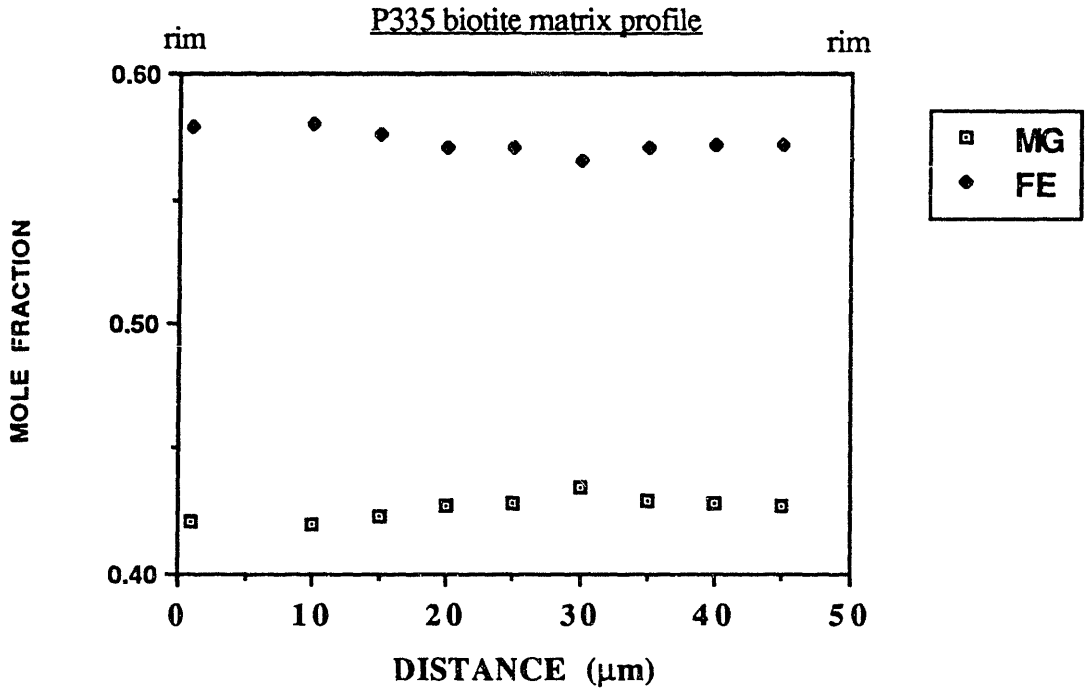
P335 biotite matrix profile
rim
rim
0.60
0.50
0.40
MOLE FRACTION
0
10
20
30
40
50
DISTANCE (μm)
MG
FE

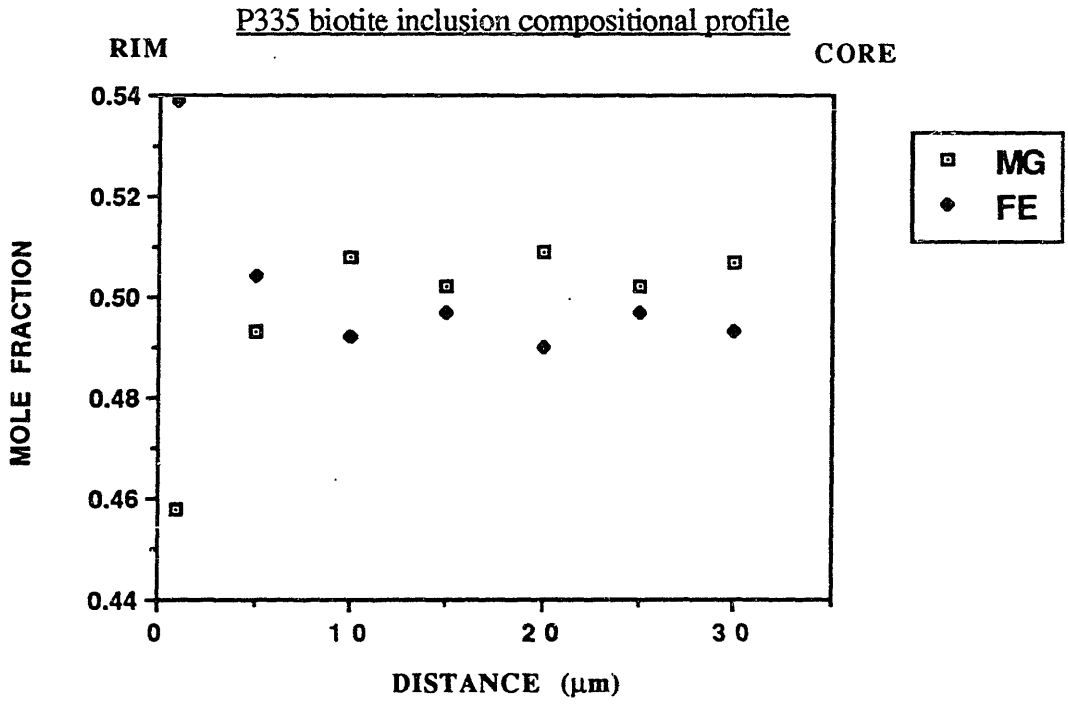
P335 biotite inclusion compositional profile
RIM
CORE
0.54
0.52
0.50
0.48
0.46
0.44
MOLE FRACTION
0
10
20
30
DISTANCE (μm)
MG
FE

Figure 2.11d

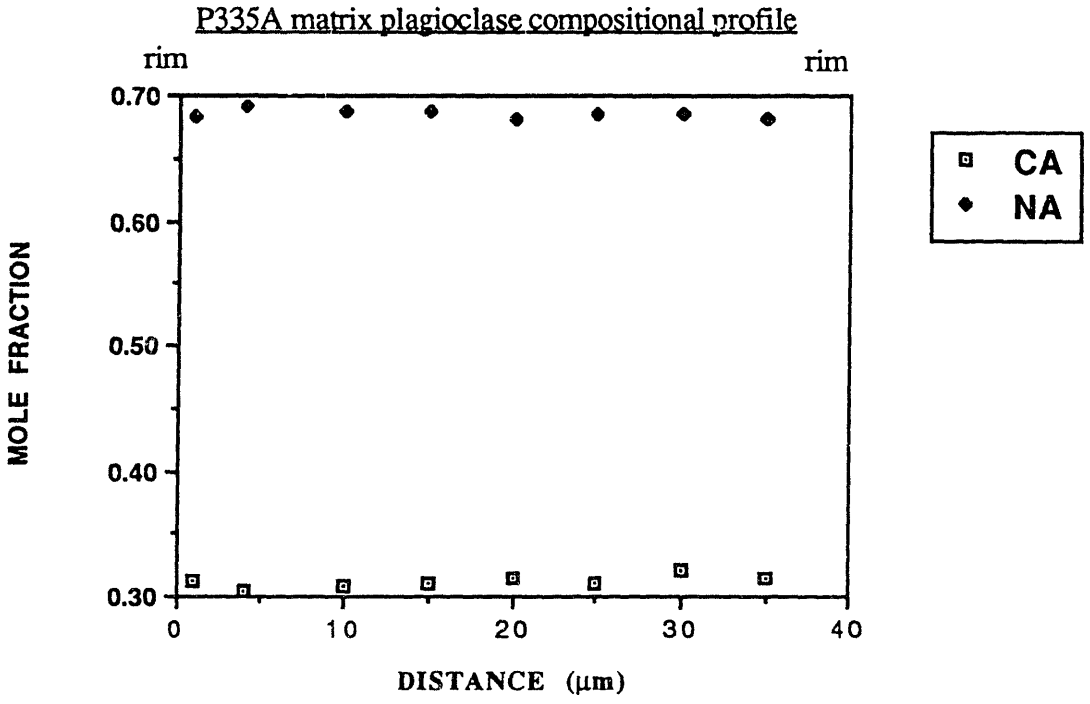
P335A matrix plagioclase compositional profile
rim
rim
0.70
0.60
0.50
0.40
0.30
MOLE FRACTION
0
10
20
30
40
DISTANCE (μm)
CA
NA

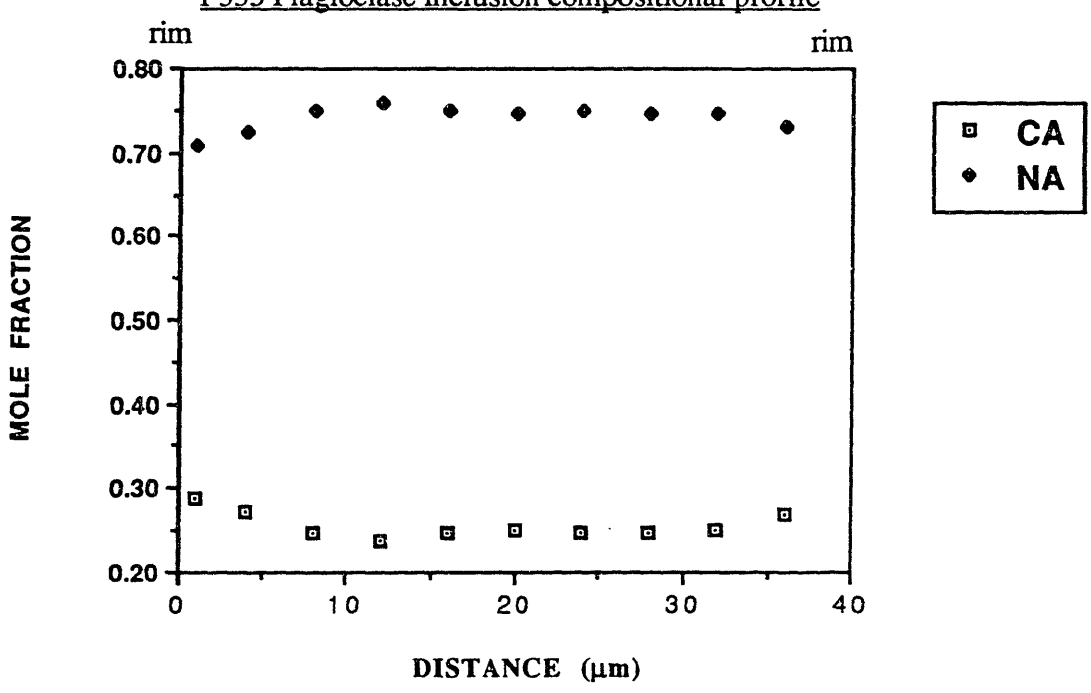
P335 Plagioclase inclusion compositional profile
rim
rim
0.80
0.70
0.60
0.50
0.40
0.30
0.20
MOLE FRACTION
0
10
20
30
40
DISTANCE (μm)
CA
NA

Figure 2.12

P92 plagioclase compositional profile

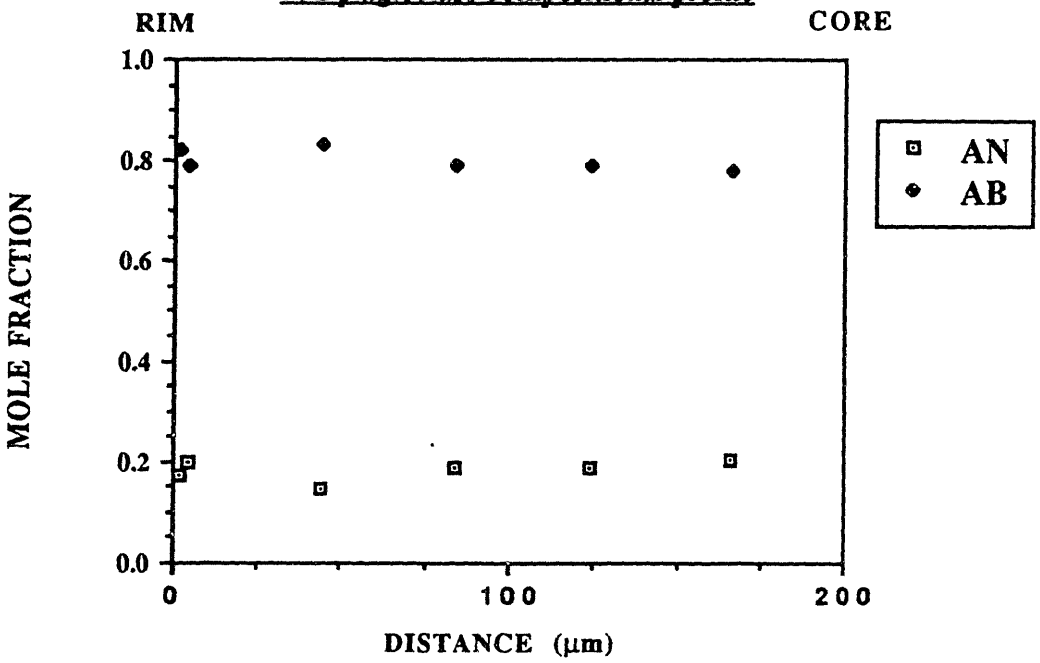


P156 hornblende total Al profile

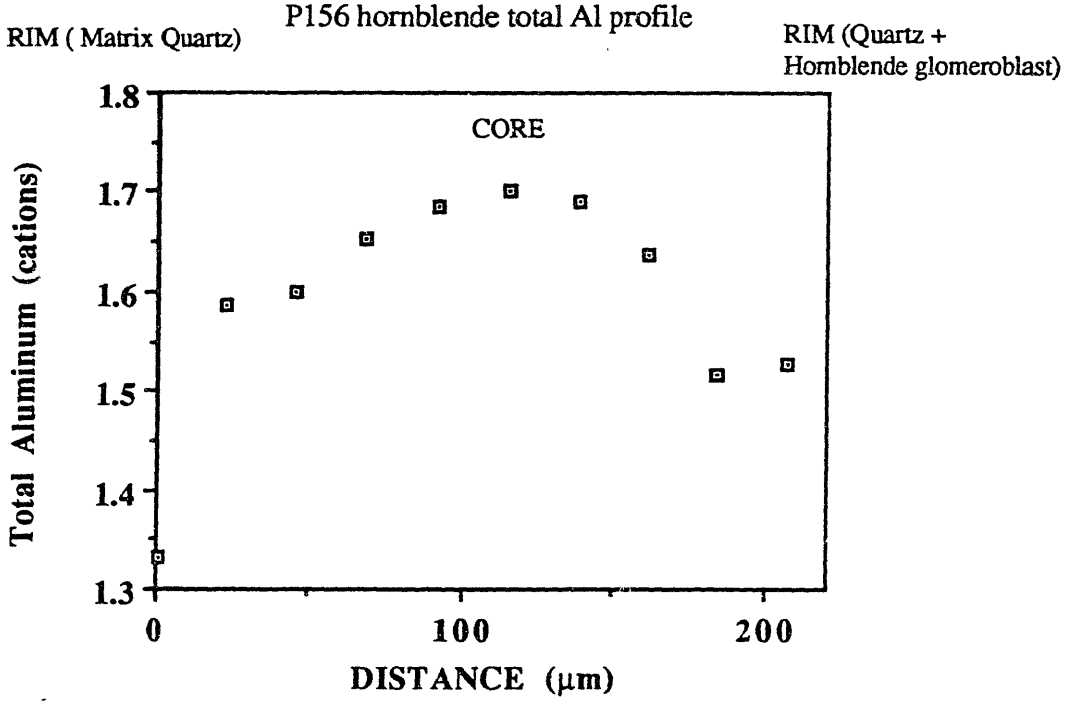

Figure 2.13a

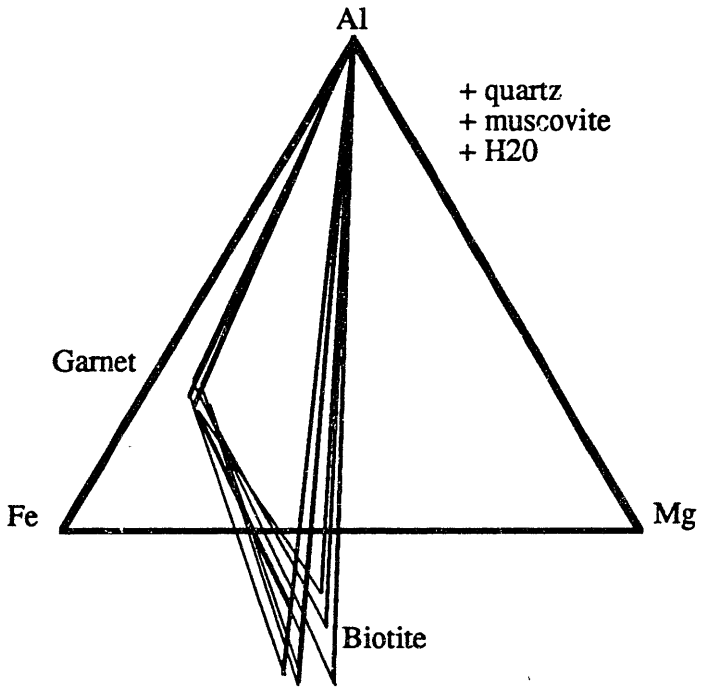

Figure 2.13b

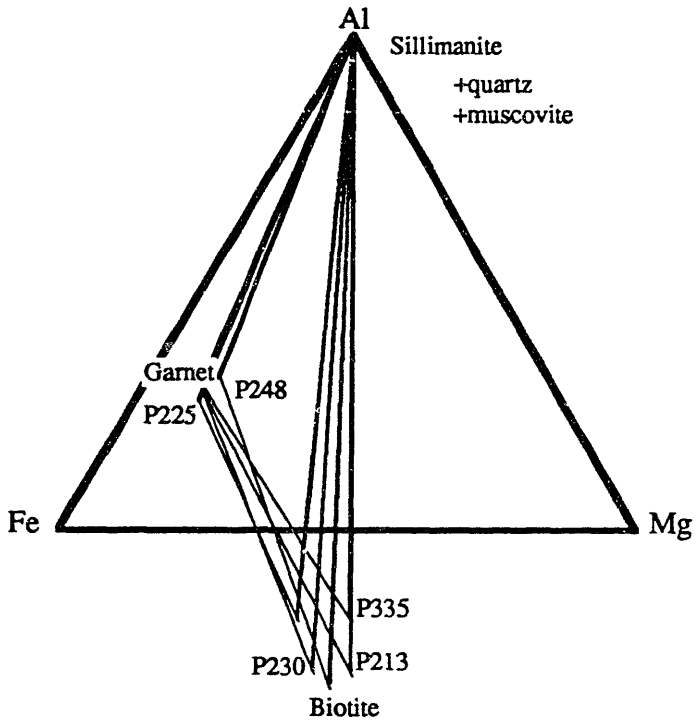
Al
Sillimanite
+quartz
+muscovite
Garnet
P248
P225
Fe
Mg
P335
P230
P213
Biotite

Figure 2.13c

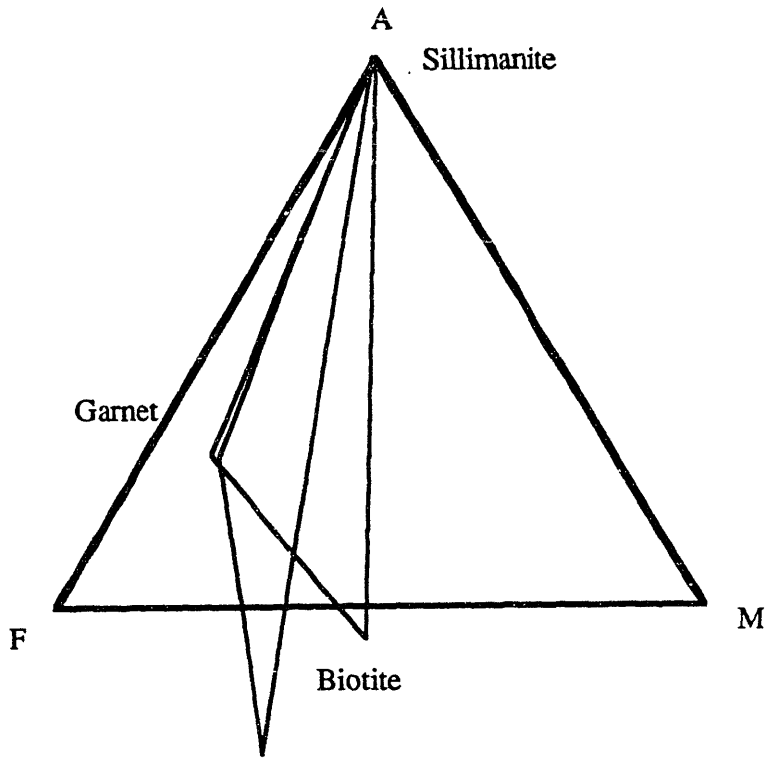

Figure 2.14a

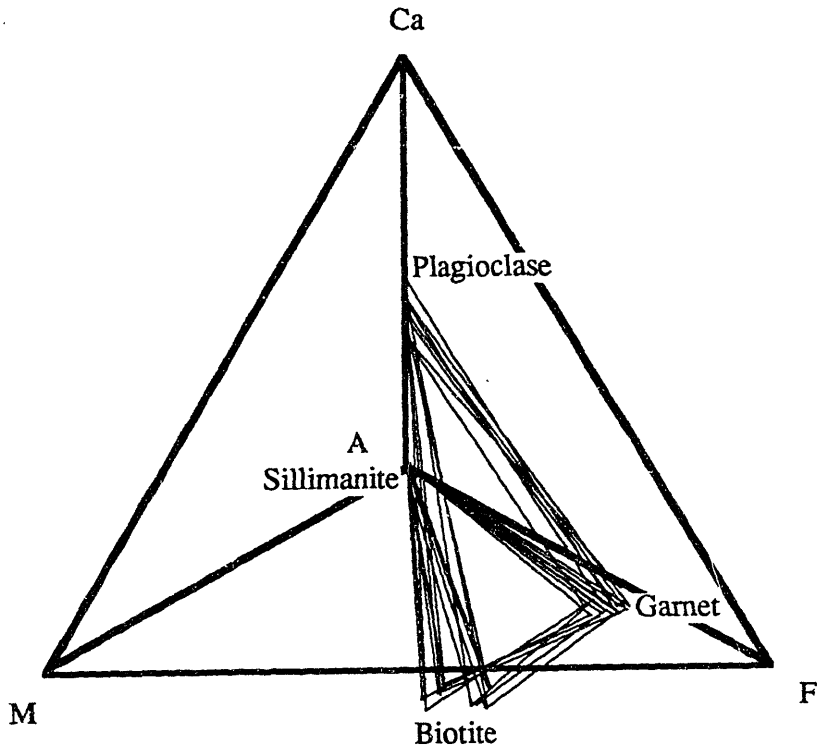

Figure 2.14b

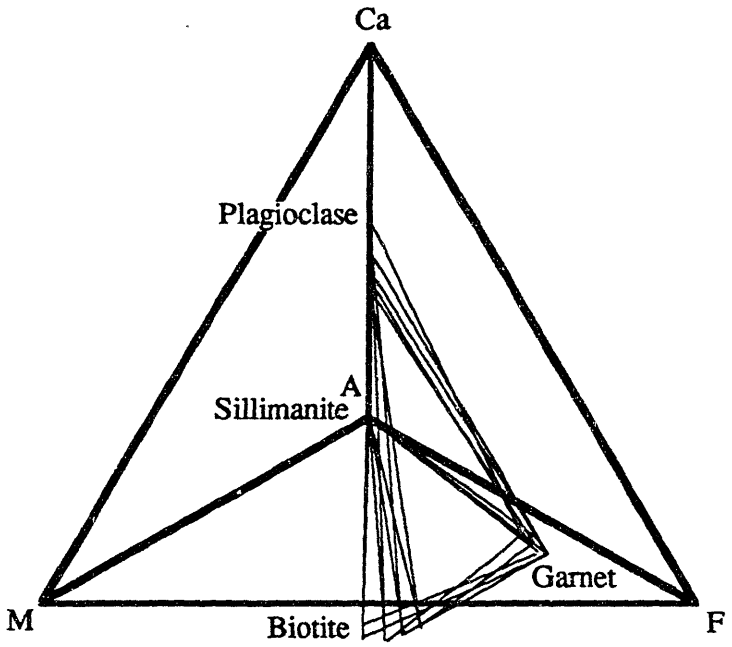


Figure 14b. Garnet inclusion assemblages projected from muscovite+quartz+H2O into the A-F-M-Ca tetrahedra.

Figure 2.14c

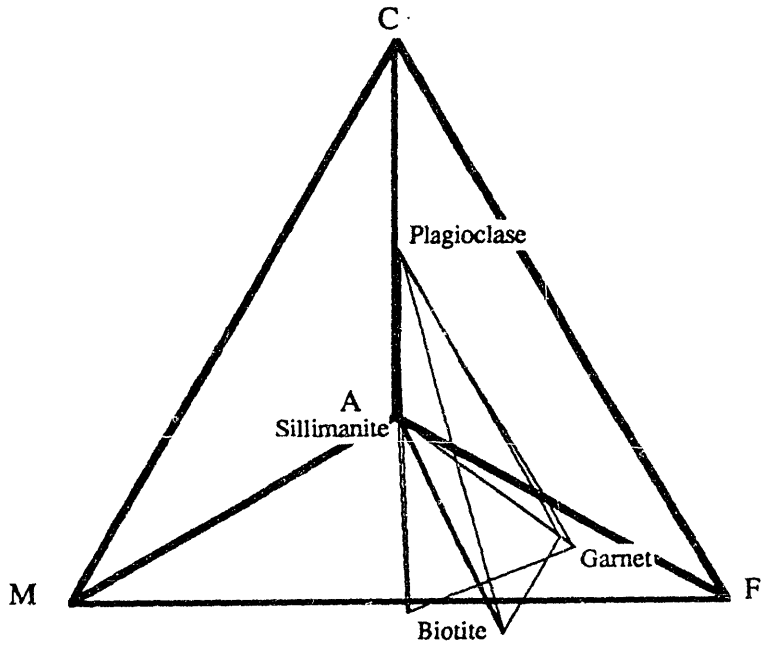


Figure 14c. Xwm phase volumes projected from quartz and muscovite into the A-F-M-Ca tetrahedra.

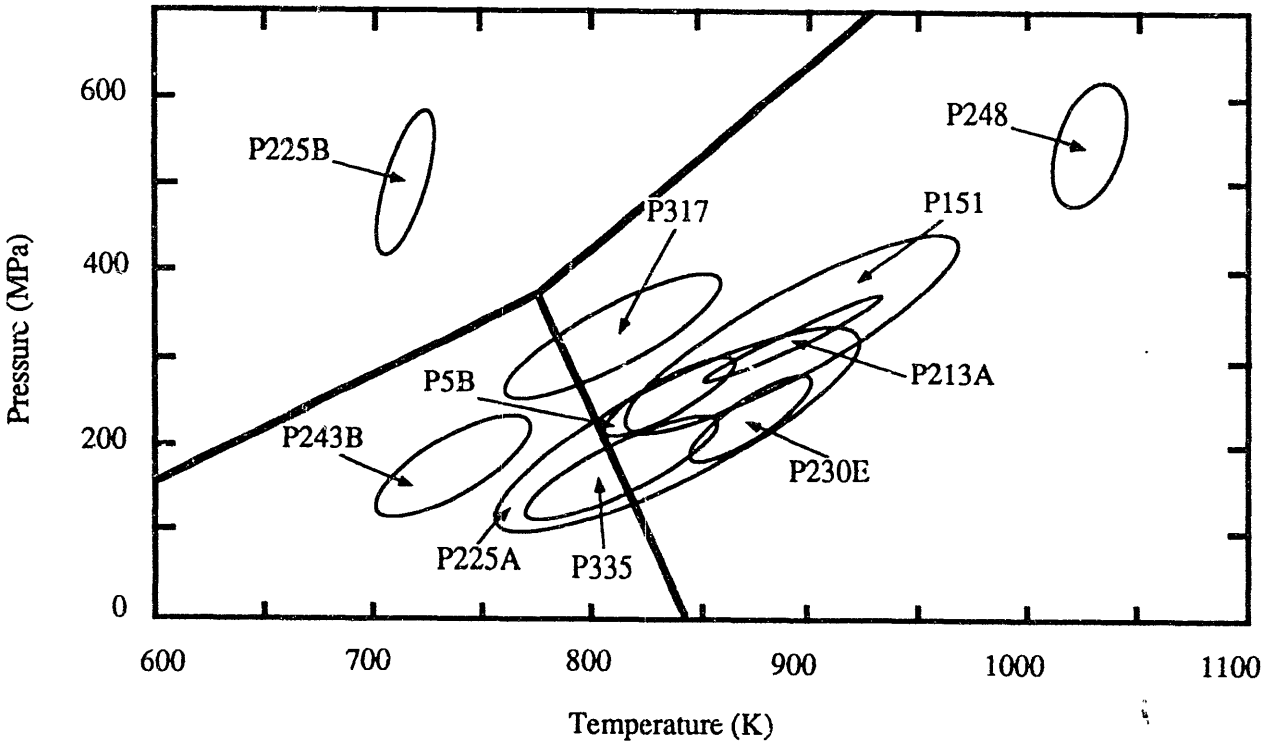
600
400
200
0
Pressure (MPa)
600
700
800
900
1000
1100
Temperature (K)
P225B
P248
P317
P151
P213A
P5B
P243B
P230E
P225A
P335

Figure 2.15

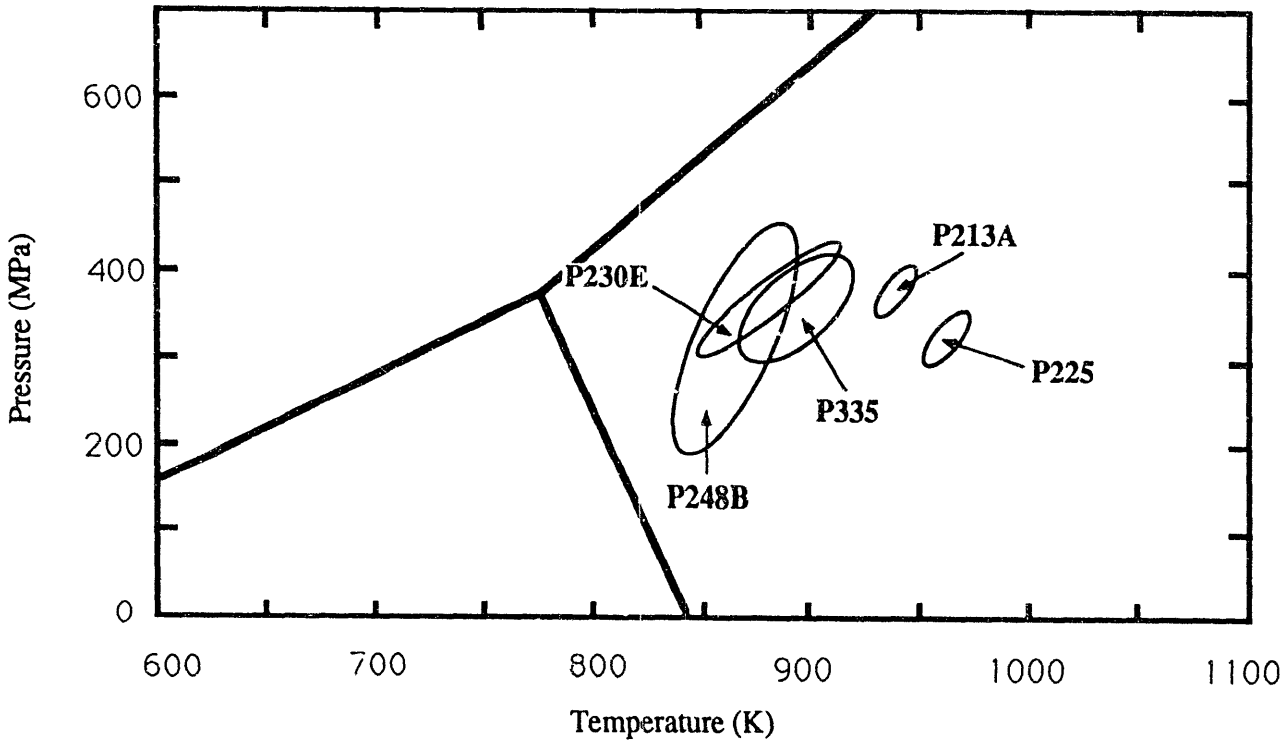
600
400
200
0
Pressure (MPa)
600
700
800
900
1000
1100
Temperature (K)
P230E
P213A
P225
P335
P248B

Figure 2.16

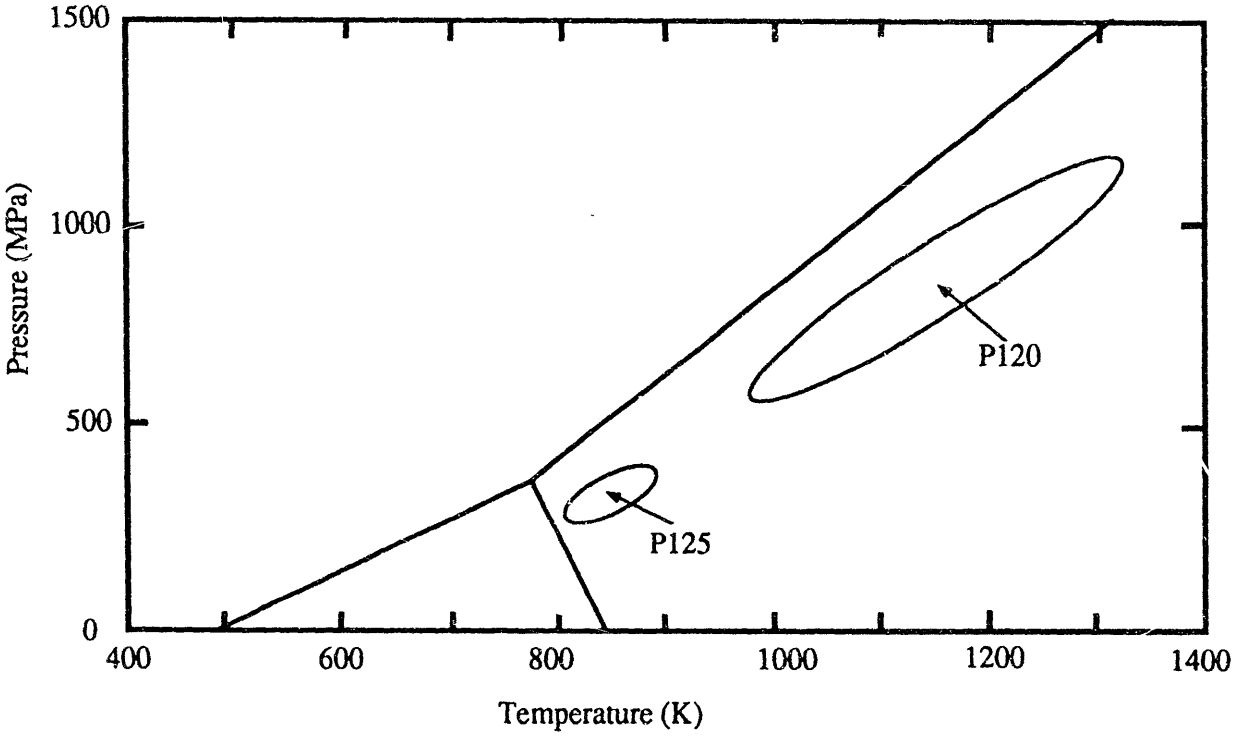
1500
1000
500
0
Pressure (MPa)
400
600
800
1000
1200
1400
Temperature (K)
P120
P125

Figure 2.17

Figure 18

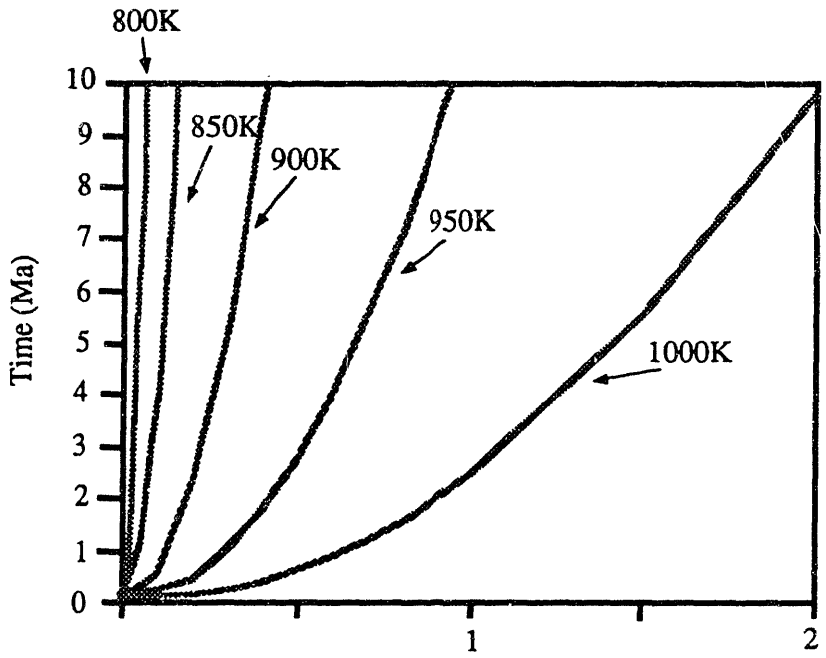
800K
850K
900K
950K
1000K
Time (Ma)
0
1
2
3
4
5
6
7
8
9
10
1
2
Penetration distance (garnet radius in mm)

Figure 2.19

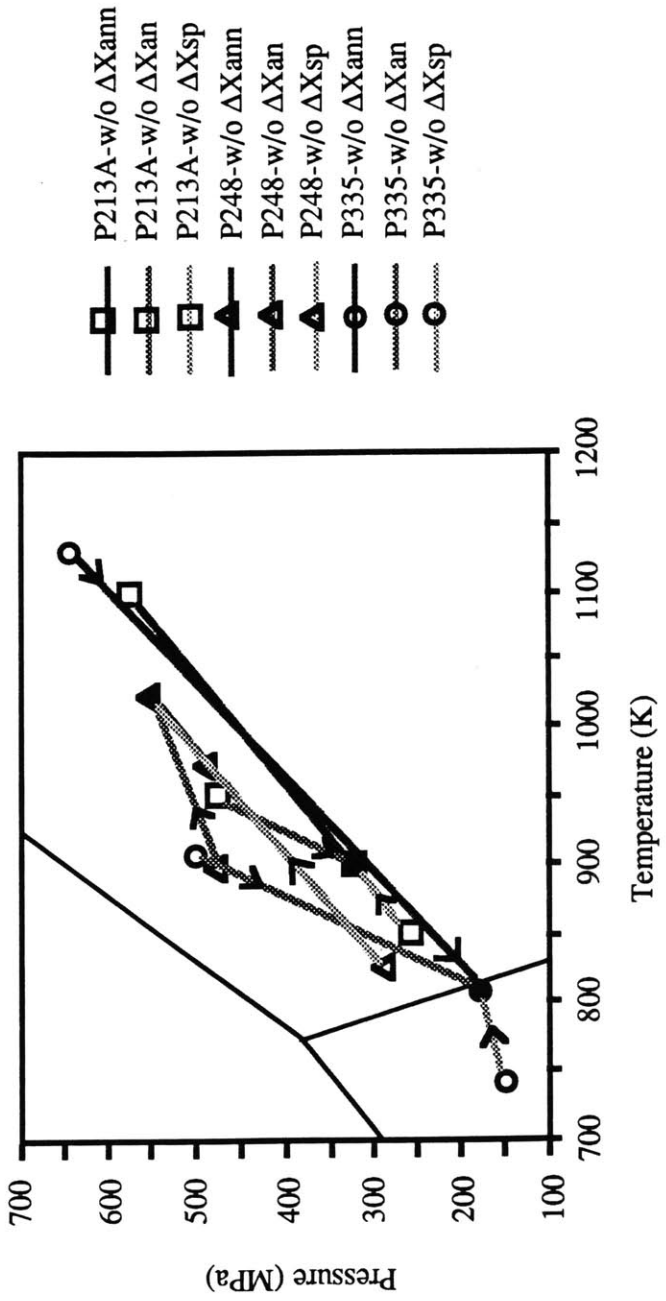
P213A-w/o ΔXann
P213A-w/o ΔXan
P213A-w/o ΔXsp
P248-w/o ΔXann
P248-w/o ΔXan
P248-w/o ΔXsp
P335-w/o ΔXann
P335-w/o ΔXan
P335-w/o ΔXsp
Pressure (MPa)
700
600
500
400
300
200
100
700
800
900
1000
1100
1200
Temperature (K)

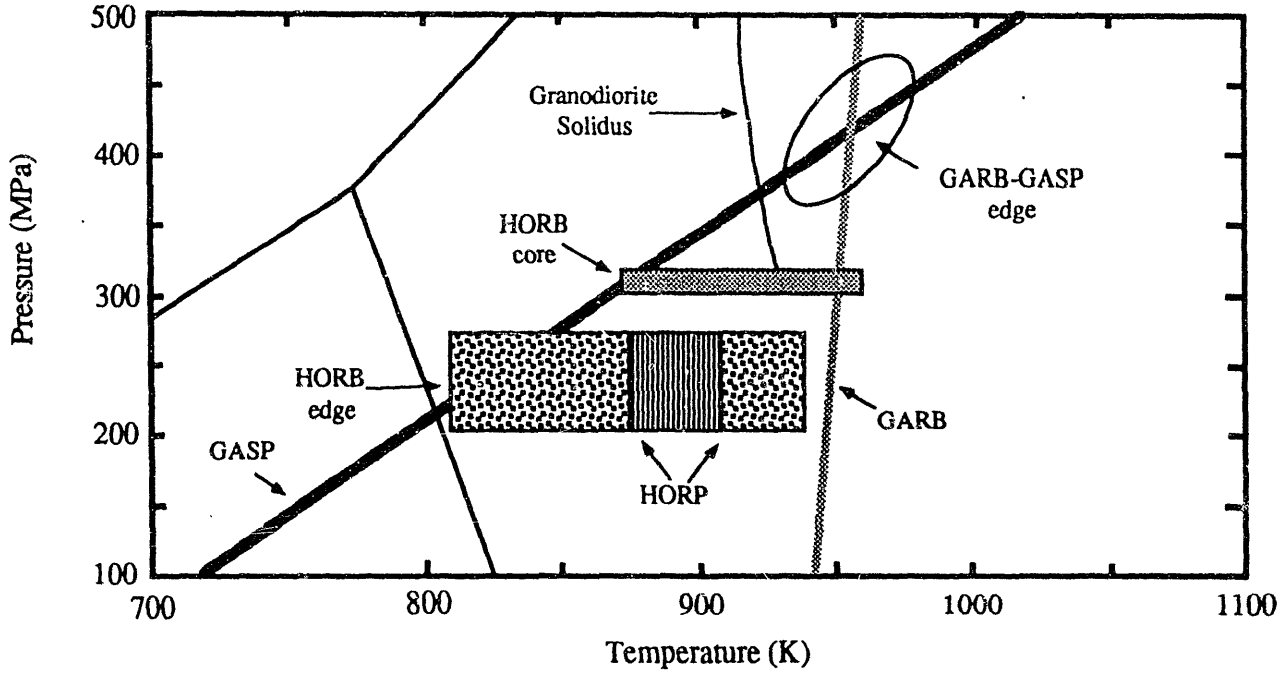
500
400
300
200
100
Pressure (MPa)
700
800
900
1000
1100
Temperature (K)
Granodiorite
Solidus
GARB-GASP
edge
HORB
core
HORB
edge
GASP
GARB
HORP

Figure 2.20

Figure 2.21

a.

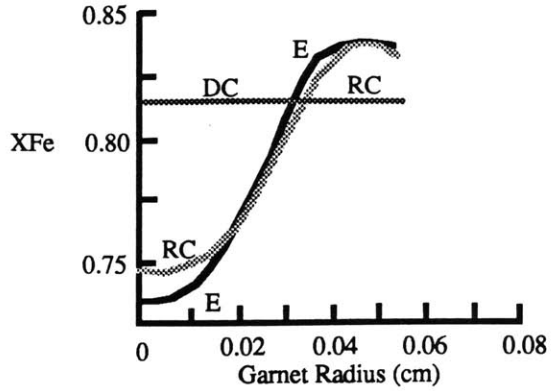


b.

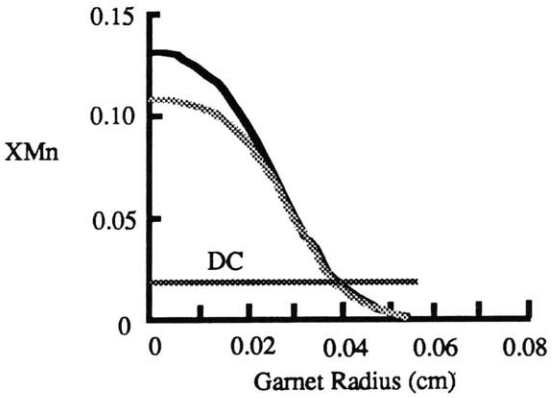


c.

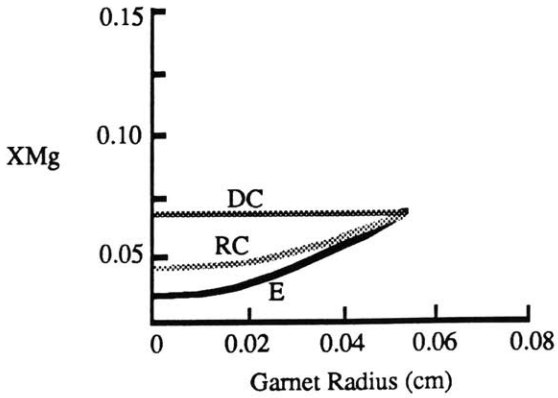

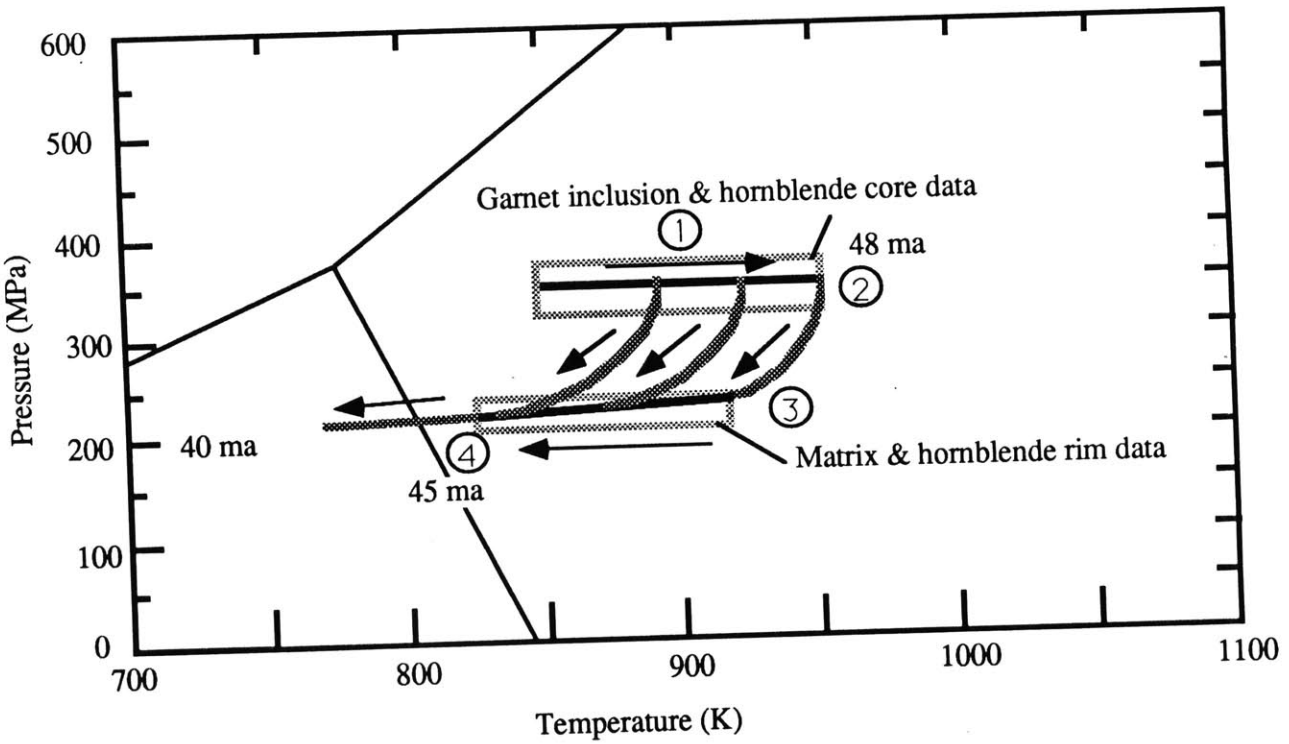
600
500
400
300
200
100
0
Pressure (MPa)
700
800
900
1000
1100
Temperature (K)
Garnet inclusion & hornblende core data
1
48 ma
2
3
4
40 ma
45 ma
Matrix & hornblende rim data

Figure 2.22

# CHAPTER 3: THERMAL EVOLUTION OF THE PIONEER METAMORPHIC CORE COMPLEX, CENTRAL IDAHO; DIACHRONOUS PALEOGENE EXTENSION OF THE MIDDLE CRUST.

D.S. Silverberg & K.V. Hodges

Department of Earth, Atmospheric and Planetary Sciences,

Massachusetts Institute of Technology,

Cambridge, Massachusetts 02139

M. Kunk & J. Sutter

United States Geologic Survey

National Center Stop 981, Reston, Virginia 22092

Abstract

New $^{40}Ar$-$^{39}Ar$ data from the Pioneer Metamorphic Core Complex, south-central Idaho, constrains three distinct temperature-time paths which are associated with a mid-Cretaceous compressional event , an Eocene extensional-magmatic event, and an Early Oligocene extensional event.

The minimum age of mid-Cretaceous dynamo-thermal metamorphism in the footwall of the core complex is constrained by a hornblende plateau date indicating cooling below roughly 800K at 79 Ma. This is consistent with the regional heating and deformation associated with emplacement of the Idaho Batholith, and with $^{40}Ar$-$^{39}Ar$ cooling dates from the Albion Mountains metamorphic core complex, southern Idaho, and suture zone rocks associated with the Seven Devils Arc Terrane.

The emplacement of the Pioneer Intrusive Suite (54-48 Ma) at a depth of 11-13 km was contemporaneous with the Challis Episode in this area (54-42 Ma) and largely post-dates a south-directed extensional episode. The cooling curves of the Pioneer Intrusive Suite and its metamorphosed country rock are coincident. Significant lateral thermal gradients in the mid-crust are suggested by the preservation of pre-Cenozoic hornblende cooling ages and a K-feldspar age of 44 Ma within the footwall and away from the Pioneer Intrusive Suite. The data suggests a time-integrated unroofing rate of 1.5 km/million years from 48 Ma to 45 Ma. This could be a result of a rapid erosion-controlled unroofing mechanism or some amount of tectonic unroofing.

Ductile deformation in the Wildhorse Detachment Fault System is early Oligocene in age. Muscovite (36 Ma), biotite (35 Ma) and K-feldspar (33 Ma) from mylonites are reset by shear heating, advection of hot fluids and/or dynamic recrystallization. The rapid cooling of shear zone rocks (50°/m.y.) suggests that tectonic denudation with incumbent

conductive cooling controls the low-temperature thermal evolution of the infrastructure of the complex.

## Introduction

The initiation of extension in the hinterland of the Sevier-Laramide Orogenic Belt ranges from Early Eocene in the north to Early Miocene in the south (Armstrong, 1982). Extension in this region has created tectonic phenomena known as metamorphic core complexes [Armstrong, 1974; Coney, 1984; Wernicke, 1981], which are typified by detachment fault systems that juxtapose an unmetamorphosed hanging wall (the suprastructure) and a complex of igneous and metamorphic tectonites in the footwall (the infrastructure). The detachment fault systems commonly superimpose extension-related fabrics on pre-extensional polyphase tectonites of the infrastructure. Structural studies of metamorphic core complexes have shown non-coaxial laminar flow in restricted zones of shear to be the dominant deformation mechanism in the ductile portion of detachment fault systems [Lister and Davis, 1989]. The footwall paleodepth at the onset of extension in many core complexes of the central latitude zone of the Cordilleran extensional corridor has been constrained to be a minimum of 10-15 km [Hodges, 1988]. Thus, the crystalline and metamorphic rocks that comprise the footwall offer an opportunity to examine the thermal evolution of the ductile mid-crust and to place significant tectonic events in both an absolute and a relative temporal framework.

The Snake River Plain in southern Idaho has been interpreted as a geologic province that separates Eocene extension to the north from Oligocene-Miocene extension to the south (Figure 1). Parrish et al., [1985] have demonstrated Early Eocene extension in the southern Shuswap Complex of southeastern British Columbia. The Priest River (Spokane Dome), Kettle and Lincoln Metamorphic Core Complexes appear to have cooled below the closure temperature for diffusion of argon in biotite (roughly 575 K; McDougall and Harrison, 1988) by 50 Ma [Miller and Clark, 1976]. Rhodes and Hyndman [1988] have interpreted these cooling dates to result from tectonic and erosional denudation associated

with crustal extension. The Okanogan Complex in northeastern Washington contains 52 million year old porphyry dikes that intrude their mylonitic host rock and are themselves mylonitized [D. Parkinson, personal communication, in Hansen and Goodge, 1988]. In addition, the 48 million year old Coyote Creek Pluton in the Okanogan Complex contains incipient mylonitic shear zones associated with extensional deformation [Atwater, 1985]. Thus, it appears that extensional deformation north of 48°N latitude is predominantly an Early to mid Eocene event. It has been proposed that extension between the Lewis and Clark Line and the Snake River Plain was largely related to movement in the "Trans-Challis Fault System" [Bennett, 1986]. Active displacement in this fault system was contemporaneous with extrusion of the Challis Volcanics that range in age from 43.0±1.3 to 50.4±1.8 Ma [Armstrong, 1975]. Garmezy and Sutter [1983] have demonstrated that mylonitization in the Bitterroot Mylonite Zone began at 45.5 Ma and continued for roughly 2 million years.

To the south of the Snake River Plain, in the northeastern Great Basin, the Albion-Raft River-Grouse Creek Metamorphic Core Complex offers the most northerly exposure of mid-crustal rocks. Saltzer and Hodges [1988] have shown that tectonic denudation in the northwest part of the complex resulted from top-to-the-west extensional shear. The associated mylonitic structures are superposed on 29±3 million year old granitic rocks of the Almo Pluton [Armstrong, 1976] and the K-Ar and fission track cooling dates of metamorphic minerals in the affected areas are Oligocene and Miocene [Armstrong, 1975; Salzter and Hodges, 1988; Snoke and Miller, 1988]. Similar temporal relations exist in the Grouse Creek Mountains where extension-related mylonitic structures are present in the Red Butte Canyon quartz monzonite pluton that is dated at 24.9±0.6 Ma [Rb-Sr whole-rock isochron; Compton et al., 1977].

The only exposure of mid-crustal rocks between the Bitterroot Mylonite Zone and the Albion-Raft River-Grouse Creek Metamorphic Core Complex lies in the footwall of the Pioneer Metamorphic Core Complex, north of the Snake River Plain in south central Idaho. It has been proposed that ductile and brittle extension of the crust in this area was related to Eocene movement on the Trans-Challis Fault System [O'Neill and Pavlis, 1988]. Alternatively, Wust[1986] has noted post-Challis brittle deformation associated with the Wildhorse Detachment Fault System, the principal structure that separates the suprastructure from the infrastructure. Unfortunately, there have been few data available to constrain the absolute age of extensional faulting in this area. In addition, the temporal relations among deformation, magmatism, and metamorphism in the infrastructure were poorly understood. The infrastructure displays a variety of cross-cutting relationships that are punctuated by the intrusion of magmatic rocks. The widespread occurence of numerous potassium-bearing phases in footwall rocks provides an opportunity to date ductile extension at mid-crustal levels and to compare the cooling curves of different structural positions in the footwall. The $^{40}Ar$-$^{39}Ar$ data presented here constrains the age of plutonic, metamorphic and deformational events in the footwall of the Pioneer Metamorphic Core Complex. The thermal history of the footwall appears to be complex and suggests that the topology of temperature-time curves can constrain the absolute timing of tectonic events as well as suggest the mechanism of unroofing.

## Geologic Setting

The Pioneer Metamorphic Core Complex is a product of Cenozoic extension superimposed on a structural culmination associated with emplacement of the westernmost allochthons of the central Idaho thrust belt. The Pioneer Mountains lie in the eroded highland of the Devonian-Mississippian Antler orogenic belt and the hinterland of the

Jurassic-Cretaceous Sevier/Laramide orogenic belt. Dover [1969, 1981, 1983] generated the first regional geologic map of the area and divided the suprastructure nappe complex into four allochthonous units (Figure 2). These unmetamorphosed units have been interpreted by Skipp [1987] to be part of three regional thrust plates: (1) the Milligan-Wood River-Grand Prize thrust complex [Hall, 1986], (2) the Copper Basin plate [Skipp and Hait, 1977], and (3) the Phi Kappa plate [Dover, 1981]. Tertiary granodiorite-quartz monzonite stocks intrude these units near the Pioneer Mountains. These include the Summit Creek Stock, the North Fork Dike Complex and the Sawtooth Batholith.

The infrastructure of the Pioneer Metamorphic Core Complex comprises an approximately 18 km by 14 km domal structure. It is composed of high-grade metamorphic rocks and Early Tertiary intrusives that are juxtaposed by the Wildhorse Detachment Fault System against the four allochthons mentioned above and Eocene volcanic rocks of the Challis suite. Rocks within the window include (Figure 3): (1) Proterozoic (?) marbles and quartzofeldspathic, psammitic, and amphibolitic gneisses of the Wildhorse Gneiss Complex; (2) metapelites, quartzites, metaconglomerates, and calc-silicate gneisses of the upper Precambrian-Ordovician(?) Hyndman Group; unconformably overlain by (3) marbles and quartzites of the Ordovician East Fork Group. Fossil control is restricted to the East Fork Group in which crinoid stems have been identified as mid-Ordovician in age [Dover, 1981]. At least two episodes of apparent compressional folding are evident in the Wildhorse Gneiss Complex ($D_1$ and $D_2$), whereas the Hyndman and East Fork Groups display evidence of only a single penetrative folding event ($D_2$). $D_2$ thrust faults and $D_3$ extensional faults have resulted in a series of allochthons that overlie the parautochthonous Wildhorse Gneiss Complex (Figure 5).

The Pioneer Intrusive Suite separates the Wildhorse Gneiss Complex from the Hyndman and East Fork Groups. It ranges from pyroxenites to quartz diorites to

clinopyroxene-hornblende-biotite granodiorites to hornblende-biotite quartz monzonites. The Pioneer Intrusive Suite was emplaced at the 11-13 km depth level and was the heat source for a low-pressure/high-temperature metamorphism in rocks of the Hyndman and East Fork Groups [Silverberg, in preparation]. Metamorphic grade in the Hyndman and East Fork Groups increases toward the contact with the Pioneer Intrusive Suite; metamorphic grade drops off to upper greenschist facies in the East Fork Group at distances greater than 4 kilometers from the Pioneer Intrusive Suite. In general, characteristic high-temperature phases are post-kinematic with respect to $D_1$ and $D_2$, and syn- to post-kinematic with respect to $D_3$ (Figure 6). Reaction isograds largely transect $D_3$ extension-related structures, with the exception of synkinematic metmaorphism in the Hyndman Shear Zone. Inclusion assemblages in garnetiferous pelitic rocks of the Hyndman Group suggest that the temperature exceeded roughly 950 K at paleodepths of roughly 11-13 kilometers.

Extension-related structures in the Pioneer Metamorphic Core Complex are diachronous and non-coaxial. A sequence of $D_3$ extensional sheets comprise the Paymaster and Southeast Corner Allochthons. Regional $D_1$ and $D_2$ fold structures within the allochthons are crosscut by $D_3$ extensional faults; $D_3$ fault fabrics are largely recrystallized due to late-kinematic emplacement of the Pioneer Intrusive Suite. The Hyndman Shear Zone, late-$D_3$, is a normal-sense shear zone that affects the Pioneer Intrusive Suite and separates the Wildhorse Gneiss Complex in the footwall from the Big Basin, Paymaster and South East Corner Allochthons in the hanging wall. Shear-related fabrics are developed best along the margins of the intrusives. This suggests that emplacement of the Pioneer Intrusive Suite was accompanied by late-$D_3$, top-to-the south sense of shear in the Hyndman Shear Zone [Silverberg, in preparation]. The final equilibration of pelitic schists in the Hyndman Shear Zone occurred at 815-855 K and 215-240 MPa (roughly 7.5-8.4 km

paleodepth). Thus the decompressional pressure-temperature path has a nominal slope of 1.3 MPa/Kelvin. This implies roughly 4.4 km of unroofing.

The window-bounding Wildhorse Detachment Fault System ($D_4$) [Wust, 1986; O'Neill and Pavlis, 1988; Silverberg, in preparation] cross-cuts all compression-relelated structures ($D_1$ and $D_2$) and the $D_3$ Hyndman Shear Zone extension fabrics; S-C fabrics [Lister and Snoke, 1984], quartz fabrics [Schmidt and Casey, 1986] and lineations suggest a top-to-the-WNW sense of shear [Silverberg, in preparation]. Where the ductile portion of the Wildhorse Detachment Fault System cross-cuts rocks of mafic composition, biotite and hornblende are variably chloritized, and feldspars display moderate sericitization. The style of deformation and stabilization of chlorite suggests that physical conditions attendant to mylonitization were characteristic of the greenschist facies. Deformation in the Wildhorse Detachment Fault System progressed temporally from ductile to brittle. $D_5$ normal faults strike northwest and have strictly brittle deformation. Little offset has been observed on these late faults, which may be associated with neotectonic processes.

## Previous Geochronology

Reconnaisance geochronology studies in the Pioneer mountains have been made by Zartman [unpublished] and Armstrong [1975, 1976] (Table 1; all ages reported at 2-sigma precision). Their results placed important constraints on the age of some intrusive units and deformational events, and suggested ways in which detailed $^{40}Ar$-$^{39}Ar$ thermochronology could improve our understanding of the thermal evolution of the infrastructure.

### *Metamorphic Tectonites of the Wildhorse Gneiss Complex*

Paragneisses and orthogneisses of the Wildhorse Gneiss Complex give Rb-Sr whole-rock model ages of 1480±30 Ma and 1290±90 Ma respectively [Zartman, unpublished], with an assumed initial $^{87}Sr/^{86}Sr$ of 0.703. Without independent constraints on the actual initial ratio, the significance of these model ages is uncertain beyond clearly suggesting Precambrian ages [Zartman, personal communication, 1988].

Armstrong [1976] determined a K-Ar age of 42.2±1.3 Ma for biotite from a gneiss sample of the Wildhorse Gneiss Complex. This age is considerably younger than the Rb-Sr model ages, suggesting a Tertiary thermal event.

*Metamorphic Tectonites of the Hyndman Group*

Armstrong [1976] determined three K-Ar biotite ages for samples of the pelitic schist formation of the Hyndman Group. These ages range from 36.2±1.1 to 43.7 ±1.3 Ma, suggesting either significant lateral thermal gradients during mid-Tertiary cooling and/or variable components of excess argon.

*Pioneer Intrusive Suite*

Zartman [unpublished] obtained U-Pb data for four zircon fractions from a quartz monzonite sample of the Pioneer Intrusive Suite collected near the contact with the Wildhorse Gneiss Complex in Wildhorse Canyon. The data yielded a linear array on a concordia diagram with a lower intercept of 48.3±0.6 Ma and a poorly constrained Precambrian upper intercept. Zartman [personal communication, 1988] interprets the lower intercept age to record the time of intrusion of this phase of the Pioneer Intrusive Suite, and suggests that the upper concordia intercept indicates a component of inherited Archean zircon, possibly derived from the underlying basement rocks.

Zartman [unpublished] also determined two K-Ar hornblende ages from granodiorite and quartz monzonite samples of the Pioneer Intrusive Suite, 65.9±1.6 and 52.6±1.3 respectively. These discordant cooling ages could either represent temporal diachroneity in cooling of the mafic and felsic phases or excess argon. In addition, a separate of biotite from the same quartz monzonite sample yielded a K-Ar age of 40.2±1.0 Ma.

Armstrong [1975] used the K-Ar method to obtain ages of 44.7±1.3 Ma and 46.0±1.4 Ma on biotites from quartz monzonite. Armstrong [1976] also obtained a 38.3±1.1 Ma age for a biotite from a dioritic gneiss. The discordance in ages probably reflects excess argon.

*Summit Creek Stock*

Zartman [unpublished] used the Rb-Sr method to obtain a whole rock-plagioclase-microcline-biotite isochron age of 48.5±3.8 Ma for a sample from the north side of Summit Creek, 3.5 miles NE of Trail Creek Summit (Figure 2). The isochron age records the time of intrusion of the Summit Creek Stock. Within the limits of analytical uncertainty it is not possible to distinguish between the age of the Summit Creek Stock and the quartz monzonite phase of the Pioneer Intrusive Suite.

Zartman [unpublished] also obtained a 48.5±2.0 Ma K-Ar age for hornblende from the same sample. The age falls within the uncertainty of the Rb-Sr isochron age suggesting rapid cooling following emplacement.

Armstrong [1975] determined a K-Ar biotite age of 45.3±1.4 Ma for a sample from the Summit Creek Stock. This age also falls within the analytical uncertainty of Rb-Sr isochron age and supports the interpretation that rapid cooling followed emplacement of the Summit Creek Stock.

*Challis Volcanics*

Idaho was affected by a period of intense igneous activity known as the Challis Episode, between 38 Ma and 54 Ma [Armstrong, 1974, 1975]. In the vicinity of the Pioneer Mountains, Armstrong [1975] obtained a K-Ar whole rock age of 42.0±1.3 Ma on a mafic member of the Challis Volcanics. He also determined a K-Ar feldspar age of 48.0±1.4 Ma for a latite collected at the base of the Challis Volcanics a few miles to the southwest of the Pioneer Metamorphic Core Complex.

## Sample Selection and Description

The widespread discordance of K-Ar ages previously determined for infrastructure units suggesed that the $^{40}Ar$-$^{39}Ar$ technique could be used to eliminate some of the ambiguity caused by excess argon. Five distinct deformational events and the low-pressure/high-temperature metamorphism associated with emplacement of the late-$D_3$ Pioneer Intrusive Suite constitute a complex scenario that demanded careful selection of sampling localities. Samples were collected from several different structural positions in the infrastructure of the Pioneer Metamorphic Core Complex (Figure 2). In order to constrain the temperature-time curve for areas not thermally affected by emplacement of the Pioneer Intrusive Suite, samples from the lowest structural level were collected roughly 4 km from the nearest outcrop of Tertiary magmatic rocks (Site 2). The thermal effects of the Pioneer Intrusive Suite are potentially extensive, and the temperature-time curve for the magmatic rocks and their thermal aureole were constrained by analysis of both the igneous rocks themselves and the adjacent metamorphic tectonites of the Hyndman Group (Sites 3,4,5). Several phases of the Pioneer Intrusive Suite were analyzed to constrain their temporal relations and to determine the age of $D_3$ extension-related faulting (Sites 1,4). The Summit Creek Stock was sampled in further constrain its cooling history and

temporal relationship with the Pioneer Intrusive Suite. Finally, mylonitic rocks from the Wildhorse detachment fault system were analyzed in order to constrain the absolute age of $D_4$ ductile deformation associated with WNW-ENE extension (Sites 7,8). Appendix I describes the sample locale, structural setting, lithology, fabric and mineralogy of each sample.

## Analytical Techniques

All samples were studied in thin section before selection for isotopic analysis. Minerals of interest were then probed on the JEOL 733 microprobe at M.I.T. in order to determine their major element chemistry and test for compositional heterogeneity (Appendix II). Following microprobe analysis the compositional data were evaluated in an attempt to date predominantly homogeneous phases. Samples were then crushed and sieved to a 0.45-0.25 mm size fraction. Nine amphibole, three muscovite, eight biotite and three potassium feldspar separates were obtained by standard magnetic and heavy liquid techniques. All samples were > 99.9 % pure, with the exception of biotite from the Wildhorse Detachment Fault System (Sample P450D) that was variably chloritized but not < 98 % pure. Samples were irradiated at either the U.S. Geological Survey TRIGA reactor [Dalrymple et al., 1981] or the Ford Reactor of the Phoenix Memorial Laboratory at the University of Michigan.

Because a variable radial gradient in fast neutron fluence had been noted in previous irradiations in the H-5 facility at the University of Michigan reactor, a new sample irradiation system was constructed to minimize the radial gradient. We replaced the open fused-silica-bucket-OSU cable system with a new system, similar in design to that used at the U.S. Geological Survey TRIGA Reactor [Dalrymple et al., 1981]. The sample vials were placed in an aluminum rack which was then sealed into an aluminum can. This

assembly was then suspended on a solid metal rod and lowered into the H-5 facility where it was rotated at one RPM for the duration of the irradiation. A comparison of the results with those of another irradiation at the Michigan reactor (Figure 7) suggest that there is no detectable radial gradient, within the limits of analytical precision, for a constant vertical position, in each of the twelve sample vials using this system. Also, because the irradiation was air moderated, the effective fast neutron fluence was about 50% higher, per unit time, than with the old fused-silica-bucket-OSU cable system.

Appendix III lists the correction factors for interfering nuclear reaction products, the irradiation site, the complete analytical results and heating schedules for each sample. Heating schedules were selected with the intent of analyzing evenly distributed components of the total reactor produced $^{39}Ar$ by consideration of similar previously analyzed samples. Appendix IV contains the age spectrum for each sample. Age "Plateaus" are defined using the criteria suggested by Snee et al. (1988). "Near plateaus" are defined as the weight-average age of contiguous increments of gas that meet all the criteria of a plateau [Snee et al., 1988] except that they together comprise only 40-50% of the total $^{39}Ar_K$ in the sample. "Minimum dates" are defined as the youngest age increment in a heating schedule. A "fusion age", essentially equivelent to a K-Ar age, is defined as the age of a one-step release. A "total gas age" is the weight average of all temperature step ages and is also roughly the equivelent of a conventional K-Ar age. Whenever samples yielded discordant release spectra suggestive of a significant trapped Ar component, further analysis was attempted using the argon isotope correlation (isochron) technique. Acceptable correlations (those with MSWD < 2.5 using three or more continuous increments) were used to calculate a "correlation age" and to better constrain the initial $^{40}Ar$-$^{36}Ar$ ratios for these samples (Table III). All data reduction was accomplished using the program *ArAr*: a computer program for reduction of 40Ar-39Ar data* [Haugerud and Kunk, 1988 with

corrections in calculation of the MSWD by Kunk, unpublished]. Release spectra are plotted at 1 sigma, however the ages are discussed with reported uncertainties of 2 sigma. Nominal closure temperatures of 800±25K, 625±25K, 575±25K and 475±50K were assumed for hornblende , muscovite , biotite and microcline respectively [McDougall and Harrison, 1988].

## Results

*Metamorphic Tectonites of the Wildhorse Gneiss Complex;*

Wildhorse Lake

Hornblende was analyzed from sample P106B. The release spectrum suggests excess argon uptake superimposed on a diffusion loss profile. The K/Ca ratio is relatively constant for all the heating increments suggesting degassing of a relatively homogeneous phase. A correlation plot, with deletion of the last 3 steps, suggests an initial $^{40}Ar/^{36}Ar$ of 417.1±7.2 and a correlation age of 49.5±0.8 Ma.

K-feldspar from sample P106A gives a release spectrum that suggests excess argon uptake superimposed on a diffusion loss profile. The near-plateau of 44.2±0.5 Ma (48.9% of $^{39}Ar_K$) may reflect the time of an early cooling below roughly 475 K. The minimum increment age of 33.0±1.2 Ma (7.7% of the $^{39}Ar_K$) may represent a maximum age for a brief thermal pulse that caused the diffusion loss profile. Alternatively, the spectrum may reflect Argon capture at sites with variable closure temperatures [Harrison et al., 1989].

Boulder Creek

Hornblende from sample P447 yields an exceptionally disturbed release spectrum that is suggestive of excess argon uptake superimposed on a diffusion loss profile. The K/Ca ratio is relatively constant for the higher temperature heating increments, implying degassing of a relatively homogeneous phase. A correlation plot, with deletion of the first 4 steps, suggests an initial $^{40}Ar/^{36}Ar$ of 794.4 and a correlation age of 53.2±7.0 Ma.

Sample P452D yields a complex hornblende age spectrum that indicates pervasive uptake of excess argon. The K/Ca ratio is constant and suggests degassing of a relatively

homogeneous phase. A correlation plot, with deletion of the first 3 steps, suggests an initial $^{40}Ar/^{36}Ar$ of 807.9 and a correlation age of 55.6±10.0 Ma.

Hornblende from sample P450E suggests very minor excess argon component superimposed on a diffusion loss profile. Slightly over half of the $^{39}Ar_K$ released (53.6%) defines a plateau age of 79.3±1.1 Ma that is interpreted as a minimum age for a Cretaceous thermal event. The minimum increment age of 49.0±13.0 Ma (5.6% of the $^{39}Ar_K$) may reflect a maximum age for the thermal event that caused the diffusive loss.

*Metamorphic Tectonites of the Hyndman and East Fork Groups:*

*North Fork Hyndman Creek*

A slight excess component is superimposed on the release spectrum of the hornblende of P143. The K/Ca ratio is constant. The hornblende data yield a plateau age of 44.4±0.5 Ma (75.2% of the $^{39}Ar_K$ on plateau). A correlation plot, with deletion of the first 2 steps, suggests an initial $^{40}Ar/^{36}Ar$ of 320.9 and a correlation age of 42.9±0.8 Ma.

Biotite from sample P143 yields an apparent plateau age of 37.9±0.4 Ma (79.6% of the $^{39}Ar_K$).

Sample P141 muscovite gives a plateau age of 36.6±0.3 Ma (80% of the $^{39}Ar_K$). Because the nominal closure temperature of muscovite is higher than that of biotite, the younger age of P141 muscovite suggests that excess argon may be incorporated into the P143 biotite.

Sample P139 muscovite gives a plateau age of 36.4±0.3 Ma, essentially identical to the plateau age of P141 muscovite.

*Pioneer Intrusive Suite:*

North Fork Hyndman Creek

The release spectrum for hornblende from sample P156 suggests very minor excess argon uptake and a plateau age of 44.6 ± 0.3 Ma (94.1% of the $^{39}Ar_K$). Fusion ages for biotite from samples P156 and P155 are 36.8±0.4 Ma and 37.5±0.4 Ma, respectively.

Betty Lake

The age spectrum for sample P92 hornblende suggests excess argon uptake superimposed on a diffusion loss profile. The minimum increment age comprises a near plateau of 52.2±0.5 Ma (49.5% of the $^{39}Ar_K$) that may constrain a maximum age for the thermal event that caused the diffusive loss. A correlation plot, with the 4 high temperature gas fractions, suggests a correlation age of 50.3±0.3 Ma.

Wildhorse Lake

Hornblende and biotite were analyzed from sample P110. The 1475K increment of the hornblende was accidentally lost during the analysis (no spectrum plotted). The 1525K and 1675K increments range in age from 48.4-49.2 Ma and account for 45.1% of the analyzed gas. It is plausible that this sample may plateau in the 48-49 Ma range. A correlation plot, with the 4 steps of analyzed gas, suggests a correlation age of 46.8±3.4 Ma. The biotite yields a fusion age of 37.8±0.4 Ma.

*Summit Creek Stock: Summit Creek*

Biotite and K-feldspar were analyzed from sample P285. The biotite yielded a fusion age of 47.1±0.6 Ma. The release spectrum for the K-feldspar suggests excess argon uptake superimposed on a minor diffusive loss profile. The plateau age of 44.5±0.5 Ma accounts for 50.4% of the $^{39}Ar_K$. The minimum increment age of 42.4±1.2 Ma (4.8% of

the $^{39}Ar_K$) may reflect a maximum age for the transient thermal wave that caused the diffusive loss.

*Tectonites of the Wildhorse Detachment Fault System*

Boulder Creek

Muscovite and biotite were analyzed from sample P450C. The muscovite data define a somewhat disturbed spectrum suggestive of minor excess argon uptake superimposed on a diffusive loss profile. Increments 1275-1425K define a four-step, contiguous-interval age (analyses lie within one-sigma uncertainty of each other) of roughly 37 Ma that comprises 36% of the $^{39}Ar_K$. This may reflect the original cooling age of the muscovite prior to mylonitization. The minimum age of 35.9±0.6 Ma may constrain a maximum age for the mylonitization. The high-temperature increments of P450C biotite define a plateau age of 34.7±0.5 Ma (62.9% of the $^{39}Ar_K$). This age is similar to the minimum increment muscovite age.

Biotite from P450D yields a fusion age of 36.1±0.4 Ma, consistent with the total gas age of P450C biotite (35.8 Ma).

Fall Creek

Sample P443 K-feldspar yields a disturbed diffusive loss spectrum. The K/Ca ratio stabilizes at the 925K increment. This heating step yields a minimum increment age of 33.0±0.5 Ma, perhaps reflecting a maximum age for the most recent cooling of the Wildhorse Detachment Fault System below the closure temperature for argon diffusion in K-feldspar.

*Shear Zones Subsidiary to the Wildhorse Detachment Fault System:*

*North Fork of Hyndman Creek*

There are several ductile shear zones in the infrastructure which are interpreted to be roughly contemporaneous with the Wildhorse Detachment Fault System because of their textural relations in the local deformation sequence. Hornblende and biotite were analyzed from a sample (P251) collected in this type of shear zone. The release spectrum for the hornblende suggests a minor uptake of excess argon. Steps corresponding to roughly 56.1% of the reactor-produced $^{39}Ar_K$ define a plateau age of 47.8±0.4 Ma. High-temperature increment steps 1475-1575K (three steps) released 11.5% of the $^{39}Ar_K$ and define a minimum interval age (contiguous increment ages are consistent) of roughly 43.3±0.8 Ma. This high temperature minimum is unusual and may indicate degassing of a different phase. However, the K/Ca ratio is roughly constant suggesting that the hornblende is rather homogeneous. A correlation plot, with only the first 4 points regressed, suggests an initial $^{40}Ar/^{36}Ar$ of 347.01±18.86 and a correlation age of 44.7±0.8 Ma.

Biotite from sample P251 yields a fusion age of 35.2±0.4 Ma.

## Tectonic Implications

Table 2 is a summary of mineral ages from this study. Figures 8-10 are plots of age versus closure temperature for various units and structural positions in the Pioneer Mountains. They include previously published geochronological data shown in Table 1. Uncertainties associated with the ages and the cooling temperatures are plotted. The apparent cooling curves reveal a consistent pattern that provides significant constraints on the absolute and relative timing of igneous, metamorphic and deformation events in the Pioneer Mountains (Figure 11).

*$D_2$ Mid-Cretaceous Compressional Dynamothermal Event*

P450E hornblende from the Wildhorse Gneiss Complex indicates pre-Cenozoic cooling below roughly 800K. This suggests that peak conditions during dynamothermal metamorphism associated with the development of the $D_2$ tectonite fabric in the mafic schist occurred before 79.3±1.1 Ma. This age is similar to Rb-Sr muscovite ages of 67 Ma and 80 Ma for the gneiss of Camel Rock in the Albion Mountains area [Armstrong, 1976]. Granodiorites and quartz diorites of the Thompson Creek stock of the SE corner of the Idaho Batholith have been dated at between 82 and 95 Ma [Bennet, 1984], as have an extensive suite of foliated tonalite/quartz dioritic plutons on the west side of the batholith [Armstrong, 1975]. In addition, hornblende and biotite from suture zone rocks in the Seven Devils Arc terrane give plateau dates of 82.5±0.8 Ma and 85.1±0.8 Ma, respectively [Lund and Snee, 1988]. Thus the Cretaceous thermal event in the Pioneer Mountains was part of a broad regional event that involved compressional deformation and magmatic activity from southern British Columbia to south of the Snake River Plain. This regional tectonic event is also evident in the hinterland of the Sevier thrust belt at latitudes 30°-40°N (e.g., Miller and Gans, 1989, and many others).

Cooling of the infrastructure may have proceeded rather slowly, by the diffusion loss model falling below 475K by 44.2±0.5 Ma (P106A). Alternatively, the near plateau of sample P106A K-feldspar may reflect pervasive diffusive loss associated with heating from the Pioneer Intrusive Suite. In this latter case, the "near plateau" would provide a minimum date for the pre-extension cooling of the infrastructure below roughly 475K.

*$D_3$ Eocene Extension and Challis Age Magmatism*

There are many Middle to Late Eocene hornblende cooling ages in the infrastructure, broadly of Challis age, which reflect the spotty but pervasive effect of the Pioneer Intrusive Suite and its transient perturbation of isotherms. The U-Pb zircon lower intercept

age of 48.3±0.6 Ma provides the best constraint on the age of intrusion of the Pioneer Intrusive Suite (Table I). P447 and P452, 53.2±7.0 Ma and 55.6±10.0 Ma respectively, suggest that Eocene reheating of the infrastrucure affected the autochthon,even at distances greater than to be expected by the outcrop pattern of the intrusives. The 50.6±0.6 Ma correlation hornblende age of an early granodiorite phase of the Pioneer Intrusive Suite (P92) suggests that emplacement of the Suite may have extended over a few million years. Emplacement ages of the western phase of the Pioneer Intrusive Suite and the Summit Creek Stock are identical within uncertainty and are similar to eruption ages of Challis volcanics. The main body of the western granodiorite phase of the Pioneer Intrusive Suite cooled below 800K at roughly 44.6±0.3 Ma (P156). The correlation age of P251 hornblende (44.7±0.8 Ma) is consistent with the well-defined plateau of P156 hornblende. Mafic dikes associated with the Pioneer Intrusive Suite (P110) cooled below 800K at 46.8±3.4 Ma, within the uncertainty of the larger plutonic bodies. The highly divergent cooling curves for the Pioneer Intrusive Suite and the Summit Creek Stock reflect the difference in the depth of emplacement (Figure 8). The Summit Creek Stock, intruded at shallow depth, cooled rapidly. Emplaced at 48.5±3.8 Ma, it then cooled to roughly 800K, 575K and 475K at 47.8±0.4 Ma, 47.1±0.6 (P285) and 44.5±0.6 Ma (P285), respectively. The steep concave-up cooling curve is typical of high-level plutons. In contrast, the main phase of the Pioneer Intrusive Suite was emplaced at a depth of 11-14 km at 48.3±0.6 Ma, and cooled more slowly. . If a temperature of 1000K is assumed for the intrusive then a time integrated cooling rate of 50K/million years is inferred. Such a rapid cooling rate implies the country rock was significantly cooler than magmatic emplacement temperatures.

The emplacement of the Pioneer Intrusive Suite created a thermal aureole that metamorphosed the nearby Hyndman and East Fork groups (Figure 9). Within the thermal aureole, the Hyndman Group cooled below 800K at 42.9±0.8 Ma (P143).

Muscovite plateau ages (P141 and P139) constrain cooling below 625K at roughly 36.5 Ma. Because the nominal closure temperature of biotite is lower than that of muscovite, the slightly older plateau age of P143 bioitite (37.9±0.4 Ma) probably reflects excess argon. However,the fusion ages of biotites for the Pioneer Intrusive Suite are similar at 36.8±0.4 (P156), 37.5±0.4 (P155), 37.8±0.4 (P110), suggesting some geological significance despite the documented presence of excess argon. The data indicate that the cooling curve of the nearby Hyndman Group is coincident with that of the Pioneer Intrusive Suite, suggesting the suite represents an advective thermal input into the mid-crust during late-$D_3$ extension. Figure 5 illustrates this effect with shallow concave up cooling curves. After an initially rapid cooling rate, the apparent moderate cooling rate in the Late Eocene (roughly 27°/m.y.) suggests a lack of rapid $D_3$ tectonic unroofing of the Pioneer Intrusive Suite. Thermobarometric data suggests that roughly 4.4 km of unroofing occurred as the Hyndman Group cooled from 950 K to 830 K. This suggests a time integrated unroofing rate of 1.5 km/million years from 48 Ma to 45 Ma. This rate is faster than that expected for simple erosion-controlled unroofing. Isostatic compensation has been suggested as a uplift mechanism during and following extensional tectonic denudation (Lister & Davis, 1989; Wernicke & Axon, 1989). It is difficult to imagine how tectonic unroofing itself should result in an isostatic rise of the region; instead, we might expect subsidence and basin development. Nevertheless, a thermal perturbation, perhaps only marginally indicated by the Pioneer Intrusive Suite, could cause a regional isostatic uplift of the crust. The widespread occurence of Eocene quartz monzonites from the Sawtooth Batholith to the Pioneer Mountains, part of the regional Challis volcanic-plutonic event, is consistent with a regionally elevated crustal geotherm. Rapid erosion-controlled unroofing could have resulted from an elevated topography following isostatic compensation of the south-central Idaho region. This "passive" unroofing mechanism should result in significant erosional

deposits. The Tertiary redbed conglomerate that underlies the Challis volcanics in this area is of the appropriate age, although its thickness and regional extent requires further study.

Alternatively, some moderate amount of "active" tectonic denudation could have occurred in the 48-45 Ma interval. The fault system along which this unroofing occurred would have been structurally higher than the presently exposed infrastructure. The orientation and geometry of this hypothetical fault system is unknown, therefore it is impossible to constrain a slip rate along this fault. Regardless of whether the unroofing is "passive" or "active", it is clearly related to extensional tectonic denudation.

In light of the thermal effects of the Eocene Pioneer Intrusive Suite on the Hyndman and East Fork Groups, it is curious that the Cretaceous hornblende age is preserved in core sample P450. In addition, the near plateau age of 44.3±0.5 Ma for P106A K-feldspar, seven million years older than muscovite ages for the intrusion's aureole, may indicate that significant lateral thermal gradients existed and/or that the core cooled slowly from the Cretaceous. Alternatively, the similarity of this age and cooling ages from the Pioneer Intrusive Suite may indicate that the Pioneer Intrusive Suite heated the core uniformly to temperatures greater than 475K, but significantly less than 800K locally (the closure temperature of Ar in hornblende).

The data unequivocally demonstrate an Eocene extensional event in southern Idaho. A curiosity lies in the fact that, in the Shuswap Complex of British Columbia, this extension follows compressional thickening of the crust by only a few million years [Brown and Journeay, 1987; Parrish, 1988]. In the Bitterroot Mylonite [Garmezy and Sutter, 1983], Eocene extension post-dates any known compressional event by almost 30 million years, although its age is similar to the poorly documented "Trans-Challis Fault System" [Bennett, 1985]. Dickenson et al. [1988] have suggested that a shallow dip and high rate of oblique convergence between the North American and Farallon plates in the

Eocene resulted in mechanical coupling between the two as well as elevated regional heat flow and strike-slip faulting within the Sevier hinterland. The Eocene event in the Pioneers, at first glance, appears to be similar to this latter event. However the vergence is different by almost 70°. Alternatively, Thorkelson and Taylor (1989) have suggested passage of a slab window beneath the west margin of North America at the latitude of central Idaho during the late Paleocene through the Middle Eocene. It is plausible that "edge effects" of a subducted Kula-Farallon spreading ridge could affect thermal and mechanical anomalies that would increase crustal elevation and contribute to tectonic denudation (Thorkelson and Taylor, 1989). The data suggest that although the Pioneers region shared a somewhat similar Eocene magmatic and thermal evolution with the greater Idaho region which may be related to plate margin processes, the inboard structural and kinematic history is somewhat different and without an obvious dynamic linkage to a regional strike slip fault system. In addition, there is no *a priori* evidence that all of the extensional allochthons in the infrastructure formed in the Eocene. The data in this paper constrain only movement on the Hyndman Shear Zone. It is entirely plausible for the Paymaster and Southeast Corner Allochthons to have been emplaced any time after $D_2$ and before the late-$D_3$ magmatic event. These allochthons may have been emplaced as a result of a Cretaceous collapse of an overthickened Sevier orogenic pile.

*$D_4$ Oligocene Extension and its Relation to Northern Great Basin Extension*

Ductile deformation in the Wildhorse Detachment Fault System ($D_4$) appears to have been an Early Oligocene event. The rapid quenching of muscovite, biotite and K-feldspar in mylonites from the principle ductile shear zone strongly suggests that tectonic unroofing and conductive re-equilibration controlled the Oligocene low-temperature cooling path. A steep concave-down cooling curve (75°/m.y.) is defined by cooling dates of 35.9±0.6 Ma,

34.7±1.0 Ma and 33.0±0.5 Ma for muscovite (P450C), biotite (P450C) and K-feldspar (P443), respectively (Figure 10). A moderate cooling rate within the Pioneer Intrusive Suite's thermal aureole had brought footwall temperatures below 625K by 36.6±0.3 Ma (P141 muscovite); thus, there is a suggestion of complete infrastructure thermal equilibration by roughly 36 Ma. However, the near plateau of P106A K-feldspar eliminates this possibility and we are forced to consider a combination of shear heating and hydrothermal fluid transport that would contribute to resetting the isotopic system of the shear zone minerals. Molnar and England (1990) have suggested that deviatoric stresses of 100 MPa could result in local rise of greater than 100 K in major shear zones. The almost concordant muscovite, biotite and K-feldspar ages from the Wildhorse Shear Zone may result from shear heating, followed by rapid conductive cooling. In this case, the coincident cooling curves for the Pioneer Intrusive Suite and the shear zone mylonites is just that, coincidence and does not characterize the entire footwall. The lack of any Challis Volcanic units in depositional contact with infrastructure rocks is consistent with the isotopic data suggesting that rapid cooling resulted from Early Oligocene tectonic unroofing associated with movement on the Wildhorse Detachment Fault System. The minimum K-feldspar ages for the shear zone and the Wildhorse Gneiss Complex may indicate footwall thermal equilibrium at roughly 425K at approximately 33 Ma.

The thermal effects associated with movement on both the principal and subsidiary shear zones of the Wildhorse Detachment Fault System were not great enough to completely reset the isotopic system of hornblende (P450E and P251). In a subsidiary shear zone, the P251 hornblende correlation age of 44.7±0.8 Ma is similar to the nearby non-mylonitic P156 hornblende that yields a well-defined plateau age of 44.6±0.3 Ma. In contrast, the P251 biotite fusion age constrains cooling of the subsidiary shear zone below 575K at 35.2±0.4 Ma. This age is one and two million years younger than fusion ages of

biotite from the nearby non-mylonitic samples, P156 and P155 respectively. The P251 biotite age is consistent with the high-temperature plateau of sample P450C biotite (34.7±1.0 Ma). These observations suggest that minor subsidiary shear zones in the infrastructure were roughly contemporaneous with ductile deformation in the Wildhorse Detachment Fault System.

The Oligocene age of ductile $D_4$ fabrics is consistent with the observation that Challis volcanics are not found in the infrastructure. Volcanic rocks are found at elevations in excess of 11,000 feet in the suprastructure and there are no recognized post-Challis normal faults with a large amount of throw. Thus we can not call on erosion to have removed all trace of Challis rocks from the infrastructure. Challis volcanism occurred before the final exposure of the core, and in fact, probably predated exposure of the core by a minimum of roughly 6 million years.

Thermobarometric data suggests a maximum infrastructure paleodepth of roughly 7.5-8.4 km at the end of the Eocene. It is hazardous to extrapolate the late-$D_3$ unroofing rate of 1.5 km/million years to the onset of $D_4$ extension. Therefore we may judisciously infer a maximum depth of 7.5-8.4 km at the onset of Oligocene extension. A significantly shallower infrastructure paleodepth at the onset of $D_4$ extension is not likely because of the > 575 K temperatures required for ductile deformation in the Wildhorse Shear Zone. Future studies should concentrate on the low-temperature and pressure evolution of the core complex in order to constrain the rate of tectonic denudation for this latter event.

Documentation of Early Oligocene extension north of the Snake River Plain suggests that the plain does not represent a fundamental boundary between different extensional age provinces, but rather extension is simply superimposed on a continuous Oligicene to Miocene extension corridor. Documentation of Early Oligocene extension north of the Snake River Plain suggests that the plain does not represent a fundamental geologic break,

but rather is superimposed on an Oligicene to Miocene extension corridor. The kinematics of this Oligocene event is similar to that reported for WNW-directed extension in the Albion Mountains [Saltzer and Hodges, 1988]. Based on current geochronological constraints, a minimum of roughly 8 million years separates the age of extension of these two regions. If Oligocene extension is associated with migration of a extensional regime southward, than with the Albion Mountains roughly 140 km south, that migration would have occurred at a rate not faster than roughly 20 km/million years.

## Acknowledgements

D.S.S. wishes to thank Gilles Wust, Ned Gates, Allison Macfarlane, Gregory Reller, Timothy East, Lawrence McKenna, Elaine Aliberti and Elaine Padovani for their help in the field. Kudos to Timothy East and Patricia for endless hospitality in Ketchum, Idaho. R. Zartman kindly shared his unpublished geochronological data. Lawrence McKenna, Brad Hager and Caroline Ruppel reviewed a early draft of this paper. D.S.S. wishes to thank The Geological Society of America for grant support that enabled his attendance at pertinent Penrose Conferences. This research was a part of a Ph.D. thesis (D.S.S.) at the Massachusetts Institute of Technology and was financially supported by U.S. National Science Foundation grant EAR-8407730 to K.V. Hodges.

## Appendix I: Sample Descriptions

*Metamorphic Tectonites of the Wildhorse Gneiss Complex*

Wildhorse Lake

Two tectonite samples were collected from the lowest structural level exposed in the core, 2 km east of Wildhorse Lake (Site 2 on Figure 2). At this locale, the lower quartzofeldspathic gneiss and the marble member of the Wildhorse Gneiss Complex is present in a series of NW-trending, east-overturned anticlines and synclines. Sample P106B is a mafic schist from the lower quartzofeldspathic gneiss. Aligned hornblende porphyroblasts are set in a well-foliated matrix of biotite, quartz, sodic plagioclase, zircon, apatite and sphene. Sample P106A was collected 1 m from sample P106B in the more typical felsic gneiss lithology of this member. The gneiss displays granoblastic texture and is composed of undulatory quartz, myrmekitic microcline, aligned biotite, normal and reverse zoned plagioclase, sericite, apatite, zircon, sphene, and opaques.

Boulder Creek

Three hornblende separates were obtained from samples collected along Boulder Creek in the mafic gneiss member of the Wildhorse Gneiss Complex (Site 8 on Figure 2). Samples P447 and P452D came from non-mylonitic amphibolitic schists. The assemblages in these amphibolitic schists include: hornblende, biotite, quartz, plagioclase, carbonate, zircon, apatite, sphene and opaques. The schistosity is defined by alignment of hornblende and biotite. Biotite is variably altered to chlorite. Sample P450E is from a mafic pod surrounded by mylonitic psammitic schist collected in the ductile Wildhorse detachment fault system. Its assemblage is identical to that of P447, except that hornblende rims are altered to actinolite. The hornblendes are somewhat fractured in this sample.

*Metamorphic Tectonites of the Hyndman Group*

North Fork Hyndman Creek

Three samples were collected from the Hyndman and East Fork groups along the north fork of Hyndman Creek (Site 3 on Figure 2), is roughly 1 km south of the contact between the Hyndman Group and the Pioneer Intrusive Suite. Sample P143 is mafic schist interlayer in the gneissose quartzite formation of the Hyndman Group. This schist contains aligned hornblende porphyroblasts, biotite, quartz, plagioclase, trace muscovite, epidote and sphene. Sample P141 was collected 10 m from sample P143 in a pelitic horizon within the gneissose quartzite. The well-foliated sample contained sillimanite, muscovite, plagioclase and quartz. Sample P139 came from a micaceous horizon in the Clayton Mine Quartzite. The mica schist contains muscovite, quartz and plagioclase.

*Pioneer Intrusive Suite*

North Fork Hyndman Creek

Samples P155 and P156 were collected at the 2980 m level of the north fork of Hyndman Creek (Site 4 of Figure 2). Sample P155 is a well-foliated dioritic gneiss that contains the assemblage: pyroxene, hornblende, biotite, undulatory plagioclase and recrystallized quartz. Two generations of biotite are present. The second generation of biotite defines the strong foliation that cross-cuts broken feldspar and hornblende phenocrysts. Sample P156 is a granodiorite collected 20 m from sample P155. Sample P156 contains hornblende, biotite, K-feldspar, plagioclase, quartz, sphene, apatite and opaques. It is well-foliated and contains relict phenocrysts of clinopyroxene with reaction rims of hornblende.

Betty Lake

Sample P92 was collected from the 3220 m level above Betty Lake in the eastern outcrop belt of the Pioneer Intrusive Suite (Site 1 of Figure 2). It is a fine-grained granodiorite with a directionless fabric. The predominant quartz monzonite phase of the Pioneer Intrusive Suite in this area contains cognate inclusions of similar rock. The quartz monzonite contact with the granodiorite is sharp; field observations suggest that the granodiorite predates emplacement of the quartz monzonite. The granodiorite assemblage includes hornblende, biotite, K-feldspar, plagioclase, quartz, sphene and opaques.

Wildhorse Lake

Sample P110 was collected from fine- to medium-grained, weathering orange, hypabyssal dikes east of Wildhorse Lake (Site 2 of Figure 2). It cross-cuts the foliation of the felsic gneiss, appears to be coherent, yet is itself cross-cut by pegmatitic veinlets. This sample is composed of hornblende, biotite, plagioclase and quartz.

*Summit Creek Stock: Summit Creek*

Sample P285 was collected from the Summit Creek Stock along Big Falls Creek, 50 m north of the Trail Creek-Summit Creek Road (Site 6 on Figure 2). This quartz monzonite sample is medium- to coarse-grained and displays a directionless fabric. It is composed of K-feldspar, plagioclase, biotite, quartz, apatite, and sphene. Phases display only weak undulatory extinction.

*Tectonites of the Wildhorse Detachment Fault System*

Boulder Creek

Samples P450C and P450D were collected from the ductile shear zone associated with the Wildhorse Detachment Fault System that affects the mafic gneiss member of the Wildhorse Gneiss Complex along the north side of Boulder Creek (Site 8 of Figure 2; Silverberg, in preparation). These samples are Type II S-C mylonites (Lister and Snoke, 1985). The C-surfaces of these mylonitic psammitic schists are delineated by the orientation of recrystallized quartz, muscovite, biotite and chlorite. Feldspar augen have asymmetric pressure shadows. The S-surfaces are expressed by an alignment of elongate quartz sub-grains and ribbon aggregates that make an angle of 20-30° with the C-surfaces. These subgrains have irregular form and display undulatory extinction, suggesting at least some component of low-temperature plasticity. The presence of chlorite in these mylonites indicates that shear deformation was accompanied by open system behaviour during which external $H_2O$ was introduced to the bulk composition.

Fall Creek

Sample P443 was collected from a mylonitic quartz monzonite in the Pioneer Intrusive Suite along the south side of Fall Creek (Site 7 of Figure 2). The rock is composed of K-feldspar, plagioclase, quartz, biotite and chlorite. Chlorite defines a foliation that is continuous through fractured feldspar grains. K-feldspar porphyroclasts define a lineation that trends N70°W. Although the rock displays a cataclastic appearance, quartz is dynamically recrystallized. The abundance of chlorite in this mylonite suggests open system behaviour during ductile deformation.

*Shear Zones Subsidiary to the Wildhorse Detachment Fault System:*
*North Fork of Hyndman Creek*

Sample P251 was collected at an elevation of 3245 m along the north fork of Hyndman Creek, comes from a 2 m-wide D4 mylonite zone in the granodiorite (Site 5 of Figure 2). The sample contains hornblende, biotite, plagioclase, quartz, K-feldspar, sphene and apatite. Cataclasis of hornblende porphyroblasts with associated rim retrogression to actinolite suggest that deformation occurred under broadly defined greenschist facies conditions.

Appendix II. Composition of samples analyzed by the 40Ar-39Ar technique.
Data is listed in numerical order by sample field number.

| | P-92 (hb) | P-106A (kfs) | P-106B (hb) | P-106C (phl) | P-110 (hb) | P-139 (m) | P-143 (hb) | P-144 (hb) |
|---|---|---|---|---|---|---|---|---|
| MgO | 11.71 | 0.03 | 15.65 | 27.38 | 18.46 | 1.11 | 12.39 | 12.45 |
| Al2O3 | 7.92 | 18.73 | 2.35 | 15.99 | 4.14 | 32.71 | 8.81 | 9.62 |
| SiO2 | 44.47 | 65.15 | 52.81 | 38.33 | 52.40 | 47.83 | 46.28 | 44.84 |
| CaO | 11.62 | 0.13 | 11.72 | 0.08 | 12.18 | 0.00 | 11.99 | 11.99 |
| TiO2 | 1.28 | | 0.10 | 0.67 | 0.41 | 1.79 | 0.62 | 0.67 |
| Cr2O3 | 0.06 | | 0.00 | | 0.11 | | 0.15 | 0.00 |
| MnO | 0.52 | | 0.43 | 0.03 | 0.18 | 0.00 | 0.43 | 0.70 |
| FeO | 17.24 | 0.00 | 13.80 | 2.15 | 8.40 | 1.81 | 15.03 | 14.60 |
| Na2O | 1.46 | 1.28 | 0.40 | 0.12 | 0.81 | 0.37 | 0.74 | 1.12 |
| K2O | 0.92 | 14.62 | 0.04 | 8.63 | 0.37 | 10.62 | 1.07 | 1.06 |
| Total | 97.19 | 99.93 | 97.28 | 93.37 | 97.46 | 96.24 | 97.53 | 97.05 |
| CATIONS | | | | | | | | |
| Mg | 2.6475 | 0.0017 | 3.3928 | 2.9098 | 3.9167 | 0.1094 | 2.7428 | 2.7773 |
| Al | 1.4148 | 1.0140 | 0.4027 | 1.3439 | 0.6946 | 2.5470 | 1.5418 | 1.6964 |
| Si | 6.7426 | 2.9929 | 7.6822 | 2.7329 | 7.4557 | 3.1605 | 6.8713 | 6.7120 |
| Ca | 1.8875 | 0.0062 | 1.8259 | 0.0059 | 1.8575 | 0.0000 | 1.9075 | 1.9224 |
| Ti | 0.1463 | | 0.0108 | 0.0359 | 0.0434 | 0.0888 | 0.0696 | 0.0757 |
| Cr | 0.0066 | | 0.0000 | | 0.0119 | | 0.0178 | 0.0000 |
| Mn | 0.0663 | | 0.0532 | 0.0017 | 0.0216 | 0.0000 | 0.0543 | 0.0889 |
| Fe | 2.1851 | 0.0000 | 1.6780 | 0.1282 | 0.9999 | 0.1000 | 1.8662 | 1.8270 |
| Na | 0.4283 | 0.1138 | 0.1114 | 0.0166 | 0.2240 | 0.0477 | 0.2125 | 0.3239 |
| K | 0.1774 | 0.8566 | 0.0070 | 0.7846 | 0.0666 | 0.8947 | 0.2017 | 0.2032 |
| Total | 15.7024 | 4.9850 | 15.1639 | 7.9594 | 15.2919 | 6.9480 | 15.4855 | 15.6267 |

| | P-156 (hb) | P-251 (hb) | P-251 (bt) | P-447 (hb) | P-450C (mu) | P-450C (bt) | P-450D (bt) | P-452D (hb) |
|---|---|---|---|---|---|---|---|---|
| MgO | 10.03 | 8.54 | 8.21 | 12.748 | 0.843 | 8.386 | 9.758 | 8.606 |
| Al2O3 | 6.65 | 7.74 | 14.81 | 9.395 | 31.616 | 16.829 | 18.720 | 11.214 |
| SiO2 | 53.66 | 45.32 | 36.20 | 45.167 | 47.533 | 35.404 | 35.933 | 42.889 |
| CaO | 10.25 | 11.69 | 0.10 | 11.360 | 0.022 | 0.026 | 0.038 | 11.707 |
| TiO2 | 0.65 | 1.02 | 2.80 | 1.599 | 1.025 | 2.671 | 1.839 | 0.393 |
| Cr2O3 | 0.04 | 0.34 | | 0.083 | | | | 0.121 |
| MnO | 0.29 | 0.55 | 0.31 | 0.352 | 0.026 | 0.276 | 0.183 | 0.165 |
| FeO | 14.36 | 20.60 | 24.05 | 14.784 | 3.226 | 23.536 | 19.879 | 19.901 |
| Na2O | 0.92 | 0.95 | 0.12 | 1.383 | 0.350 | 0.057 | 0.314 | 1.042 |
| K2O | 0.67 | 0.81 | 9.01 | 1.016 | 10.271 | 9.670 | 9.259 | 1.314 |
| Total | 97.50 | 97.56 | 95.61 | 97.890 | 94.910 | 96.860 | 95.920 | 97.350 |
| CATIONS | | | | | | | | |
| Mg | 2.1543 | 1.9433 | 0.9520 | 2.8152 | 0.0846 | 0.9600 | 1.1013 | 1.9628 |
| Al | 1.1299 | 1.3927 | 1.3581 | 1.6400 | 2.5084 | 1.5230 | 1.6701 | 2.0218 |
| Si | 7.7329 | 6.9194 | 2.8164 | 6.6903 | 3.2000 | 2.7187 | 2.7202 | 6.5613 |
| Ca | 1.5825 | 1.9122 | 0.0080 | 1.8027 | 0.0016 | 0.0021 | 0.0031 | 1.9187 |
| Ti | 0.0702 | 0.1176 | 0.1640 | 0.1781 | 0.0519 | 0.1542 | 0.1047 | 0.0452 |
| Cr | 0.0043 | 0.0407 | | 0.0098 | | | | 0.0146 |
| Mn | 0.0353 | 0.0708 | 0.0207 | 0.0441 | 0.0015 | 0.0180 | 0.0117 | 0.0214 |
| Fe | 1.7303 | 2.6299 | 1.5646 | 1.8311 | 0.1816 | 1.5113 | 1.2584 | 2.5458 |
| Na | 0.2563 | 0.2804 | 0.0184 | 0.3971 | 0.0457 | 0.0085 | 0.0461 | 0.3089 |
| K | 0.1223 | 0.1571 | 0.8943 | 0.1920 | 0.8820 | 0.9472 | 0.8941 | 0.2564 |
| Total | 14.8182 | 15.4641 | 7.7964 | 15.6003 | 6.9573 | 7.8429 | 7.8096 | 15.6569 |

# Appendix III: $^{40}Ar$-$^{39}Ar$ Heating Schedules and Analytical Data for All Samples

Heating schedules are compiled in numerical order by sample field number.

P92 HORNBLENDE (TRIGA; RD42; J=0.003580; wt.=0.9905 g); Total Gas Age = 56.40 Ma; Correlation Age = 50.3±0.3 Ma.

| TEMP (K) | 40Ar/39Ar | 37Ar/39Ar | 36Ar/39Ar | 39Ar (MOLE) | %39Ar released | K/Ca | AGE ± 1 s.d. Ma | %40Ar RAD |
|---|---|---|---|---|---|---|---|---|
| 1375 | 12.741 | 6.449E+00 | 1.234E-02 | 2.506E-12 | 5.3 | 8.00E-02 | 57.80±0.63 | 71.4 |
| 1425 | 13.380 | 6.741E+00 | 1.201E-02 | 1.574E-11 | 33.3 | 8.00E-02 | 62.41±0.32 | 73.5 |
| 1475 | 9.326 | 6.267E+00 | 3.683E-03 | 2.360E-11 | 50.0 | 8.00E-02 | 52.45±0.27 | 88.3 |
| 1525 | 10.551 | 6.292E+00 | 7.851E-03 | 3.215E-12 | 6.8 | 8.00E-02 | 53.95±0.33 | 80.4 |
| 1625 | 11.958 | 6.498E+00 | 1.025E-02 | 1.389E-12 | 2.9 | 8.00E-02 | 56.74±0.41 | 74.7 |
| 1725 | 13.844 | 7.190E+00 | 1.522E-02 | 7.823E-13 | 1.7 | 7.00E-02 | 59.35±1.90 | 67.5 |

P106A K-FELDSPAR (MICHIGAN; RM4; J=0.007180; wt.=0.1055 g); Total Gas Age = 41.91 Ma; Near Plateau = 44.2±0.3 Ma.

| TEMP (K) | 40Ar/39Ar | 37Ar/39Ar | 36Ar/39Ar | 39Ar (MOLE) | %39Ar released | K/Ca | AGE ± 1 s.d. Ma | %40Ar RAD |
|---|---|---|---|---|---|---|---|---|
| 925 | 6.246 | 1.143E-02 | 4.331E-03 | 1.617E-12 | 6.2 | 45.48 | 63.22±0.43 | 79.5 |
| 1025 | 3.591 | 1.597E-02 | 1.359E-03 | 1.258E-12 | 4.8 | 32.56 | 40.84±0.82 | 88.8 |
| 1125 | 2.805 | 1.300E-02 | 5.826E-04 | 1.102E-12 | 4.2 | 40.01 | 33.77±1.04 | 93.9 |
| 1225 | 2.716 | 2.082E-02 | 4.789E-04 | 1.996E-12 | 7.7 | 24.99 | 33.04±0.58 | 94.8 |
| 1325 | 2.770 | 1.206E-02 | 3.135E-04 | 2.389E-12 | 9.2 | 43.12 | 34.36±0.39 | 96.7 |
| 1425 | 2.959 | 1.001E-02 | 6.525E-04 | 2.429E-12 | 9.3 | 51.95 | 35.47±0.49 | 93.5 |
| 1525 | 3.397 | 1.028E-02 | 9.267E-04 | 2.018E-12 | 7.7 | 50.57 | 40.01±0.77 | 91.9 |
| 1625 | 3.796 | 1.628E-02 | 1.415E-03 | 2.065E-12 | 7.9 | 31.93 | 43.23±0.41 | 89.0 |
| 1725 | 3.946 | 1.427E-02 | 1.503E-03 | 2.983E-12 | 11.4 | 36.44 | 44.77±0.44 | 88.7 |
| 1825 | 3.875 | 4.593E-03 | 1.345E-03 | 5.430E-12 | 20.8 | 113.20 | 44.48±0.29 | 89.7 |
| 1925 | 3.927 | 1.498E-02 | 1.793E-03 | 2.275E-12 | 8.7 | 34.72 | 43.48±0.64 | 86.5 |
| 2025 | 4.665 | 5.293E-02 | 3.712E-03 | 5.248E-13 | 2.0 | 9.82 | 45.62±0.62 | 76.5 |

P106B HORNBLENDE (MICHIGAN; RM4; J=0.007345; 0.7011 g); Total Gas Age = 55.55 Ma; Correlation Age = 49.5±0.4 Ma.

| TEMP (K) | 40Ar/39Ar | 37Ar/39Ar | 36Ar/39Ar | 39Ar (MOLE) | %39Ar released | K/Ca | AGE±1 s.d. Ma | %40Ar RAD |
|---|---|---|---|---|---|---|---|---|
| 1225 | 17.473 | 7.035E+00 | 3.395E-02 | 2.256E-13 | 2.1 | 7.00E-02 | 95.98±3.88 | 42.6 |
| 1325 | 7.704 | 6.697E+00 | 9.697E-03 | 7.364E-13 | 7.0 | 8.00E-02 | 62.99±1.25 | 62.8 |
| 1375 | 6.149 | 6.797E+00 | 5.895E-03 | 1.151E-12 | 10.9 | 8.00E-02 | 57.48±0.66 | 71.7 |
| 1425 | 5.564 | 6.739E+00 | 4.188E-03 | 1.088E-12 | 10.3 | 8.00E-02 | 56.46±0.19 | 77.8 |
| 1475 | 4.409 | 5.455E+00 | 1.525E-03 | 4.132E-12 | 39.2 | 1.00E-01 | 51.69±0.17 | 89.8 |
| 1525 | 4.705 | 5.258E+00 | 1.785E-03 | 2.187E-12 | 20.7 | 1.00E-01 | 54.53±0.44 | 88.8 |
| 1575 | 5.466 | 5.216E+00 | 3.809E-03 | 6.153E-13 | 5.8 | 1.00E-01 | 56.63±0.62 | 79.4 |
| 1725 | 5.585 | 5.664E+00 | 4.777E-03 | 4.170E-13 | 4.0 | 9.00E-02 | 54.47±2.47 | 74.7 |

P110 HORNBLENDE (TRIGA; RD42; J=0.003520; wt.=0.3487 g); Total Gas Age = 50.82 MA; Correlation Age = 46.8±1.7 Ma.

| TEMP (K) | 40Ar/39Ar | 37Ar/39Ar | 36Ar/39Ar | 39Ar (MOLE) | %39Ar released | K/Ca | AGE ± 1 s.d. Ma | %40Ar RAD |
|---|---|---|---|---|---|---|---|---|
| 1375 | 16.629 | 1.408E+01 | 2.724E-02 | 7.445E-14 | 20.2 | 4.00E-02 | 53.66±1.16 | 51.6 |
| 1425 | 15.202 | 1.293E+01 | 2.349E-02 | 9.078E-14 | 24.6 | 4.00E-02 | 51.73±0.88 | 54.4 |
| 1475 | LOST | LOST | LOST | LOST | LOST | LOST | LOST | LOST |
| 1525 | 11.903 | 1.272E+01 | 1.389E-02 | 7.846E-14 | 21.3 | 4.00E-02 | 48.84±1.28 | 65.5 |
| 1450 | 10.864 | 1.353E+01 | 9.912E-03 | 1.250E-13 | 33.9 | 4.00E-02 | 49.69±1.00 | 73.0 |

P110 BIOTITE (TRIGA; RD42; J=0.003430; wt.=0.0648 g); Total Gas Age = 37.79±0.21 Ma.

| TEMP (K) | 40Ar/39Ar | 37Ar/39Ar | 36Ar/39Ar | 39Ar (MOLE) | %39Ar released | K/Ca | AGE ± 1 s.d. Ma | %40Ar RAD |
|---|---|---|---|---|---|---|---|---|
| FUSE | 8.501 | 4.386E-02 | 7.869E-03 | 6.07E-02 | 100.0 | 1.19E+01 | 37.79±0.21 | 72.6 |

P139 MUSCOVITE (MICHIGAN; RM4; J=0.0.006770; wt.=0.0710 g); Total Gas Age = 36.37 Ma; Plateau Age = 36.4±0.3 Ma.

| TEMP (K) | 40Ar/39Ar | 37Ar/39Ar | 36Ar/39Ar | 39Ar (MOLE) | %39Ar released | K/Ca | AGE ± 1 s.d. Ma | %40Ar RAD |
|---|---|---|---|---|---|---|---|---|
| 725 | 29.142 | 8.946E-02 | 9.291E-02 | 1.037E-13 | 0.8 | 5.81E+00 | 20.53±3.12 | 5.8 |
| 825 | 6.271 | 0.000E+00 | 1.024E-02 | 1.527E-13 | 1.2 | 0.00E+00 | 39.23±2.39 | 51.8 |
| 925 | 3.876 | 2.671E-02 | 2.563E-03 | 3.318E-13 | 2.7 | 1.95E+01 | 37.70±1.88 | 80.5 |
| 1025 | 3.666 | 1.188E-02 | 1.751E-03 | 4.676E-13 | 3.8 | 4.38E+01 | 38.04±4.18 | 85.9 |
| 1125 | 3.983 | 1.109E-02 | 3.181E-03 | 1.290E-12 | 10.5 | 4.69E+01 | 36.79±1.12 | 76.4 |
| 1225 | 3.596 | 6.818E-03 | 2.023E-03 | 3.721E-12 | 30.3 | 7.63E+01 | 36.23±0.38 | 83.4 |
| 1325 | 3.484 | 1.275E-02 | 1.580E-03 | 2.200E-12 | 17.9 | 4.08E+01 | 36.47±0.44 | 86.6 |
| 1425 | 3.248 | 1.451E-02 | 8.024E-04 | 3.451E-12 | 28.1 | 3.58E+01 | 36.40±0.41 | 92.7 |
| 1525 | 3.370 | 9.276E-02 | 1.333E-03 | 4.943E-13 | 4.0 | 5.61E+00 | 35.99±2.35 | 88.3 |
| 1625 | 5.091 | 4.733E-01 | 0.000E+00 | 5.345E-14 | 0.4 | 1.10E+00 | 33.55±16.76 | 54.5 |

P141 MUSCOVITE (MICHIGAN; RM4; J=0.007386; wt.=0.0716 g); Total Gas Age = 36.58 Ma; Plateau Age = 36.6±0.3 Ma.

| TEMP (K) | 40Ar/39Ar | 37Ar/39Ar | 36Ar/39Ar | 39Ar (MOLE) | %39Ar released | K/Ca | AGE ± 1 s.d. Ma | %40Ar RAD |
|---|---|---|---|---|---|---|---|---|
| 725 | 16.637 | 4.908E-02 | 4.613E-02 | 9.575E-14 | 0.7 | 1.06E+01 | 39.64±14.35 | 18.1 |
| 825 | 4.836 | 0.000E+00 | 8.343E-03 | 1.213E-13 | 0.9 | 0.00E+00 | 31.31±11.79 | 49.0 |
| 925 | 3.410 | 1.543E-02 | 2.887E-03 | 2.397E-13 | 1.9 | 3.37E+01 | 33.75±4.02 | 75.0 |
| 1025 | 3.548 | 1.024E-02 | 2.950E-03 | 4.634E-13 | 3.6 | 5.08E+01 | 35.30±3.22 | 75.4 |
| 1125 | 3.336 | 4.749E-03 | 1.702E-03 | 1.707E-12 | 13.3 | 1.10E+02 | 37.34±0.53 | 84.9 |
| 1225 | 3.118 | 1.280E-03 | 1.181E-03 | 4.051E-12 | 31.6 | 4.06E+02 | 36.52±0.43 | 88.8 |
| 1325 | 3.211 | 8.500E-03 | 1.435E-03 | 1.433E-12 | 11.2 | 6.12E+01 | 36.76±0.60 | 86.8 |
| 1425 | 3.054 | 3.695E-03 | 1.007E-03 | 2.460E-12 | 19.2 | 1.41E+02 | 36.37±0.37 | 90.3 |
| 1525 | 2.952 | 4.872E-03 | 5.920E-04 | 2.108E-12 | 16.4 | 1.07E+02 | 36.62±0.52 | 94.1 |
| 1625 | 3.673 | 0.000E+00 | 0.000E+00 | 1.571E-13 | 1.2 | 0.00E+00 | 41.08±6.11 | 84.9 |

P143 HORNBLENDE (MICHIGAN; RM4; J=0.007220; wt.=0.6407); Total Gas Age = 46.73 Ma; Correlation Age = 42.9±0.4 Ma.

| TEMP (K) | 40Ar/39Ar | 37Ar/39Ar | 36Ar/39Ar | 39Ar (MOLE) | %39Ar released | K/Ca | AGE ± 1 s.d. Ma | % 40Ar RAD |
|---|---|---|---|---|---|---|---|---|
| 975 | 23.253 | 2.124E+00 | 5.338E-02 | 2.321E-13 | 2.2 | 2.40E-01 | 94.84±3.52 | 32.2 |
| 1125 | 16.772 | 1.681E+00 | 3.916E-02 | 1.453E-13 | 1.4 | 3.10E-01 | 66.55±10.88 | 31.0 |
| 1325 | 8.698 | 5.754E+00 | 1.651E-02 | 9.503E-13 | 9.1 | 9.00E-02 | 49.10±1.31 | 43.9 |
| 1425 | 5.921 | 5.633E+00 | 8.170E-03 | 3.649E-12 | 34.8 | 9.00E-02 | 45.10±0.45 | 59.2 |
| 1525 | 4.745 | 5.889E+00 | 4.396E-03 | 4.240E-12 | 40.4 | 9.00E-02 | 44.35±0.24 | 72.6 |
| 1625 | 5.694 | 6.692E+00 | 7.275E-03 | 1.134E-12 | 10.8 | 8.00E-02 | 45.58±0.58 | 62.2 |
| 1675 | 11.915 | 7.117E+00 | 2.637E-02 | 1.415E-13 | 1.3 | 7.00E-02 | 52.91±4.78 | 34.6 |

P143 BIOTITE (MICHIGAN; RM4; J=0.007360; wt.=0.0714 g); Total Gas Age = 37.11 Ma; Plateau Age = 37.9±0.4 Ma.

| TEMP (K) | 40Ar/39Ar | 37Ar/39Ar | 36Ar/39Ar | 39Ar (MOLE) | %39Ar released | K/Ca | AGE ± 1 s.d. Ma | %40Ar RAD |
|---|---|---|---|---|---|---|---|---|
| 925 | 4.866 | 8.952E-03 | 7.528E-03 | 2.423E-12 | 20.4 | 5.81E+01 | 34.75±0.53 | 54.3 |
| 1075 | 3.733 | 7.461E-03 | 3.015E-03 | 2.517E-12 | 21.2 | 6.97E+01 | 37.35±0.56 | 76.1 |
| 1225 | 4.032 | 2.306E-02 | 3.692E-03 | 1.596E-12 | 13.4 | 2.26E+01 | 38.63±0.71 | 72.9 |
| 1325 | 3.714 | 7.639E-03 | 2.758E-03 | 2.198E-12 | 18.5 | 6.81E+01 | 38.08±0.56 | 78.1 |
| 1425 | 3.508 | 1.016E-02 | 2.026E-03 | 2.138E-12 | 18.0 | 5.12E+01 | 38.22±1.04 | 82.9 |
| 1525 | 3.433 | 5.073E-02 | 2.292E-03 | 8.779E-13 | 7.4 | 1.03E+01 | 36.23±1.58 | 80.3 |
| 1625 | 4.767 | 2.740E-01 | 8.453E-03 | 1.461E-13 | 1.2 | 1.90E+00 | 29.87±5.16 | 47.6 |

P155 BIOTITE (TRIGA; RD42; J=0.003500; wt.=0.1106 g); Total Gas Age = 37.5 Ma.

| TEMP (K) | 40Ar/39Ar | 37Ar/39Ar | 36Ar/39Ar | 39Ar (MOLE) | %39Ar released | K/Ca | AGE ± 1 s.d. Ma | %40Ar RAD |
|---|---|---|---|---|---|---|---|---|
| FUSE | 6.590 | 9.930E-03 | 1.959E-03 | 8.49E-12 | 100.0 | 5.24E+01 | 37.52±0.2 | 91.1 |

P156 HORNBLENDE (TRIGA; RD42; J=0.003540; wt.=0.9393 g); Total Gas Age = 45.49 Ma; Plateau Age = 44.6±0.3 Ma.

| TEMP (K) | 40Ar/39Ar | 37Ar/39Ar | 36Ar/39Ar | 39Ar (MOLE) | %39Ar released | K/Ca | AGE ± 1 s.d. Ma | %40Ar RAD |
|---|---|---|---|---|---|---|---|---|
| 925 | 60.085 | 1.138E+00 | 1.113E-01 | 6.58E-14 | 0.4 | 4.57E-01 | 166.23±2.24 | 45.4 |
| 1025 | 33.848 | 1.022E+00 | 7.186E-02 | 8.26E-14 | 0.6 | 5.09E-01 | 79.25±0.56 | 37.5 |
| 1125 | 27.268 | 1.661E+00 | 7.009E-02 | 5.35E-14 | 0.4 | 3.13E-01 | 42.15±1.51 | 24.5 |
| 1225 | 14.769 | 4.349E+00 | 2.595E-02 | 2.85E-13 | 1.9 | 1.19E-01 | 46.84±0.36 | 50.3 |
| 1325 | 9.094 | 4.761E+00 | 8.155E-03 | 1.86E-12 | 12.6 | 1.09E-01 | 44.44±0.25 | 77.5 |
| 1375 | 8.305 | 4.778E+00 | 5.358E-03 | 2.75E-12 | 18.6 | 1.08E-01 | 44.68±0.24 | 85.4 |
| 1425 | 8.061 | 4.752E+00 | 4.594E-03 | 3.05E-12 | 20.7 | 1.09E-01 | 44.56±0.25 | 87.7 |
| 1475 | 7.926 | 4.739E+00 | 4.155E-03 | 2.62E-12 | 17.7 | 1.09E-01 | 44.52±0.25 | 89.1 |
| 1525 | 7.876 | 4.720E+00 | 3.755E-03 | 2.16E-12 | 14.6 | 1.10E-01 | 44.93±0.26 | 90.5 |
| 1625 | 7.842 | 4.833E+00 | 3.857E-03 | 1.44E-12 | 9.8 | 1.07E-01 | 44.59±0.25 | 90.2 |
| FUSE | 9.680 | 4.957E+00 | 8.404E-03 | 3.86E-13 | 2.6 | 1.05E-01 | 47.73±0.28 | 78.3 |

P156 BIOTITE (TRIGA; RD42; J=0.003470); Total Gas Age = 36.81 Ma.

| TEMP (K) | 40Ar/39Ar | 37Ar/39Ar | 36Ar/39Ar | 39Ar (MOLE) | %39Ar released | K/Ca | AGE ± 1 s.d. Ma | %40Ar RAD |
|---|---|---|---|---|---|---|---|---|
| FUSE | 6.524 | 2.551E-02 | 1.966E-03 | 2.36E-11 | 100.0 | 2.04E+01 | 36.81±0.18 | 91.0 |

P251 HORNBLENDE (MICHIGAN; RM4; J=0.007410; wt.=0.5226); Total Gas Age = 47.14 Ma; Correlation Age = 44.7±0.8 Ma.

| TEMP (K) | 40Ar/39Ar | 37Ar/39Ar | 36Ar/39Ar | 39Ar (MOLE) | %39Ar released | K/Ca | AGE ± 1 s.d. Ma | %40Ar RAD |
|---|---|---|---|---|---|---|---|---|
| 1325 | 5.755 | 4.738E+00 | 6.822E-03 | 2.033E-12 | 20.1 | 1.10E-01 | 49.31±0.47 | 65.0 |
| 1375 | 5.214 | 4.792E+00 | 5.431E-03 | 1.816E-12 | 18.0 | 1.10E-01 | 47.60±0.64 | 69.2 |
| 1400 | 4.675 | 4.859E+00 | 3.760E-03 | 2.664E-12 | 26.4 | 1.10E-01 | 47.02±0.61 | 76.2 |
| 1425 | 4.986 | 4.938E+00 | 4.389E-03 | 1.179E-12 | 11.7 | 1.10E-01 | 48.63±0.72 | 74.0 |
| 1450 | 5.167 | 5.086E+00 | 5.987E-03 | 7.464E-13 | 7.4 | 1.00E-01 | 44.86±1.42 | 65.8 |
| 1475 | 5.496 | 5.129E+00 | 7.759E-03 | 3.980E-13 | 3.9 | 1.00E-01 | 42.32±1.40 | 58.3 |
| 1525 | 5.208 | 4.997E+00 | 6.494E-03 | 4.307E-13 | 4.3 | 1.00E-01 | 43.43±0.92 | 63.1 |
| 1625 | 5.311 | 4.938E+00 | 7.055E-03 | 3.296E-13 | 3.3 | 1.10E-01 | 42.63±3.57 | 60.8 |

P251 BIOTITE (MICHIGAN; RM4; J=0.007422; wt.=0.1027 g); Total Gas Age = 35.18 Ma.

| TEMP (K) | 40Ar/39Ar | 37Ar/39Ar | 36Ar/39Ar | 39Ar (MOLE) | %39Ar released | K/Ca | AGE ± 1 s.d. Ma | %40Ar RAD |
|---|---|---|---|---|---|---|---|---|
| FUSE | 4.272 | 1.595E-02 | 5.473E-03 | 1.569E-11 | 100.0 | 3.26E+01 | 35.18±0.20 | 62.1 |

P285 BIOTITE (MICHIGAN; RM4; J=0.007423; wt.=0.0708 g); Total Gas Age = 47.10 Ma.

| TEMP (K) | 40Ar/39Ar | 37Ar/39Ar | 36Ar/39Ar | 39Ar (MOLE) | %39Ar released | K/Ca | AGE ± 1 s.d. Ma | %40Ar RAD |
|---|---|---|---|---|---|---|---|---|
| FUSE | 4.105 | 1.110E-01 | 1.833E-03 | 6.536E-12 | 100.0 | 4.68E+00 | 47.10±0.32 | 86.8 |

P285 K-FELDSPAR (MICHIGAN; RM4; J=0.007060; wt.=0.1086 g); Total Gas Age = 44.83 Ma; Plateau Age = 44.5±0.5 Ma.

| TEMP (K) | 40Ar/39Ar | 37Ar/39Ar | 36Ar/39Ar | 39Ar (MOLE) | %39Ar released | K/Ca | AGE ± 1 s.d.M | %40ArRAD |
|---|---|---|---|---|---|---|---|---|
| 925 | 5.264 | 1.822E-02 | 4.295E-03 | 2.270E-12 | 9.5 | 28.54 | 50.18±0.58 | 75.9 |
| 1025 | 4.264 | 1.211E-02 | 1.848E-03 | 1.009E-12 | 4.2 | 42.95 | 46.74±0.69 | 87.2 |
| 1125 | 3.683 | 2.371E-03 | 0.000E+00 | 7.254E-13 | 3.0 | 219.37 | 43.97±0.82 | 94.9 |
| 1225 | 3.630 | 1.319E-02 | 6.500E-04 | 1.083E-12 | 4.5 | 39.44 | 43.26±0.57 | 94.7 |
| 1325 | 3.753 | 1.170E-02 | 1.155E-03 | 1.158E-12 | 4.9 | 44.44 | 42.93±0.46 | 90.9 |
| 1425 | 3.873 | 1.219E-02 | 1.587E-03 | 1.624E-12 | 6.8 | 42.66 | 42.83±0.32 | 87.9 |
| 1525 | 3.884 | 9.302E-03 | 1.387E-03 | 3.968E-12 | 16.6 | 55.91 | 43.70±0.32 | 89.4 |
| 1625 | 3.875 | 4.149E-03 | 1.148E-03 | 7.277E-12 | 30.5 | 125.35 | 44.48±0.23 | 91.2 |
| 1725 | 3.969 | 2.141E-03 | 1.344E-03 | 3.865E-12 | 16.2 | 242.92 | 44.94±0.32 | 90.0 |
| 1825 | 4.166 | 0.00E+00 | 0.000E+00 | 8.733E-13 | 3.7 | 0.00 | 45.16±3.78 | 86.2 |

P443 K-FELDSPAR (MICHIGAN; RM4; J=0.007150; wt.=0.1055 g); Total Gas Age = 37.09 Ma; Minimum Age = 33.0±0.6 Ma.

| TEMP (K) | 40Ar/39Ar | 37Ar/39Ar | 36Ar/39Ar | 39Ar (MOLE) | %39Ar released | K/Ca | AGE ± 1 s.d. Ma | %40Ar RAD |
|---|---|---|---|---|---|---|---|---|
| 925 | 3.406 | 3.951E-01 | 2.798E-03 | 2.481E-12 | 10.8 | 1.32E+00 | 32.97±0.30 | 75.7 |
| 1025 | 3.674 | 1.893E-01 | 1.823E-03 | 1.219E-12 | 5.3 | 2.75E+00 | 40.01±0.52 | 85.3 |
| 1125 | 4.781 | 2.276E-01 | 1.326E-03 | 6.844E-13 | 2.9 | 2.28E+00 | 55.74±0.97 | 91.8 |
| 1225 | 2.759 | 2.698E-02 | 3.399E-04 | 4.552E-12 | 19.8 | 1.93E+01 | 33.98±0.26 | 96.4 |
| 1300 | 2.861 | 1.894E-02 | 2.955E-04 | 5.492E-12 | 23.9 | 2.75E+01 | 35.43±0.27 | 96.9 |
| 1375 | 3.038 | 2.453E-02 | 3.920E-04 | 4.977E-12 | 21.9 | 2.12E+01 | 37.31±0.22 | 96.2 |
| 1450 | 3.110 | 2.464E-02 | 6.000E-04 | 2.250E-12 | 9.8 | 2.11E+01 | 37.43±0.47 | 94.3 |
| 1525 | 3.625 | 6.316E-02 | 1.332E-03 | 8.934E-13 | 3.9 | 8.23E+00 | 41.21±1.31 | 89.1 |
| 1600 | 4.318 | 1.019E-01 | 1.497E-03 | 4.113E-13 | 1.8 | 5.10E+00 | 49.32±1.26 | 89.8 |

P447 HORNBLENDE (MICHIGAN; RM4; J=0.007409; wt.=0.6867 g); Total Gas Age = 137.82 Ma; Correlation Age = 53.2 ±7.0 Ma.

| TEMP | 40Ar/39Ar | 37Ar/39Ar | 36Ar/39Ar | 39Ar (MOLE) | %39Ar | K/Ca | AGE ± 1 s.d. | %40Ar |
|---|---|---|---|---|---|---|---|---|

| (K) | | | | | released | | Ma | RAD |
|---|---|---|---|---|---|---|---|---|
| 925 | 115.525 | 1.573E+00 | 1.501E-01 | 2.029E-13 | 3.2 | 3.30E-01 | 764.03±4.21 | 61.6 |
| 1125 | 36.119 | 1.237E+00 | 5.121E-02 | 2.105E-13 | 3.3 | 4.20E-01 | 260.73±5.72 | 58.1 |
| 1225 | 18.860 | 4.561E+00 | 3.458E-02 | 2.333E-13 | 3.6 | 1.10E-01 | 111.97±3.79 | 45.8 |
| 1325 | 12.356 | 7.791E+00 | 1.727E-02 | 4.613E-13 | 7.2 | 7.00E-02 | 94.39±2.05 | 58.7 |
| 1375 | 11.273 | 7.804E+00 | 1.181E-02 | 5.866E-13 | 9.1 | 7.00E-02 | 101.15±0.61 | 69.1 |
| 1425 | 11.274 | 7.574E+00 | 9.288E-03 | 5.659E-13 | 8.8 | 7.00E-02 | 110.52±1.33 | 75.7 |
| 1475 | 10.527 | 7.392E+00 | 8.457E-03 | 7.147E-13 | 11.1 | 7.00E-02 | 104.22±1.65 | 76.3 |
| 1525 | 9.940 | 6.674E+00 | 7.389E-03 | 1.176E-12 | 18.3 | 8.00E-02 | 100.76±0.55 | 78.0 |
| 1575 | 11.840 | 6.198E+00 | 9.750E-03 | 1.723E-12 | 26.9 | 8.00E-02 | 115.95±0.67 | 75.7 |
| 1725 | 10.997 | 5.464E+00 | 9.533E-03 | 5.889E-13 | 8.4 | 9.00E-02 | 115.67±2.04 | 74.4 |

P450C MUSCOVITE (MICHIGAN; RM4; J=0.007374; wt.=0.0743 g); Total Gas Age = 38.04Ma; Minimum Age = 35.9±0.6 Ma,

| TEMP (K) | 40Ar/39Ar | 37Ar/39Ar | 36Ar/39Ar | 39Ar (MOLE) | %39Ar released | K/Ca | AGE ± 1 s.d. Ma | %40Ar RAD |
|---|---|---|---|---|---|---|---|---|
| 725 | 9.664 | 8.789E-02 | 2.065E-02 | 1.932E-13 | 1.6 | 5.92E+00 | 46.76±4.33 | 36.9 |
| 825 | 4.806 | 7.789E-02 | 5.423E-03 | 2.316E-13 | 1.9 | 6.68E+00 | 42.13±5.58 | 66.7 |
| 925 | 3.584 | 5.195E-02 | 2.701E-03 | 3.965E-13 | 3.3 | 1.00E+01 | 36.68±2.83 | 77.7 |
| 975 | 3.649 | 1.359E-01 | 2.741E-03 | 4.429E-13 | 3.7 | 3.83E+00 | 37.38±1.95 | 77.8 |
| 1075 | 3.431 | 5.901E-02 | 1.642E-03 | 9.257E-13 | 7.7 | 8.81E+00 | 38.76±0.38 | 85.9 |
| 1175 | 3.183 | 1.717E-02 | 1.537E-03 | 2.146E-12 | 17.9 | 3.03E+01 | 35.94±0.28 | 85.7 |
| 1225 | 3.216 | 2.292E-02 | 1.113E-03 | 2.089E-12 | 17.4 | 2.27E+01 | 38.01±0.36 | 89.8 |
| 1275 | 3.252 | 2.118E-02 | 1.506E-03 | 7.438E-13 | 6.2 | 2.46E+01 | 36.96±2.15 | 86.3 |
| 1325 | 3.263 | 1.925E-02 | 1.513E-03 | 9.340E-13 | 7.8 | 2.70E+01 | 37.08±0.70 | 86.3 |
| 1375 | 3.245 | 2.449E-02 | 1.592E-03 | 9.895E-13 | 8.3 | 2.12E+01 | 36.55±0.52 | 85.5 |
| 1425 | 3.274 | 2.386E-02 | 1.130E-03 | 1.636E-12 | 13.7 | 2.18E+01 | 38.68±0.62 | 89.8 |
| 1475 | 3.437 | 4.828E-02 | 1.461E-03 | 8.581E-13 | 7.2 | 1.08E+01 | 39.53±0.82 | 87.4 |
| 1525 | 4.419 | 7.310E-02 | 4.535E-03 | 2.216E-13 | 1.9 | 7.12E+00 | 40.48±1.60 | 69.7 |
| 1575 | 6.558 | 1.499E-01 | 7.716E-03 | 1.171E-13 | 1.0 | 3.47E+00 | 56.03±10.15 | 65.2 |
| 1725 | 13.037 | 4.705E-01 | 3.327E-02 | 5.239E-14 | 0.4 | 1.11E+00 | 42.17±33.10 | 24.6 |

P450C BIOTITE (MICHIGAN; RM4; J=0.007362; wt.=0.0395); Total Gas Age = 35.79 Ma; Plateau Age = 34.7±0.5 Ma.

| TEMP (K) | 40Ar/39Ar | 37Ar/39Ar | 36Ar/39Ar | 39Ar (MOLE) | %39Ar released | K/Ca | AGE ± 1 s.d. Ma | %40Ar RAD |
|---|---|---|---|---|---|---|---|---|
| 725 | 5.558 | 1.381E-02 | 9.425E-03 | 6.522E-13 | 12.1 | 3.77E+01 | 36.45±1.24 | 49.9 |
| 925 | 3.420 | 6.434E-03 | 2.298E-03 | 1.347E-12 | 25.0 | 8.08E+01 | 36.05±0.56 | 80.1 |
| 1025 | 2.963 | 3.910E-03 | 9.649E-04 | 1.082E-12 | 20.1 | 1.33E+02 | 35.23±1.70 | 90.4 |
| 1125 | 3.122 | 2.605E-02 | 2.196E-03 | 3.594E-13 | 6.7 | 2.00E+01 | 32.55±4.99 | 79.2 |
| 1225 | 3.432 | 0.000E+00 | 2.524E-03 | 3.339E-13 | 6.2 | 0.00E+00 | 35.34±4.84 | 78.3 |
| 1325 | 3.188 | 4.126E-03 | 1.356E-03 | 5.659E-13 | 10.5 | 1.26E+02 | 36.64±1.79 | 87.4 |
| 1425 | 3.019 | 1.531E-02 | 1.442E-03 | 5.863E-13 | 10.9 | 3.40E+01 | 34.11±0.61 | 85.9 |
| 1525 | 3.123 | 6.719E-02 | 0.000E+00 | 3.481E-13 | 6.5 | 7.74E+00 | 36.92±1.55 | 90.0 |
| 1625 | 3.550 | 7.785E-02 | 0.000E+00 | 1.168E-13 | 2.2 | 6.68E+00 | 46.70±12.52 | 100.0 |

P450D BIOTITE (MICHIGAN; RM4; J=0.007411; wt.=0.1012 g); Total Gas Age = 36.1 Ma.

| TEMP (K) | 40Ar/39Ar | 37Ar/39Ar | 36Ar/39Ar | 39Ar (MOLE) | %39Ar released | K/Ca | AGE ± 1 s.d. Ma | %40Ar RAD |
|---|---|---|---|---|---|---|---|---|
| FUSE | 2.893 | 1.335E-02 | 5.732E-04 | 1.491E-11 | 100.0 | 3.89E+01 | 36.05±0.19 | 94.1 |

P450E HORNBLENDE (MICHIGAN; RM4; J=0.007421; wt.=0.3490 g); Total Gas Age = 73.99 Ma; Plateau Age = 79.3±1.1 Ma.

| TEMP (K) | 40Ar/39Ar | 37Ar/39Ar | 36Ar/39Ar | 39Ar (MOLE) | %39Ar released | K/Ca | AGE ± 1 s.d. Ma | %40Ar RAD |
|---|---|---|---|---|---|---|---|---|
| 725 | 129.671 | 2.340E+00 | 2.205E-01 | 4.496E-14 | 1.5 | 2.20E-01 | 705.51±12.48 | 49.7 |
| 925 | 42.843 | 1.217E+00 | 6.864E-02 | 5.994E-14 | 2.0 | 4.30E-01 | 279.22±24.02 | 52.7 |
| 1125 | 14.042 | 1.866E+00 | 3.250E-02 | 6.828E-14 | 2.3 | 2.80E-01 | 58.47±22.05 | 31.6 |
| 1225 | 10.563 | 5.793E+00 | 2.320E-02 | 1.635E-13 | 5.6 | 9.00E-02 | 48.97±6.74 | 35.1 |
| 1300 | 8.803 | 1.060E+01 | 1.236E-02 | 2.808E-13 | 9.6 | 5.00E-02 | 67.65±2.64 | 58.5 |
| 1350 | 9.163 | 1.120E+01 | 1.230E-02 | 3.537E-13 | 12.1 | 5.00E-02 | 72.52±2.77 | 60.3 |
| 1395 | 8.846 | 1.146E+01 | 1.093E-02 | 3.881E-13 | 13.3 | 5.00E-02 | 73.67±1.34 | 63.5 |
| 1435 | 8.689 | 1.170E+01 | 9.620E-03 | 3.813E-13 | 13.0 | 4.00E-02 | 76.61±3.08 | 67.3 |
| 1475 | 7.791 | 1.166E+01 | 5.678E-03 | 6.959E-13 | 23.8 | 4.00E-02 | 80.04±1.24 | 78.5 |
| 1515 | 8.326 | 1.158E+01 | 8.010E-03 | 3.136E-13 | 10.7 | 4.00E-02 | 78.04±2.45 | 71.6 |
| 1575 | 10.884 | 1.150E+01 | 1.716E-02 | 1.097E-13 | 3.7 | 5.00E-02 | 76.25±13.21 | 53.4 |
| 1725 | 14.726 | 1.123E+01 | 3.451E-02 | 6.879E-14 | 2.3 | 5.00E-02 | 59.62±17.45 | 30.7 |

P452D HORNBLENDE (MICHIGAN; RM4; J=0.007415; wt.=0.6346 g); Total Gas Age = 66.81 Ma; Correlation Age = 55.6±10 Ma.

| TEMP (K) | 40Ar/39Ar | 37Ar/39Ar | 36Ar/39Ar | 39Ar (MOLE) | %39Ar released | K/Ca | AGE ± 1 s.d. Ma | %40Ar RAD |
|---|---|---|---|---|---|---|---|---|
| 1225 | 14.664 | 5.203E+00 | 2.543E-02 | 3.992E-13 | 3.0 | 1.00E-01 | 93.23±3.11 | 48.8 |
| 1325 | 6.805 | 4.755E+00 | 5.228E-03 | 2.936E-12 | 22.3 | 1.10E-01 | 69.00±0.78 | 77.3 |
| 1375 | 5.458 | 4.314E+00 | 2.954E-03 | 2.979E-12 | 22.6 | 1.20E-01 | 60.31±0.39 | 84.0 |
| 1400 | 6.023 | 4.317E+00 | 2.287E-03 | 1.740E-12 | 13.2 | 1.20E-01 | 70.16±1.00 | 88.8 |
| 1425 | 5.714 | 4.172E+00 | 1.792E-03 | 2.205E-12 | 16.7 | 1.20E-01 | 68.05±0.80 | 90.7 |
| 1450 | 5.296 | 4.144E+00 | 1.175E-03 | 1.926E-12 | 14.6 | 1.30E-01 | 65.01±0.86 | 93.4 |
| 1475 | 5.300 | 4.223E+00 | 1.465E-03 | 9.847E-13 | 7.5 | 1.20E-01 | 63.95±0.73 | 91.8 |

40Ar is total measured 40Ar (Initial + Radiogenic).
39Ar is Potassium-derived 39Ar.
37Ar are corrected values determined using a Ca-decay constant of 8.25E-4 disintegrations/hour for 37Ar.
36Ar is initial 36Ar corrected for Cl- and Ca-produced 36Ar.
K/Ca are calculated using the equation given in Fleck et al., 1977.
Decay constants as in Steiger and Jaeger, 1977.
Uncertainties are calculated as in Haugerud and Kunk, 1988.

Michigan Reactor Constants:
Ca-factors: 3637=2.6e-4±7.0e-6; 3837=5.1e-5±1.1e-5; 3937=7.6e-4±6.4e-6.
K-factors: 3739=0.0±0.0; 3839=1.2e-2±1.8e-4; 4039=2.3e-2±2.2e-3

Appendix IV: $^{40}Ar$-$^{39}Ar$ Release Spectrum and Isotope Correlation Plots for All Samples: Compiled in numerical order by sample field number.

P92 hornblende

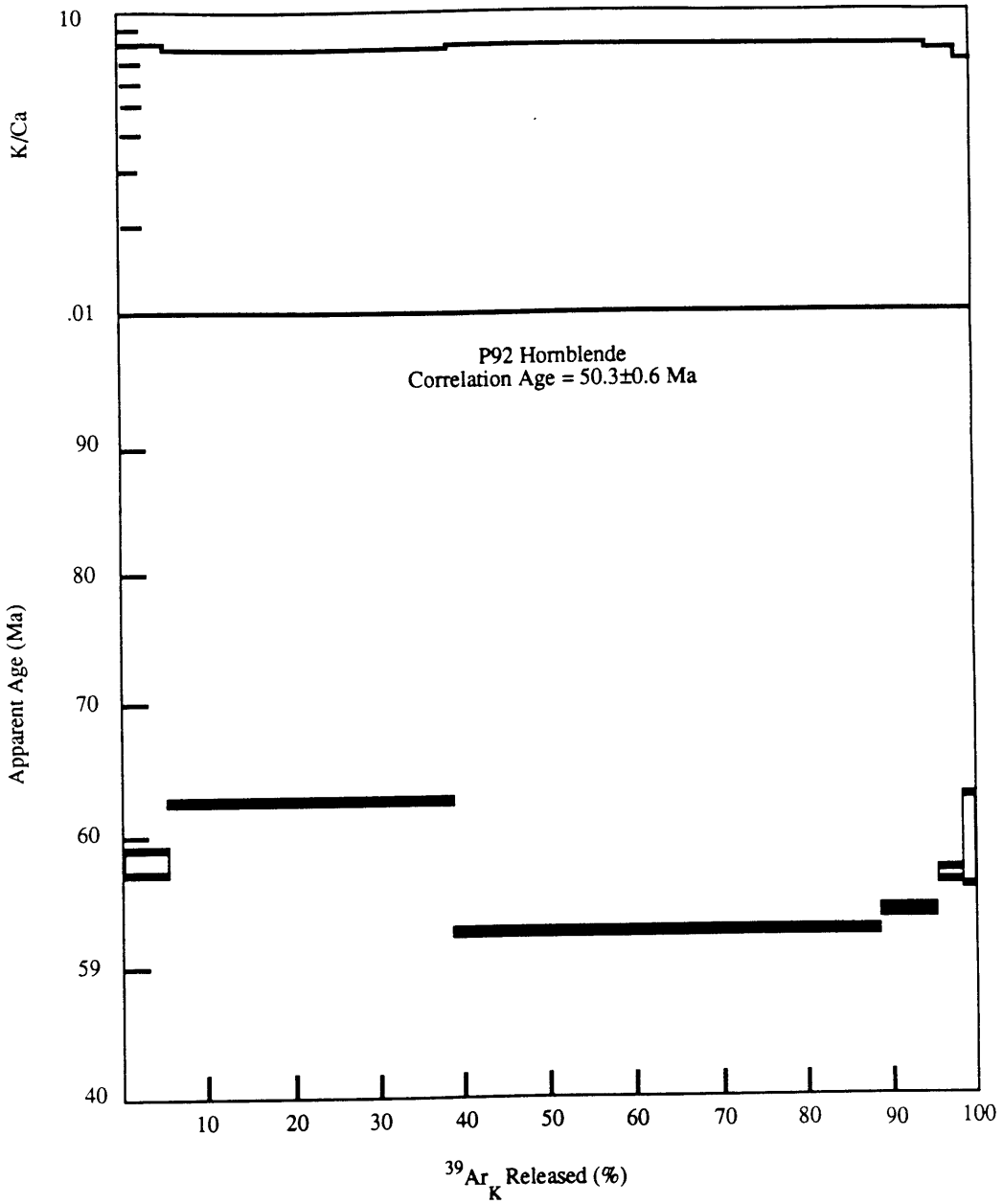

P92 hornblende

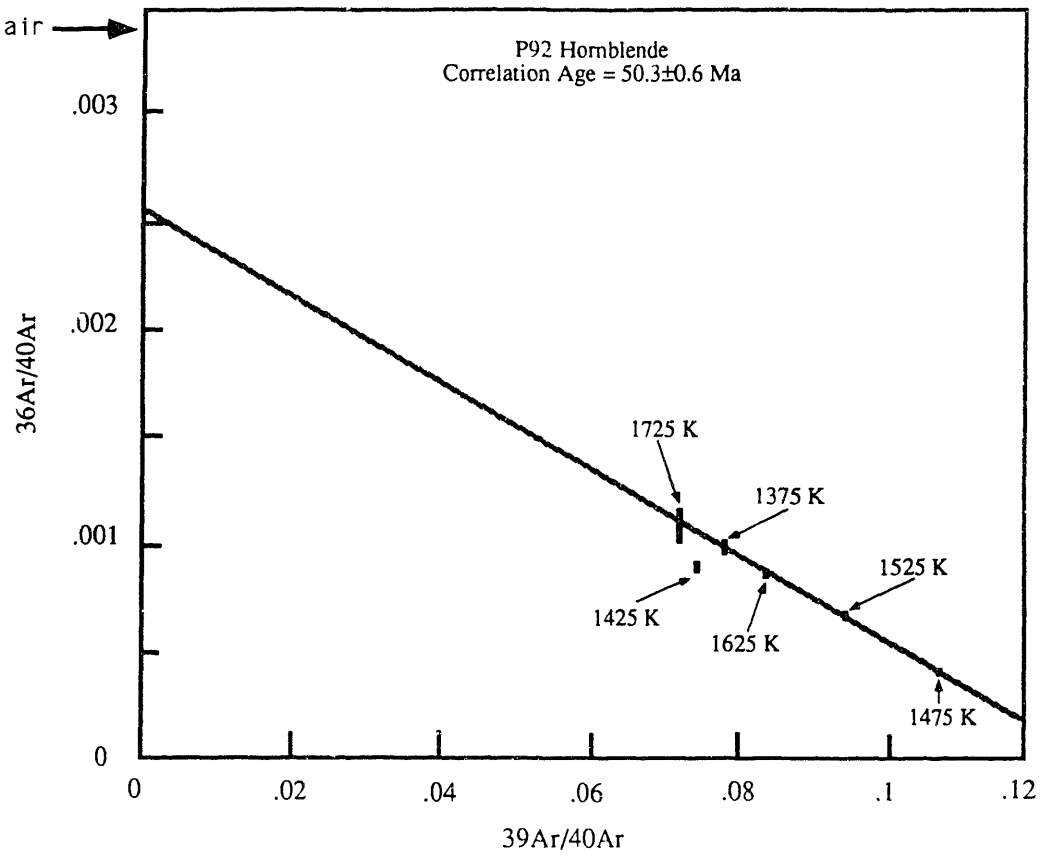

P106A K-feldspar

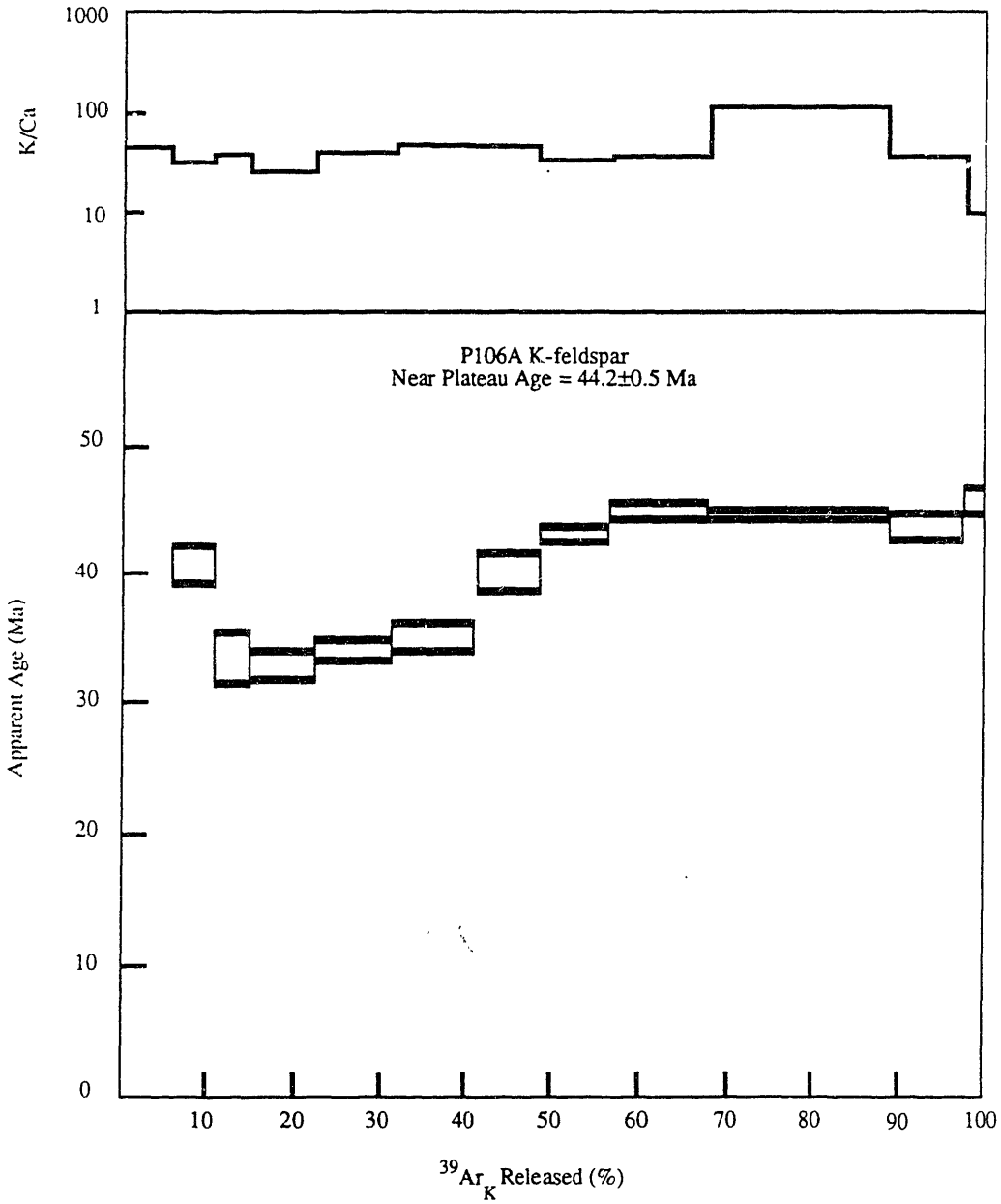

P106B hornblende

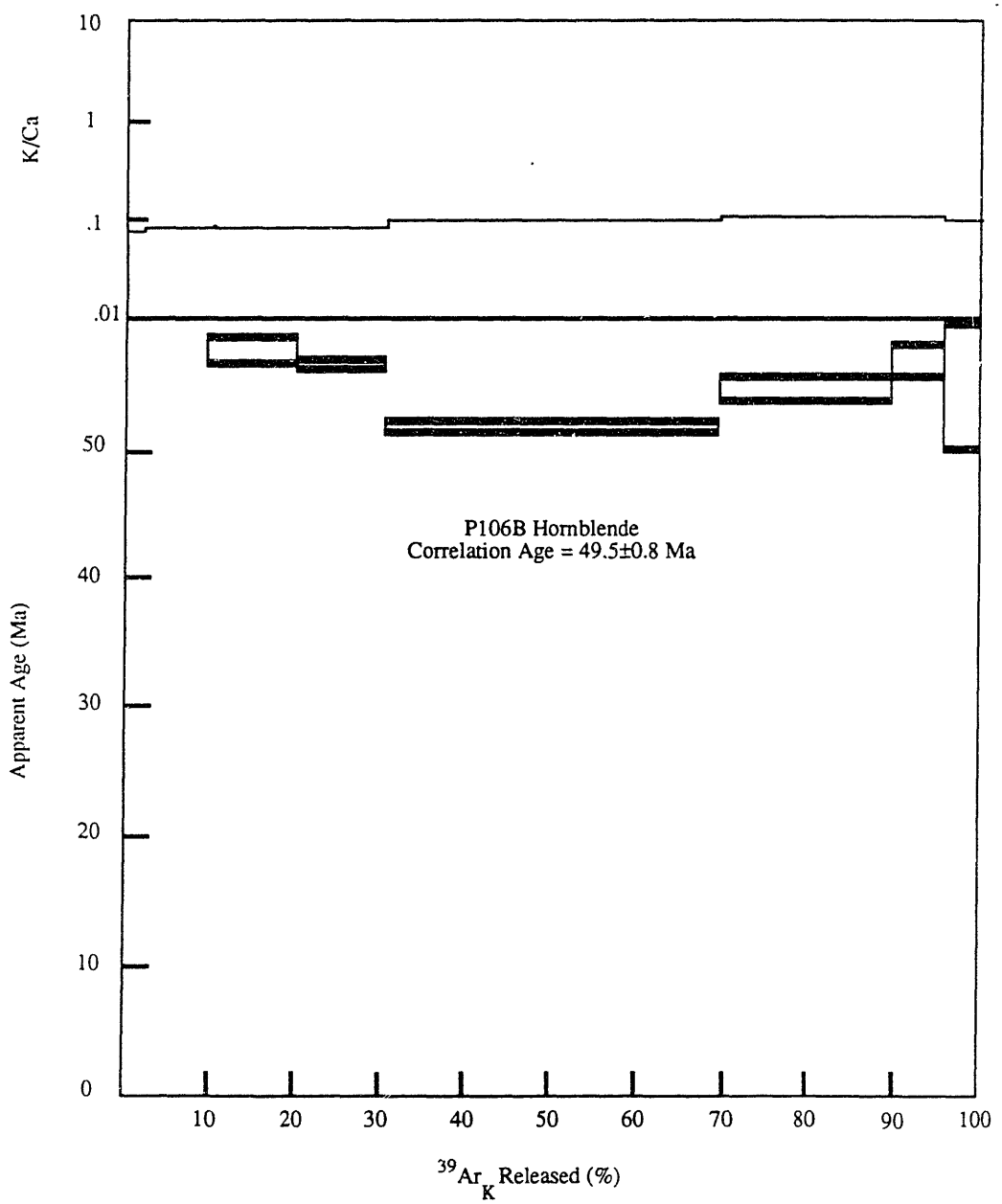

P106B hornblende

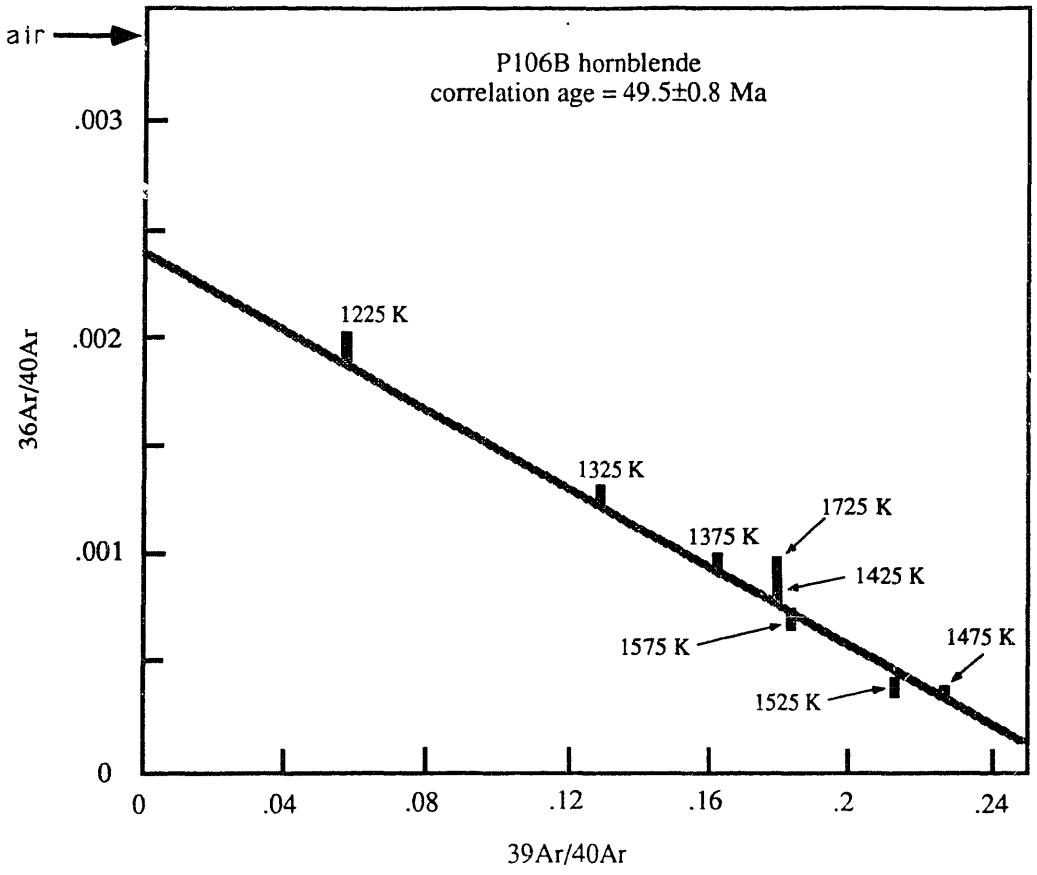

P110 hornblende

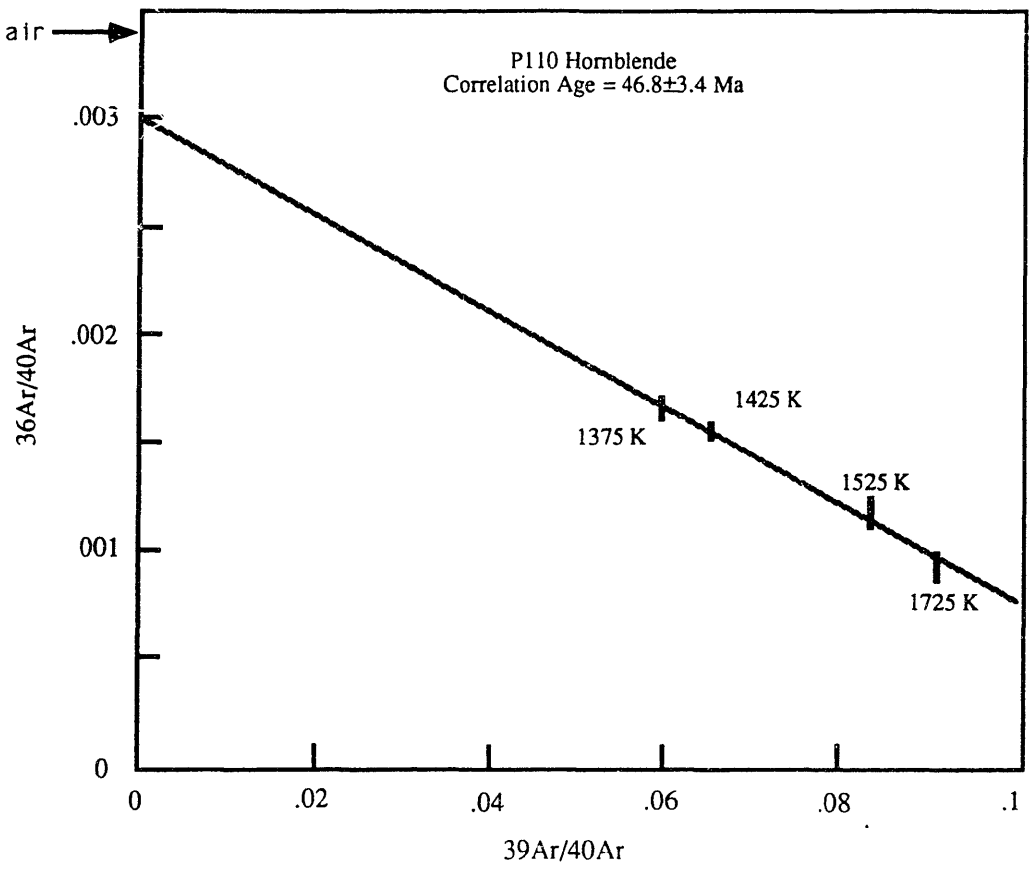

P139 muscovite

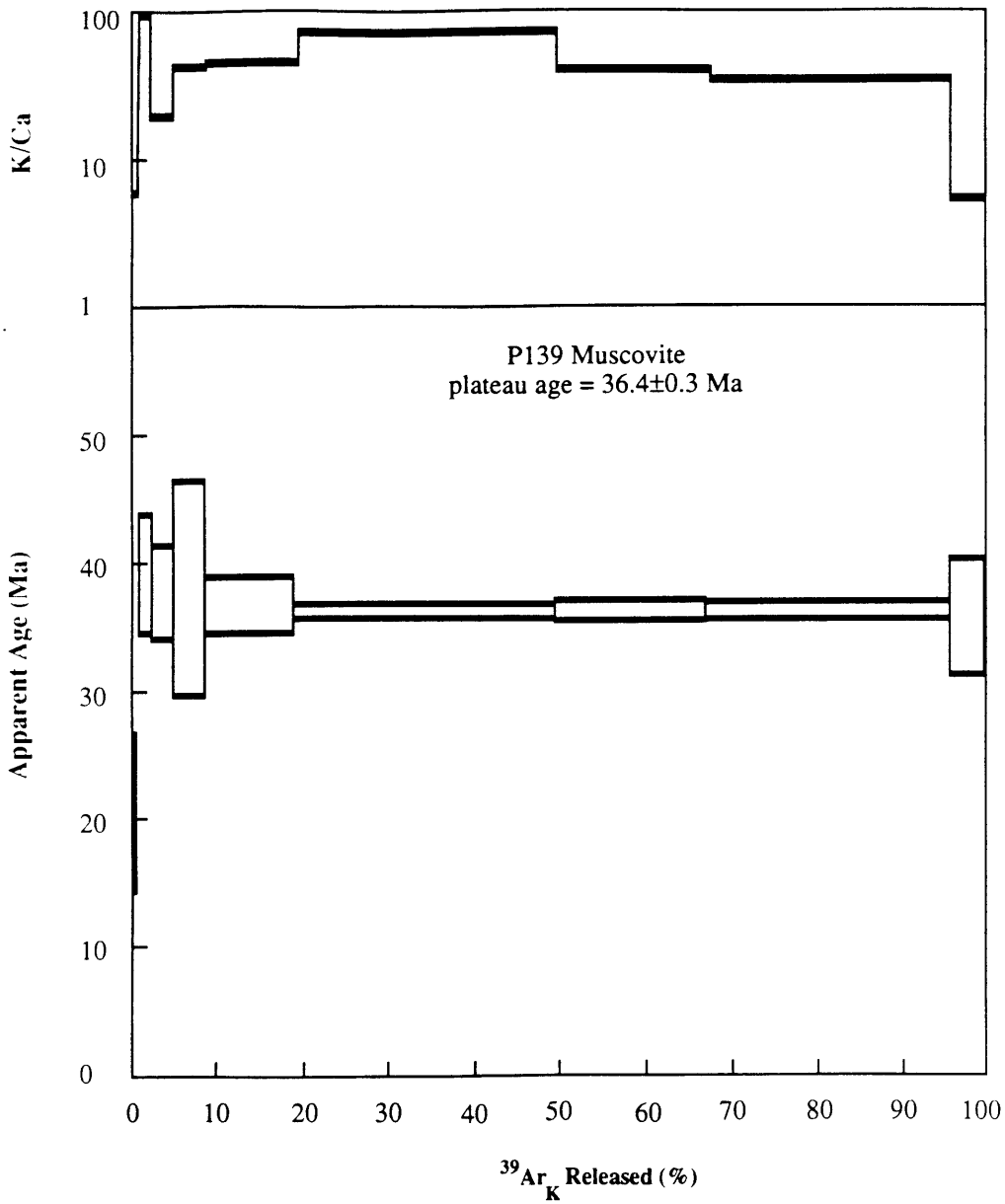

P141 muscovite

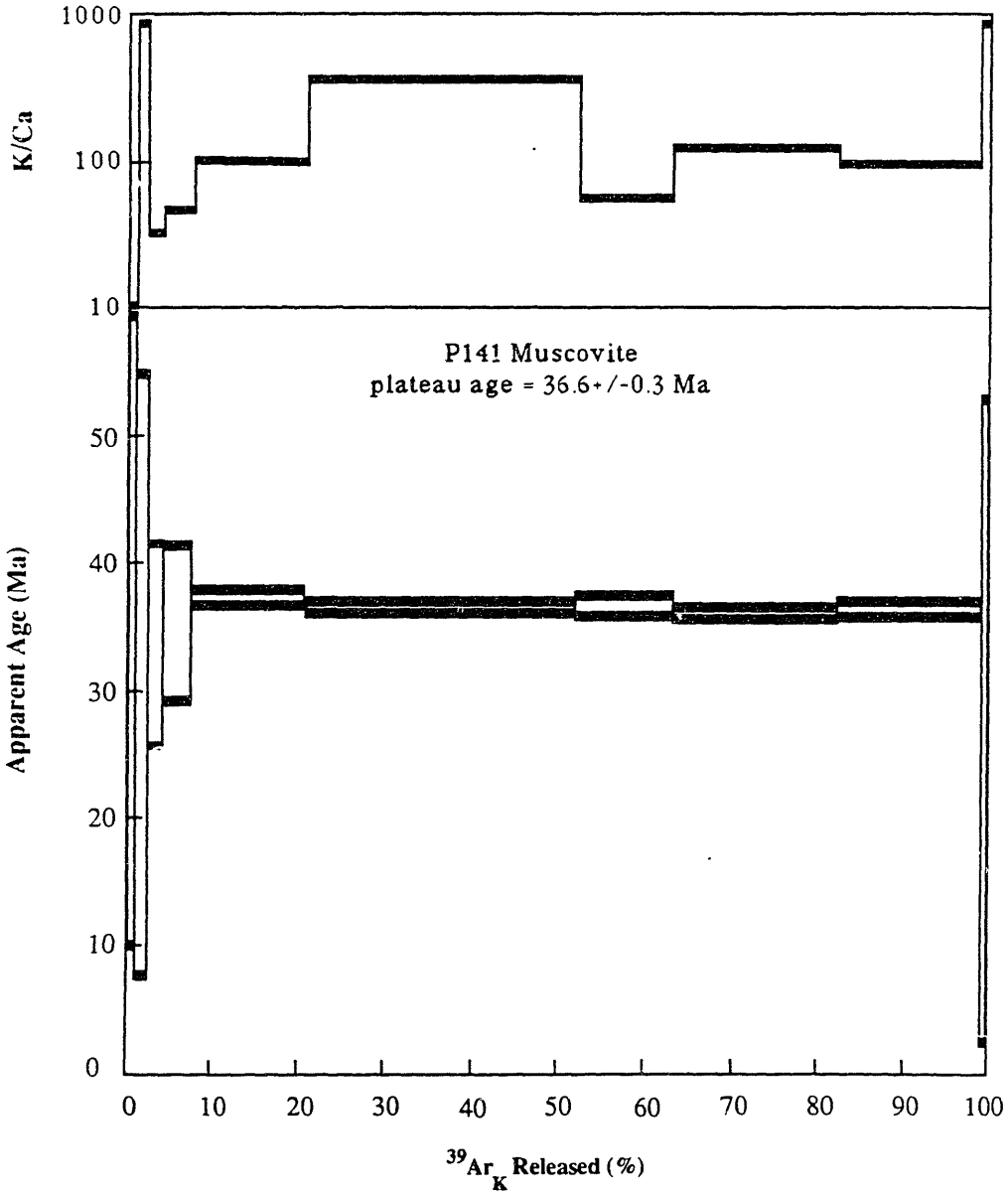

P143 hornblende

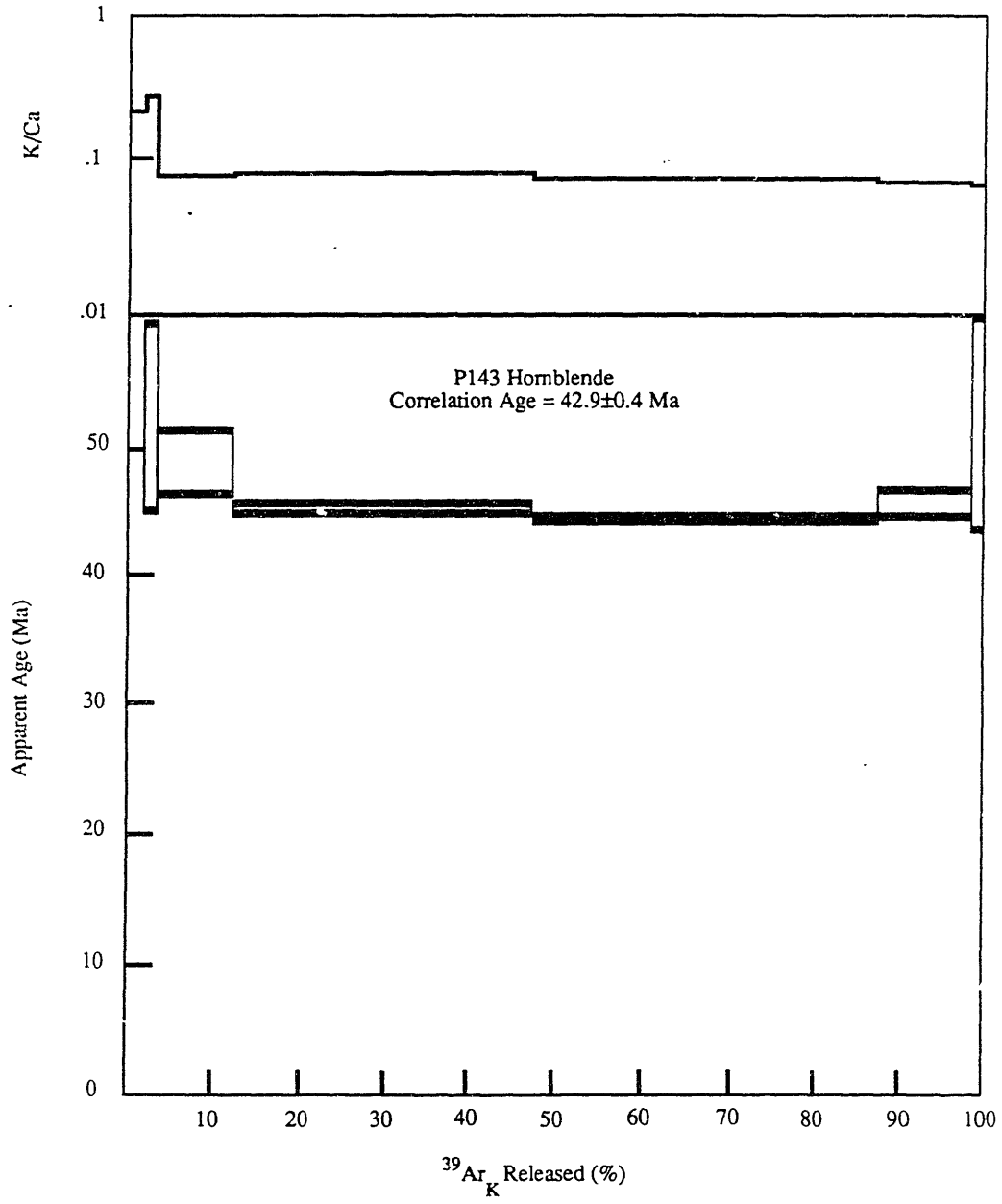

P143 hornblende

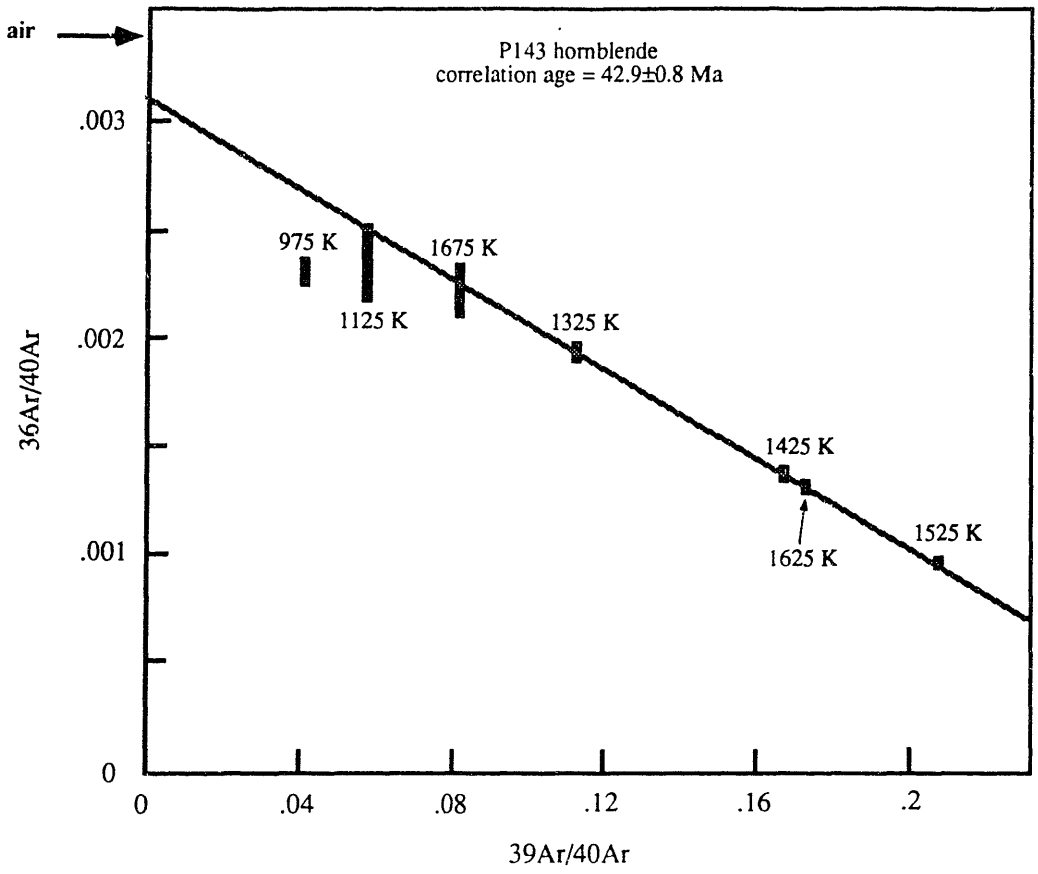

P143 biotite

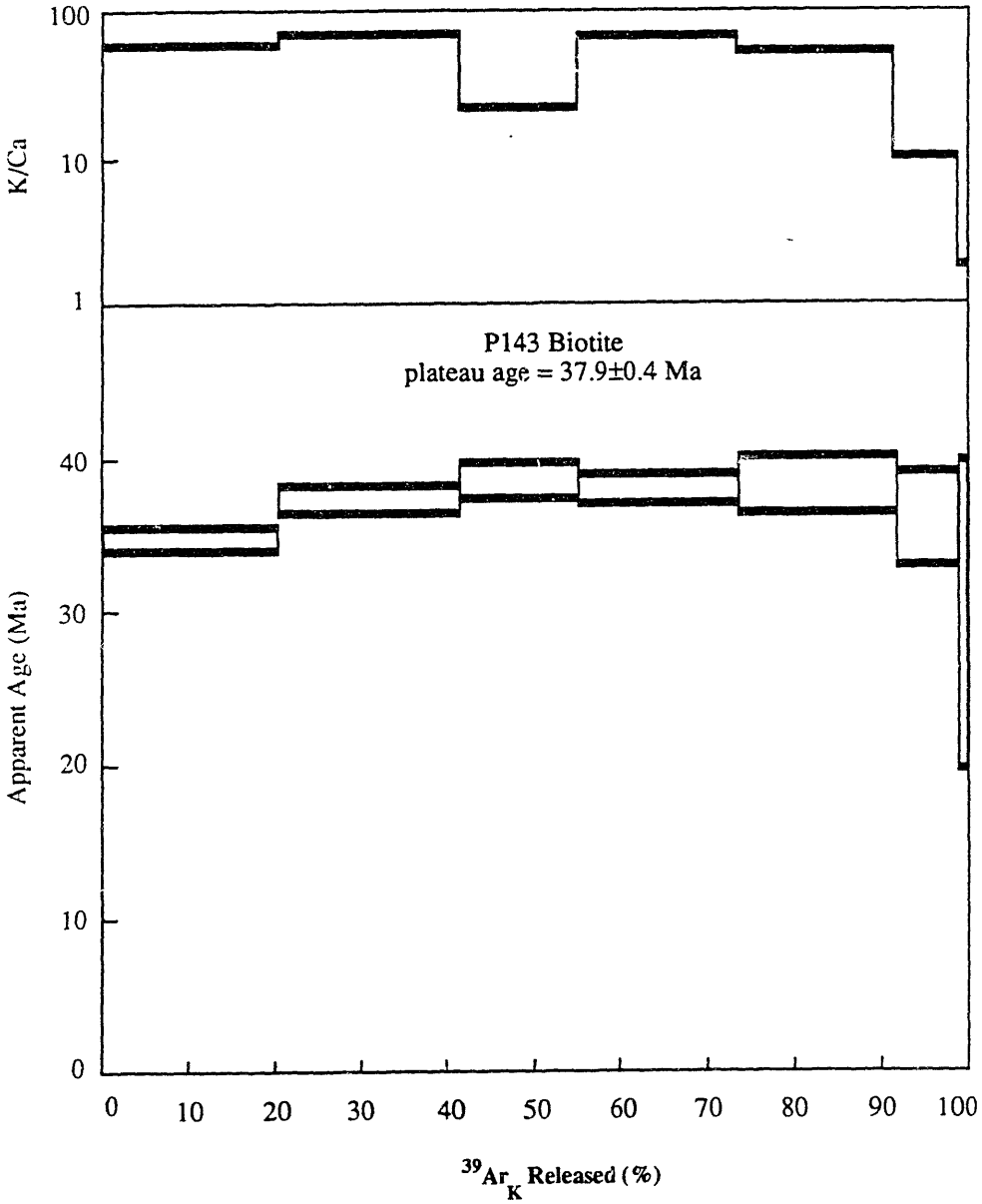

P156 horblende

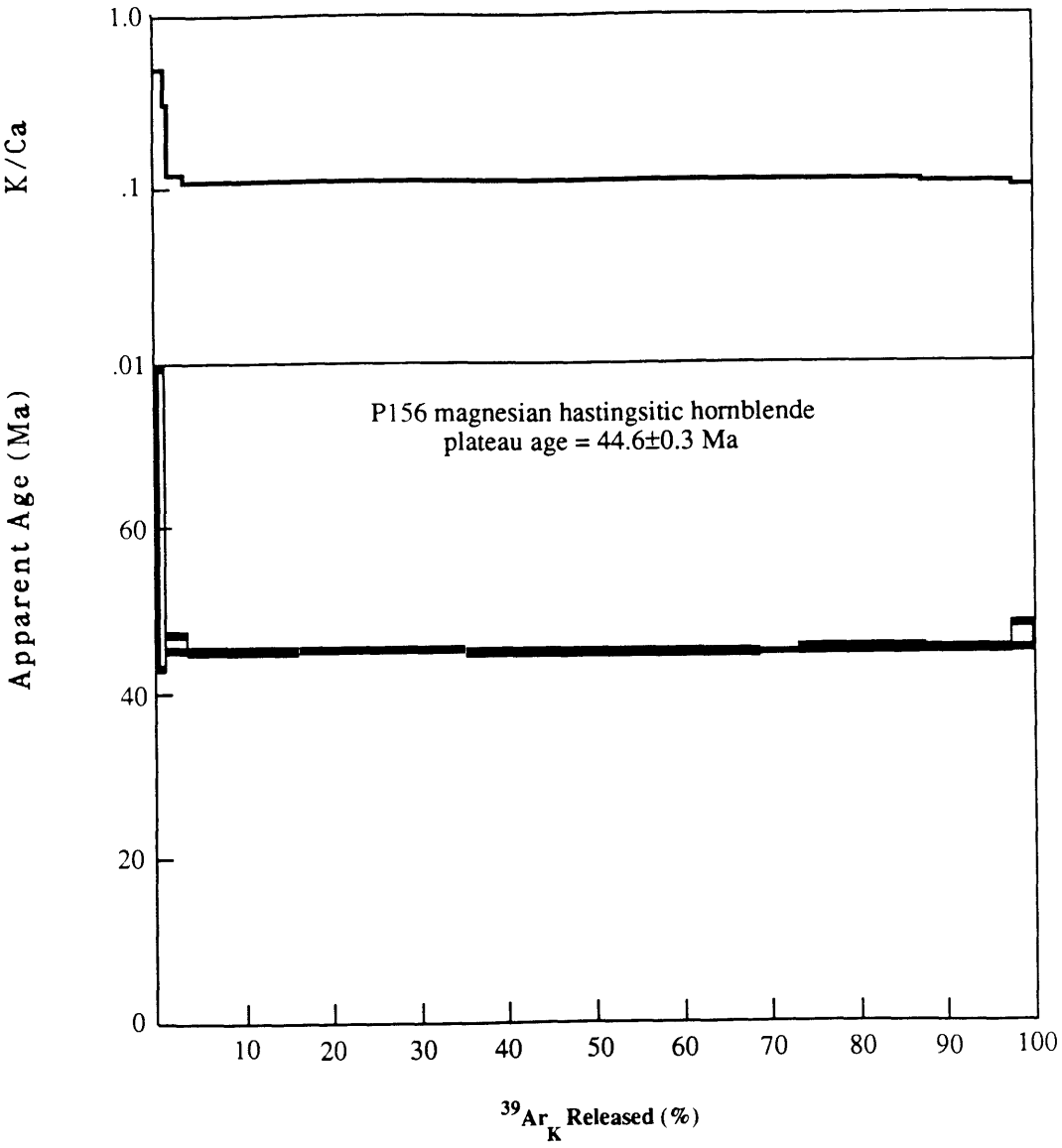

P251 hornblende

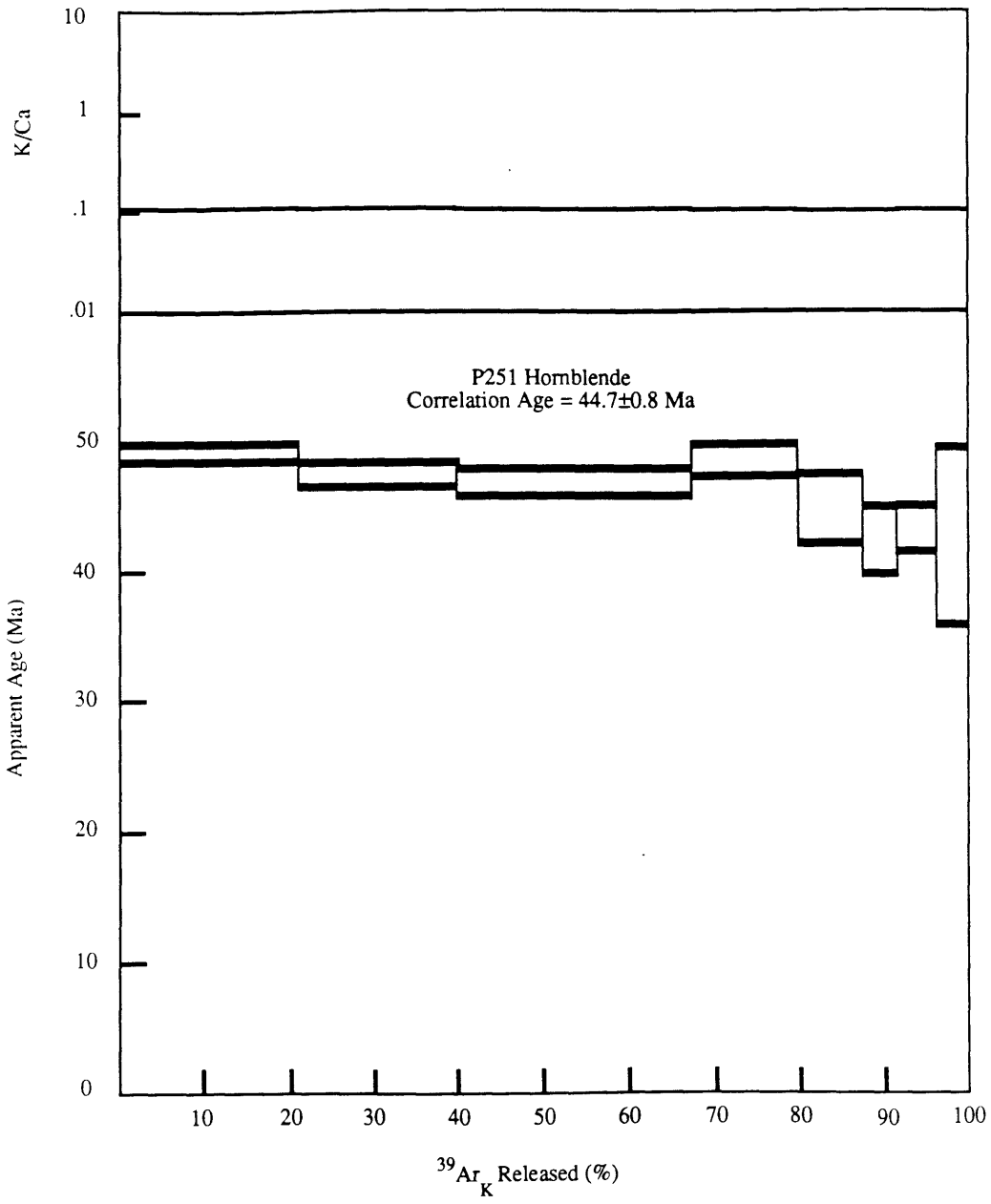

P251 hornblende

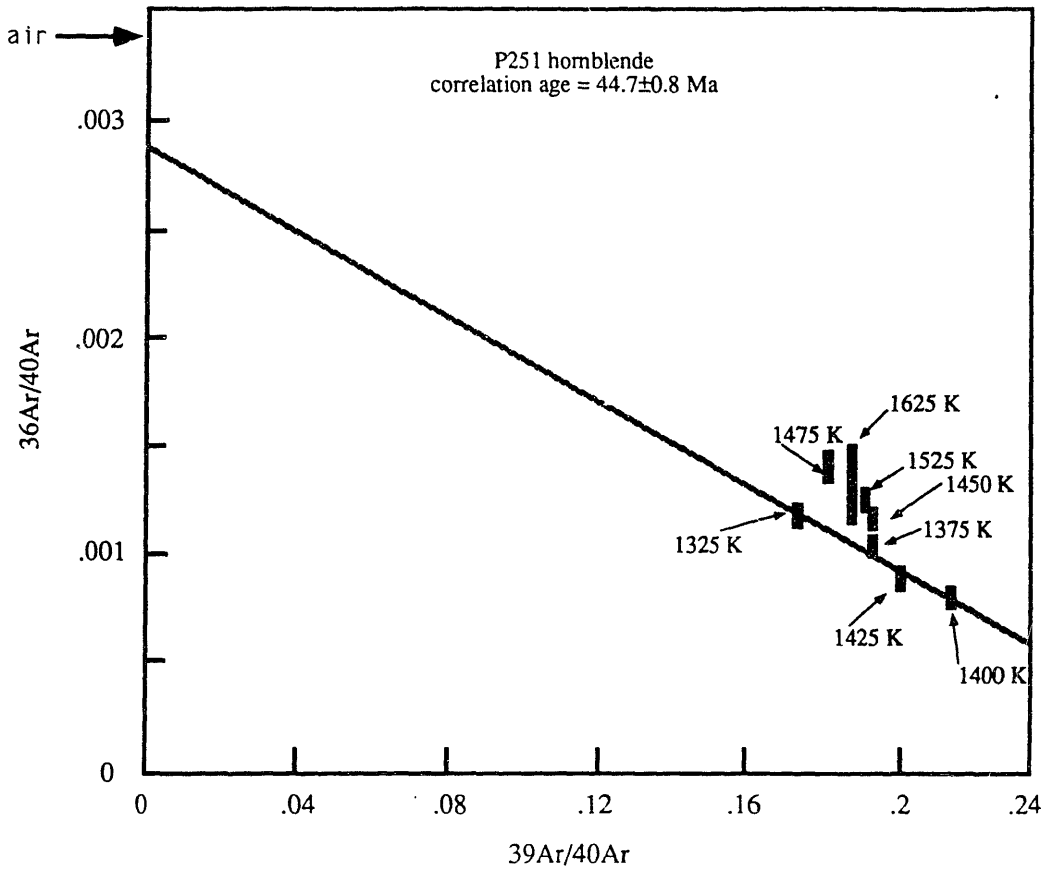

P285 K-feldpsar

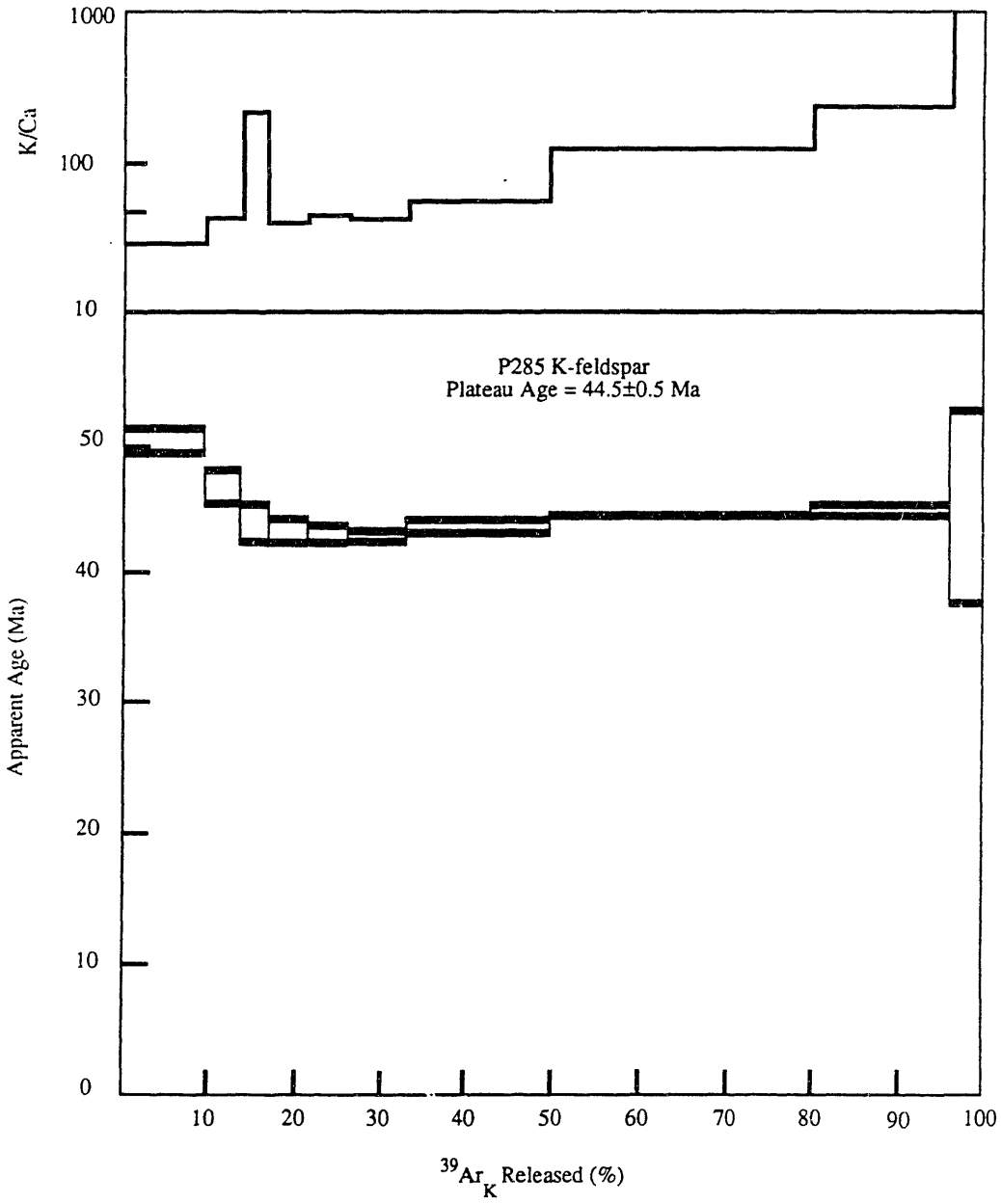

P443 K-feldspar

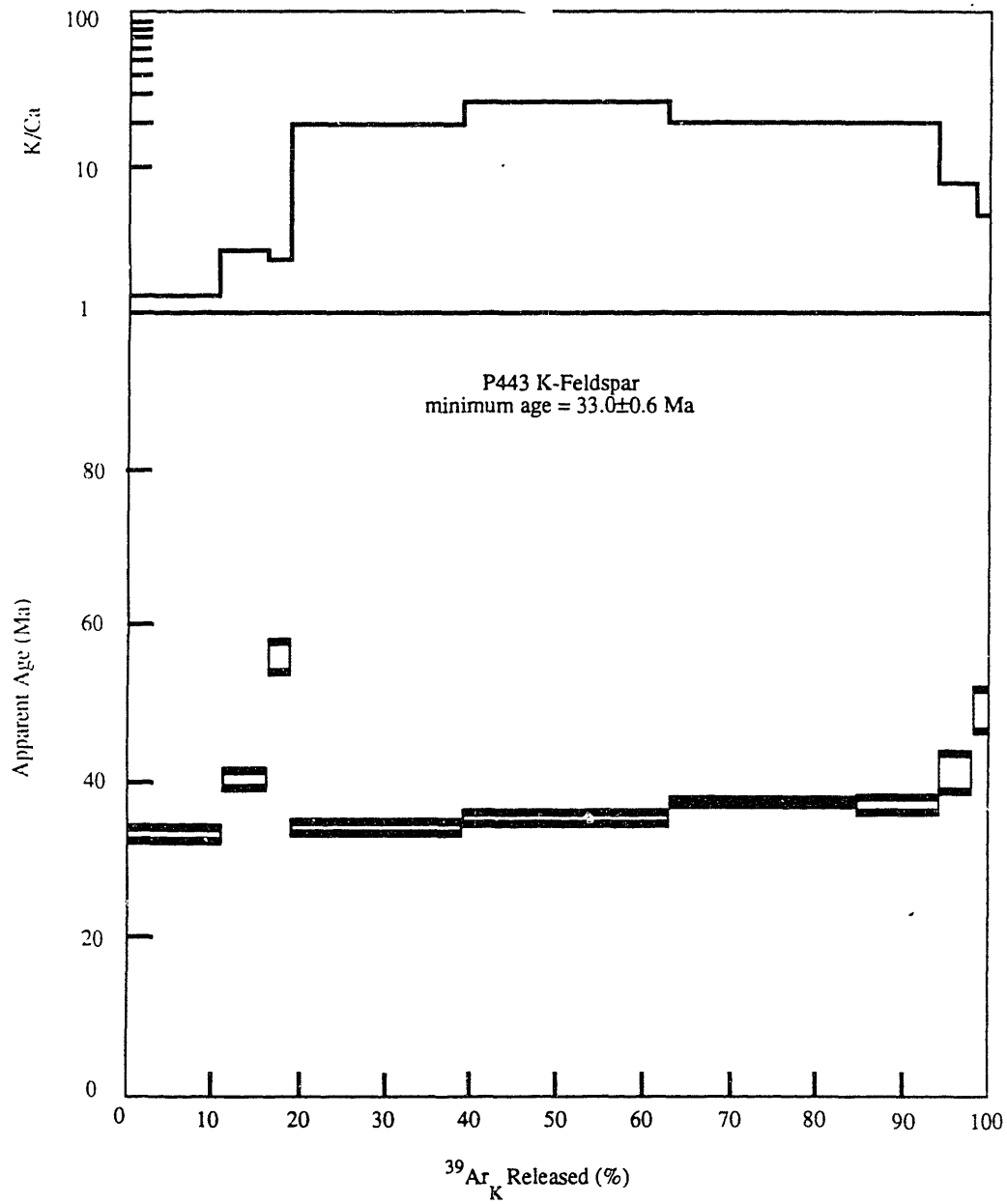

P447 hornblende

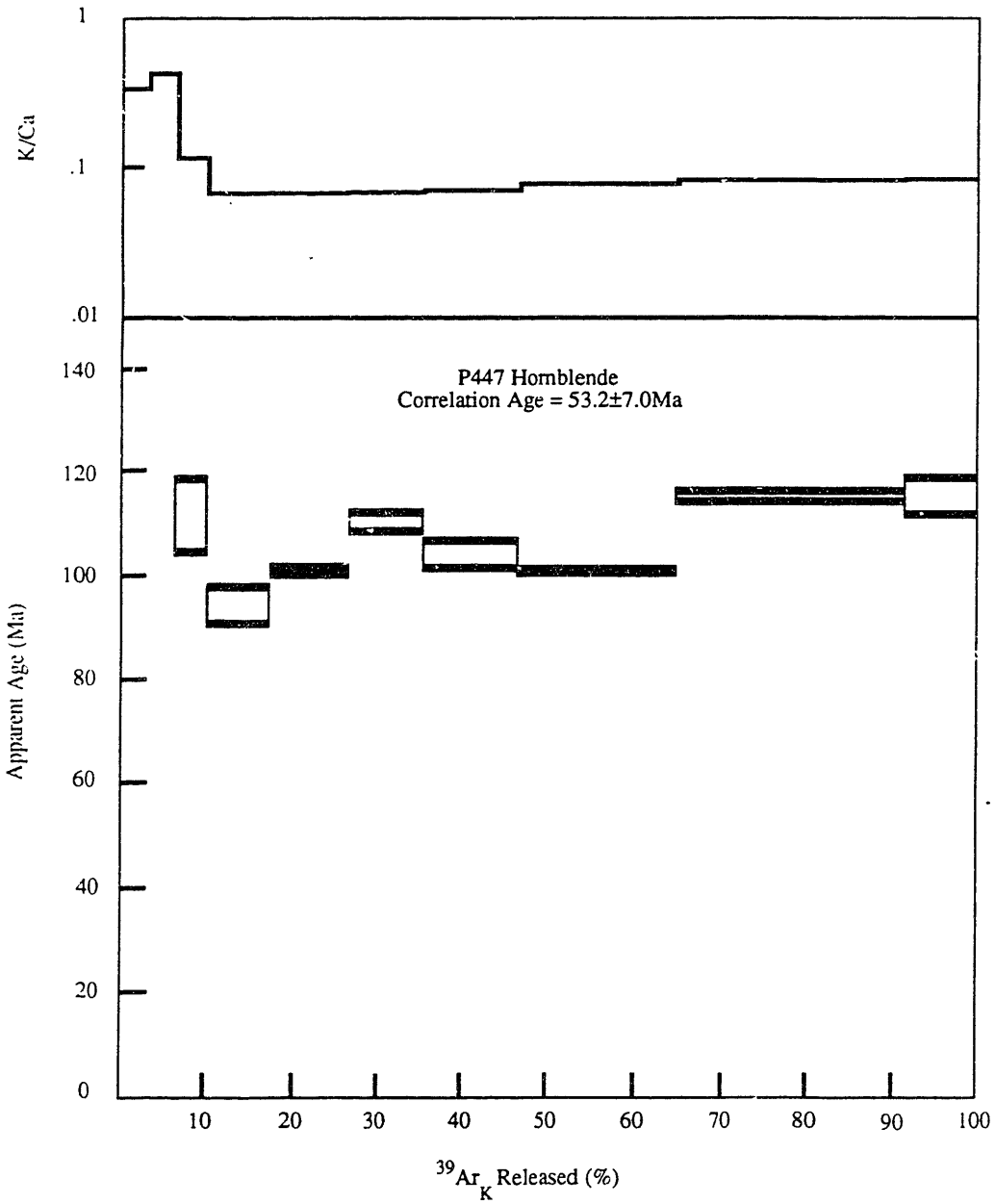

P447 hornblende

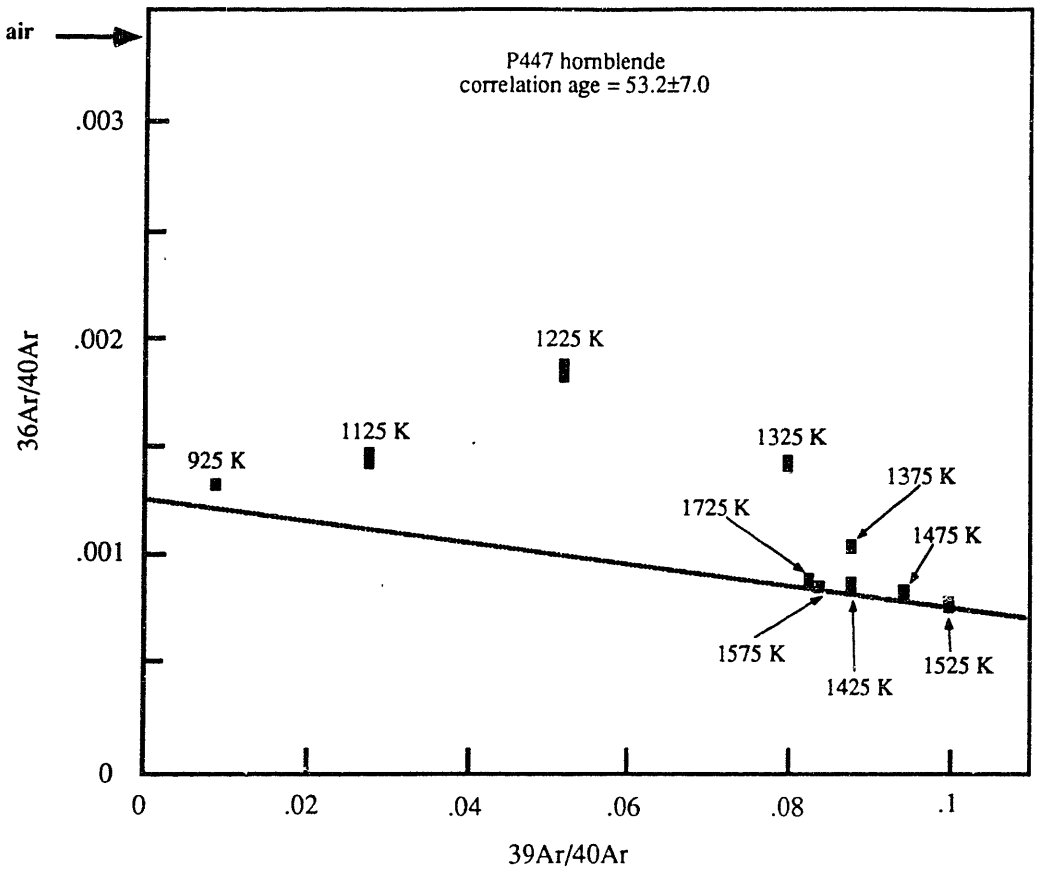

P450C muscovite

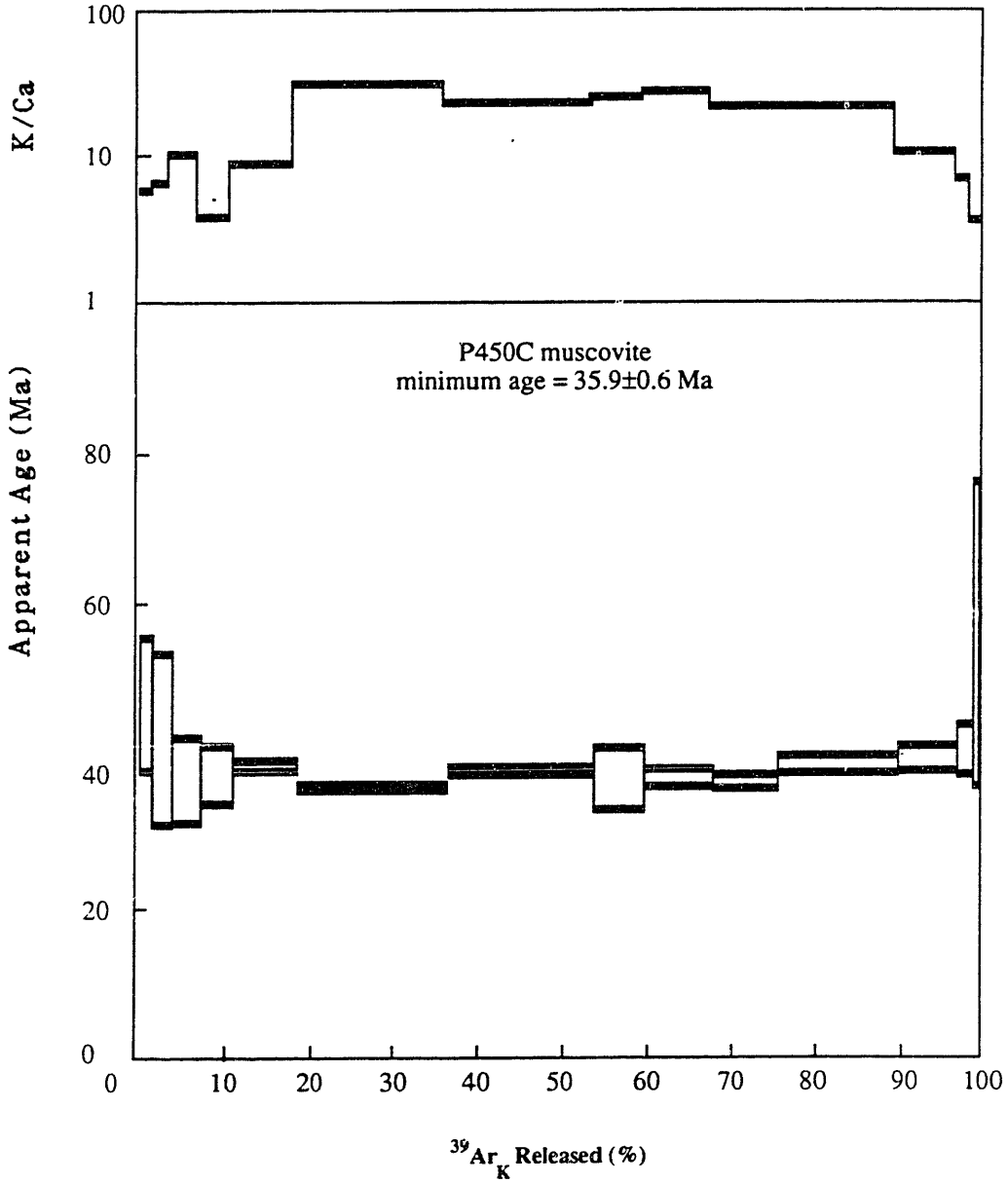

P450C biotite

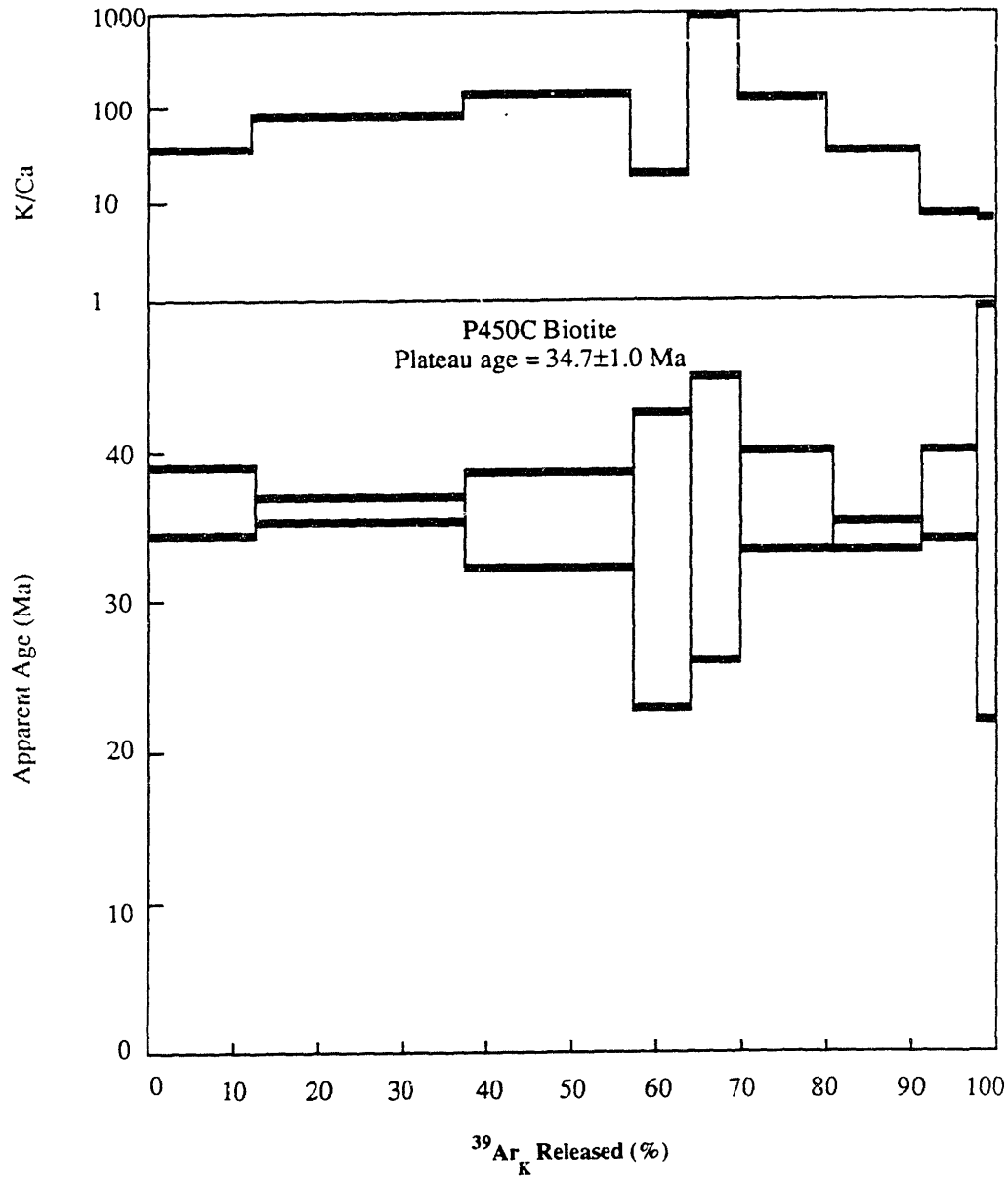

P450E hornblende

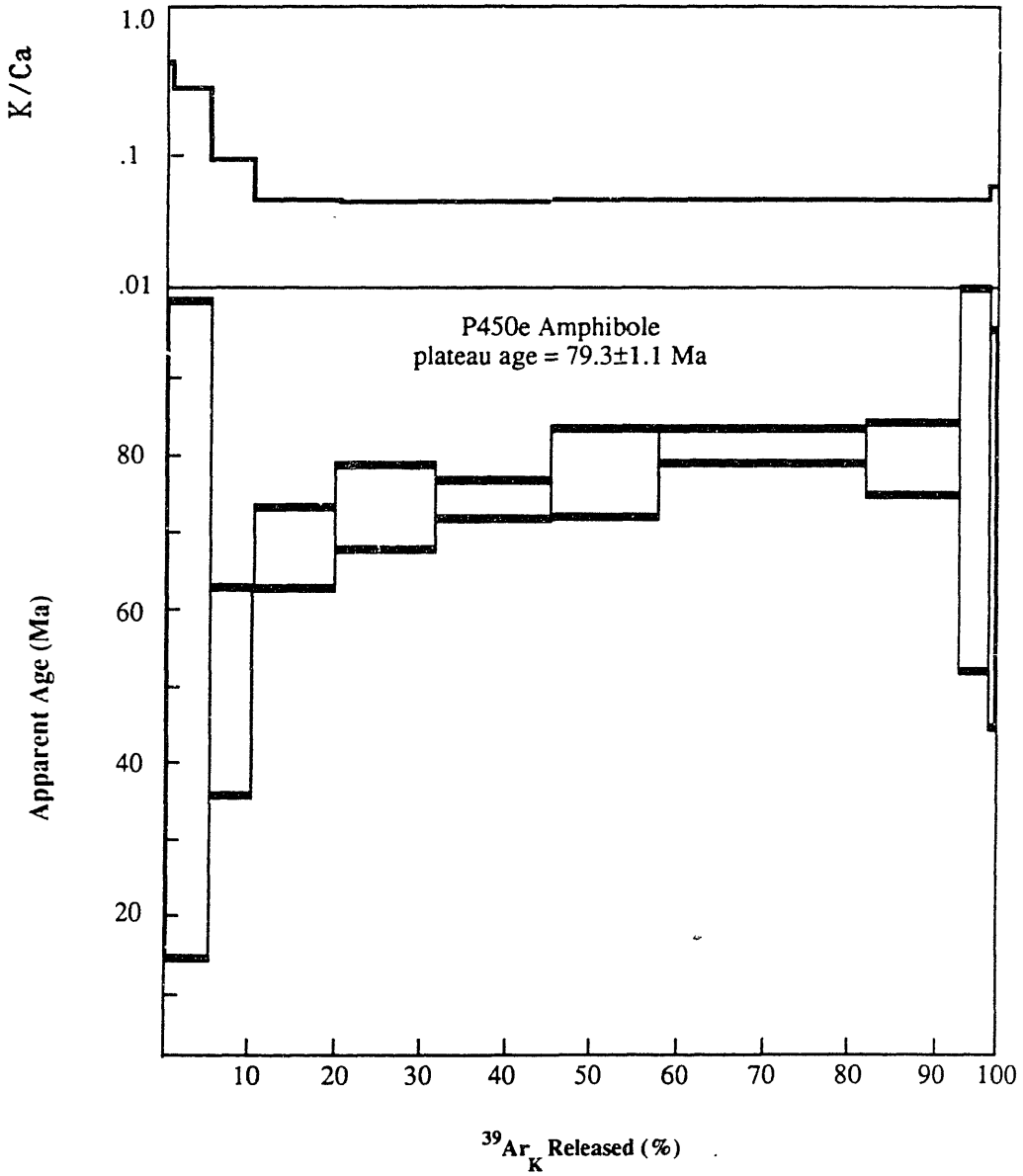

P452 hornblende

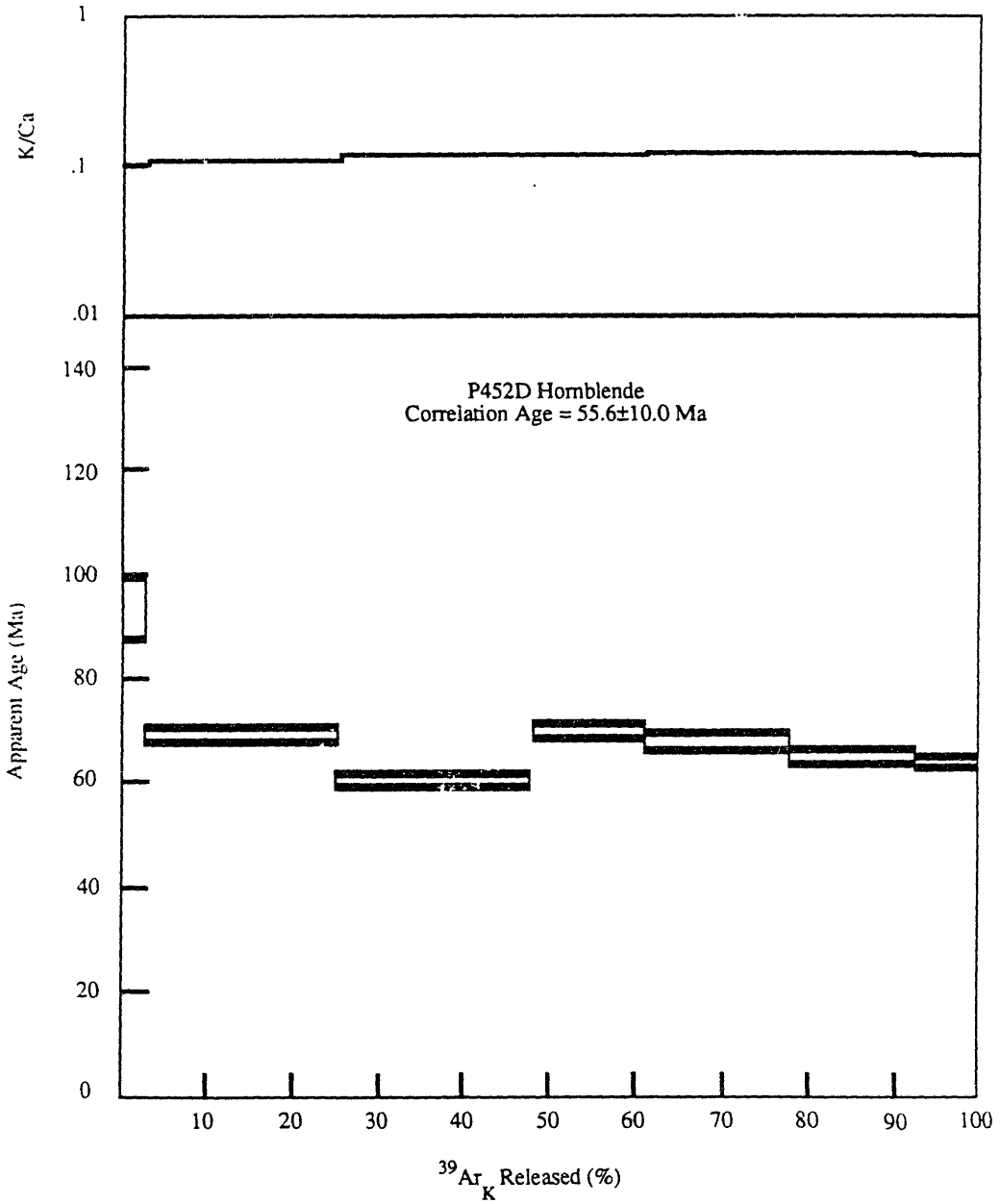

P452 hornblende

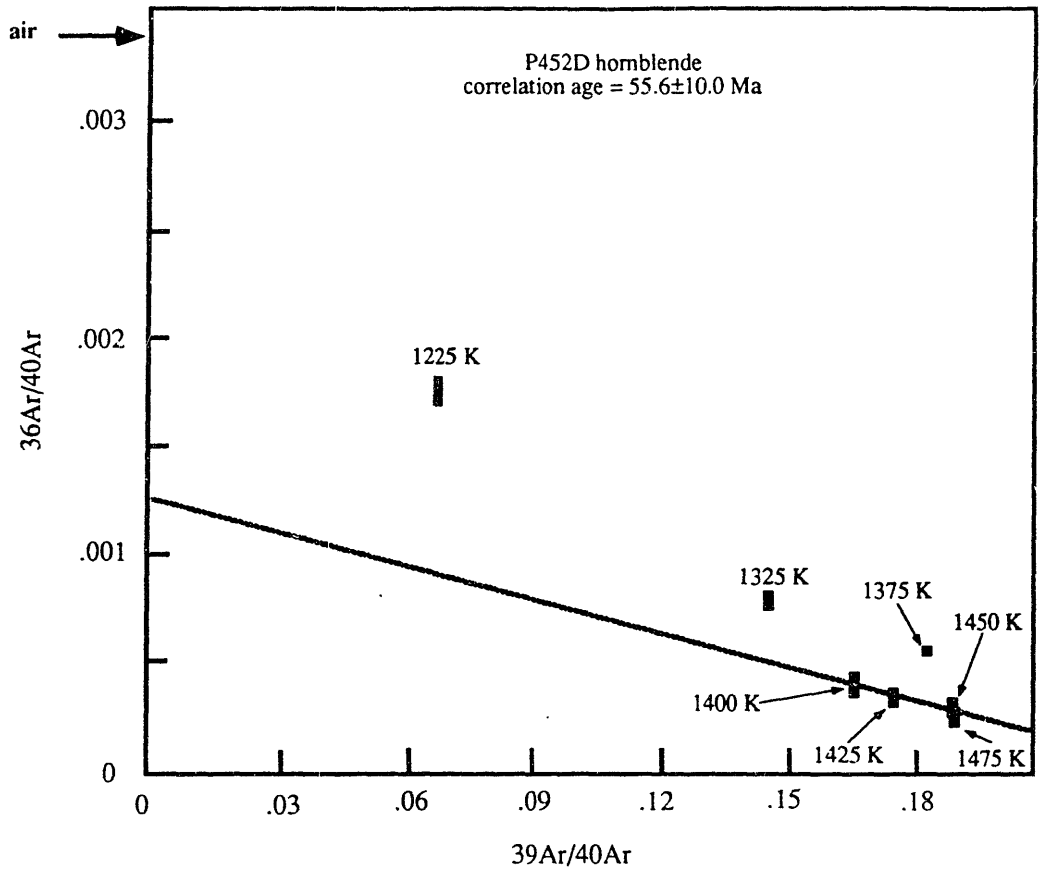

## References


Armstrong, R.L., Geochronometry of the Eocene volcanic-plutonic episode in Idaho, *Northwest Geology, 3,* 1-15, 1974.

Armstrong, R.L., The geochronometry of Idaho (part1), *Isochron West, 14,* 1-50, 1975.

Armstrong, R.L., The geochronometry of Idaho (part 2), *Isochron West, 15,* 1-34, 1976.

Atwater, B.F., Contemportaneity of the Republic Graben and Okanogan Gneiss Dome - Evidence from the Coyote Creek Pluton, southern Okanogan County, Washington [abs.], *Geol. Soc. Am. Abstr. Programs, 17,* 338, 1985.

Bennett, E.H., Relationship of the Trans-Challis fault system in central Idaho to Eocene basin and range extensions, *Geology, 14,* 481-484, 1986.

Brown, R.L. and Journeay, J.M., Tectonic denudation of the Shuswap metamorphic terrain of southeastern British Columbia, *Geology, 15,* 142-146, 1987.

Compton, R.R., Todd, V.R., Zartman, R.E. and Naeser, C.W., Oligocene and Miocene metamorphism, folding, and low-angle faulting in northwestern Utah, *Geol. Soc. Am. Bull., 8,* 1237-1250, 1977.

Coney, P.J. and Harms, T.A., Cordilleran metamorphic core complexes: Cenozoic extensional relics of Mesozoic compression., *Geology, 12,* 550-554, 1984.

Dallmeyer, R.D., Snoke, A.W. and McKee, E.H., The Mesozoic-Cenozoic tectonothermal evolution of the Ruby Mountains - East Humbolt Range, Nevada - A Cordilleran metamorphic core complex, *Tectonics, 5,* 931-954, 1986.

Dalrymple, U.S. Geol. Surv. Prof. Paper 1176, 1981.

Dover, J.H., Bedrock geology of the Pioneer Mountains, central Idaho, Ph.D., 139 pp., University of Washington, 1966.

Dover, J.H., Bedrock geology of the Pioneer Mountains, Blaine and Custer counties, central Idaho, *Idaho Bureau of Mines and Geology Pamphlet 142, 66,* 1969.

Dover, J.H., Geology of the Boulder-Pioneer wilderness study area, Blaine and Custer counties, Idaho, *U. S. Geol. Surv. Bull. 1497-A,* 21-75, 1981.

Dover, J.H., Geologic map and sections of the central Pioneer mountains, Blaine and Custer counties, *U. S. Geol.Surv. Miscellaneous Investigation Series, I-1319,* 1983.

Fleck, Sutter, J., and Eliot, Interpretation of discordant 40Ar/39Ar age spectra of Mesozoic Tholeiites from Anarctica, *Geochem. Et. Cosmochim. Acta., 41,* 15-32, 1977.

Garmezy, L. and Sutter, J.F., Mylonitization coincident with uplift in an extensional setting, Bitterroot Range, Montana-Idaho, *Geol. Soc. Amer. Abs. w. Prog., 15,* 578, 1983.

Hall, W.E., Stratigraphy of and mineral deposits in middle and upper Paleozoic rocks of the Black-Shale mineral belt, central Idaho, *U. S. Geol. Surv. Bull. , 1658-J,* 117-131, 1986.

Hansen, V.L. and Goodge, J.W., Metamorphism, structural petrology, and regional evolution of the Okanogan complex, northeastern Washington, in *Metamorphism and Crustal Evolution of the Western United States*, edited by Ernst, W.G., pp. 233-270, Prentice Hall, Englewood Cliffs, NJ, 1988.

Haugerud, R.A. and Kunk, M.J, ArAr*, a computer program for reduction of 40Ar-39Ar data, U.S. Geol. Surv. Open File Report 88-261, 1988

Hodges, K.V., Metamorphic and geochronologic constraints on the uplift history of Cordilleran metamorphic core complexes., *Geol. Soc. Amer. Abs. w. Prog., 20,* A18, 1988.

Lister, G.S. and Davis, G.A., The origin of metamorphic core complexes and detachment faults during Tertiary continental extension in the northern Colorado river region, U.S.A., *J. Struct. Geol., 11,* 65-94, 1989.

Lister, G.S. and Snoke, A.W., S-C mylonites, *J. Struct. Geol., 6,* 617-638, 1984.

McDougall, I. and Harrison, T.M., *Geochronology and Thermochronology by the 40Ar/39Ar Method*,, pp. 212, Oxford University Press, New York, 1988.

Miller, E.L. and Gans, P.B., Cretaceous crustal structure and metamorphism in the hinterland of the Sevier thrust belt, western U.S. Cordillera, *Geology, 17,* 59-62, 1989.

Miller, F.K. and Clark, L.D., Geology of the Chewelah-Loon Lake area, Stevens and Spokane Counties, Washington, *U.S. Geol. Surv. Prof. Paper, 805,* 76, 1976.

Molnar, P. and England, P., 1990. JGR.

O'Neill, R.L. and Pavlis, T.L., Superposition of Cenozoic extension on Mesozoic compressional structures in the Pioneer mountains metamorphic core complex, central Idaho, *Geol. Soc. Am. Bull., 100,* 1833-1845, 1988.

Parrish, R.R., Carr, S.D. and Parkinson, D., Metamorphic complexes and extensional tectonics, southern Shuswap complex, southeastern British Columbia, *Geol. Soc. Am. Cordilleran Section, Field Trip Guidebook, Trip 12, 15,* 1985.

Parrish, R.R., Carr, S.D. and Parkinson, D.L., Eocene extensional tectonics and geochronology of the southern Omineca belt, British Columbia and Washington, *Tectonics, 7,* 181-212, 1988.

Rhodes, B.P. and Hyndman, D.W., Regional metamorphism, structure and tectonics of northeastern Washington and northern Idaho, in *Metamorphism and Crustal Evolution of the Western United States*, edited by Ernst, W.G., pp. 271-295, Prentice Hall, Englewood Cliffs, NJ, 1988.

Saltzer, S. and Hodges, K.V., The Middle Mountain shear zone, southern Idaho: Kinematic analysis of a Tertiary, high-temperature detachment, *Geol. Soc. Amer. Bull., 100,* 96-103, 1988.

Schmidt, S.M. and Casey, M., Complete fabric analysis of some commonly observed quartz C-axis patterns, in *Mineral and rock deformation: laboratory studies-The Paterson Volume*, edited by Hobbs, B.E. and Heard, H.C., pp. American Geophysical Union, Washington, D.C., 1986.

Silverberg, D.S., Metamorphic petrology and structure of the Hyndman and East Fork formations of the Pioneer core complex, Idaho [abs.], *Geol. Soc. Am. Abstr. Programs, 18,* 185, 1986.

Silverberg, D.S., Petrologic, 40Ar-39Ar isotopic, and structural constraints on the Tertiary tectonic evolution of the Pioneer core complex, south-central Idaho, *Geol. Soc. Amer. Abs. Programs., 20,* A18, 1988.

Silverberg, D.S., Petrologic constraints on the tectonic evolution of the Pioneer Metamorphic Core Complex, south-central Idaho: depth-temperature-time paths in the upper amphibolite facies, in preparation.

Silverberg, D.S., Multiphase extension in the south-central Idaho region: structural evolution of the Pioneer Metamorphic Core Complex, in preparation.

Skipp, B., Basement thrust sheets in the Clearwater orogenic zone, central Idaho and western Montana, *Geology, 15,* 220-224, 1987.

Skipp, B. and Hait, M.H., Allochthons along the northeastern margin of the Snake River Plain, Idaho, in *Rocky Mountain thrust belt geology and resources: Wyoming Geological Association, 29th Field Conference, Guidebook*, edited by Heisey, E.L., pp. 499-515, 1977.

Snoke, A.W. and Miller, D.M., Metamorphic and tectonic history of the northeastern Great Basin, in *Metamorphism and Crustal Evolution of the Western United States*, edited by Ernst, W.G., pp. 606-648, Prentice-Hall, Englewood Cliffs, NJ, 1988.

Steiger and Jaeger, Subcommision on geochronology: convention of the use of decay constants in geo- and cosmochronology, *Earth and Planetary Science Letters, 36*, 359-362, 1977.

Wernicke, B.P., Low-angle faults in the Basin and Range Province—Nappe tectonics in an extending orogen, *Nature, 291*, 645-648, 1981.

Wust, S.L., Extensional deformation with northwest vergence, Pioneer core complex, central Idaho, *Geology, 14*, 712-714, 1986.

Wust, S.L., Tectonic development of the Pioneer Structural Complex, Pioneer Mountains, central Idaho, Ph.D., 79 pp., University of Arizona, 1986.

## Figure Captions

Fig. 3.1. Simplified regional tectonic map of the Idaho area. Rectangle shows the location of Fig. 3.2. lr = Lost River Range; sb = Sawtooth Batholith; gc = Goose Creek Mountains; am = Albion Mountains; rr = Raft River mountains; bm = Boulder mountains.

Fig. 3.2. Simplified tectonic map of the Pioneer Metamorphic Core Complex, south-central Idaho (after published mapping of J. Dover, 1981 and unpublished mapping of D.S. Silverberg). Points A-A' show the cross-section transect of Fig. 3.4. kc = Kane Creek; whc = Wildhorse Canyon; fc = Fall Creek; cc = Corral Creek; pc = Pioneer Cabin; hc = Hyndman Creek; bb = Big Basin; wr = Wood River; bc = Boulder Creek; kce = East Kane Creek; wkc = West Kane Creek; sc = Summit Creek; ir = Imbricate Ridge. Sample localities are numbered and keyed to Table 3.2.

Fig. 3.3. Tectonic stratigraphic column of the infrastructure in the Pioneer Metamorphic Core Complex. Lithostratigraphy as in Dover, 1983.

Fig. 3.4. Cross-section along the A-A' transect of Fig. 3.2. Unit abbreviations as in Figs. 3.2 & 3.3. pct = Pioneer Cabin Thrust; hsz = Hyndman Shear Zone; wdfs = Wildhorse Detachment Fault System.

Fig. 3.5. Synopsis of deformation events in the Pioneer Metamorphic Core Complex. Tc = cooling age as constrained by $^{40}Ar$-$^{39}Ar$ plateau ages; MM = style & maximum grade of dynamothermal metamorphism (syn-K = syn-kinematic, post-K = post-kinematic); PIS = Pioneer Intrusive Suite.

Fig. 3.6. Timing relationships between petrofabrics and principal porphyroblast growth in the pelitic schist of the Hyndman Group.

Figure 3.7. Radial variation in J-value for a constant vertical geometry in irradiation package RM1 and RM4. All twelve vials in RM4 were evenly spaced about the

periphery of a 2-1/2 inch diameter aluminum can that was sealed at 1 atmosphere in air. All twelve vials in RM1 were evenly spaced about the periphery of an open fused silica bucket (water filled). The analytical uncertainty in J for any vial in RM4, for a constant vertical geometry, is less than or equal to .25%. The variation in J from vial to vial in RM4 is less than or equal to .25%.

Figue 3.8. Temperature-time plot for the Pioneer Intrusive Suite and the Summit Creek Stock. Age uncertainties are 2 s.d. and closure temperature uncertainties as cited in text. U-Pb zircon, $^{40}Ar$-$^{39}Ar$ hornblende, muscovite and biotite ages provide temperature-time points for Pioneer Intrusive Suite. Rb-Sr mineral isochron, $^{40}Ar$-$^{39}Ar$ hornblende, biotite, K-feldspar provide temperature-time points for Summit Creek Stock.

Figure 3.9. Temperature-time plot for the Pioneer Intrusive Suite and high-grade metamorphic tectonites of the Hyndman and East Fork Groups. Age uncertainties are 2 s.d. and closure temperature uncertainties as cited in the text. Hornblende, muscovite and biotite provide temperature-time points.

Figure 3.10. Temperature-time plot for mylonites from the Wildhorse Detachment Fault System. Age uncertainties are 2 s.d. and closure temperature uncertainties as cited in the text. Muscovite, biotite and K-feldspar provide temperature-time points.

Figure 3.11. Generalized cooling curves for various structural positions in the Pioneer Mountains. PCwgc = Precambrian Wildhorse Gneiss Complex; Escs = Eocene Summit Creek Stock; Epis = Eocene Pioneer Intrusive Suite; Owdfs = Oligocene Wildhorse Detachment Fault System.

Table 3.1. Summary of previous geochronologic results.

| SYSTEM | ROCK TYPE | UNIT | MINERAL | AGE | SOURCE | FIELD # |
|---|---|---|---|---|---|---|
| Rb-Sr | quartz monzonite | Escs | w.r.-p-kf-bi | 48.5±3.8 Ma | 1 | RDS-13 |
| Rb-Sr | paragneiss | Xwgc | whole rock | 1480±30 Ma | 1 | 5088 |
| Rb-Sr | orthogneiss | Xwgc | whole rock | 1290±90 Ma | 1 | 5080 |
| U-Pb | quartz monzonite | Epis | zircon | 48.3±0.6 Ma | 1 | RDS-9 |
| K-Ar | quartz monzonite | Epis | hornblende | 52.6±1.3 Ma | 1 | 4356 |
| K-Ar | quartz monzonite | Epis | biotite | 40.2±1.0 Ma | 1 | 4356 |
| K-Ar | quartz monzonite | Epis | biotite | 44.7±1.3 Ma | 2 | 66-74 |
| K-Ar | quartz monzonite | Epis | biotite | 46.0±1.4 Ma | 2 | 66-336 |
| K-Ar | granodiorite | Epis | hornblende | 65.9±1.6 Ma | 1 | 4309 |
| K-Ar | dioritic gneiss | Epis | biotite | 38.3±1.1 Ma | 3 | 64-472 |
| K-Ar | quartz monzonite | Escs | hornblende | 48.5±2.0 Ma | 1 | RDS-13 |
| K-Ar | quartz monzonite | Escs | biotite | 45.3±1.4 Ma | 2 | 66-11 |
| K-Ar | pelitic schist | Yps | whole rock | 36.2±1.1 Ma | 3 | 7.8.65.8a |
| K-Ar | pelitic schist | Yps | biotite | 43.7±1.3 Ma | 3 | 8.14.10a |
| K-Ar | pelitic schist | Yps | biotite | 38.0±1.1 Ma | 3 | 8.14.11a |
| K-Ar | migmatitic gneiss | Xwgc | biotite | 42.2±1.3 Ma | 3 | 66-342 |
| K-Ar | quartz monzonite | Enfdc | hornblende | 47.7±1.1 Ma | 1 | 5212 |

1 = Zartman, unpublished; 2 = Armstrong, 1975; 3 = Armstrong, 1976.

Xwlg = Precambrian (x?) Wildhorse Gneiss Complex lower gneiss member,
Xwc = Precambrian (X?) Wildhorse Gneiss Complex Marble, Xwm = Precambrian (X?) Wildhorse Gneiss Complex mafic schist,
Ygq = Precambrian (Y?) gneissose quartzite formation of the Hyndman Group, Oc = Clayton Mine Quartzite formation of the East Fork Group,
Ed = Eocene dike, Escs = Eocene Summit Creek Stock
Epis = Eocene Pioneer Intrusive Suite, Enfdc = Eocene North Fork Dike Complex.

Table 3.2. Summary of new 40Ar-39Ar ages.

| SAMPLE # | SITE | UNIT | ROCK TYPE | MINERAL | AGE |
|---|---|---|---|---|---|
| P92 | 1 | Epis | granodiorite | hornblende | 50.3±0.6 Ma (C) |
| P106A | 2 | Xwlg | Q-F gneiss | k-feldspar | 44.2±0.5 Ma (NP) |
| P106B | 2 | Xwlg | mafic schsit | hornblende | 49.5±0.8 Ma (C) |
| P110* | 2 | Ed | hypabyssal mafic dike | hornblende | 46.8±3.4 Ma (C) |
| P110 | 2 | Ed | hypabyssal mafic dike | biotite | 37.8±0.4 Ma (F) |
| P139 | 3 | Oc | quartzite | muscovite | 36.4±0.3 Ma (P) |
| P141 | 3 | Ygq | mica schsit | muscovite | 36.6±0.3 Ma (P) |
| P143 | 3 | Ygq | mafic schist | hornblende | 42.9±0.8 Ma (C) |
| P143 | 3 | Ygq | mafic schist | biotite | 37.9±0.4 Ma (P) |
| P155 | 4 | Epis | dioritic gneiss | biotite | 37.5±0.4 Ma (F) |
| P156 | 4 | Epis | granodioritic gneiss | hornblende | 44.6±0.3 Ma (P) |
| P156 | 4 | Epis | granodioritic gneiss | biotite | 36.8±0.4 Ma (F) |
| P251 | 5 | Epis | granodioritic gneiss (m) | hornblende | 44.7±0.8 Ma (C) |
| P251 | 5 | Epis | granodioritic gneiss (m) | biotite | 35.2±0.4 Ma (F) |
| P285 | 6 | Escs | quartz monzonite | biotite | 47.1±0.6 Ma (F) |
| P285 | 6 | Escs | quartz monzonite | k-feldspar | 44.5±0.5 Ma (P) |
| P443 | 7 | Epis | quartz monzonite (m) | k-feldspar | 33.0±0.6 Ma (M) |
| P447 | 8 | Xwm | amphibolitic schist | hornblende | 53.2±7.0 Ma (C) |
| P450C | 8 | Xwm | psammitic schist (m) | muscovite | 35.9±0.6 Ma (M) |
| P450C | 8 | Xwm | psammitic schist (m) | biotite | 34.7±1.0 Ma (P) |
| P450D | 8 | Xwm | psammitic schist (m) | biotite | 36.1±0.4 Ma (F) |
| P450E | 8 | Xwm | amphibolitic schist (m) | hornblende | 79.3±1.1 Ma (P) |
| P452D | 8 | Xwm | amphibolitic schist | hornblende | 55.6±10.0 Ma (C) |

M = Minimum, P = Plateau with atmospheric 40/36, NP = Near Plateau with atmospheric 40/36
C = Correlation Age, * = increment lost during experiment and not plotted.

Xwlg = Precambrian (x?) Wildhorse Gneiss Complex lower gneiss member,
Xwc = Precambrian (X?) Wildhorse Gneiss Complex Marble, Xwm = Precambrian (X?) Wildhorse Gneiss Complex mafic schist,
Ygq = Precambrian (Y?) gneissose quartzite formation of the Hyndman Group,
Oc = Clayton Mine Quartzite formation of the East Fork Group, Ed = Eocene dike,
Epis = Eocene Pioneer Intrusive Suite, Escs = Eocene Summit Creek Stock.

Table 3.3. Isotope Correlation Data.

| Sample | P92 hornblende |
|---|---|
| Steps Included | 1475 K, 1525 K, 1625 K, 1725 K |
| Steps Excluded | 1375 K, 1425 K |
| % of Total 39ArK represented by regressed data | 61.4 |
| MSWD | 2.145 |
| Initial 40Ar/36Ar | 389.3±7.5 |
| 39Ar/40Ar | 0.127 |
| Apparent Age from Correlation Diagram | 50.3±0.6 Ma |

| Sample | P106B hornblende |
|---|---|
| Steps Included | 1225 K, 1325 K, 1375 K, 1425 K, 1475 K |
| Steps Excluded | 1525 K, 1575 K, 1725 K |
| % of Total 39ArK represented by regressed data | 69.5 |
| MSWD | 2.4 |
| Initial 40Ar/36Ar | 417.1±7.2 |
| 39Ar/40Ar | 0.264 |
| Apparent Age from Correlation Diagram | 49.5±0.8 Ma |

| Sample | P110 hornblende |
|---|---|
| Steps Included | 1375 K, 1425 K, 1525 K, 1725 K |
| Steps Excluded | NONE |
| % of Total 39ArK represented by regressed data | 100 |
| MSWD | 0.716 |
| Initial 40Ar/36Ar | 332.41±13.34 |
| 39Ar/40Ar | 0.134 |
| Apparent Age from Correlation Diagram | 46.8±3.4 |

| Sample | P143 hornblende |
|---|---|
| Steps Included | 1325 K, 1425 K, 1525 K, 1625 K, 1675 K |
| Steps Excluded | 975 K, 1125 K |
| % of Total 39ArK represented by regressed data | 96.4 |
| MSWD | 0.7 |
| Initial 40Ar/36Ar | 320.9±5.8 |
| 39Ar/40Ar | 0.3 |
| Apparent Age from Correlation Diagram | 42.9±0.8 Ma |

| Sample | P251 hornblende |
|---|---|
| Steps Included | 1325 K, 1375 K, 1400 K, 1425 K |
| Steps Excluded | 1450 K, 1475 K, 1525 K, 1625 K |
| % of Total 39ArK represented by regressed data | 76.2 |
| MSWD | 1.4 |
| Initial 40Ar/36Ar | 347.0±18.9 |
| 39Ar/40Ar | 0.296 |
| Apparent Age from Correlation Diagram | 44.7±0.8 Ma |

| | |
|---|---|
| Sample | P447 hornblende |
| Steps Included | 1425 K, 1475 K, 1525 K, 1575 K, 1725 K |
| Steps Excluded | 925 K, 1125 K, 1225 K, 1325 K, 1375 K |
| % of Total 39ArK represented by regressed data | 73.5 |
| MSWD | 0.6 |
| Initial 40Ar/36Ar | 797.4±33.2 |
| 39Ar/40Ar | 0.247 |
| Apparent Age from Correlation Diagram | 53.2±7.0 Ma |

| | |
|---|---|
| Sample | P452D hornblende |
| Steps Included | 1400 K, 1425 K, 1450 K, 1475 K |
| Steps Excluded | 1225 K, 1325 K, 1375 K |
| % of Total 39ArK represented by regressed data | 52.0 |
| MSWD | 0.634 |
| Initial 40Ar/36Ar | 807.9±230.3 |
| 39Ar/40Ar | 0.237 |
| Apparent Age from Correlation Diagram | 55.6±10.0 Ma |

Figure 3.1

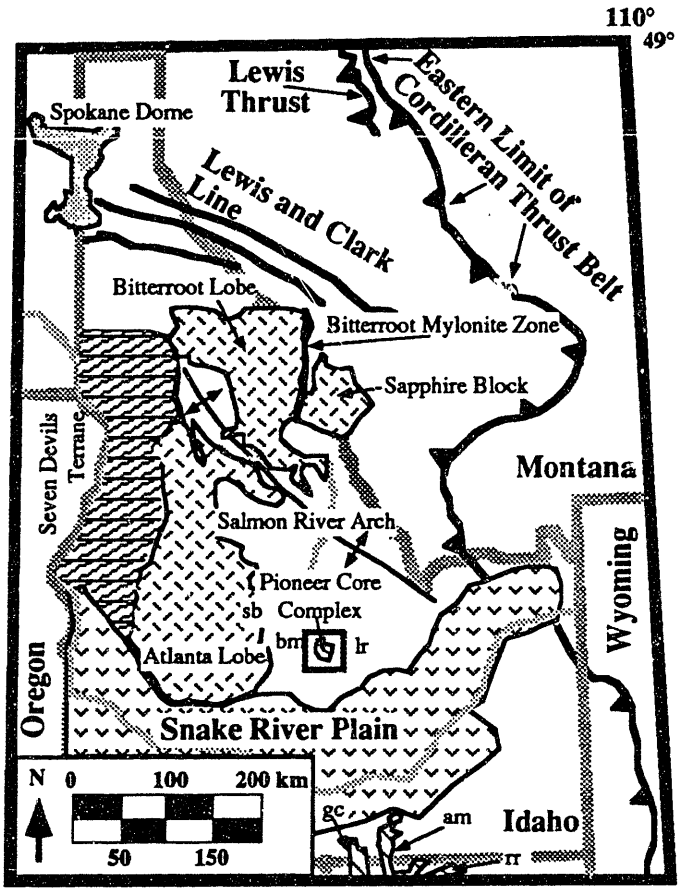
110°
49°
Lewis Thrust
Eastern Limit of Cordilleran Thrust Belt
Spokane Dome
Lewis and Clark Line
Bitterroot Lobe
Bitterroot Mylonite Zone
Sapphire Block
Seven Devils Terrane
Montana
Salmon River Arch
Pioneer Core
sb Complex
bm
lr
Atlanta Lobe
Wyoming
Oregon
Snake River Plain
N 0 100 200 km
50 150
gc
am
Idaho
rr

Figure 3.2

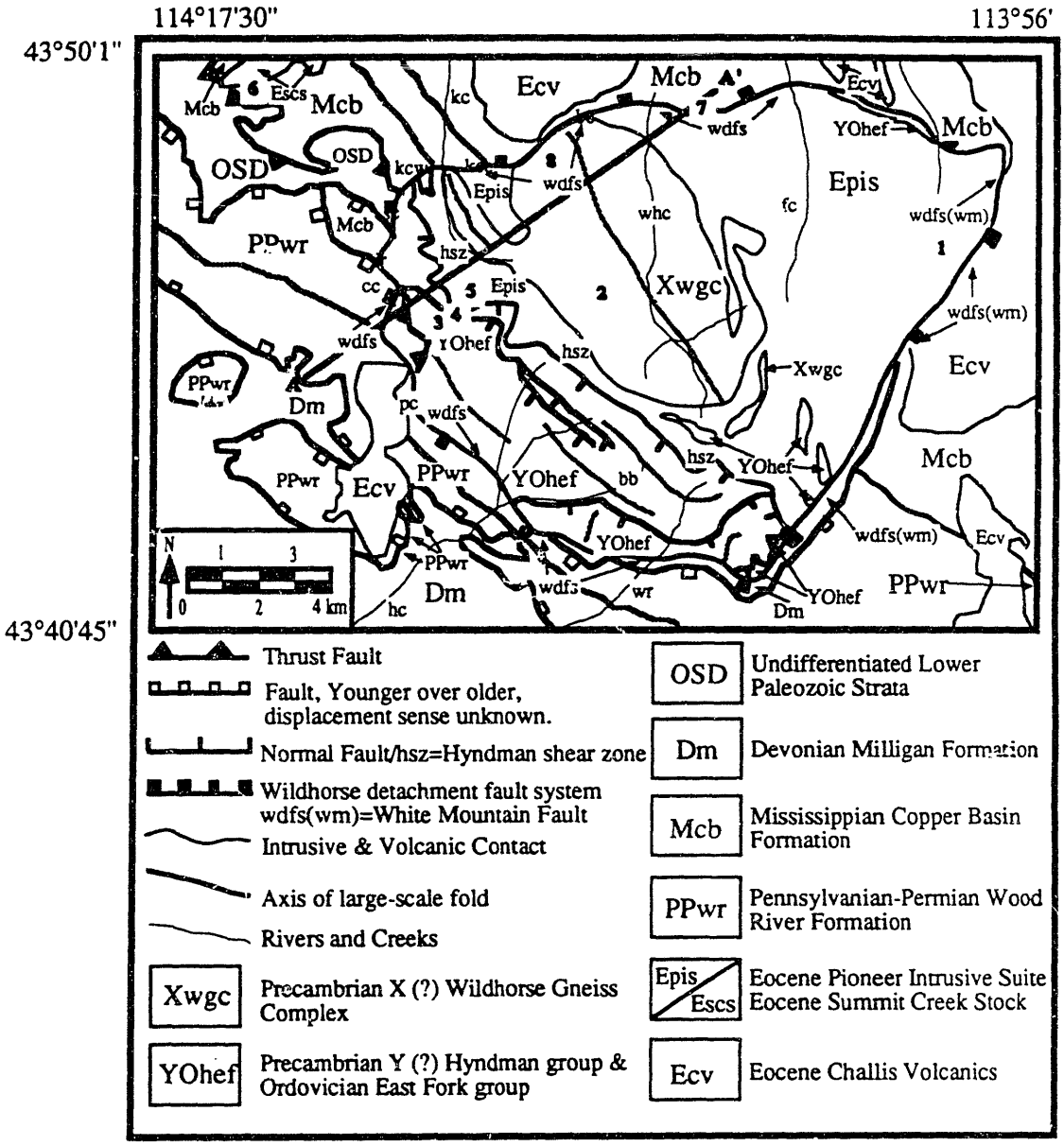
114°17'30"
113°56'
43°50'1"
43°40'45"
Mcb
Escs
kc
Ecv
A
A'
wdfs
YOhef
Epis
OSD
kcw
whc
fc
wdfs(wm)
PPwr
hsz
cc
Xwgc
Dm
pc
bb
0 2 4 km
hc
wr
Thrust Fault
Fault, Younger over older, displacement sense unknown.
Normal Fault/hsz=Hyndman shear zone
Wildhorse detachment fault system
wdfs(wm)=White Mountain Fault
Intrusive & Volcanic Contact
Axis of large-scale fold
Rivers and Creeks
Precambrian X (?) Wildhorse Gneiss Complex
Precambrian Y (?) Hyndman group & Ordovician East Fork group
Undifferentiated Lower Paleozoic Strata
Devonian Milligan Formation
Mississippian Copper Basin Formation
Pennsylvanian-Permian Wood River Formation
Eocene Pioneer Intrusive Suite
Eocene Summit Creek Stock
Eocene Challis Volcanics

Figure 3.3

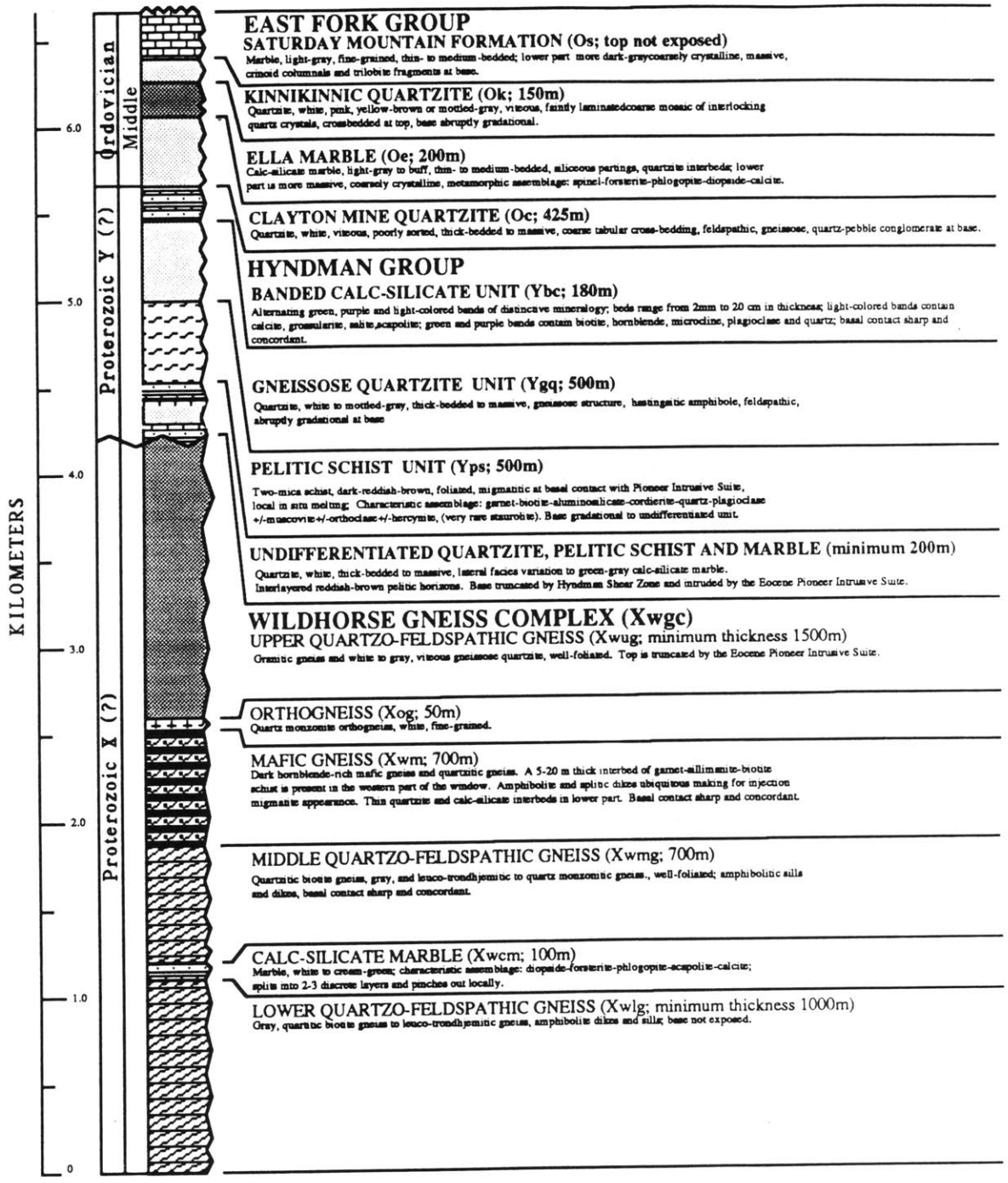
KILOMETERS
6.0
5.0
4.0
3.0
2.0
1.0
0
Ordovician
Middle
Proterozoic Y (?)
Proterozoic X (?)
EAST FORK GROUP
SATURDAY MOUNTAIN FORMATION (Os; top not exposed)
Marble, light-gray, fine-grained, thin- to medium-bedded; lower part more dark-gray coarsely crystalline, massive, crinoid columnals and trilobite fragments at base.
KINNIKINNIC QUARTZITE (Ok; 150m)
Quartzite, white, pink, yellow-brown or mottled-gray, vitreous, faintly laminated coarse mosaic of interlocking quartz crystals, crossbedded at top, base abruptly gradational.
ELLA MARBLE (Oe; 200m)
Calc-silicate marble, light-gray to buff, thin- to medium-bedded, siliceous partings, quartzite interbeds; lower part is more massive, coarsely crystalline, metamorphic assemblage: spinel-forsterite-phlogopite-diopside-calcite.
CLAYTON MINE QUARTZITE (Oc; 425m)
Quartzite, white, vitreous, poorly sorted, thick-bedded to massive, coarse tabular cross-bedding, feldspathic, gneissose, quartz-pebble conglomerate at base.
HYNDMAN GROUP
BANDED CALC-SILICATE UNIT (Ybc; 180m)
Alternating green, purple and light-colored bands of distinctive mineralogy; beds range from 2mm to 20 cm in thickness; light-colored bands contain calcite, grossularite, salite,scapolite; green and purple bands contain biotite, hornblende, microcline, plagioclase and quartz; basal contact sharp and concordant.
GNEISSOSE QUARTZITE UNIT (Ygq; 500m)
Quartzite, white to mottled-gray, thick-bedded to massive, gneissose structure, hastingsitic amphibole, feldspathic, abruptly gradational at base
PELITIC SCHIST UNIT (Yps; 500m)
Two-mica schist, dark-reddish-brown, foliated, migmatitic at basal contact with Pioneer Intrusive Suite, local in situ melting; Characteristic assemblage: garnet-biotite-aluminosilicate-cordierite-quartz-plagioclase +/-muscovite+/-orthoclase+/-hercynite, (very rare staurolite). Base gradational to undifferentiated unit.
UNDIFFERENTIATED QUARTZITE, PELITIC SCHIST AND MARBLE (minimum 200m)
Quartzite, white, thick-bedded to massive, lateral facies variation to green-gray calc-silicate marble. Interlayered reddish-brown pelitic horizons. Base truncated by Hyndman Shear Zone and intruded by the Eocene Pioneer Intrusive Suite.
WILDHORSE GNEISS COMPLEX (Xwgc)
UPPER QUARTZO-FELDSPATHIC GNEISS (Xwug; minimum thickness 1500m)
Granitic gneiss and white to gray, vitreous gneissose quartzite, well-foliated. Top is truncated by the Eocene Pioneer Intrusive Suite.
ORTHOGNEISS (Xog; 50m)
Quartz monzonite orthogneiss, white, fine-grained.
MAFIC GNEISS (Xwm; 700m)
Dark hornblende-rich mafic gneiss and quartzitic gneiss. A 5-20 m thick interbed of garnet-sillimanite-biotite schist is present in the western part of the window. Amphibolite and aplitic dikes ubiquitous making for injection migmatite appearance. Thin quartzite and calc-silicate interbeds in lower part. Basal contact sharp and concordant.
MIDDLE QUARTZO-FELDSPATHIC GNEISS (Xwmg; 700m)
Quartzitic biotite gneiss, gray, and leuco-trondhjemitic to quartz monzonitic gneiss., well-foliated; amphibolitic sills and dikes, basal contact sharp and concordant.
CALC-SILICATE MARBLE (Xwcm; 100m)
Marble, white to cream-green; characteristic assemblage: diopside-forsterite-phlogopite-scapolite-calcite; splits into 2-3 discrete layers and pinches out locally.
LOWER QUARTZO-FELDSPATHIC GNEISS (Xwlg; minimum thickness 1000m)
Gray, quartzitic biotite gneiss to leuco-trondhjemitic gneiss, amphibolite dikes and sills; base not exposed.

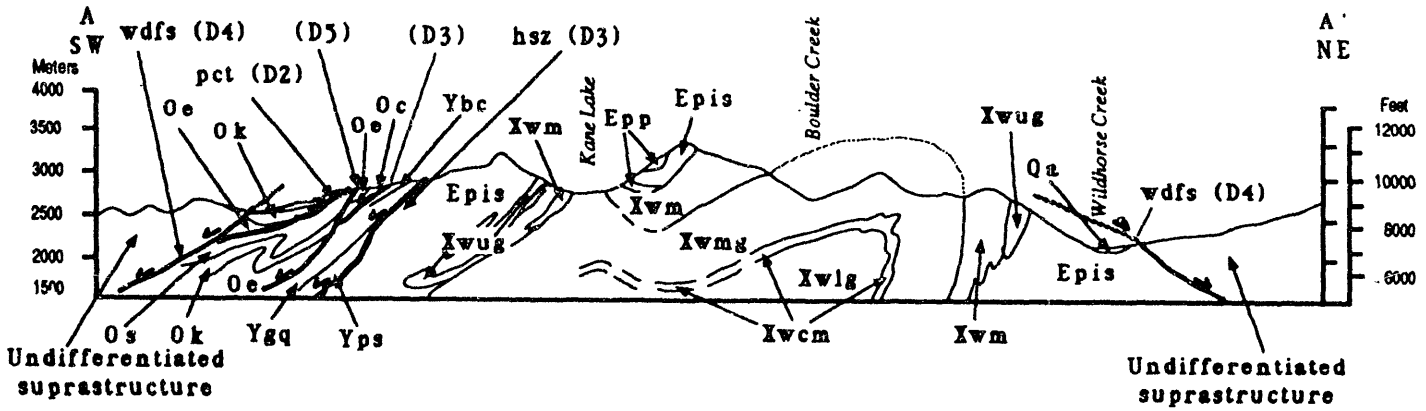
A
SW
wdfs (D4)
(D5)
(D3)
hsz (D3)
pct (D2)
Meters
4000
3500
3000
2500
2000
1500
Oe
Ok
Oe
Oc
Ybc
Xwm
Kane Lake
Epp
Epis
Boulder Creek
Xwug
Qa
Wildhorse Creek
wdfs (D4)
A'
NE
Feet
12000
10000
8000
6000
Epis
Xwm
Xwug
Xwmg
Xwlg
Epis
Oe
Os
Ok
Ygq
Yps
Xwcm
Xwm
Undifferentiated
suprastructure
Undifferentiated
suprastructure

Figure 3.4

| ROCK UNIT | D1 | D2 | D3 | D4 | D5 |
|---|---|---|---|---|---|
| | | Tc (800K) = 79 ma | Tc (800K) = 46 ma | Tc (675-475K) = 36-33 ma | |
| Eocene Pioneer Intrusive Suite | | | S3: N65°W, 30°SW; L3: S10°W, Late D3 Emplacement | S4: variable; L4: N68W; MM: greenschist facies; brittle D4 superimposed on ductile | Local brittle extension along NE-SW axis of extension |
| Precambrian-Ordovician Hyndman and East Fork Groups | | F2: NW Trend, isoclinal, recumbent Axial Plane SW Dip MM: syn-kinematic amphibolite facies Post F2 Thrust Faults | Pre-PIS emplacment of allochthons; Syn-PIS Hyndman Shear Zone; protomylonite, S3: N65°W, 30°SW; MM: Syn-K: Sill, Cdt; post-K: Garnet | S4: variable; L4: N68W; MM: greenschist facies; brittle D4 superimposed on ductile | Local brittle extension along NE-SW axis of extension |
| Precambrian Wildhorse Gneiss Complex | Cryptic dome & basin interference patterns suggest an early deformation event. | F2: NW Trend, isoclinal, overturned Axial Plane: SW dip MM: syn-kinematic amphibolite facies | F3: Broad megascale folds, NNW-SSE trend; Minor Intraformational Faults | S4: variable; L4: N68W; MM: greenschist facies; brittle D4 superimposed on ductile | Local brittle extension along NE-SW axis of extension |

Figure 3.5

Figure 3.6

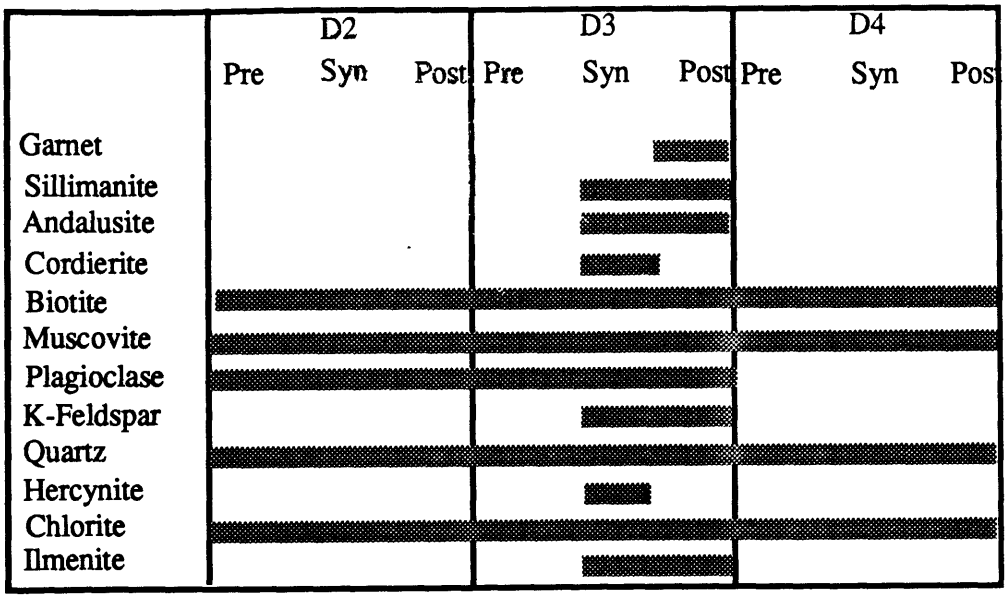
D2
D3
D4
Pre
Syn
Post
Pre
Syn
Post
Pre
Syn
Pos
Garnet
Sillimanite
Andalusite
Cordierite
Biotite
Muscovite
Plagioclase
K-Feldspar
Quartz
Hercynite
Chlorite
Ilmenite

Figure 3.7

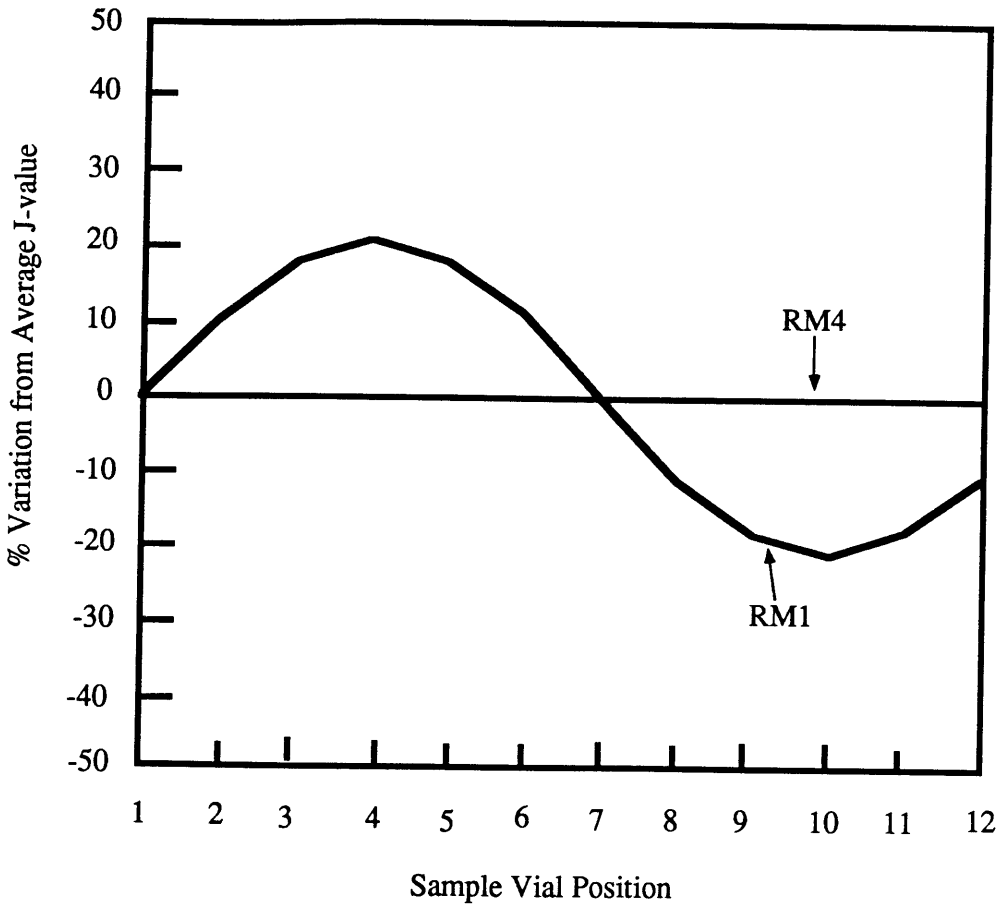
50
40
30
20
10
0
-10
-20
-30
-40
-50
% Variation from Average J-value
RM4
RM1
1
2
3
4
5
6
7
8
9
10
11
12
Sample Vial Position

Figure 3.8

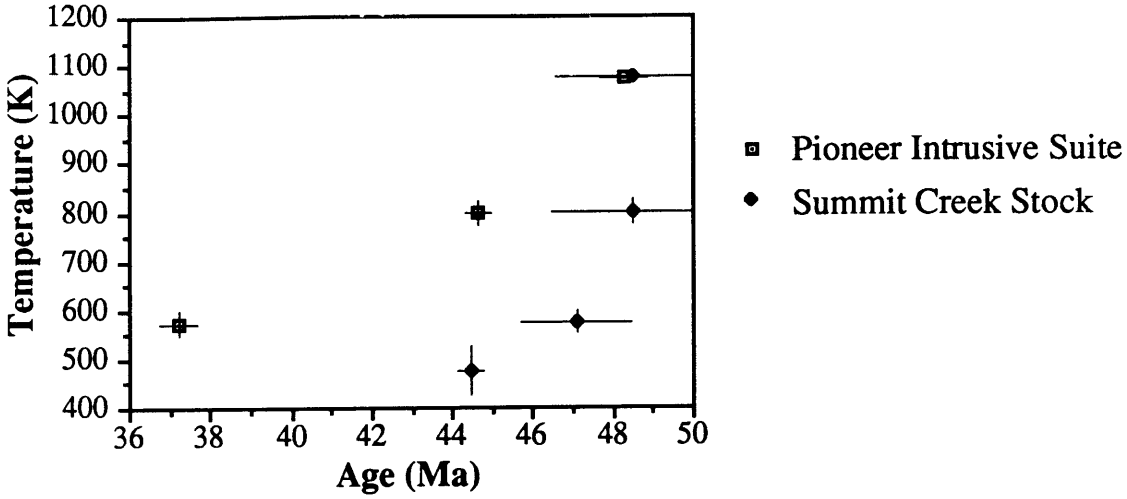
Temperature (K)
1200
1100
1000
900
800
700
600
500
400
36
38
40
42
44
46
48
50
Age (Ma)
Pioneer Intrusive Suite
Summit Creek Stock

Figure 3.9

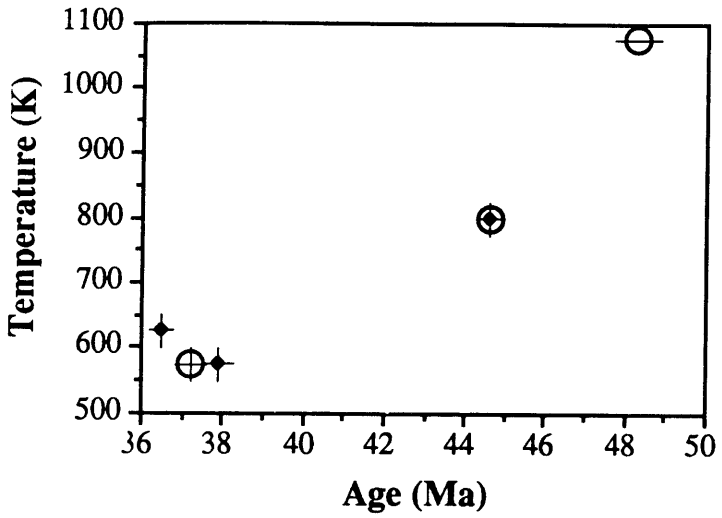
1100
1000
900
800
700
600
500
Temperature (K)
36
38
40
42
44
46
48
50
Age (Ma)

Figure 3.10

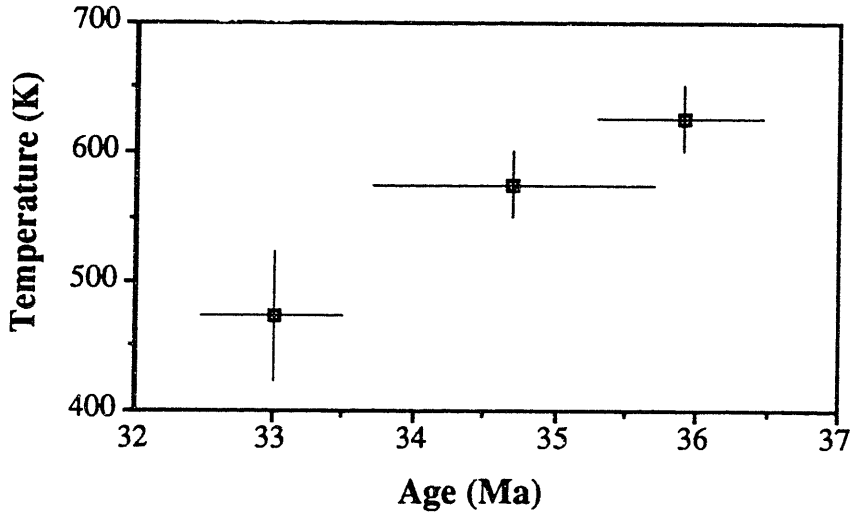

Figure 3.11

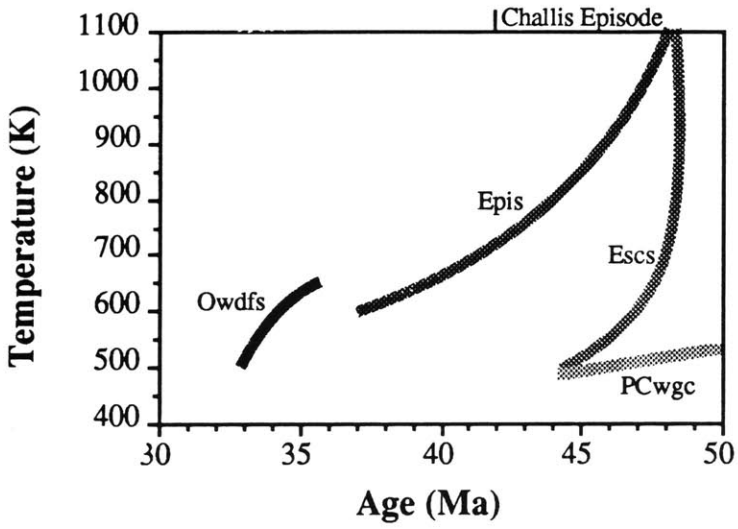
Challis Episode
Epis
Escs
Owdfs
PCwgc
Temperature (K)
1100
1000
900
800
700
600
500
400
30
35
40
45
50
Age (Ma)

CHALLIS NATIONAL FOREST

SAWTOOTH NATIONAL FOREST

PIONEER MOUNTAINS

Epis Xwus Xwm Xwmg Xwcm Xwlg Xwug Qa Qc Qd Qr Oc Oe Ok Os Ybc Yps Ygq

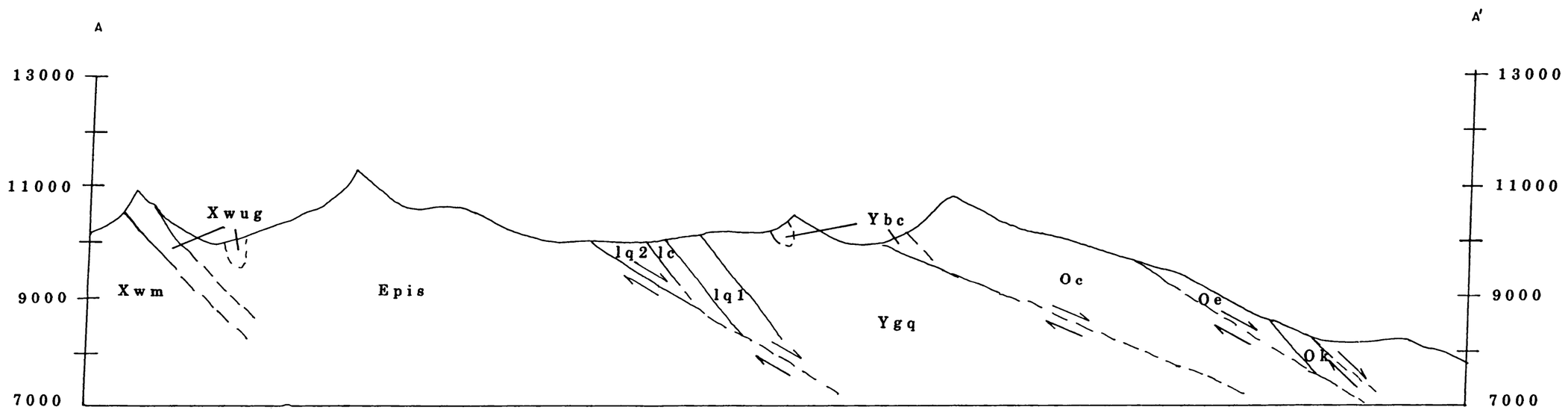
A
A'
13000
11000
9000
7000
Xwug
Xwm
Epis
lq2 lc
lq1
Ybc
Ygq
Oc
Oe
Ok

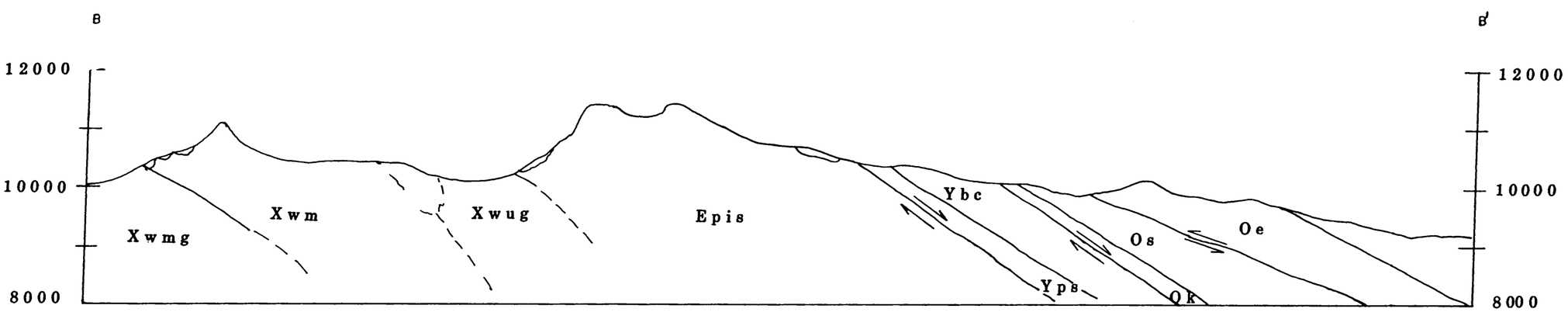
B
B'
12000
10000
8000
Xwmg
Xwm
Xwug
Epis
Ybc
Yps
Os
Ok
Oe